European Journal of Anatomy

Volume 28 - Number 5 September 2024

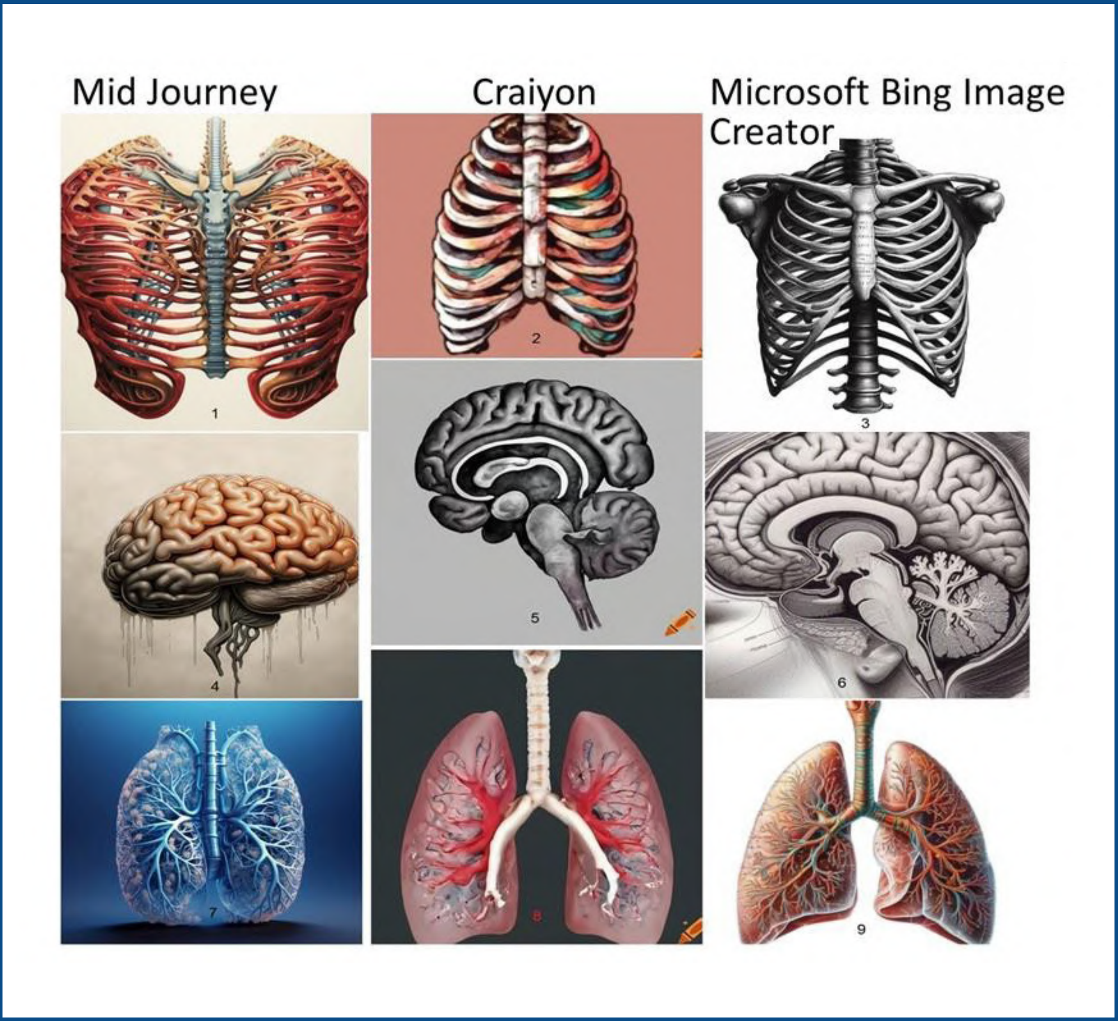

Indexed in:

CLARIVATE
- JCR:2020
- Q4 (21/23)
- I.F. J.C.I.: 0.19

DIALNET
EMBASE / Excerpta Medica

SCOPUS
- SJCR: 2020
- Q4 (31/39)
- I.F.: 0.162

Emerging Sources Citation Index
LATINDEX. Catálogo v1.0 (2002-2017)

Official Journal
of the Spanish
Society of Anatomy

Published by: **LOKI & DIMAS**

European Journal of Anatomy

Volume 28 - Number 5 September 2024

ORIGINAL ARTICLES

CASE REPORTS

TEACHING IN ANATOMY

LETTER TO THE EDITOR

ORIGINAL ARTICLE

Eur J Anat, 28 (5): 525-532 (2024)

The applicability of dental age estimation based on the staging and atlas approaches in Indonesian children and adolescents

Arofi Kurniawan[1], Prasetyaning A. Damayanti[1], An'nisaa Chusida[1], Beta N. Rizky[1], Beshlina F.W.R. Prakoeswa[1], Mieke S. Margaretha[1], Destiana H. Putri[1], Nabila A. Putri[1], Anand Marya[2,3]

[1] *Department of Forensic Odontology, Faculty of Dental Medicine, Universitas Airlangga, Surabaya, Indonesia*

[2] *Department of Orthodontics, Faculty of Dentistry, University of Puthisastra, Phnom Penh, Cambodia*

[3] *Center for Transdisciplinary Research, Saveetha Dental College, Saveetha Institute of Medical and Technical Science, Saveetha University, Chennai, India*

SUMMARY

Accurate age estimation holds paramount importance across various fields, encompassing forensic sciences, civil law, and the medicolegal domain. The applicability of the staging and atlas method for calculating dental age in Indonesian children and adolescents was assessed for this purpose. This study encompassed 104 orthopantomographs from outpatients (54 males and 50 females, aged 5-18 years) at the Airlangga University Dental Hospital in Surabaya, Indonesia. An analysis was conducted to determine the significance of the difference and the correlation between chronological age (CA) and estimated dental age (EDA). The findings unveiled a robust correlation between CA and EDA, with correlation coefficients surpassing 0.9 for both approaches. Although the London Atlas method exhibited a marginally lower Mean Absolute Error (MAE) of 0.81 years in comparison to the Nolla method's MAE of 0.88 years, the difference between the two was deemed insignificant. The outcomes of this study provide valuable insights into the utility of the Nolla and London Atlas methods for estimating dental age among Indonesian youth. However, it is imperative to note that further investigations are warranted to validate these findings and to ascertain the generalizability of these methods across diverse populations.

Key words: Adolescent – Dental age estimation – Forensic dentistry – Human rights – Jurisprudence

INTRODUCTION

The Interpol Disaster Victim Identification (DVI) Guide 2018 recommends three primary methods for identifying humans: deoxyribonucleic acid (DNA), fingerprints, and dental records (INTERPOL, 2018). The field of forensic sciences has seen a significant rise in interest in dental identification due to the valuable information that teeth may offer, including characteristics such as sex, age, and population affinity (Grover

---

Corresponding author:
Arofi Kurniawan, DDS., Ph.D. Department of Forensic Odontology, Faculty of Dental Medicine, Universitas Airlangga, Jl. Mayjend. Prof. Dr. Moestopo 47 Surabaya 60132, Indonesia. E-mail: arofi.kurniawan@fkg.unair.ac.id

Submitted: January 25, 2024. **Accepted:** March 1, 2024

https://doi.org/10.52083/UJVG7422

et al., 2012). Accurately determining an individual's age holds great significance across forensic sciences, civil law, and medicolegal domains, encompassing areas such as school enrollment, marriage, employment, and the establishment of criminal responsibility (Sousa et al., 2020; Ishwarkumar et al., 2022). The precise age documentation is vital in addressing legal inquiries and upholding human rights. Additionally, age estimation is crucial in identifying unknown human remains, particularly in scenarios involving crime scenes and mass disasters (Cameriere et al., 2009; Kurniawan et al., 2022; Prakoeswa et al., 2022). Assessing the dental age of a patient is one of the most important aspects of orthodontic diagnosis, especially for planning and initiating fixed appliance orthodontic therapy. Sukhia et al. demonstrated that initiating orthodontic treatment at a later stage in patients with delayed dental maturity resulted in reduced treatment duration and enhanced treatment stability (Sukhia et al., 2012).

The Arbeitsgemeinschaft für Forensische Altersdiagnostik (AGFAD) study group specializing in forensic age diagnostics proposes three examinations for achieving reliable age estimation results: a physical examination, radiographic assessment of the left hand, and dental evaluation (Schmeling et al., 2016; Paz Cortés et al., 2019). Dental age estimation encompasses the assessment of tooth development, histological changes, and biochemical analysis. The development and eruption sequences of permanent teeth are considered highly accurate age indicators in children due to their minimal susceptibility to external influences. Similarly, the progression of the third molar serves as a dependable parameter for estimating the biological age of adolescents (Erbudak et al., 2012; Naik et al., 2017). Regarding dental age estimation, the literature supports the preference for radiographic methods due to their cost-effectiveness, non-invasive nature, ease of use, and applicability to both living and deceased individuals (Sharma and Wadhwan, 2020).

Previous studies indicate that variations in developmental rates within some populations can impact age estimations. It is advisable to consider population-specific criteria for individuals with known population affinity. However, for circumstances when the population affinity is unknown it is preferable to use aging standards derived from a diverse sample (Adams et al., 2019). The precision of an age-estimating method is affected by the possibility of correctly interpreting the teeth's staging and the statistical methodologies used. Therefore, it is essential to consider population-specific standards and the potential impact of different developmental rates on the accuracy of dental age estimation methods (Mohammed et al., 2015)

The present study aims to evaluate the efficacy of dental age estimation methods in Indonesian children and adolescents by assessing the staging and atlas approaches. The results of this research will increase understanding and practical application of dental age estimation techniques in Indonesian youths, thus facilitating forensic identification and supporting law enforcement efforts.

MATERIALS AND METHODS

The current study obtained ethical approval from the Faculty of Dental Medicine Universitas Airlangga (permit number: 479/HRECC.FODM/VII/2021). A cross-sectional retrospective study utilized orthopantomography (OPG) to scrutinize 104 outpatients (54 males and 50 females) aged 5 to 18 years at the Airlangga University Dental Hospital in Surabaya, Indonesia. The inclusion criteria consisted of high-quality digital OPGs together with the presence of patients' age and sex information. The exclusion criteria included radiographs that were insufficient for visualizing tooth development, radiographs taken from patients using orthodontic appliances, and radiographs from patients with systemic diseases.

This study assesses the chronological age (CA) and estimated dental age (EDA) using teeth development indicators. The calculation of CA involved subtracting the patient's birthdate from the date of the OPG examination, resulting in a decimal number. The EDA was assessed using two techniques: the Nolla method, which classifies dental maturation into ten stages per tooth (ranging from stage 0, indicating the absence of calcification, to stage 10, indicating complete closure of the tooth's apex), and the London Atlas of Tooth

Development method, which presents visual depictions of each tooth's development and eruption stage through colored diagrams (Nolla, 1960; AlQahtani et al., 2010) The staging determination and EDA calculation were performed three times, with a two-week interval between each measurement, to confirm the reproducibility of the results.

The statistical analysis of this study utilized IBM® SPSS® Statistics version 23.0 (IBM, Armonk, NY, USA) with a 95% confidence interval. Descriptive statistics were employed to summarize data, including the age difference, mean absolute error (MAE), and discrepancies between sexes and age groups. Overestimation of age was defined as a positive difference between DA and CA, while a negative value denoted underestimation.

The intraclass correlation coefficient (ICC) test was used to assess the reliability of the measurements. The Wilcoxon signed-rank test was utilized to compare the performance of EDA and CA within the different approaches. The differences between DA and CA were calculated and compared based on sex and age group to evaluate the accuracy of dental age estimation. Pearson's correlation test was also conducted to examine the correlation between CA and EDA using the London Atlas and Nolla methods.

RESULTS

This study examined 104 digital OPGs from outpatients at Airlangga University Dental Hospital, comprising 54 males and 50 females. The average chronological age (CA) for the study group was 11.61 ± 3.58 years. Males had an average CA of 11.53 ± 3.53 years, while females had an average CA of 11.70 ± 3.67 years. The reliability of EDA calculation using the London Atlas and Nolla methods was deemed excellent, as evidenced by an ICC value exceeding 0.9.

Table 1 presents a summary of the mean EDA using both the London Atlas and Nolla methods. The overall mean EDA using the London Atlas was 12.09 ± 3.59 years, with males and females showing mean EDA values of 12.09 ± 3.54 years and 12.08 ± 3.67 years, respectively. The disparity between CA and EDA using the London Atlas method varied among groups, with values of 0.48 ± 0.92 years for the entire subjects, 0.56 ± 0.75 years for males, and 0.38 ± 1.08 years for females. In the 14.00–14.99 age group, there was an observed underestimation of -0.31 years. The MAE for the entire study population was 0.81 years, indicating a statistically significant difference between CA and EDA ($p<0.05$). For males, the MAE was 0.76 ($p<0.05$), while for females, it was 0.87 ($p<0.05$). Notably, the London Atlas method exhibited

Table 1. Descriptive analysis of the chronological age (CA) and estimated dental age (EDA) using the London Atlas and Nolla's method.

Subjects	**CA**	**London Atlas**			**Nolla**		
		x̄ + SD	**Age diff.**	**MAE**	**x̄ + SD**	**Age diff.**	**MAE**
All subjects	11.61+3.58	12.09+3.59	+0.48*	0.81	11.75+3.25	+0.14	0.88
Male	11.53+3.53	12.09+3.54	+0.56*	0.76	12.08+3.25*	+0.55	0.96
Female	11.70+3.67	12.08+3.67	+0.38*	0.87	11.39+3.25	-0.31	0.79
Age group							
5.00 - 5.99	5.47 + 0.29	6.50+0.00	+1.03	1.03	6.78+0.38	+1.31	1.31
6.00 - 6.99	6.44 + 0.25	7.13+0.52	+0.68	0.69	7.46+0.78	+1.02	1.07
7.00 - 7.99	7.59 + 0.27	8.14+0.81	+0.55	0.62	8.55+0.75	+0.96	0.99
8.00 - 8.99	8.57 + 0.26	9.06+0.53	+0.48	0.55	8.74+0.70	+0.17	0.58
9.00 - 9.99	9.44 + 0.24	10.06+0.53	+0.61	0.61	9.78+0.60	+0.33	0.54
10.00-10.99	10.49+0.26	10.72+0.97	+0.23	0.60	10.59+0.72	+0.10	0.42
11.00-11.99	11.58+0.26	12.13+1.19	+0.55	1.09	11.33+1.43	-0.24	1.27
12.00-12.99	12.55+0.29	13.50+1.15	+0.95	1.13	13.48+1.83	+0.92	1.38
13.00-13.99	13.47+0.36	14.00+1.31	+0.53	1.17	13.42+1.42	-0.05	0.94
14.00-14.99	14.47+0.39	14.17+1.86	-0.31	1.19	13.56+1.77	-0.92	1.14
15.00-15.99	15.43+0.24	15.50+1.15	+0.07	0.95	14.90+0.66	-0.52	0.61
16.00-16.99	16.43+0.26	16.79+0.83	+0.36	0.65	15.76+1.07	-0.67	0.90
17.00-17.99	17.31+0.19	18.10+0.55	+0.79	0.79	17.40+0.89	+0.09	0.59

CA chronological age, *SD* standard deviation, *MAE* mean absolute error
+ indicates overestimation, – indicates underestimation, * indicates a significant difference between CA and EDA

the lowest MAE in the 8.00-8.99 age group (0.55 years) and the highest MAE in the 14.00-14.99 age group (1.19 years).

On the other hand, employing Nolla method yielded a mean EDA of 11.75 ± 3.25 years for the entire study population. The overall age difference between EDA and CA using Nolla method was 0.14 ± 1.18 years, a non-significant finding ($p>0.05$). In terms of sexes, males demonstrated an overestimation of EDA (0.55 ± 1.08 years), while females exhibited an underestimation (-0.31 ± 1.14 years). Specific age groups, namely 11.00–11.99 and 13.00–16.99, displayed underestimation ranging from -0.05 to 0.92 years. The MAE values for Nolla method in the entire study population, males and females, were 0.88, 0.96, and 0.79, respectively (refer to Table 1). The age group with the smallest MAE using Nolla method was 10.00-10.99 (0.42 years), while the highest MAE was observed in the 12.00-12.99 age group (1.38 years). Notably, the mean age difference using Nolla method was not statistically significant for females ($p>0.05$), whereas for males, there was a statistically significant difference between the mean CA and EDA ($p<0.05$).

While evaluating the entire subject population, the London Atlas method exhibited a lower MAE compared to the Nolla method. However, the Mann-Whitney U test did not reveal a statistically significant difference in MAE between the London Atlas and Nolla methods ($p>0.05$). Pearson's correlation test results showed a noteworthy correlation between CA and EDA in both the London Atlas and Nolla methods, with correlation coefficients of 0.967 and 0.945, respectively (see Table 2).

Table 2. Correlation of the chronological age (CA) with estimated dental age (EDA) in total subjects, males and females.

Group	Methods	Correlation with CA	
		***r*-value**	***p*-value**
Total	London Atlas	0.967	<0.05*
	Nolla	0.945	<0.05*
Male	London Atlas	0.978	<0.05*
	Nolla	0.953	<0.05*
Female	London Atlas	0.957	<0.05*
	Nolla	0.953	<0.05*

* Indicates a significant correlation between CA and EDA

DISCUSSION

Accurate dental age estimation holds significant importance in forensic sciences, particularly when determining the chronological age of individuals without proper legal records. The discourse on dental age estimation in children and adolescents encompasses several vital considerations. This discussion is centered on identifying the most precise and reliable methods for assessing dental age, taking into account factors such as tooth development, eruption patterns, and root formation (Kurniawan et al., 2020; Schmeling, 2023). The progression of permanent tooth development typically follows a sequential timeline, with first molars emerging around ages 6 to 7, incisors between 6 and 9, canines around 9 to 12, and concluding with the eruption of the third molars at approximately age 21 (Singh and Juneja, 2007).

The assessment of dental age in children through the analysis of tooth morphology using dental radiography is widely recognized as a highly dependable technique for age estimation, applicable to both deceased and living individuals. OPG is preferred for age estimation in children and adolescents among various imaging techniques due to challenges in obtaining distortion-free intraoral radiographs (Grover et al., 2012). The accuracy of dental age estimation holds immense significance in forensic sciences, ensuring that the estimated age closely corresponds to the actual chronological age. Over time, advancements in dental age estimation methods have introduced various approaches, including the atlas and staging methods explicitly tailored for age estimation in children and adolescents (Lewis and Senn, 2015).

This study evaluated the effectiveness of two distinct methods for estimating dental age in children and adolescents. The staging approach was assessed using the Nolla method, while the atlas approach was evaluated based on the London Atlas of Tooth Developments. A total of 104 OPGs were meticulously selected, ensuring ethnic homogeneity among subjects to account for potential variations in tooth development across different populations. The analysis of both methods revealed a general tendency to overestimate EDA compared to CA, with the Nolla method showing a more negligible age difference that was not statistically significant. Moreover, when assessing age differences based on sexes, the Nolla method indicated underestimation in female subjects, while the London Atlas demonstrated overestimation in both males and females.

The Nolla method utilizes a scale from 1 to 10 to intricately categorize tooth development stages, aiming for greater precision in dental age estimation. This approach evaluates the calcification stages of seven permanent tooth buds, encompassing the central incisor to the second molar, in both the upper and lower jaws (Kırzıoğlu and Ceyhan, 2012). Nevertheless, an ongoing debate surrounds the potential influence of expanding the number of developmental stages on observer errors and the overall accuracy of the outcomes (Hegde et al., 2017).

The present study's findings indicate that the Nolla method demonstrates a heightened level of reliability, as evidenced by the absence of a statistical difference between EDA and CA ($p>0.05$). The MAE associated with the Nolla method in this investigation falls within an acceptable range (MAE=0.88). These results align with previous studies conducted by Nur et al. and Maber et al. on the Turkish, Bangladeshi, and British Caucasian populations. Regarding sex-based EDA using the Nolla method, this study's outcomes are in line with the findings by Koc et al. (2021) of overestimation in males and underestimation in females (Maber et al., 2006; Nur et al., 2012; Koç et al., 2021). Similar trends were also reported by Duruk et al. (2022) and Miloglu et al. (2011), suggesting higher accuracy of the Nolla method in males than females. In our study, a significant age difference was observed in male subjects. Furthermore, within the specific age range of 9 to 11 years, the Nolla method demonstrated increased accuracy for both sexes, with an MAE ranging from 0.42 to 0.54 years. This result coincides with the findings by Duruk et al. (2022) on the Eastern Turkish population. In contrast, a study on a Brazilian population revealed underestimation in both males and females (Kurita et al., 2007; Miloglu et al., 2011; Duruk et al., 2022).

The application of the London Atlas approach in this study resulted in a notable overestimation in both male and female subjects, with an MAE of 0.76 years and 0.87 years, respectively. These findings corroborate the results of previous studies undertaken by Koc et al. (2021) and McCloe et al. (2018), which similarly identified age overestimation through the utilization of the London Atlas approach. In a study conducted by Pavlović et al. (2017) on the Portuguese population, a notable distinction between CA and EDA was found in males, while no statistically significant difference was detected in females. The present study revealed a tendency to underestimate ages between 14 and 14.99 in certain age groups. In addition, Ismail et al. (2018) studied Malay children and discovered that the London Atlas underestimated the ages of ten-year-old and 15-year-olds. In contrast, overestimation was reported in the five-year-old group. Ghafari et al. (2018) reported a decrease in the accuracy of the London Atlas method for individuals older than 12 years. However, the MAE increased from 11 years old in our study. In contrast to our findings, Alsudairi and AlQahtani (2019) found consistent underestimation among Saudi Arabian children aged 6-15, with no statistically significant difference between sexes.

The specific reasons for the observed differences among diverse populations remain unclear. Previous studies have proposed that factors like sample size, distribution, scoring criteria, and statistical analyses may play a role in these variations (Liversidge, 2010). However, recent findings suggest that disparities in dental maturity persist across various populations. Chaillet et al. (2005) conducted a comparative study on dental maturity in eight countries, revealing inter-ethnic differences categorized into three major groups. Additionally, Demirjian et al. (1973) suggested that population-specific standards could enhance the accuracy of converting maturity scores into dental ages, highlighting the impact of population differences on precision. The accuracy of a specific age estimation method may vary across different populations, with one method displaying higher accuracy in one study and the opposite pattern in another study involving a distinct population (McCloe et al. 2018).

In summary, the estimated dental age of the London Atlas and Nolla methods significantly correlates with the chronological age of the Indonesian population. The Nolla method exhibited a smaller age difference, while the London Atlas displayed a diminished MAE. However, a population-specific dental age estimation method is suggested to be developed to achieve more accurate results.

CONCLUSIONS

The careful selection of reliable and culturally appropriate methods for dental age estimation holds significant importance, especially when dealing with diverse populations such as Indonesian children and adolescents. A thorough examination of the effectiveness of the Nolla method and London Atlas was performed in this study, uncovering limitations in their accuracy for predicting chronological age within this specific demographic.

REFERENCES

ADAMS DM, RALSTON CE, SUSSMAN RA, HEIM K, BETHARD JD (2019) Impact of population-specific dental development on age estimation using dental atlases. *Am J Phys Anthropol*, 168: 190-199.

ALQAHTANI SJ, HECTOR MP, LIVERSIDGE HM (2010) Brief communication: The London atlas of human tooth development and eruption. *Am J Phys Anthropol*, 142: 481-490.

ALSUDAIRI DM, ALQAHTANI SJ (2019) Testing and comparing the accuracy of two dental age estimation methods on Saudi children: Measurements of open apices in teeth and the London Atlas of Tooth Development. *Forensic Sci Int*, 295: 226.e1-226.e9.

CAMERIERE R, CUNHA E, SASSAROLI E, NUZZOLESE E, FERRANTE L (2009) Age estimation by pulp/tooth area ratio in canines: Study of a Portuguese sample to test Cameriere's method. *Forensic Sci Int*, 193: 128.e1-128.e6.

CHAILLET N, NYSTRÖM M, DEMIRJIAN A (2005) Comparison of dental maturity in children of different ethnic origins: international maturity curves for clinicians. *J Forensic Sci*, 50: 1164-1174.

DEMIRJIAN A, GOLDSTEIN H, TANNER JM (1973) A new system of dental age assessment. *Hum Biol*, 45: 211-227.

DURUK G, GUNDOGDU OZDAL TP, DUMAN S (2022) Accuracy of age estimation with Demirjian and Nolla methods in Eastern Turkish children aged 3-17 years old. *Eur Oral Res*, 56: 80-87.

ERBUDAK H ÖZGE, ÖZBEK M, UYSAL S, KARABULUT E (2012) Application of Kvaal et al.'s age estimation method to panoramic radiographs from Turkish individuals. *Forensic Sci Int*, 219: 141-146.

GHAFARI R, GHODOUSI A, POORDAVAR E (2019) Comparison of the accuracy of the London atlas and Smith method in dental age estimation in 5-15.99-year-old Iranians using the panoramic view. *Int J Legal Med*, 133: 189-195.

GROVER S, MARYA CM, AVINASH J, PRUTHI N (2012) Estimation of dental age and its comparison with chronological age: Accuracy of two radiographic methods. *Med Sci Law*, 52: 32-35.

HEGDE S, PATODIA A, DIXIT U (2017) A comparison of the validity of the Demirjian, Willems, Nolla and Häävikko methods in determination of chronological age of 5-15 year-old Indian children. *J Forensic Leg Med*, 50: 49-57.

INTERPOL (2018) Disaster Victim Identification (DVI) Guide.

ISHWARKUMAR S, PILLAY P, CHETTY M, SATYAPAL KS (2022) Employing the London atlas in the age estimation of a select South African population. *Dent J (Basel)*, 10: 171.

ISMAIL AF, OTHMAN A, MUSTAFA NS, KASHMOOLA MA, MUSTAFA BE, MOHD YUSOF MYP (2018) Accuracy of different dental age assessment methods to determine chronological age among Malay children. *J Phys Conf Ser*, 1028: 012102.

KIRZIOĞLU Z, CEYHAN D (2012) Accuracy of different dental age estimation methods on Turkish children. *Forensic Sci Int*, 216: 61-67.

KOÇ A, ÖZLEK E, ÖNER TALMAÇ AG (2021) Accuracy of the London atlas, Willems, and Nolla methods for dental age estimation: a cross-sectional study on Eastern Turkish children. *Clin Oral Investig*, 25: 4833-4840.

KURITA LM, MENEZES AV, CASANOVA MS, HAITER-NETO F (2007) Dental maturity as an indicator of chronological age: radiographic assessment of dental age in a Brazilian population. *J Appl Oral Sci*, 15: 99-104.

KURNIAWAN A, AGITHA SRA, MARGARETHA MS, UTOMO H, CHUSIDA A, SOSIAWAN A, MARINI MI, RIZKY BN (2020) The applicability of Willems dental age estimation method for Indonesian children population in Surabaya. *Egypt J Forensic Sci*, 10: 5.

KURNIAWAN A, CHUSIDA A, ATIKA N, GIANOSA TK, SOLIKHIN MD, MARGARETHA MS, UTOMO H, MARINI MI, RIZKY BN, PRAKOESWA BFWR, ALIAS A, MARYA A (2022) The applicable dental age estimation methods for children and adolescents in Indonesia. *Int J Dent*, 2022: 1-6.

LEWIS JM, SENN DR (2015) Forensic dental age estimation: an overview. *J Calif Dent Assoc*, 43: 315-319.

LIVERSIDGE HM (2010) Interpreting group differences using Demirjian's dental maturity method. *Forensic Sci Int*, 201: 95-101.

MABER M, LIVERSIDGE HM, HECTOR MP (2006) Accuracy of age estimation of radiographic methods using developing teeth. *Forensic Sci Int*, 159: S68-S73.

MCCLOE D, MARION I, DA FONSECA MA, COLVARD M, ALQAHTANI S (2018) Age estimation of Hispanic children using the London Atlas. *Forensic Sci Int*, 288: 332.e1-332.e6.

MILOGLU O, CELIKOGLU M, DANE A, CANTEKIN K, YILMAZ AB (2011) Is the assessment of dental age by the Nolla method valid for Eastern Turkish children? *J Forensic Sci*, 56: 1025-1028.

MOHAMMED RB, SANGHVI P, PERUMALLA KK, SRINIVASARAJU D, SRINIVAS J, KALYAN US, RASOOL SMI (2015) Accuracy of four dental age estimation methods in southern Indian children. *J Clin Diagn Res*, 9: HC01-8.

NAIK V, PRAKASH S, YEN SZ, ROSLAN SB, RAMASAMY SAL (2017) Evaluating the reliability of two dental age estimating methods in younger individuals of Malaysian population - A radiographic study. *Indian J Forensic Community Med*, 4: 128-133.

NOLLA CA (1960) The development of the permanent teeth. *J Dent Child*, 27: 254-266.

NUR B, KUSGOZ A, BAYRAM M, CELIKOGLU M, NUR M, KAYIPMAZ S, YILDIRIM S (2012) Validity of Demirjian and Nolla methods for dental age estimation for Northeastern Turkish children aged 5-16 years old. *Med Oral Patol Oral Cir Bucal*, 17: 3-9.

PAVLOVIĆ S, PALMELA PEREIRA C, VARGAS DE SOUSA SANTOS RF (2017) Age estimation in Portuguese population: The application of the London atlas of tooth development and eruption. *Forensic Sci Int*, 272: 97-103.

PAZ CORTÉS MM, ROJO R, MOURELLE MARTÍNEZ MR, DIEGUEZ PÉREZ M, PRADOS-FRUTOS JC (2019) Evaluation of the accuracy of the Nolla method for the estimation of dental age of children between 4–14 years old in Spain: A radiographic study. *Forensic Sci Int*, 301: 318-325.

PRAKOESWA BFWR, KURNIAWAN A, CHUSIDA A, MARINI MI, RIZKY BN, MARGARETHA MS, UTOMO H, I'ZAAZ DARMAWAN A, AISYAH AKN, ALIAS A, WAHJUNI OR, MARYA A (2022) Children and adolescent dental age estimation by the Willems and Al Qahtani methods in Surabaya, Indonesia. *Biomed Res Int*, 2022: 1-4.

SCHMELING A (2023) Morphological age estimation. In: *Encyclopedia of Forensic Sciences, Third Edition*. Elsevier, pp 629-636.

SCHMELING A, DETTMEYER R, RUDOLF E, VIETH V, GESERICK G (2016) Forensic age estimation: methods, certainty, and the law. *Dtsch Arztebl Int*, 113: 44-50.

SHARMA P, WADHWAN V (2020) Comparison of accuracy of age estimation in Indian children by measurement of open apices in teeth with the London Atlas of tooth development. *J Forensic Odontostomatol*, 38: 39-47.

SINGH G, JUNEJA T (2007) Development of Dentition. In: *Textbook of Orthodontics*. Jaypee Brothers Medical Publishers (P) Ltd., pp 37-47.

SOUSA AM DA S, JACOMETTI V, ALQAHTANI S, SILVA RHA DA (2020) Age estimation of Brazilian individuals using the London Atlas. *Arch Oral Biol*, 113: 104705.

SUKHIA RH, FIDA M, AZAM SI (2012) Dental age table for a sample of Pakistani children. *Eur J Orthod,* 34: 77-82.

ORIGINAL ARTICLE Eur J Anat, 28 (5): 533-542 (2024)

Comparison of craniofacial anthropometric measurements with the golden ratio in young adults

Emre Atay[1], **Aleyna Tok**[2], **Buse İrem Öztürk**[2], **Musa Özcan**[2], **Zeynep Kuş**[2], **Abdülkadir Bilir**[1], **Tolga Ertekin**[1]

[1] *Department of Anatomy, Faculty of Medicine, Afyonkarahisar Health Sciences University, Afyonkarahisar, Turkey*
[2] *Faculty of Medicine Student, Afyonkarahisar Health Sciences University, Afyonkarahisar, Turkey*

SUMMARY

There is evidence showing the existence of the golden ratio in many fields from architecture to medicine, from art to philosophy. The aim of this study is to investigate the relationship between the measurements taken from the face area and the golden ratio (1.618) value and to present results by comparing the determined measurement parameters with the existing literature. A total of 101 university students aged between 18-25 participated in this study on a voluntary basis. In this study, data were collected by photographing method. Photographs of each individual were taken from 3 angles: the front and both sides. After the photographs were transferred to digital media, measurement was performed by means of a software program (ImageJ). In the study, data were presented as mean±standard deviation in the form of descriptive statistics. In order to compare the measurement points within the scope of the study with the golden ratio, 23 measurement indices (ratio) were determined. Proportional Index Calculation was done as follows. Head Index Ratio=Head Height/Total Cranial Head Height. A statistically significant difference was determined when the mean value of this index was compared according to sex ($p<0.05$). As a result, we think that the data we obtained in the study will be useful in the fields of science and art and may be a pioneer for the golden ratio studies to be done later.

Key words: Golden ratio – Anthropometry – Anatomy – Craniofacial measurement

INTRODUCTION

The golden ratio is a series of complex numbers connected by a very special mathematical formula (like 2, 3, 5, 8, 13, 21, 34, 55, 89). The ratio between these numbers (1.618) is an irrational, continuous and non-repeating number that goes on forever, like the number PI. The golden ratio is denoted by the symbol “Fi” (Φ) and is also called the Fi number (Φ) in the literature. Basically, the following mathematical rule is used to find the golden ratio. If a line AB is divided from any point C to give the ratio AB/AC = AC/CB, C is the golden part of AB, and the ratio AB/AC and AC/CB that creates this ratio is called the golden ratio (Markowsky, 1992; Mitchison, 1977).

Corresponding author:
Emre Atay. Department of Anatomy, Faculty of Medicine, Afyonkarahisar Health Sciences University, Afyonkarahisar, Turkey. Phone: +90272 246 33 01. E-mail: emre.atay@afsu.edu.tr / eemreatay@gmail.com - Orcid: 0000-0002-2378-1183

Submitted: January 26, 2024. **Accepted:** March 7, 2024

https://doi.org/10.52083/DOLL3265

In nature, there is the golden ratio as a geometric and numerical ratio relation, which is thought to be the best in terms of harmony in the shapes or structures of countless living or inanimate beings. Since ancient Greek times, the golden ratio is believed to be found in nature and human body anthropometry, although there are not many written sources on the subject. However, there is evidence showing the existence of the golden ratio in mathematics, architecture, art and many other fields (Livio, 2002; Mamarelis et al., 2022; Mitchison, 1977; Sen and Agarwal, 2008).

Considering the studies related to the golden ratio in the human body, the studies of Leonardo Da Vinci come to mind first. It is one of the important studies of Da Vinci that he applied the golden ratio in his work called The Vitruvian Man, which is thought to have been drawn at the end of the 1400s. The German artist Albrecht Durer applied the golden ratio in his works at the beginning of the sixteenth century. When evaluated in general, it is seen that artists and scientists use the golden ratio as a measure for their studies of the human body (Beyoğlu, 2016; Hastürk, 2014; İlden Yıldız and Bostancı, 2022; Livio, 2002).

There are many objective studies in the literature on the perception of attractiveness/beauty, which is a value that varies from person to person (Chatrath et al., 2007; Kürkçüoğlu et al., 2016; Pallett et al., 2010; Yalcinkaya et al., 2022). Various definitions and details have been made since the Renaissance, especially regarding facial proportions, and these have been a guide for anthropometric studies. With the introduction of anthropometry into clinical practice at the end of the nineteenth century, the number of studies covering measurements based on the face, head and neck region has also increased (Anand et al., 2015; Yalcinkaya et al., 2022).

One of the first studies on the golden ratio in facial structures was published in 1946 by Matila Ghyka in his *The Geometry of Art and Life*, in which he performed a facial analysis of tennis champion Helen Wills. In this study, it was reported that the golden ratio was found between many lengths in facial structures (Ghyka, 1977). In the literature review conducted by us, it was determined that there were studies conducted under the titles of evaluation of lower face heights, determination of nasal width and length ratios, nasolabial angle measurement, and determination of columella ratios (Abbas et al., 2015; Aki Abaci et al., 2020; Chatrath et al., 2007; Kürkçüoğlu et al., 2016; Salinas et al., 2023; Varlık et al., 2010; Zwahlen et al., 2022). However, it has been determined by us that the number of studies on the golden ratio of the face is not very high, and that it is still worthy of study in terms of contribution to the literature.

The aim of this study is to investigate the relationship between the measurements taken from the facial region and the golden ratio (1.618) value, and to present results by comparing the determined measurement parameters with the existing literatures.

MATERIALS AND METHODS

Ethics Committee permission, dated 03.12.2021 and numbered 2021/565, was obtained from Afyonkarahisar Health Sciences University (AFSU) Clinical Research Ethics Committee for the study. Within the scope of the study, a total of 101 Medical Faculty students aged between 18 and 25 years participated on a completely voluntary basis. The study was conducted in accordance with the principles of the Declaration of Helsinki.

Data were collected by photography method (photoanthropometry). A camera with at least 12 megapixels, stabilization and autofocus was used for photography (Nikon D3100, Nikon Corporation, Japan). The camera was fixed using a tripod. To ensure standardization in all photographs, these were taken from a distance of one meter without using the zoom function of the camera, providing a clear view of the face and facial features. In the anterior photographs, the plane cutting the pupils was parallel to the ground, the jaw was in the center, and the lips were closed without tension. Before lateral photographs were taken, the head was adjusted to the Frankfort plane position (i.e., individuals were positioned so that the upper part of the eye and the auricle were aligned, the jaw was in the center, and the lips were closed without tension). After all these standards were met, each individual was photographed from a total of three angles, including the front and both sides (Fig. 1).

Fig. 1.- Illustration by drawing of the photographs taken from the front (**b**) and both sides (**a**, **c**) of each individual.

Literature was used to determine reference points for the measurements (Aki Abaci et al., 2020; Khoshab et al., 2022). The reference points for anthropometric measurements in the craniofacial region were presented in Fig. 2. After the photographs were digitized, measurement was performed with ImageJ (National Institutes of Health and The Laboratory for Optical and Computational Instrumentation [LOCI], University of Wisconsin, Madison, USA) software program (Fig.

Maximum head width (eu-eu)
Maximum frontal width (ft-ft)
Maximum head length (g-op)
Head height (v-n)
Total craniofacial head height (v-gn)
Maximum face width (zy-zy)
Mandibular width (go-go)
Internal channel distance (en-en)
Biocular width (ex-ex)
Eye fissure length (en-ex)
Nose width (al-al)
Nose height (n-sn)
Labial fissure width (ch-ch)
Ear length (sa-sba)
Ear width (pra-pa)
Length between tragion postaurale
Subnasale stamion (sn-sto)
Stomion-gnation (sto-gn)
Trichion-nasion (tr-n)

Fig. 2.- The reference points for anthropometric measurements in the craniofacial region.

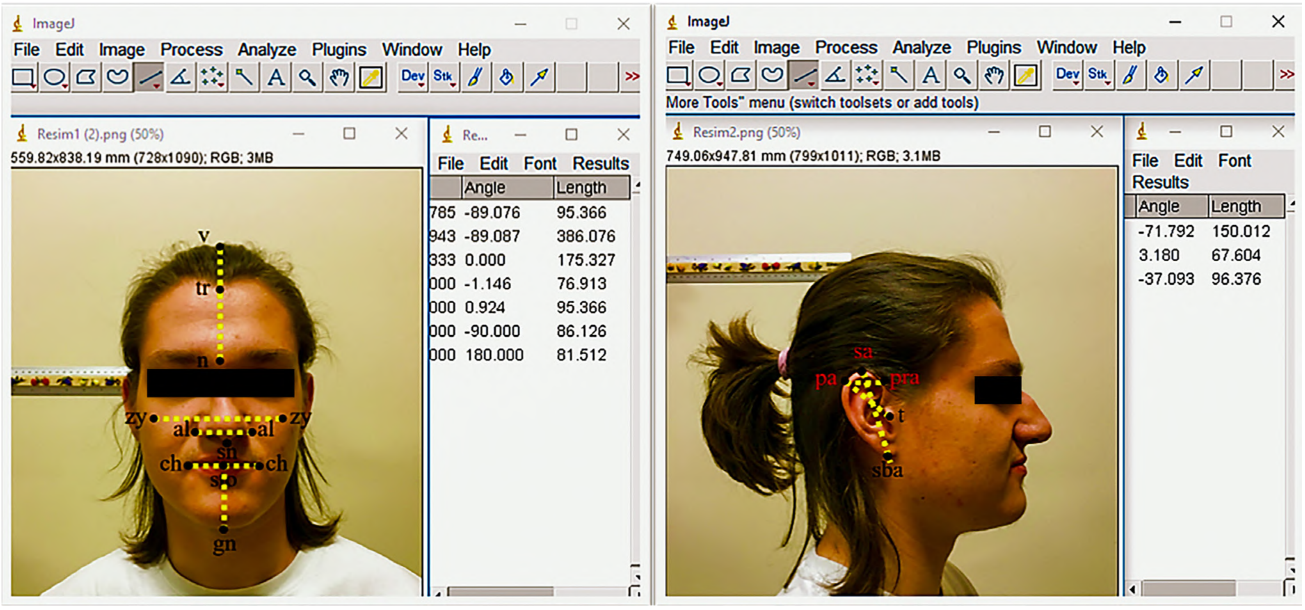

[redacted]

[redacted]

	Angle	Length
785	-89.076	95.366
943	-89.087	386.076
333	0.000	175.327
000	-1.146	76.913
000	0.924	95.366
000	-90.000	86.126
000	180.000	81.512

Angle	Length
-71.792	150.012
3.180	67.604
-37.093	96.376

Fig. 3.- Measurements made with ImageJ software program.

3). Individuals were photographed with a ruler to ensure calibration in the measurements.

Exclusion Criteria

Individuals who did not show normal growth and development, had undergone previous orthodontic-surgical treatment, had a history of facial trauma, and/or had congenital defects were not included in the study.

Limitations of the Study

Participants were included in the study on a voluntary basis. At the same time, plans were made to include only medical faculty students in the study population. Along with all these factors, the intensity of students' theoretical and practical courses is seen as one of the important limitations in terms of include to the entire universe. However, considering the power analysis results, a sufficient number of samples was reached.

Statical Analysis

G-power 3.1.9.4 software program (Heinrich Heine Universität Düsseldorf, Düsseldorf, Germany) was used in the power analysis to determine the sample size of this study. By setting the type 1 error level to be 5%, the power to be 95%, and the effect size to be 0.9508, the sufficient sample size was determined to be minimum 47 people for each sex group. In this study, all analyses were performed using IBM Statistical Package for the Social Sciences (SPSS) 25 software program. Normality of distribution was assessed using five parameters: standard deviation/mean, skewness-kurtosis, histogram, Q–Q plots,Shapiro–Wilk Test (Batın et al., 2023). Depending on the results of the evaluation, Wilcoxon sign and Mann Whitney U tests were used for pairwise group comparisons by asymmetry and sex, respectively, while the nonparametric One Sample T-test was used for the comparison of indices with the golden ratio. Data with $p<0.05$ were considered significant. Data were shown as mean±standard deviation (M±SD) and median (minimum-maximum) (Md(Min-Max)) values.

RESULTS

A total of 101 students (47 males (46.5%) and 54 females (53.5%) from AFSU Medical Faculty participated in this study. The mean age was 21.5±2.3 years in men and 21.5±2 years in women.

All anthropometric measurements were presented in millimeters (mm). In addition, all findings obtained from men and women were compared with the golden ratio value. Measurement indices (ratios) were determined to compare the measurement points within the scope of the study with the golden ratio.

Proportional Index Calculation was done as in the example shown below:

$$\text{Head Index Ratio} = \frac{\text{Head Height}}{\text{Total Cranial Head Height}}$$

For the evaluation of facial asymmetry in the study, a bilateral comparison of the indices was made on the right and left sides. In addition, the differences between sexes for all measurement indices obtained from men and women were evaluated and compared separately by including the golden ratio value in all measurements.

Facial asymmetry was evaluated in the first phase of the study (Table 1). Depending on the results of the evaluation, a statistically significant difference was determined in the Eye Fissure Length/Biocular Width Index and Eye Fissure Length/Eye Internal Canal Length Index in the asymmetry comparison of all cases, and the right-side indices were found to be larger (p=0.003, p=0.039, respectively). However, when asymmetry differences in men and women were evaluated separately, no statistically significant difference was found (p>0.05).

In the second stage of the study, sex-related differences were evaluated (Table 2). Based on the results of the statistical evaluation, when compared according to sex, The Inner Eye Canal Length/Biocular Width, Nasal Width/Nasal Height, Nasal Width/Maximum Facial Width and Nasal Width/Labial Fissure Length indices were found to be statistically significantly greater in males than in females (p=0.004, p<0.001, p<0.001, p<0.001, p<0.001, respectively). The Head Height/Total Cranial Head Height index was found to be statistically significantly greater in females than in males (p<0.001).

In terms of closeness to the golden ratio in the face area, women and men were analyzed separately and the results are shown in Table 3. In the analysis, it was found that no index was similar to the golden ratio value of 1.618 regardless of sex or depending on sex (p<0.001).

DISCUSSION

Parts of the human body have been measured for various reasons since ancient times. While body measurements (anthropometry) were mostly used in figurative arts in ancient times, it began to be used in the naturalistic field to describe the basic morphological features of humans, especially since the seventeenth century (Albrizio, 2007; Lieberman, 1996). Craniofacial anthropometry, one of the branches of anthropometry,

Table 1. Comparison of right and left side indices of the facial region.

Index M±SD		Right		Left		p
		Md (Min-max)	M±SD	Md (Min-max)		
Female	Eye Fissur Length/Biocular Width Index	0.3±0.02	0.31 (0.26-0.33	0.3±0.02	0.3 (0.25-0.36)	0.3
	Eye Fissur Length/Eye Internal Canal Length Index	0.91±0.1	0.92 (0.71-1.12	0.89±0.11	0.89 (0.69-1.18)	0.154
	Ear Width/Ear Length Index	0.54±0.06	0.53 (0.42-0.76	0.55±0.06	0.55 (0.69-0.75)	0.326
	Ear Width/Trichion-Postaurale Length Index	0.25±0.04	0.25 (0.17-0.37	0.25±0.04	0.24 (0.69-0.4)	0.503
Male	Eye Fissur Length/Biocular Width Index	0.31±0.03	0.31 (0.27-0.48)	0.3±0.03	0.3 (0.25-0.47)	0.37
	Eye Fissur Length/Eye Internal Canal Length Index	0.89±0.09	0.88 (0.76-1.14)	0.86±0.1	0.84 (0.69-1.11)	0.126
	Ear Width/Ear Length Index	0.54±0.05	0.55 (0.44-0.65)	0.54±0.06	0.53 (0.42-0.67)	0.838
	Ear Width/Trichion-Postaurale Length Index	0.25±0.03	0.24 (0.18-0.34)	0.24±0.03	0.24 (0.2-0.33)	0.386
Total	Eye Fissur Length/Biocular Width Index	0.31±0.03	0.31 (0.26-0.48)	0.3±0.03	0.3 (0.25-0.47)	**0.003***
	Eye Fissur Length/Eye Internal Canal Length Index	0.9±0.1	0.9 (0.71-1.14)	0.87±0.1	0.86 (0.69-1.18)	**0.039***
	Ear Width/Ear Length Index	0.54±0.06	0.54 (0.42-0.76)	0.54±0.06	0.54 (0.42-0.75)	0.539
	Ear Width/Trichion-Postaurale Length Index	0.25±0.04	0.25 (0.17-0.37)	0.25±0.04	0.24 (0.18-0.4)	0.34

* Wilcoxon sign test, statistically significant difference was found.

Table 2. Comparison of sex-related index differences.

Index	Male (n=47)		Female (n=54)		Total (n=101)		p
	M±SD	**Md (Min-Max)**	**M±SD**	**Md (Min-Max)**	**M±SD**	**Md (Min-Max)**	
Head Height/Total Cranial Head Height Index	0.38±0.02	0.38 (0.32-0.44)	0.41±0.03	0.41 (0.33-0.47)	0.4±0.03	0.39 (0.32-0.47)	<0.001*
Maximum Frontal Width/ Maximum Head Width Index	0.97±0.03	0.98 (0.89-1)	0.96±0.02	0.97 (0.9-0.99)	0.96±0.03	0.97 (0.89-1)	0.6
Maximum Face Width/ Maximum Head Width Index	1.03±0.08	1.03 (0.88-1.18)	1.04±0.09	1.06 (0.88-1.18)	1.04±0.08	1.04 (0.88-1.18)	0.658
Maximum Frontal Width/ Maximum Face Width Index	0.94±0.07	0.94 (0.79-1.1)	0.93±0.08	0.91 (0.82-1.09)	0.93±0.08	0.93 (0.79-1.1)	0.344
Eye Fissure Length/Biocular Width Index (Right)	0.31±0.03	0.31 (0.27-0.48)	0.3±0.02	0.31 (0.26-0.33)	0.31±0.02	0.31 (0.26-0.48)	0.387
Eye Fissure Length/Biocular Width Index (Left)	0.3±0.03	0.3 (0.25-0.47)	0.3±0.02	0.3 (0.25-0.36)	0.3±0.03	0.3 (0.25-0.47)	0.591
Maximum Head Length/ Total Cranial Head Height Index	0.96±0.16	0.97 (0.12-1.23)	0.96±0.12	0.97 (0.75-1.27)	0.96±0.14	0.97 (0.12-1.27)	0.643
Mandibular Width/Maximum Face Width Index	0.74±0.06	0.73 (0.58-0.89)	0.72±0.06	0.73 (0.55-0.84)	0.73±0.06	0.73 (0.55-0.89)	0.218
Mandibular Width/Maximum Frontal Width Index	0.79±0.09	0.79 (0.56-1.06)	0.78±0.1	0.8 (0.59-0.99)	0.79±0.09	0.79 (0.56-1.06)	0.989
Eye Internal Canal Length/Biocular Width Index	0.35±0.03	0.35 (0.29-0.52)	0.34±0.02	0.33 (0.29-0.39)	0.34±0.03	0.34 (0.29-0.52)	**0.004***
Eye Fissure Length/Eye Internal Canal Length Index (Right)	0.89±0.09	0.88 (0.76-1.14)	0.91±0.1	0.92 (0.71-1.12)	0.9±0.09	0.9 (0.71-1.14)	0.079
Eye Fissure Length/Eye Internal Canal Length Index (Left)	0.86±0.1	0.84 (0.69-1.11)	0.89±0.11	0.88 (0.69-1.18)	0.87±0.1	0.86 (0.69-1.18)	0.144
Subnasale-Stamion/Stamion-Gnathion Index	0.47±0.05	0.48 (0.37-0.62)	0.47±0.05	0.46 (0.37-0.58)	0.47±0.05	0.47 (0.37-0.62)	0.728
Stamion/Gnathion Index	0.72±0.1	0.72 (0.53-1)	0.71±0.09	0.71 (0.5-0.94)	0.72±0.09	0.71 (0.5-1)	0.87
Subnasale-Stamion Length/Trichion-Nasion Length Index	0.34±0.05	0.34 (0.24-0.53)	0.33±0.04	0.33 (0.25-0.48)	0.34±0.05	0.33 (0.24-0.53)	0.591
Nose Width/Nose Height Index	0.8±0.13	0.79 (0.55-1.13)	0.71±0.14	0.68 (0.48-1.14)	0.75±0.14	0.74 (0.48-1.14)	**<0.001***
Nose Height/Total Cranial Head Height Index	0.07±0.01	0.07 (0.05-0.1)	0.07±0.01	0.07 (0.05-0.11)	0.07±0.01	0.07 (0.05-0.11)	0.728
Nose Width/Maximum Face Width Index	0.09±0.02	0.08 (0.07-0.14)	0.08±0.01	0.07 (0.06-0.12)	0.08±0.01	0.08 (0.06-0.14)	**<0.001***
Nose Height/Head Height Index	0.19±0.03	0.19 (0.14-0.25)	0.18±0.04	0.18 (0.11-0.3)	0.18±0.03	0.19 (0.11-0.3)	0.093
Labial Fissure Length/ Mandibular Width Index	0.15±0.04	0.14 (0.08-0.27)	0.15±0.02	0.14 (0.11-0.25)	0.15±0.03	0.14 (0.08-0.27)	0.957
Nose Width/Labial Fissure Length Index	0.79±0.13	0.78 (0.49-1.38)	0.72±0.07	0.71 (0.58-0.89)	0.75±0.11	0.75 (0.49-1.38)	<0.001*
Ear Width/Ear Length Index (Right)	0.54±0.05	0.55 (0.44-0.65)	0.54±0.06	0.53 (0.42-0.76)	0.54±0.06	0.54 (0.42-0.76)	0.822
Ear Width/Ear Length Index (Left)	0.54±0.06	0.53 (0.42-0.67)	0.55±0.06	0.54 (0.42-0.75)	0.54±0.06	0.54 (0.42-0.75)	0.41
Ear Width/Trichion-Postaurale Length Index (Right)	0.25±0.03	0.24 (0.18-0.34)	0.25±0.04	0.25 (0.17-0.37)	0.25±0.04	0.25 (0.17-0.37)	0.759
Ear Width/Trichion-Postaurale Length Index (Left)	0.24±0.03	0.24 (0.2-0.33)	0.25±0.04	0.24 (0.18-0.4)	0.25±0.04	0.24 (0.18-0.4)	0.454

* Mann Whitney U test, statistically significant difference was found.

Table 3. Analysis results of length measurements taken from the facial region compared with golden ratio (1.618) for the whole sex.

Index	**p***		
	Male (n=47)	**Female (n=54)**	**Total (n=101)**
Head Height/Total Cranial Head Height Index	<0.001	<0.001	<0.001
Maximum Frontal Width/Maximum Head Width Index	<0.001	<0.001	<0.001
Maximum Face Width/Maximum Head Width Index	<0.001	<0.001	<0.001
Maximum Frontal Width/Maximum Face Width Index	<0.001	<0.001	<0.001
Eye Fissure Length/Biocular Width Index (Right)	<0.001	<0.001	<0.001
Eye Fissure Length/Biocular Width Index (Left)	<0.001	<0.001	<0.001
Maximum Head Length/Total Cranial Head Height Index	<0.001	<0.001	<0.001
Mandibular Width/Maximum Face Width Index	<0.001	<0.001	<0.001
Mandibular Width/Maximum Frontal Width Index	<0.001	<0.001	<0.001
Eye Internal Canal Length/Biocular Width Index	<0.001	<0.001	<0.001
Eye Fissure Length/Eye Internal Canal Length Index (Right)	<0.001	<0.001	<0.001
Eye Fissure Length/Eye Internal Canal Length Index (Left)	<0.001	<0.001	<0.001
Subnasale-Stamion/Stamion-Gnathion Index	<0.001	<0.001	<0.001
Stamion/Gnathion Index	<0.001	<0.001	<0.001
Subnasale-Stamion Length/Trichion-Nasion Length Index	<0.001	<0.001	<0.001
Nose Width/Nose Height Index	<0.001	<0.001	<0.001
Nose Height/Total Cranial Head Height Index	<0.001	<0.001	<0.001
Nose Width/Maximum Face Width Index	<0.001	<0.001	<0.001
Nose Height/Head Height Index	<0.001	<0.001	<0.001
Labial Fissure Length/Mandibular Width Index	<0.001	<0.001	<0.001
Nose Width/Labial Fissure Length Index	<0.001	<0.001	<0.001
Ear Width/Ear Length Index (Right)	<0.001	<0.001	<0.001
Ear Width/Ear Length Index (Left)	<0.001	<0.001	<0.001
Ear Width/Trichion-Postaurale Length Index (Right)	<0.001	<0.001	<0.001
Ear Width/Trichion-Postaurale Length Index (Left)	<0.001	<0.001	<0.001

* One Sample T test was used for the comparison of indices with the golden ratio.

includes head and face measurements on living, cadaveric and radiological samples (Bahşi et al., 2021; Golalipour, 2006; Güler et al., 2023; Güler et al., 2023; Umar et al., 2006). The appearance of the face, which is the most variable part of the human body, is affected by factors such as age, sex, race and ethnicity. In this context, studies based on facial area (craniofacial) measurements have an important place in attractiveness. In addition, craniofacial measurements are used in symmetry and asymmetry research, orthodontics, plastic and reconstructive surgery, anthropology and many other scientific fields, and they also have an important place in people's perception of beauty (Choe et al., 2004; Farkas et al., 2005; Porter and Olson, 2001).

It is seen that there are some ratios, canons and ideal angles in the literature on concepts such as facial beauty and ideal proportions for the face. However, these ratios and values are based on faces perceived as beautiful or the preferences of the authors. These ratios and values, which are associated with attractive faces regardless of factors such as age, sex and ethnicity, lead away from an objective perspective. From a clinical point of view, orthodontists, oral and maxillofacial surgeons, and plastic surgeons accept reference points based on final treatment results in both sexes and races as ideal impression ratios. This is because the perception of facial attractiveness varies according to race and ethnicity, and they do not think it is correct to apply some traditional rules for ideal facial attractiveness (Kiekens et al., 2008; Malkoc and Fidancioglu, 2016; Rhee, 2018). With all this literature information, there are still debates about which ratios and angles are valid: golden and/or divine ratios are important according to some researchers and not so important according to others. Based on all these ideas, our study was planned and we investigated whether parameters such as ideal reference points and proportions, which were previously mentioned in the literature, affect the aesthetic evaluation of Turkish adolescents and young people. Considering the literature information, craniofacial measurements were compared with the golden ratio in our study. We think that the results of the study will be useful for branches of science such as anatomy, surgical medicine and anthropometry.

In our literature review, it was determined that there is a relationship between the golden ratio and various parts of the human body such as limbs, facial features, heart and teeth (Abbas et al., 2015; Aki Abaci et al., 2020; Henein et al., 2011; Zwahlen et al., 2022). In the study conducted by Seçkin and Bülbül (2020), morphometric measurements of anatomical regions (hand, face, head, omos, belly areas) in 16 individuals, 8 men and 8 women, were examined for compliance with the golden ratio. In the measurements made, it was observed that the subjects had different measurements, and the golden ratio was approached in some regions while more distant results were obtained in other regions. In particular, the ratio of the middle finger measurement of the hand to the whole hand was found to be similar in all subjects. It was stated that the closest results to the golden ratio value belong to the measurements taken from this region. As a result, it was stated in the study that all living and non-living beings in nature naturally have a ratio due to creation. In addition, the importance of interdisciplinary work was emphasized, and they expressed their belief that the results of the study would shed light on new research (Seçkin and Bülbül, 2020). Although, according to our study results, there is no similarity between the indices obtained as a result of the measurements made in the face area and the golden ratio, we believe that there is a certain order and ratio between the body parts. Our analysis reveals that there was no index close to the golden ratio value of 1.618, neither sex-dependent nor sex-independent. We think that the data we have revealed can be a source for other studies.

In their 2016 study, Malkoç and Fidancioglu made various aesthetic evaluations in photographs of adolescents' facial regions and examined the role of ideal angles and proportions. As a result of the study, according to the angles and proportions measured in the photographs, it was observed that the clinician eye (orthodontists) noticed the sagittal position of the lower jaw, the distance between the eyes and the length of the face, while laymen noticed only the distance between the eyes and the length of the face. However, no statistically significant relationship was found between any of the various ratios (such as divine ratio, golden ratio) and facial aesthetics (Malkoc and Fidancioglu, 2016).

In our study, various indices of the facial region were extracted and compared with the golden ratio. However, no significant relationship was found in the statistical analysis. However, it was found that there were statistical differences in the comparison of these indices according to sex. These results are similar to those reported in the study by Malkoc and Fidancioglu (2016). It is accepted that there are certain proportions in the human body. However, it is not always possible for these ratios to be similar to concepts such as the golden ratio or the divine ratio. This is because the presence of factors such as age, sex and race, which vary from individual to individual, as well as the presence of relative factors such as beauty and perceptions of beauty, affect the results of the study. Based on our study results, it is seen that there are differences in the measurements made between the reference points accepted by the literature and the indices created between them according to both sex and right-left distinction (right and left side of the face). We think that these results will contribute more to the literature, both because they are obtained from more objective reference points and because they can be used more in the clinic (for fields such as anthropometry, head and neck facial surgery, facial aesthetic applications).

Khoshab et al. (2022) systematically reviewed the literature in their study on the applicability of the golden ratio for anthropometric facial assessment. In their literature review, they conducted a systematic analysis of a total of 27 articles. They stated that the mean values of Canon 2 (tr-n and sn-menton), Canon 6 (en-en and ex-en) and Canon 8 (zy-zy and al-al) showed significant differences between ethnic groups in men, while Canon 5 (en-en and al-al) and Canon 8 (zy-zy and al-al) showed significant differences between ethnic groups in women. They also analyzed whether there was significant inter-ethnic variability in measurements made in the face and ear region. In the analysis of various golden ratio indices (indices such as Phi 1; en-en/sa-sba, Phi 2; al-al/sa-sba, Phi 5; en-en/ch-ch, Phi 8; en-en/ex-en, Phi 10; ex-en/al-al), they reported that no ethnic/sex group indices consistently approached the "ideal/golden ratio" (Khoshab et al., 2022).

In our study, the results in Table 2 show the analysis of various index values by sex. According to Table 2, it is stated that Head Height/Total Cranial Head Height Index, Eye Internal Canal Length/Biocular Width Index, Nose Width/Nose Height Index, Nose Width/Maximum Face Width Index and Nose Width/Labial Fissure Length Index values differ according to sex ($p<0.05$). We think that these results according to sex are due to the differences in the anatomical structure of men and women. However, according to the results of the analysis in Table 3, where the length measurements taken from the facial region were compared with the golden ratio (1.618) for all sexes, it was found that none of the indices were similar/close to the golden ratio value of 1.618. Based on the results in the meta-analysis study of Khoshab et al. (2022), we can say that our study results are similar to the literature.

In conclusion, when our study is evaluated as a whole, we think that it is at a level that will contribute to the literature in different aspects in terms of its results. In today's conditions, with the increasing demand for plastic surgery worldwide at the point of beauty perception, it is very important to study ideal anthropometric measurements in a systematic way and to make new contributions to the literature. At the point of designing our study, it was aimed to reveal the existence of the relationship between the young population's perception of beauty and the golden ratio.

As we have stated before, beauty perception is a relative concept and it is important to understand the complexities of this concept objectively. We think that there will be no change in the perception of beauty even when the values that exist and accepted in nature such as "ideal/golden ratio" do not fit human body parts. In addition to all these, we believe that in planning scientific research based on anthropometric measurements, it would be correct to act by taking into account that many ethnic groups have different facial features and that each individual can be beautiful without adopting a single aesthetic.

ACKNOWLEDGEMENTS

This study was planned within the scope of the Project Implementation Study course in the course curriculum of AFSU Faculty of Medicine. This study was presented as an Oral Presentation by our students who carried out the study in the end-of-term program of the Project Implementation Study course (https://afsu.edu.tr/afsu-lu-tip-fakultesi-ogrencilerinin-bilimsel-sunumlari-odullendirildi/). We declare that none of us have any financial or personal relationships with other people or organizations that can inappropriately influence our work, there was no professional or other personal interest in our work.

REFERENCES

ABBAS OL, KÜRKÇÜOĞLU A, PELIN C, YAZICI AC (2015) Anthropometric measurement and analysis of the lower face in Turkish rhinoplasty patients. *Eur J Plast Surg*, 38(6): 449-458.

AKI ABACI Y, KÜRKÇÜOĞLU A, ŞENÇELİKEL T (2020) Genç erişkin bireylerde vücutta altın oran değerlendirmesi. *Antropoloji*, 40: 92-104.

ALBRIZIO A (2007) Biometry and anthropometry: from Galton to constitutional medicine. *J Anthropol Sci*, 85: 101-123.

ANAND S, TRIPATHI S, CHOPRA A, KHANEJA K, AGARWAL S (2015) Vertical and horizontal proportions of the face and their correlation to phi among Indians in Moradabad population: A survey. *J Indian Prosthodont Soc*, 15(2): 125.

BAHŞI I, ORHAN M, KERVANCIOĞLU P, KARATEPE Ş, SAYIN S (2021) Craniofacial anthropometry of healthy Turkish young adults: analysis of head and face. *J Craniofac Surg*, 32(4): 1535-1539.

BATIN S, EKINCI Y, GÜRBÜZ K, PAYAS A, KURTOGLU E, UÇAR I, SEBER T, ARIK M, YILMAZ H, UNUR E (2023) The role of pineal gland volume in the development of scoliosis. *Eur Spine J*, 32: 181-189.

BEYOĞLU A (2016) Sanat eğitiminde altın oran ve leonardo da vinci'nin eserleri arasındaki ilişkinin incelenmesi. *Van Yüzüncü Yıl Üniversitesi Eğitim*

Fakültesi Dergisi, 13(1): 360-382.

CHATRATH P, DE CORDOVA J, NOURAEI SAR, AHMED J, SALEH HA (2007) Objective assessment of facial asymmetry in rhinoplasty patients. *Arch Facial Plast Surg*, 9(3): 184-187.

CHOE KS, SCLAFANI AP, LITNER JA, YU GP, ROMO IIIT (2004) The Korean American woman's face. *Arch Facial Plast Surg*, 6(4): 244-252.

FARKAS LG, KATIC MJ, FORREST CR (2005) International anthropometric study of facial morphology in various ethnic groups/races. *J Craniofac Surg*, 16(4): 615-646.

GHYKA M (1977) *The Geometry of Art and Life* (2nd ed.). Dover Publications, USA, pp 124-155.

GOLALIPOUR MJ (2006) The effect of ethnic factor on cephalic index in 17-20 years old females of north of Iran. *Int J Morphol*, 24(3): 319-322.

GÜLER H, YILMAZ H (2023) Can cranium size be predicted from orbit dimensions? *Med Records*, 5(3): 460-464.

GÜLER H, YILMAZ H (2023) Magnificent harmony in morphometric measurements of orbita and foramen magnum. *Int J Morphol*, 41(2): 445-450.

HASTÜRK EY (2014) Antropometrik verilerde altın oran. *Mesleki Bilimler Dergisi*, 3(2): 173-177.

HENEIN MY, ZHAO Y, NICOLL R, SUN L, KHIR AW, FRANKLIN K, LINDQVIST P (2011) The human heart: application of the golden ratio and angle. *Int J Cardiol*, 150(3): 239-242.

İLDEN YILDIZ S, BOSTANCI E (2022) Ideal perception of beauty and beauty in female figures in Matthias Verginer's sculptures. *Art Time*, 3: 17-33.

KHOSHAB N, DONNELLY MR, SAYADI LR, VYAS RM, BANYARD DA (2022) Historical tools of anthropometric facial assessment: a systematic raw data analysis on the applicability of the neoclassical canons and golden ratio. *Aesthet Surg J*, 42(1): NP1-NP10.

KIEKENS RMA, KUIJPERS-JAGTMAN AM, VAN 'T HOF MA, VAN 'T HOF BE, STRAATMAN H, MALTHA JC (2008) Facial esthetics in adolescents and its relationship to "ideal" ratios and angles. *Am J Orthod Dentofacial Orthop*, 133(2): 188.e1-188.e8.

KÜRKÇÜOĞLU A, ABBAS OL, AYAN DM, BAYKAN R, DEMIRKAN E, ÖZKAN Ö, ÖZKUBAT I, ŞIMŞEK M (2016) Comparison of objective and subjective assessments for perception of facial symmetry. *Anatomy*, 10(2): 94-98.

LIEBERMAN LS (1996) Anthropometry: the individual and the population. *Am J Hum Biol*, 8(1): 91-92.

LIVIO M (2002) *The golden ratio: the story of phi, the world's most astonishing number*. Broadway Books, USA, pp 25-35.

MALKOC S, FIDANCIOGLU A (2016) The role of ideal angles, ratios, and divine proportions in aesthetic evaluation of adolescents. *Aesthetic Plast Surg*, 40(1): 1-12.

MAMARELIS G, KARAM E, SOHAIL MZ, KEY S (2022) The golden ratio in pediatric wrist anatomy: a divine symmetry. *Cureus*, 14(7): e26939.

MARKOWSKY G (1992) Misconceptions about the golden ratio. *Coll Mathematics J*, 23(1): 2-19.

MITCHISON GJ (1977) Phyllotaxis and the fibonacci series. *Science*, 196(4287): 270-275.

PALLETT PM, LINK S, LEE K (2010) New "golden" ratios for facial beauty. *Vision Res*, 50(2): 149-154.

PORTER JP, OLSON KL (2001) Anthropometric facial analysis of the African American woman. *Arch Facial Plast Surg*, 3(3): 191-197.

RHEE SC (2018) Differences between Caucasian and Asian attractive faces. *Skin Res Technol*, 24(1): 73-79.

SALINAS CA, LIU A, SHARAF BA (2023) Facial morphometrics in black celebrities: contemporary facial analysis using an artificial intelligence platform. *J Clin Med*, 12(13): 4499.

SEÇKIN F, BÜLBÜL M (2020) İnsan anatomisinde altın oranlama ve sanat eserlerindeki karşılaştırmalı analizi. *Temel Eğitim*, 2(4): 6-20.

SEN SK, AGARWAL RP (2008) Golden ratio in science, as random sequence source, its computation and beyond. *Comput Mathematics Applicat*, 56(2): 469-498.

UMAR M, SINGH R, SHUGABA A (2006) Cephalometric indicies among Nigerians. *J Appl Sci*, 6(4): 939-942.

VARLIK SK, DEMIRBAŞ E, ORHAN M (2010) Influence of lower facial height changes on frontal facial attractiveness and perception of treatment need by lay people. *The Angle Orthodontist*, 80(6): 1159-1164.

YALCINKAYA E, KOCAMAN SA, YUKSEKKAYA M (2022) Attractive versus golden ratios: formula of utopian beauty through comparison of facial proportions among worldwide celebrities and average people. *J Craniofac Surg*, 33(7): 1950-1955.

ZWAHLEN RA, TANG ATH, LEUNG WK, TAN SK (2022) Does 3-dimensional facial attractiveness relate to golden ratio, neoclassical canons, 'ideal' ratios and 'ideal' angles? *Maxillofac Plast Reconstr Surg*, 44(1): 28.

ORIGINAL ARTICLE Eur J Anat, 28 (5): 543-549 (2024)

Analysis of the structural organization of the human hand using anatomical network models

Alexander Ermolenko

Doctor Chuchkalov Ulyanovsk Regional Clinical Center of Specialized Types of Medical Care, Ulyanovsk, Russian Federation

SUMMARY

Despite the fact that morphogenetic mechanisms of transformation of the hand during ontogenesis are currently known, the question remains as to how its various anatomical parts are (metacarpal bones, phalanges of fingers) organized into a complex integrated structure. This question remains unanswered for several reasons, including the lack of consensus about conceptual definitions and approaches, including the lack of tools to assess and compare variations in different anatomical parts of the hand.

The aim of this study is to assess the structural organization of the metacarpal bones and phalanges of the fingers of the human hand by Anatomical Network Analysis (AnNA). In this study, the functions of the IGRAPH package in the R data analysis programming environment were used for AnNA. The modeling and layout of the network is performed using the Fruchterman-Reingold algorithm. The Spinglass algorithm is used to determine modularity in anatomical networks.

For AnNA, X-ray osteometric indicators of the length (joint length) of the metacarpal bones and phalanges of the fingers of 100 middle-aged men and 100 women without traumatic changes, deformities and developmental abnormalities were used. AnNA demonstrates that the organization of the elements of the rays of the hand is represented by two modules – the proximal, which includes (metacarpal bones and proximal phalanges) and the distal, which includes the middle and distal phalanges. When comparing the characteristics of the network models of the hands, it was found that in women the organization of the metacarpal bones and phalanges of the fingers is characterized by higher morphological integration and modularity (modularity 0.31) than in men (modularity 0.45).

Morphological modularity and integration are the organizing factors of the structure of morphological parameters of various parts of the hand. The structural organization of the hand is a system consisting of two modules – the proximal (metacarpal bones and proximal phalanges) and the distal (middle and distal phalanges).

Key words: Human hand – Structural organization – Network analysis – Morphological modularity – Morpho-logical integration.

Corresponding author:
Alexander Ermolenko. 28 Koryukin st., Ulyanovsk, Russian Federation, 432063. Phone: +79372753757. E-mail: osteon@yandex.ru

Submitted: March 5, 2024. **Accepted:** March 5, 2024

https://doi.org/10.52083/XRGL4531

INTRODUCTION

The morphological substrate of the pentadactyly of the distal segments of the upper extremities of primates and in humans in particular are rays, each of which is formed by the metacarpal bone and the phalanges of its corresponding finger (Patel and Maiolino, 2016). The development and growth of the rays of the hand is determined by morphogenetic mechanisms that are uniform for all their elements in time and space (Glover et al., 2023). Subsequent ontogenetic transformations lead to the formation of the preaxial (I finger and I metacarpal bone) and postaxial (II–V metacarpal bones and II–V fingers) ray groups of the hand (Shubin and Alberch, 1986). However, despite the fact that the morphofunctional aspects are the same for each of the rays, the ratios of the elements of the postaxial group of the latter determine the morphological patterns of the hand: ectaxonic (the length of the IV ray prevails over the rest), paraxonic (the length of the III-IV rays prevails over the rest, while the length of these rays is the same) and mesaxonic (the length of the III ray prevails over the rest) (Preuschoft and Chivers, 1993).

Considering the above, the question arises as to how such a morphologically complex part of the human body as the hand evolved, taking into account the limitations caused by genetic factors, developmental factors, as well as locomotor functions, which has been the subject of study for many decades (Perepelkin et al., 2020). In the middle of the 20th century, the study of covariance (conjugate variation) of morphological features and the consequences of this for evolutionary diversification was developed within the framework of the general concept of “morphological modularity and integration” – i.e., the development of phenotypic structures of biological objects does not proceed in isolation, but is organized into modular units that are relatively independent of each other, while morphological features, the variability of which is due to embryogenetic or morphofunctional factors, have a high degree of integration and develop to some extent as a whole (Klingenberg, 2014). Taking into account the model of polygenic inheritance underlying the quantitative features of the skeleton, including the hand, as well as the existence of differential pleiotropic effects, it is assumed that variations in the comparison of genotype with phenotype can lead to the appearance of semi-autonomous “modules” that have a relatively stronger integration between morphological features within them. This concept is also closely related to the question of the ability of anatomical structures to respond to the selective pressure of environmental factors. For example, some authors argue that modularity provides flexibility of the anatomical structure, since the direction and magnitude of evolutionary changes between parts and within the structure can vary without compromising the function of the latter (Raff, 1996). However, other authors believe that higher integration within the anatomical structure contributes to its evolutionary transformations (Conaway and von Cramon-Taubadel, 2022). The study of structural organization is especially important for understanding the transformation of the hand, which differs among primates in the scale of morphological changes during their evolution (Chavez and Morrell, 2022).

Ideas about the morphological modularity, integration, and structural organization of the postcranial skeleton remain somewhat limited due to the difficulty of studying the many interactions between the bones of its various departments (Conaway and Adams, 2022). Moreover, due in no small part to the complexity of analyzing data sets and understanding them, most studies have focused on the skeleton of the girdle and the free part of the upper and lower limbs, with the exception of the distal segments (Conaway and von Cramon-Taubadel, 2022). Thus, the problem of the structure of the skeleton of the human hand in the context of architectonics and the organization of morphological indicators of its bones is relevant, which requires a new methodology based on the identification and comparison of morphological modularity and integration between the elements of the rays of the hand and their morphometric parameters in order to obtain a comprehensive assessment and an integrative look at the evolution and morphology of distal segments of the upper extremities.

One of the new powerful tools for studying patterns of interrelation between parts of the anatomical structure is Anatomical Network analysis

(AnNA) (Ziermann et al., 2021). Unlike quantitative morphometric methods, a unique feature of AnNA is a direct comparison of different parts of the studied object (McQueen and Towers, 2020). In particular, AnNA evaluates connectivity patterns using tools and statistics borrowed from network theory, formalizing parts of the studied object as nodes and connections between them as a network model to assess structural organization and identify patterns of integration and modularity between parts of the anatomical structure (Rasskin-Gutman and Esteve-Altava, 2009). It is noteworthy that AnNA represents a formal basis for the study of morphological organization, free from a priori assumptions and hypotheses about the development, functional and phylogenetic relationships between parts of anatomical structures (Diogo et al., 2018).

Using AnNA provides an opportunity to explore which patterns of integration/modularity have an impact on the structural organization of a person's hand.

The aim of this study was to study the structural organization of the elements of the rays of the human hand with the help of AnNA.

MATERIALS AND METHODS

Sample

In this work, we used the results of morphometry of certified digital radiographs of the hands of 200 people (100 men and 100 women) from the databases "Biometric description of X-ray osteometric signs of the metacarpal bones of the human hand" and "X-ray osteometric characteristics of the phalanges of the fingers of the human hand" (Ermolenko, 2021a, b). The average age of men was 46.3±1.1 years, the average age of women was 49.2±0.9 years (M±m).

AnNA

For the analysis, the indicators of articular length (the distance between the center of the articular area of the base and the point furthest from it on the head of the bone) of the metacarpal bones and phalanges of the fingers of the hand were used. Anatomical networks have been modeled as systems of connections between nodes, information about which is encoded in the form of adjacency correlation matrices: a square symmetric matrix where each row and column repre-

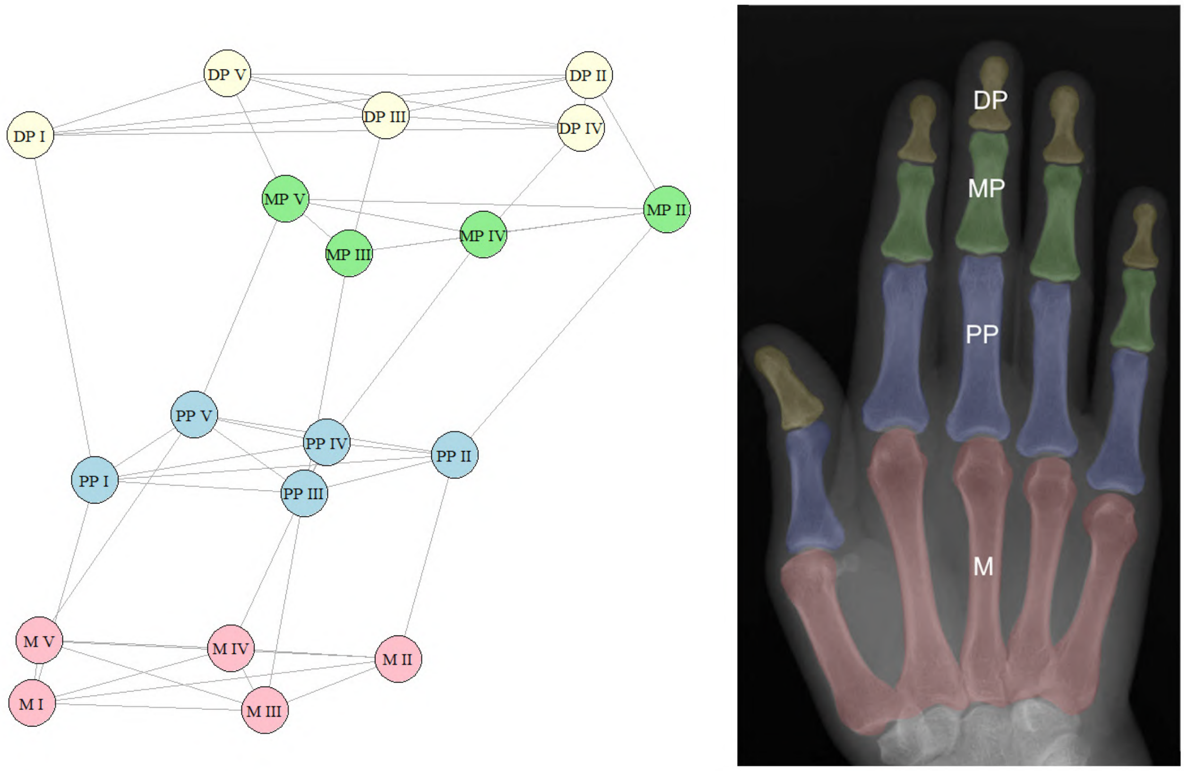

Fig. 1.- The scheme hand, formalized in the form of a network.

sent one anatomical part. For the hands (pastern and distal part of the hand (fingers)) men and women have built network models in which nodes represent bones (Fig. 1).

The measure of quantification of the connection between nodes was the weight of the connection. The nodes are arranged using the Fruchterman-Reingold algorithm. To determine modularity in anatomical networks, the Spinglass algorithm was used, the implementation of which is based on paired interactions in the system based on the assumption that the connections between nodes are in similar "spin" states, which determines the morphological context of modularity (Yan et al., 2016). In this study, the functions of the IGRAPH package in the R data analysis programming environment were used to build the network (Csardi and Nepusz, 2006). The quantitative assessment of the main network parameters included: connection density (the number of existing connections relative to the total maximum possible in accordance with the total number of nodes), the average clustering coefficient (the arithmetic mean of the clustering coefficient of all nodes in the network), the average distance between nodes (the average value of the sum of the distances between two nodes in the network), modularity (the value of indicating how well the network parts (modules) are separated from each other), heterogeneity of compounds (the ratio between the standard deviation and the average value of compounds).

RESULTS

Anatomical networks representing the hands of men and women were analyzed (Fig. 2).

Analysis of the relationship between nodes within the module and between nodes of modules of each module, regardless of gender and body side, demonstrates the absence of grouping within each module, which allows us to distinguish two modules. Module 1 (proximal) included the I-V metacarpal bones and the proximal IV fingers. Module 2 (distal) included the middle phalanges of the II-V fingers and the distal phalanges of the I-V fingers (Fig. 3).

The name of each module refers only to the anatomical area it occupies, and excludes any interpretation related to development and function. The

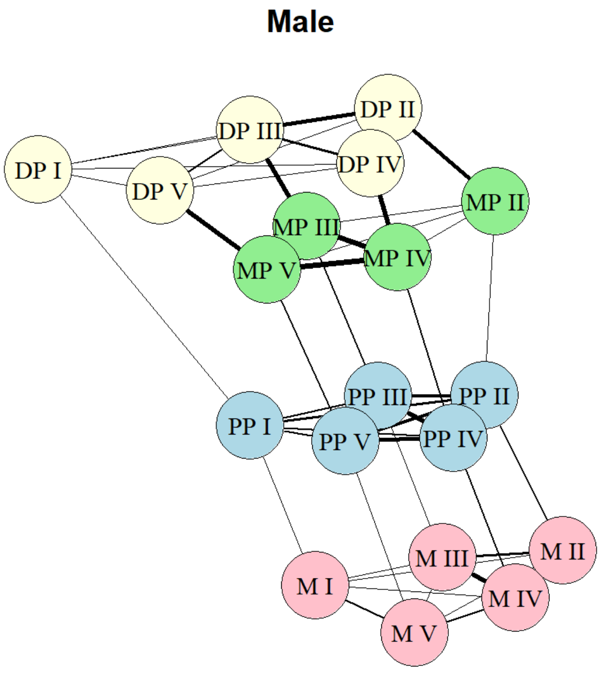

Fig. 2.- Network hand models.

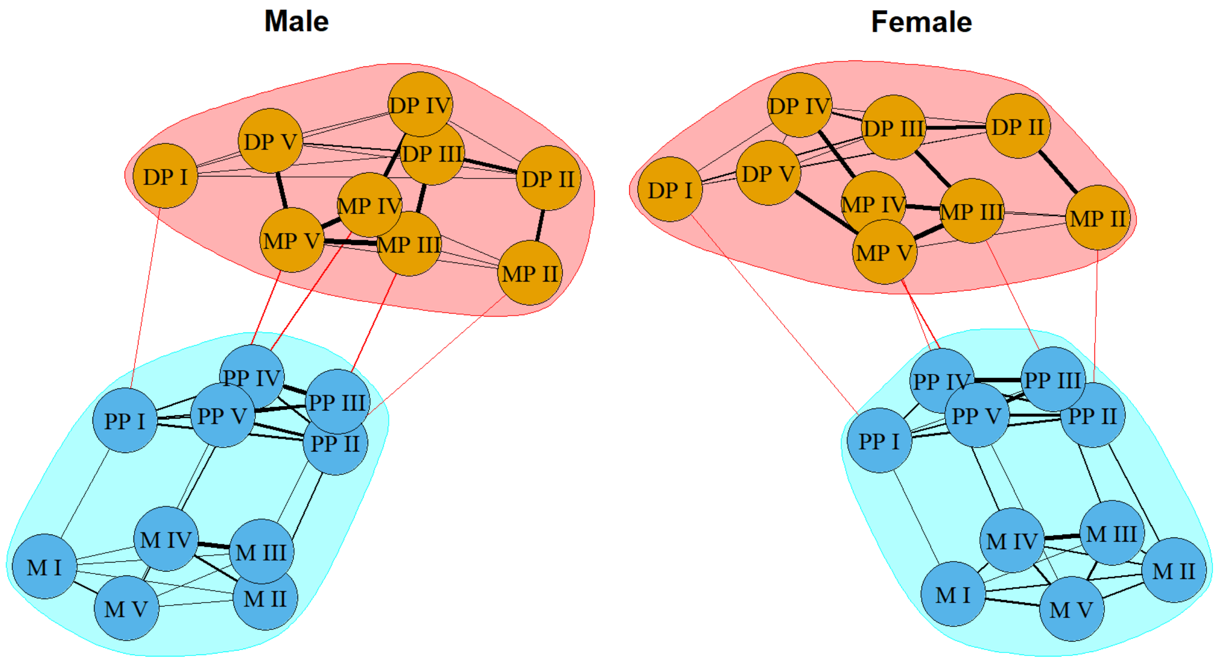

Fig. 3.- Hand modules.

analysis of network models of the hands demonstrates that in women, if compared with men, the organization of the metacarpal bones and phalanges of the fingers is characterized by higher morphological integration and modularity (Table 1).

Table 1. Parameters of anatomical network models of the hand.

Parameter	Male	Female
Number of nodes	19	
Number of connections	63	
Connection density	0.18	0.15
Clustering coefficient	0.43	0.47
Average distance between nodes	0.41	0.75
Modularity	0.31	0.45
Heterogeneity of compounds	0.79	0.64

Thus, we observe distinct proximal and distal modules in the human hand.

DISCUSSION

The obtained results demonstrate the possibilities of AnNA for studying the structural organization of the human hand. In previous studies, it was shown that differences in the structural organization of the hand in primates and humans in particular lie in the plane of differences between the morphometric parameters of the ray elements, which manifests itself in various proportional ratios between the metacarpal bones and phalanges of the fingers, identified using classical morphometry methods (Preuschoft and Chivers, 1993; Patel and Maiolino, 2016). Thus, the use of AnNA is an important step in assessing the structural organization of the hand in humans.

In this study, anatomical network models of the human hand were created. Despite the fact that the metacarpal bones and phalanges of the fingers are closely evolved modules of the hand, the results obtained confirm the hypothesis of an integration gradient in the postcranial skeleton (Chavez and Morrell, 2022). The development, growth and differentiation of the skeleton of the hand have a genetic determination and occur simultaneously in three planes as a continuum. These coordinated development processes ensure the integration of hand segments (Glover et al., 2023). Thus, the development of the structures of the proximal module (metacarpal bones and proximal phalanges) and distal modules (middle and distal phalanges) are regulated jointly, which leads to highly coordinated anatomical and functional relationships (Perepelkin et al., 2020).

The stronger relationships between the elements of each of the anatomical modules of the hand are consistent with its morphogenesis relative to the radiolateral (transverse) axis, which is due to the high proliferative activity of mesodermal cells forming a zone of polarizing activity located postaxially on the most distal part of the rudiment of the hand (McQueen and Towers, 2020).

In several anatomical studies, AnNA was used for comparative assessment, modeling of the development, functioning, and evolution of various morphological systems of the postcranial skeleton (Diogo et al., 2018; Ziermann et al., 2021). However, the research of the human hand with the help of AnNA focused on the analysis of the relationship of bone structures with tendons and muscles, while the structural organization was not considered in the context of organic integrity. The allocation of a two-level structure in the organization of the hand in the form of proximal and distal morphological modules possibly reveals the evolutionary aspect of the transformation from a hand with a force grip (the length of the fingers exceeds the length of the metacarpal bones), which is necessary for locomotion in lower primates to a hand with a precision grip (metacarpal bones and proximal phalanges provide the grip force, while the middle and distal phalanges play a role in precision grip), which is observed in higher primates, including humans, when manipulating objects.

Thus, a network model of the hand was built, which, apparently, reflects in the form of a network the morphogenetic effects underlying the coordinated development of human hand segments. The results of the study confirm that AnNA is an important tool for studying the distal segments of the human postcranial skeleton.

The results obtained cannot be considered in the context of the existence of a relationship between modularity and the complex structure of the skeleton of the hand from a morphological point of view. At the same time, attempts to limit the definition of the complexity of the structure of the skeleton of the hand confirm the positive feedback between modularity and structure. However, this thesis should be considered with some caution, due to the small number of metacarpal bones and phalanges of fingers in humans.

The results of the study demonstrate that the determining factors of the structural organization of the hand are morphological integration and modularity. This is the first study using AnNA to assess the structural organization of the hand based on radiography data. AnNA can be used to study the anatomical variability of the skeleton of the hand in terms of morphological modularity and integration.

ACKNOWLEDGEMENTS

The author expresses gratitude to the radiology department of the Doctor Chuchkalov Ulyanovsk Regional Clinical Center of Specialized Types of Medical Care for providing digital images of hand radiographs.

REFERENCES

CHAVEZ TJ, MORRELL NT (2022) The evolution of the human hand from an anthropologic perspective. *J Hand Surg Am*, 47(2): 181-185.

CONAWAY MA, ADAMS DC (2022) An effect size for comparing the strength of morphological integration across studies. *Evolution*, 76(10): 2244-2259.

CONAWAY MA, VON CRAMON-TAUBADEL N (2022) Morphological integration of the hominoid postcranium. *J Hum Evo*, 171: 103239.

CSARDI G, NEPUSZ T (2006) The igraph software package for complex network research. *Int J Complex systems*, 1695(5): 1-9.

DIOGO R, MOLNAR JL, ROLIAN C, ESTEVE-ALTAVA B (2018) First anatomical network analysis of fore- and hindlimb musculoskeletal modularity in bonobos, common chimpanzees, and humans. *Sci Rep*, 8(1): 6885.

ERMOLENKO AS (2021a) Certificate of the Russian Federation on state registration of the database “Biometric description of X-ray osteometric signs of the metacarpal bones of the human hand”, №2021621827.

ERMOLENKO AS (2021b) Certificate of the Russian Federation on the state registration of the database “X-ray osteometric characteristics of the phalanges of the fingers of the human hand”, №2021622030.

GLOVER JD, SUDDERICK ZR, SHIH BB, BATHO-SAMBLAS C, CHARLTON L, KRAUSE AL, ANDERSON C, RIDDELL J, BALIC A, LI J, KLIKA V, WOOLLEY TE, GAFFNEY EA, CORSINOTTI A, ANDERSON RA, JOHNSTON LJ, BROWN SJ, WANG S, CHEN Y, CRICHTON ML, HEADON DJ (2023) The developmental basis of fingerprint pattern formation and variation. *Cell*, 186(5): 940-956.e20.

MCQUEEN C, TOWERS M (2020) Establishing the pattern of the vertebrate limb. *Development*, 147(17): dev177956.

KLINGENBERG CP (2014) Studying morphological integration and modularity at multiple levels: concepts and analysis. *Philos Trans R Soc Lond B Biol Sci*, 369(1649): 20130249.

PATEL BA, MAIOLINO SA (2016) Morphological diversity in the digital rays of primate hands. In: Kivell T, Lemelin P, Richmond B, Schmitt D (eds.). *The Evolution of the Primate Hand. Developments in Primatology: Progress and Prospects*. Springer, New York, pp 55-100.

PEREPELKIN AI, KRAYUSHKIN AI, DORONIN AB, ATROSCHENKO ES, KRAYUSHKIN SS, editors (2020) Human autopodium (anatomy of the foot and hand). Publishing house of VolgSMU, Volgograd.

PREUSCHOFT H, CHIVERS DJ, editors (1993) Hands of Primates. Springer-Verlag, Vienna.

RAFF RA, editor (1996) The shape of life: genes, development, and the evolution of animal form. University of Chicago Press, Chicago.

RASSKIN-GUTMAN D, ESTEVE-ALTAVA B (2009) Connecting the dots: anatomical network analysis in morphological EvoDevo. *Biol Theory,* 9(2): 178-193.

SHUBIN NH, ALBERCH P (1986) A morphogenetic approach to the origin and basic organization of the tetrapod limb. In: Hecht MK, Wallace B, Prance GT (eds.). *Evolutionary Biology*. Springer, Boston, pp 319-387.

YANG Z, ALGESHEIMER R, TESSONE CJ (2016) A comparative analysis of community detection algorithms on artificial networks. *Sci Rep,* 6(1): 30750.

ZIERMANN JM, BOUGHNER JC, ESTEVE-ALTAVA B, DIOGO R (2021) Anatomical comparison across heads, fore- and hindlimbs in mammals using network models. *J Anat,* 239(1): 12-31.

Investigation of sphenoid spine morphometry for skull base surgery and relation to foramen spinosum localization

Eda Duygu Ipek, Berrin Ozustun, Ilgaz Akdogan

Aydin Adnan Menderes University, Faculty of Medicine, Department of Anatomy, Aydin, Turkey

SUMMARY

Our study aimed to investigate the sphenoid spine morphological characterization, as well as the distances to important surgical points and its relation to foramen spinosum localization. On a total of 65 skulls, the distances of the sphenoid spine to various surgically important anatomical landmarks were measured from both the right and left sides. The length of the sphenoid spine was measured and classified morphologically. Localization of the foramen spinosum relation to the sphenoid spine was evaluated. The sphenoid spine length was statistically different which was found to be 6.71±1.97 and 6.14±1.93 on the right and left sides, respectively (p=0.027). The most commonly encountered shape of the sphenoid spine on both sides was quadrangular, followed by spine shape. The foramen spinosum was most frequently located anteromedially and least frequently located anterolaterally in relation to the sphenoid spine. In our study, it was determined that the localization of the foramen spinosum is associated with the shape of the sphenoid spine, on both the right (p=0.012) and left (p=0.016) sides. Our study provides morphometric data on the sphenoid spine and reports the association between the localization of the foramen spinosum and the type of sphenoid spine.

Key words: Sphenoid spine – Foramen spinosum – Infratemporal fossa – Endoscopic approach – Skull base

INTRODUCTION

The sphenoid spine, described as spina ossis sphenoidalis in anatomical terminology, is a pointed protrusion extending downward from the junction of the squamosal and posterior borders of the greater wings of the sphenoid bone. Three ligaments, ligamentum sphenomandibulare, mallei anterius and pterygospinosus, two muscles, musculus tensor veli palatini and tensor tympani, are attached to the sphenoid spine. Furthermore, it is adjacent to the cartilaginous part of the external auditory canal and chorda tympani medially, and to the auriculotemporal nerve laterally (Infant Reshawn and Yuvaraj Babu, 2020).

Technological advancements have significantly expanded the range of areas accessible through endoscopic approaches in skull base surgeries, but the complications attributed to these

---

Corresponding author:
Asst. Prof. Eda Duygu Ipek. Aydin Adnan Menderes University, Faculty of Medicine, Department of Anatomy, Efeler 09010, Aydin, Turkey. Phone: +90 545 684 86 73; Fax: +90 256 212 31 69. E-mail: eda.cakir@adu.edu.tr

Submitted: March 12, 2024. **Accepted:** March 31, 2024

https://doi.org/10.52083/KGHN8857

approaches have also increased proportionally (Fang et al., 2020). The internal carotid artery (ICA) is the most feared structure by endoscopic surgeons for its complications in skull base surgeries. In particular, there is a lack of anatomical landmarks that allows the safe exposure of the cervical portion of the ICA, which is surrounded by soft tissues throughout the parapharyngeal area in infratemporal fossa, and access to this segment of the ICA is less defined (Liu et al., 2019; Fang et al., 2020). In endoscopic transpterygoid approach, the pterygoid plate, mandibular nerve, Eustachian tube, and styloid process have been reported as reliable landmarks for reaching the parapharyngeal ICA (Falcon et al., 2011). Liu et al. (2014) reported that the sphenoid spine and foramen spinosum are anatomical landmarks for the cartilaginous and bony junction of the Eustachian tube, and parapharyngeal ICA was located immediately posteroinferior to the sphenoid spine. Liu et al. (2019) also found that the sphenoid spine, tympanic crest and vaginal process of tympanic bone were the closest anatomical landmarks to the parapharyngeal ICA in the endoscopic transmasticator approach. Li et al. (2022) reported that in transoral nasopharyngectomy, it is mandatory to define the parapharyngeal ICA before transection of the Eustachian tube, and the best landmarks defining it are the sphenoid spine, the petrotympanic fissure and the pterigoid hamulus.

The foramen spinosum, through which the middle meningeal vessels and the meningeal branch of the mandibular nerve pass to middle cranial fossa, is located in the greater wing of the sphenoid bone. It is named ‘spinosum’ due to its close proximity to the sphenoid spine, and it is described in classical anatomy texts to be located on the anteromedial side of sphenoid spine (Worku and Clarke, 2021; Sugano et al., 2022; Sink et al., 2023). Although it has been evaluated in very few studies in the literature, it is observed that the localization of foramen spinosum varies relation to the sphenoid spine (Sophia and Kalpana, 2015; Worku and Clarke, 2021; Sink et al., 2023). The localization of the foramen spinosum is important in various procedures, such as endovascular embolization of dural arteriovenous fistulas and meningiomas through the middle meningeal artery (Sink et al., 2023), in bypass operations where middle meningeal artery is used as a graft (Sophia and Kalpana, 2015). Also, it has been reported that anatomical variations of the foramen spinosum may be associated with abnormal development of the middle meningeal artery (Sugano et al., 2022). Therefore, a more detailed understanding of the localization of the foramen spinosum is necessary in the preoperative assessment of possible changes in the trajectory of neurovascular structures. The sphenoid spine is used as a landmark during infratemporal surgical approaches due to its close proximity to the foramen spinosum, parapharyngeal ICA, Eustachian tube and chorda tympani (Worku and Clarke, 2021). Despite its clinical importance, there is a lack of data in the literature regarding the anatomical variations of the sphenoid spine, and studies investigating its relationship with adjacent structures are insufficient. In the present study, considering the importance of the topography of the sphenoid spine and foramen spinosum in skull base surgeries, to the aim was to examine in more detail the relation between the foramen spinosum to the sphenoid spine, as well as the morphometric analysis of sphenoid spine with related structures.

MATERIALS AND METHODS

In this study, 65 adult skulls of unknown gender, obtained from the bone archive of Aydin Adnan Menderes University, Faculty of Medicine, Department of Anatomy, were used. Damaged skulls that did not allow examination of the targeted structures were not included in the study. The distance of the sphenoid spine to the tip of mastoid process (SMP), to the tip of tuberculum articulare (STA), to the anterior border of the external orifice of the carotid canal (SCC), to the point where the sutura sphenosquamosa intersects the crista infratemporalis (SO), to the most lateral (SPFl) and medial (SPFm) endpoints of the petrotympanic fissure, to the sphenoidal tubercle (STS), and the length of the sphenoid spine (SL) were measured on the right and left sides, using a digital Vernier caliper (eSynic, Hong Kong, China) with a precision of 0.01 mm.

The morphological characterization of the sphenoid spine was classified into five types: spine, quadrangular, pyramidal, plate and cup-shaped, as shown in Fig. 1.

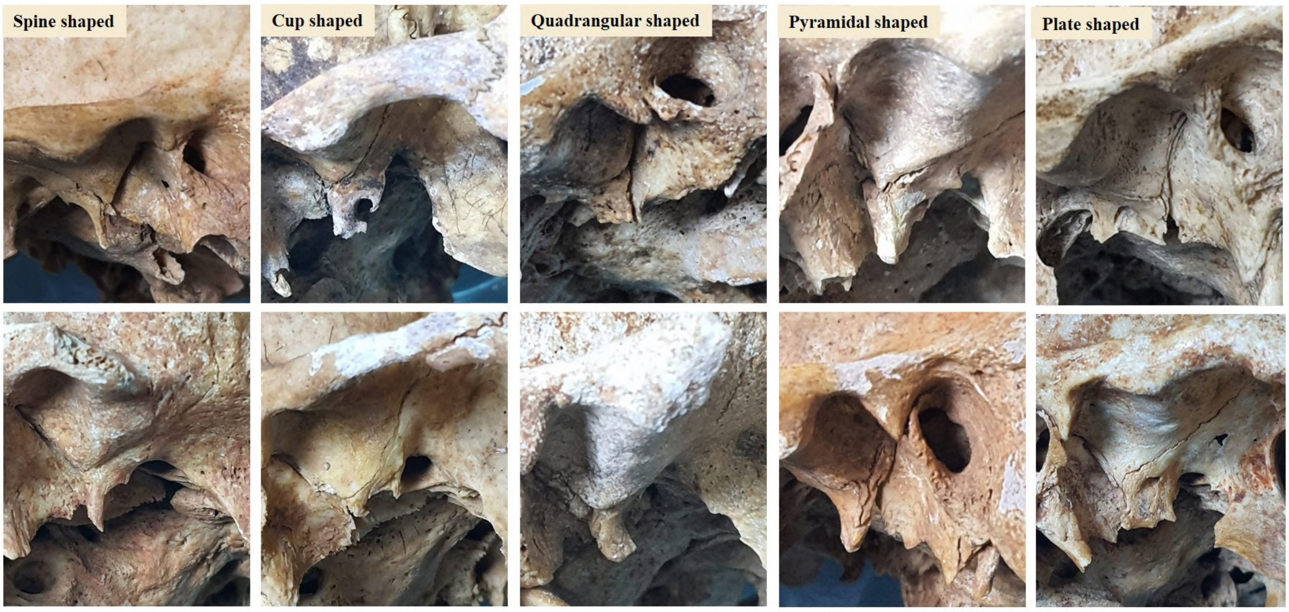

Fig. 1.- Examples of sphenoid spine morphological types.

The localization of the foramen spinosum relation to the sphenoid spine was examined from the basis cranii externa. A sagittal line was passed through the center of the foramen spinosum as shown in Fig. 2. The location of the foramen spinosum was classified as medial (M), lateral (L), anterior (A), anteromedial (AM), anterolateral (AL) and anterior-on-the-line (AO), medial-on-the-line (MO) and lateral-on-the-line (LO). In M and L placement, the line passed through the medial and lateral sides of the sphenoid spine while intersected with the sphenoid spine in A placement. In the AM and AL placement, the foramen spinosum was in front of the sphenoid spine and the line was on the medial and lateral sides of the sphenoid spine, respectively. Skulls with a line transition similar to the M, L and A placement of the foramen spinosum, but where the middle meningeal artery groove was observed on the sphenoid spine root, were classified as MO, LO and AO, respectively.

SPSS (Version 22.0, SPSS Inc., Chicago, IL, USA) program was used for statistical analysis of the data. The distribution pattern of the data was evaluated with the Kolmogorov Smirnov test, and paired-t test was applied to compare the right and left morphometric parameters. Chi-square test

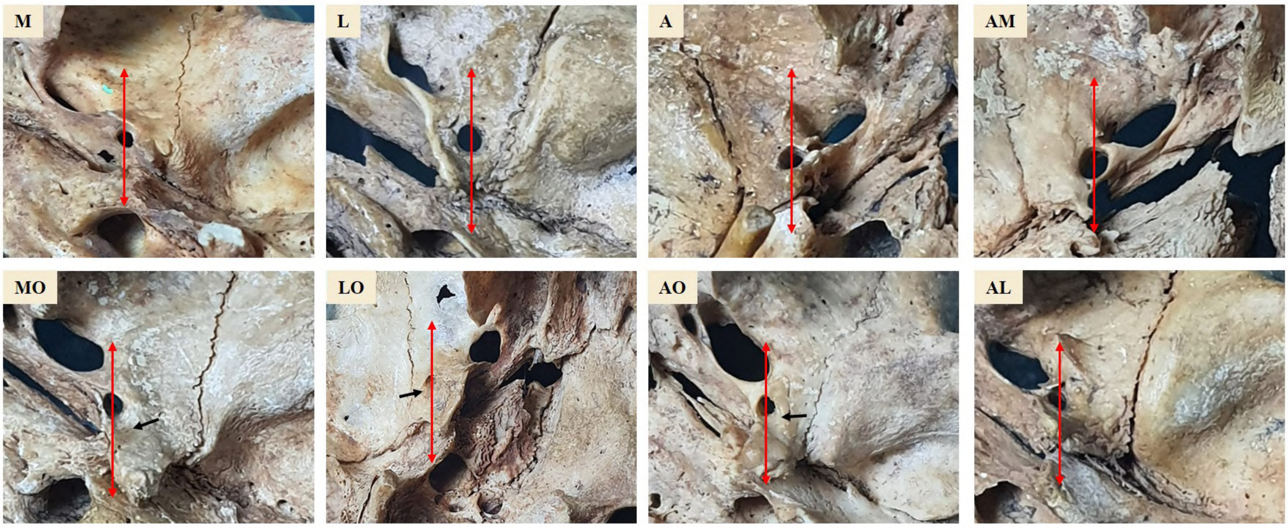

Fig. 2.- The foramen spinosum localization in relation to the sphenoid spine: medial (M), lateral (L), anterior (A), anteromedial (AM), anterolateral (AL) and anterior-on the line (AO), medial-on the line (MO) and lateral-on the line (LO). The black arrows show the middle meningeal artery groove observed at the root of the sphenoid spine.

Table 1. Mean, minimum and maximum values of morphometric parameters. See material and methods section for abbreviations.

	Right side **mean±sd (min–max)** **n=65**	**Left side** **mean±sd (min–max)** **n=65**	**p value** **(Sig. 2-tailed)**
STA	29.08±2.67 (22.7-35.6)	28.57±2.36 (22.1-34.3)	0.71
SMP	32.97±2.79 (26.6-44,1)	33.67±2.93 (25.8-41.4)	0.63
SPFl	23.98±3.03 (17.5-30.4)	23.79±2.68 (18-29.6)	0.602
SPFm	4.05±1.27 (2.2-5.8)	4.21±1.27 (2.1-6.3)	0.512
SO	29.98±4.17 (21.3-40.4)	29.76±4.01 (20.7-39.9)	0.635
SCC	6.53±1.86 (2.2-11.1)	6.74±2.28 (2.4-12.4)	0.426
STS	33.13±3.57 (20.5-41.4)	33.37±4.94 (25.3-42.7)	0.729
SL	6.71±1.97 (2.3-10.7)	6.14±1.93 (2-10.4)	0.027

sd: standart deviation, The p values represent the diference between left and right sides

was used to evaluate the localization of the foramen spinosum according to sphenoid spine morphological types.

RESULTS

The descriptive statistics of the morphometric measurements we conducted are indicated in Table 1. In comparing the morphometric measurements between the right and left sides, it was found that only the length of the sphenoid spine was statistically higher on the right side (p=0.027).

The most commonly encountered morphological type of the sphenoid spine on both the right and left sides was quadrangular, 35.35% of the total, followed by a spine shape. On the left side, the least encountered morphological type of the sphenoid spine was plate-shaped (10.8%), while on the right side, it was cup-shaped (12.3%). We found that the tip of the sphenoid spine was bifurcated unilaterally in a total of 3 skulls (4.61%), one with pyramidal and two with quadrangular shape. Additionally, pterygospinous bar and pterygospinous foramen, formed by the ossification of the pterygopinous ligament, were detected unilaterally on two sides (1.53%). The mentioned variations are shown in Fig. 3. Morphometric measurement mean values and frequency of sphenoid spine types are given in Table 2.

Table 2. Morphometric parameters in sphenoid spine morphological types. See material and methods section for abbreviations.

	Spine		**Quadrangular**		**Pyramidal**		**Cup**		**Plate**	
	Right side n=15. 23.1%	Left side n=12. 18.5%	Right side n=22. 33.8%	Left side n=24. 36.9%	Right side n=10. 15.4%	Left side n=11. 16.9%	Right side n=11. 16.9%	Left side n=8. 12.3%	Right side n=7. 10.8%	Left side n=10. 15.4%
STA	27.91±2.16	27.84±2.08	29.81±2.84	28.9±2.58	29.02±25.5	29.2±2.01	29.4±2.05	28.1±1.92	28.6±3.84	28.1±2.81
SMP	32.6±2.44	32.3±3.41	33.3±3.66	33.8±2.55	32.06±1.6	33.8±2.64	33.38±1.87	35.1±3.85	33.2±3.21	33.4±2.5
SPFl	23.7±3.25	23.09±3.1	24.1±3.23	23.9±2.89	24.3±3.15	24.1±2.68	24.3±2.93	23.4±1.4	22.8±2.31	24.05±26
SPFm	4.97±1.12	4.12±0.8	3.96±0.75	4.01±1.04	4.62±1.2	4.34±0.92	3.92±0.76	4.3±1.11	3.2±0.76	3.5±0.88
SO	29.5±5.59	27.8±3.52	29.9±3.18	30.24±4.2	32.07±4.09	30.13±3.5	29.3±3.04	28.3±3.26	29.1±5.23	31.6±4.31
SCC	6.6±2.17	6.51±2.23	6.57±2.15	6.55±2.47	5.6±1.27	7.81±1.57	7.08±1.66	7.5±2.9	6.68±1.01	5.69±1.68
STS	32.4±3.51	32.36±3.9	33.2±3.36	33.5±2.63	34.8±2.31	35.38±2.7	32.9±3.14	33.31±4.11	32.1±6.02	31.89±10
SL	6.8±2.45	6.37±1.63	6.7±2.05	5.66±1.85	7.18±0.94	5.09±1.13	6.67±1.65	4.87±195	5.98±2.39	5.4±2.01

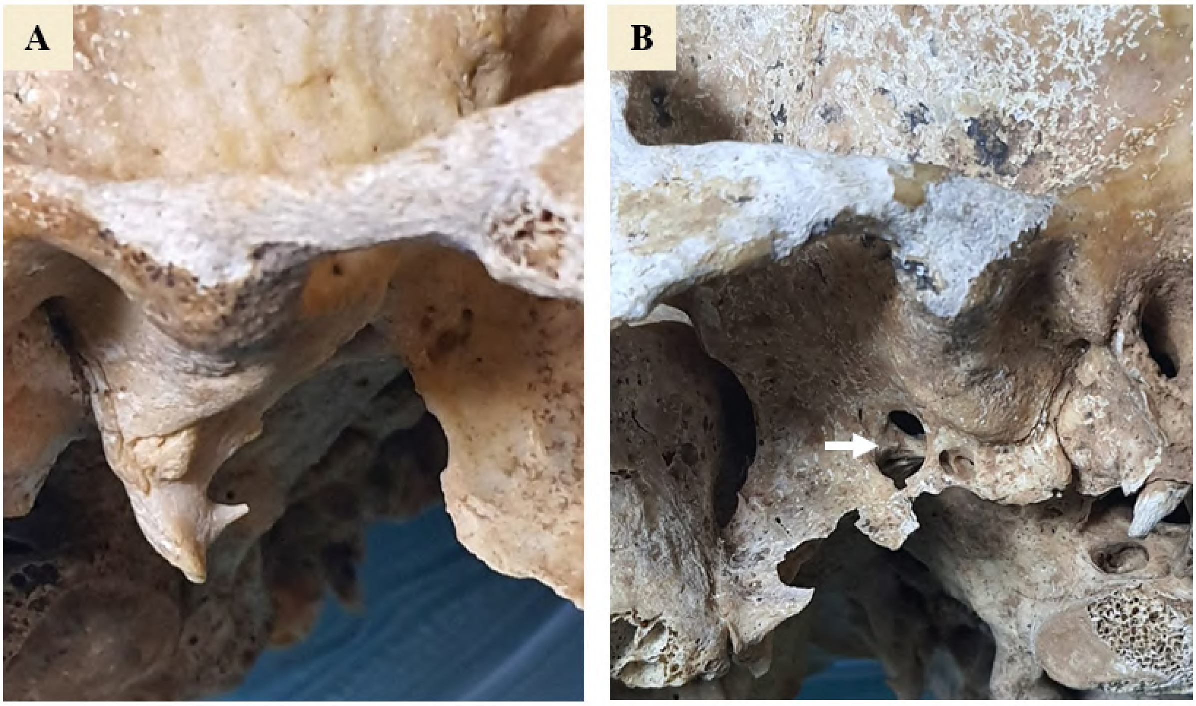

Fig. 3.- A: Bifurcated sphenoid spine. **B**: White arrow indicates pterygospinosus foramen (Civinini's foramen).

As shown in Table 3, it was determined that the foramen spinosum is frequently located in the anteromedial aspect of the sphenoid spine on both sides. It can be said that the foramen spinosum is frequently located anteromedially in skulls with spine, quadrangular, and pyramidal shapes of the sphenoid spine, while in plate shape, lateralization of the foramen spinosum is more commonly observed. According to the Chi-square test result, the localization of the foramen spinosum was associated with the morphological type of the sphenoid spine on both sides.

DISCUSSION

The safe exposure of the parapharyngeal segment of the ICA is necessary for many surgical procedures that will be performed through the infratemporal fossa. In addition to the sphenoid spine being an important anatomical landmark for identifying the internal carotid artery, its re-

Table 3. Foramen spinosum localisation according to sphenoid spine morphology: medial (M), lateral (L), anterior (A), anteromedial (AM), anterolateral (AL) and anterior-on the line (AO), medial-on the line (MO) and lateral-on the line (LO).

	A		M		L		MO		AM		AO		AL		LO		p
	Right %4.6	Left %4.6	Right %9.2	Left %9.2	Right %6.2	Left %6.2	Right %4.6	Left %1.5	Right %33.8	Left %38.5	Right %33.8	Left %26.2	Right %7.7	Left %10.8	Right -	Left %3.1	
Spine	1	0	1	1	0	0	2	1	5	6	6	3	0	0	0	1	**0.012a** **0.016b**
Quadrangular	0	3	1	1	0	2	1	0	10	9	9	8	1	0	0	1	
Pyramidal	1	0	1	1	0	0	0	0	5	6	2	4	1	0	0	0	
Cup	1	0	3	2	2	0	0	0	2	3	3	1	0	2	0	0	
Plate	0	0	0	1	2	2	0	0	0	1	2	1	3	5	0	0	

The Pearson Chi square p values represent the location of the foramen spinosum is related to the type of sphenoid spine on the right[a] and left[b] sides lationship with the position of the foramen spinosum is also clinically important. However, its anatomical variations and relationships with other structures in the infratemporal fossa have not been precisely elucidated.

In this study, we did not find statistical difference between the right and left sides in SMP and STA values similar to Infant Reshawn and Yuvaraj Babu (2020). They reported SMP values in 30 skulls as 30.56±1.10 mm and 30.66±1.12 mm, STA values as 22.07±2.12 mm and 22.13±2.12 mm, on the right and left sides, respectively. While the SMP values in our study are close to their findings, our STA values are higher. Liu and Yi (2020) defined the intersection point of the sphenosquamous suture with the infratemporal crest as ‘‘point O’, and reported that point O can be used as a reliable landmark in lateral skull base surgeries when other landmark points cannot be identified. Our distance values between the sphenoid spine and O point were not statistically different between the right and left sides. However, they were found to be distributed in a wide range, 21.3 mm-40.4 mm and 20.7 mm-39.9 mm, respectively. Another surgical reference point used in infratemporal fossa surgeries is a bony prominence located at the anterior end of the infratemporal crest, referred to as the sphenoidal tubercle in the literature. It is confused with the sphenoid spine in some studies (Stajcic et al., 2010; Rusu et al., 2019). Our mean STS values on the right and left sides were found to be quite close to each other. The lateral pterygoid muscle, the only muscle responsible for opening the jaw, attaches to the sphenoidal tubercle, and the sphenomandibular ligament, extending between the sphenoid spine and mandibular lingula, is tense when the jaw is open (Simonds et al., 2017). Therefore, the anatomy of the sphenoid spine and the sphenoidal tubercle may be related. Furthermore, it is reported that there is a close relationship between the temporomandibular joint and the middle ear, explained by the presence of the discomalleolar ligament, anterior mallear ligament and the sphenomandibulare ligament. It is considered that the presence of otological symptoms in patients with temporomandibular joint disorders may be associated with the petrotympanic fissure morphology and ossification. (Almaşan et al., 2022). We did not find difference for SPFm and SPFl between the right and left sides. As seen in Table 2, the SPFm distance was the lowest in plate-shaped sphenoid spines. Considering the frequent lateral placement of the foramen spinosum in these shapes, it can be said that, as mentioned by Sugano et al. (2022), the foramen spinosum is very close to the petrotympanic fissure in these skulls. Liu et al. (2019) reported that the distance from the sphenoid spine to the external orifice of the carotid canal, from 2.5 to 6.1 mm, was highly variable. Although our data are variably similar to their findings, ranged from 2.2 to 11.1 and 2.4 to 12.4 on the right and left sides, respectively, they reveal a significantly higher maximum value. Our SCC findings are closer to the values reported by Sink et al. (2023) as 8.02±1.35 mm (5.13 mm-13.60 mm) and 8.22±1.47 mm (5.04 mm-14.97 mm) on the right and left sides, respectively. Li et al. (2019) reported that the sphenoid spine length was also variable. We found that only the sphenoid spine length was statistically different between the right and left sides and our mean values are close to their finding of 5.98 mm. They reported that the tip of the sphenoid spine bifurcated in 10% of the specimens, which is higher than the rate of 3.07% we identified. However, they used only 10 skulls. Iwanaga et al. (2020), detected bony pterygospinosus bar on two sides (%6.66) in 15 cadaveric head specimens which was higher than our study (Fig. 3).

In the literature, only Infant Reshawn and Yuvaraj Babu (2020) categorized sphenoid spine morphology as sharp, rounded, blunt, and pointed in 30 skulls. However, they did not provide detailed information or examples related to this morphological classification in their reports. We classified sphenoid spine types into 5 categories, as seen in Fig. 1. Infant Reshawn and Yuvaraj Babu (2020) most commonly identified a rounded shape. Interestingly, we found that the sphenoid spine, which we know as a spiny protrusion, was often quadrangular shape not spiny. A significant association were found between the morphological shape of the sphenoid spine and the location of the foramen spinosum on both sides. Worku and Clarke (2021) and Sophia et al. (2015) classified the position of the foramen spinosum in relation to the sphenoid spine as normal (anteromedial), lateral, and medial placements. Worku and Clarke (2021) found that the foramen spinosum anteromedially located in 61 of a total of 64 skulls. Sophia et al. (2015) reported that the rate of anteromedial location of the foramen spinosum as 25% in 40 skulls on 80 sides. The total anteromedial placement percentage of our study is 36.15%, lower than Worku and Clarke (2021) and higher than Sophia et al. (2015). Worku and Clarke (2021) reported lateral and medial placement on 4 and 2 sides, respectively. Sophia et al. (2015) reported the highest lateral placement on 21 sides, medial placement on three sides. Sugano et al. (2022) detected laterally located foramen spinosum on 2 sides in 30 skulls. In this study, we classified the position of the foramen spinosum relation to sphenoid spine in more detail, as merely classifying it as lateral and medial did not provide an assessment in the anteroposterior direction, as in its normal anatomical position. The classification by Sink et al. (2023) of foramen spinosum localization is similar to our study, but they did not evaluate the relation of the sphenoid spine morphological types with foramen spinosum localization. They found posterolateral (%3.5), posteromedial (%0.39), and posteriorly (%0.78) located foramen spinosum, although we did not identify any in our skulls. While their percentages of anteromedial (%48.64), anterolateral (%20.3) and anteriorly (%14.79) located foramen spinosum are higher than in our study, the lateral placement value is close to the findings of our study (%5.84).

CONCLUSION

The relationship between foramen spinosum localization and sphenoid spine shape, as we have determined in our study, the increased lateralization of foramen spinosum in plate shaped sphenoid spine may affect the course of the middle meningeal artery, nervus spinosus, chorda tympani and auriculotemporal nerves. Therefore, variations in anatomical structures and their relationships with each other should be considered in the evaluation of pathologies in the middle cranial fossa and in the planning of surgical interventions for this region.

AUTHOR CONTRIBUTIONS

Conceptualization: Eda Duygu Ipek; Data collection and analysis: Eda Duygu Ipek, Berrin Ozustun; Manuscript writing: Eda Duygu Ipek; Manuscript review and editing: Eda Duygu Ipek, Ilgaz Akdogan; Supervision: Eda Duygu Ipek, Ilgaz Akdogan.

REFERENCES

ALMASAN O, LEUCUTA DC., DINU C, BUDURU S, BACIUT M, HEDESIU M (2022) Petrotympanic fissure architecture and malleus location in temporomandibular joint disorders. *Tomography*, 8(5): 2460-2470.

FALCON RT, RIVERA SERRANO CM, MIRANDA JF, PREVEDELLO DM, SNYDERMAN CH, KASSAM AB, CARRAU RL (2011) Endoscopic endonasal dissection of the infratemporal fossa: anatomic relationships and importance of eustachian tube in the endoscopic skull base surgery. *The Laryngoscope*, 121(1): 31-41.

FANG X, DI G, ZHOU W, JIANG X (2020) The anatomy of the parapharyngeal segment of the internal carotid artery for endoscopic endonasal approach. *Neurosurg Rev*, 43: 1391-1401.

INFANT RESHAWN I, YUVARAJ BABU K (2020) Morphometric analysis of locations, shape and variations of spine of sphenoid and its clinical importance. *Biosci Biotechnol Res Commun Special Isuue*, 13(8): 551-554.

IWANAGA J, CLIFTON W, DALLAPIAZZA RF, MIYAMOTO Y, KOMUNE N, GREMILLION HA, DUMONT AS, TUBBS RS (2020) The pterygospinous and pterygoalar ligaments and their relationship to the mandibular nerve: Application to a better understanding of various forms of trigeminal neuralgia. *Ann Anat*, 229: 151466.

LI L, XU H, JIN Y, CHEN X, CARRAU RL, LONDON JR NR (2022) Exploration of anatomical landmarks for performing an endoscopic transoral nasopharyngectomy. *Head Neck*, 44(11): 2378-2385.

LIU J, PINHEIRO-NETO CD, FERNANDEZ-MIRANDA JC, SNYDERMAN CH, GARDNER PA, HIRSCH BE, WANG E (2014) Eustachian tube and internal carotid artery in skull base surgery: an anatomical study. *The Laryngoscope*, 124(12): 2655-2664.

LIU W, CHAE R, RUBIO RR, BENET A, MEYBODI AT, FENG X, HUANG G, EL-SAYED IH (2019) Characterization of anatomical landmarks for exposing the internal carotid artery in the infratemporal fossa through an endoscopic transmasticator approach: a morphometric cadaveric study. *World Neurosurg*, 131: e415-e424.

LIU Z, YI Z (2020) A new bony anatomical landmark for lateral skull base surgery. *J Craniofacial Surg*, 31(4): 1157-1160.

RUSU MC, CIULUVICĂ, RC VRAPCIU AD, CHIRIȚĂ AL, PREDOIU M, MĂRU N (2019) Bilateral giant and unilateral duplicated sphenoidal tubercle. *Folia Morphologica*, 78(4): 893-897.

SIMONDS E, IWANAGA J, OSKOUIAN RJ, TUBBS RS, SIMONDS EA (2017) Duplication of the sphenomandibular ligament. *Cureus*, 9(10): 1-4.

ŠINK Ž, UMEK N, CVETKO E (2023) Morphometric and morphologic analysis of the foramen spinosum in the Slovenian population with clinical correlations. *Peer J*, 11: e16559.

SOPHIA MM, KALPANA R (2015) A study on foramen spinosum. *IJHSR*, 5(2): 187-193.

STAJČIĆ LS, GAČIĆ B, POPOVIĆ N, STAJČIĆ Z (2010) Anatomical study of the pterygopalatine fossa pertinent to the maxillary nerve block at the foramen rotundum. *Int J Oral Maxillofacial Surg*, 39(5): 493-496.

SUGANO GT, PAURIS CC, SILVA YBE, PANDINI FE, PALERMO RBS, BUCHAIM DV, BUCHAIM RL, CHACON EL, CASTRO CA, PAGANI BT, CUNHA MR (2022) Topographic and morphometric study of the foramen spinosum of the skull and its clinical correlation. *Medicina*, 58(12): 1740.

WORKU MG, CLARKE E (2021) Morphometric analysis of the foramen spinosum and variations of its shape, number, and relation to the spine of the sphenoid bone. *Transl Res Anat*, 24: 100124.

ORIGINAL ARTICLE Eur J Anat, 28 (5): 559-568 (2024)

Investigation of the effects of pomegranate juice against toxicity in the testes in lead-administered rats

Hıdır Pekmez[1], Ebru Annaç[2], Özgür Bulmuş[3], Gökçe Bağcı Uzun[1], Merve Aydın[1], Ali Aydın[2,4]

[1] Department of Anatomy, Faculty of Medicine, Malatya Turgut Özal University, Malatya, Turkey
[2] Department of Histology and Embryology, Faculty of Medicine, Adıyaman University, Adıyaman, Turkey
[3] Department of Physiology, Faculty of Medicine, Balıkesir University, Balıkesir, Turkey
[4] Department of Anatomy, Faculty of Medicine, Adıyaman University, Adıyaman, Turkey

SUMMARY

Lead (Pb) is a heavy metal that can damage various organs, tissues, and systems. Antioxidants are used to prevent or reduce the negative effects of heavy metals. Pomegranate juice (PJ) is one of the antioxidants that alleviate the harmful effects of heavy metals. In this study, 28 Wistar albino rats were divided into four groups. These groups were determined as control (C), lead acetate (LA) (50 mL/kg per rat), PJ (1 mL), and LA + PJ. It was observed that the malondialdehyde level of the LA+PJ decreased compared to the LA. The glutathione level of the LA decreased compared to other groups. LA + PJ had higher glutathione S-transferase enzyme activity than C and lower than LA. Carboxylesterase activity increased in the LA + PJ compared to C and LA. Pb level in the LA + PJ was higher than C and lower than LA. Also, Mn levels increased in LA+PJ compared to LA. Testosterone decreased in LA but increased in PJ and LA+PJ compared to LA. LA and PJ had similar histological structures to C and PJ. It was determined that PJ had a curative effect against Pb toxicity in testicular tissue.

Key words: Antioxidants – Lead acetate – Oxidative stress – Pomegranate juice – Testes

INTRODUCTION

Population growth and industrialization result in heavy metal pollution that harms living organisms ecologically, physiologically, biologically, and economically (Li et al., 2021).

Lead (Pb) is considered one of the top ten most hazardous substances by the World Health Organization, as it can linger in the body for extended periods (Kucukler et al., 2021). Exposure to Pb can lead to renal dysfunction, liver cirrhosis, damage to the cardiovascular system, and anemia. It can cause pathological damage to the ovaries and testes, resulting in poor reproductive performance. Furthermore, lead has the potential to cause harm to cells and be toxic when it interacts with biological materials. In recent years, research has focused on using antioxidants as a preservative against the harmful effects of lead (Oyeyemi et al., 2022).

Corresponding author:
Hıdır Pekmez. Department of Anatomy, Faculty of Medicine, Malatya Turgut Özal University, Alacakapı Mah. Kırkgöz Cad. No: 70 P.K. 44210 Battalgazi, Malatya, Turkey. E-mail: hidir.pekmez@ozal.edu.tr

Submitted: February 12, 2024. **Accepted:** April 8, 2024

https://doi.org/10.52083/ZELQ3438

This metal, commonly found in household products and paints, can mix with soil and air as dust or flakes, leading to pollution of water, food, and air (Jahan et al., 2021; Khodabandeh et al., 2021). Exposure in humans occurs through water, food intake, and respiration (Jahan et al., 2021; Yousef et al., 2019). Lead absorbed into soft tissues may cause dysfunction in organs including the liver, kidney, brain, testis, uterus, and ovary (Abdelhamid et al., 2020; Dumitrescu et al., 2015). In addition, it has been reported to have adverse effects on the cardiovascular, digestive, and skeletal systems (Davuljigari and Gottipolu, 2020; El-Khadragy et al., 2020). Pb poisoning usually occurs with chronic exposure. However, occupational exposure to lead-containing agents and accidental or suicidal ingestion of these agents can cause acute poisoning (Samarghandian et al., 2021).

The use of antioxidants to prevent or reduce the adverse effects of heavy metals has attracted significant interest from researchers (Ozkaya et al., 2016; Yousef et al., 2019). One of the antioxidants, Pomegranate juice (PJ) contains compounds that mitigate the harmful effects of heavy metals. PJ contains ascorbic acid and minerals Fe, Ca, Mg, Se, and Zn (Aksu et al., 2017). PJ has three times the free radical scavenging and iron-reducing capacity of both red wine and green tea (Aksu et al., 2017). The beneficial effects of pomegranate, which is widely grown in Mediterranean countries, have been known for a long time (El-Beltagi et al., 2020; Mayuoni-Kirshenbaum et al., 2013). The pomegranate plant has multiple uses in traditional medicine, with its seeds and peels treating diarrhea, flowers used for diabetes, bark and roots for ulcers, and leaves for digestive disorders (Pepe et al., 2020). Studies have shown that pomegranate consumption leads to healthier cell growth and longer life span in rats (Alsataf et al., 2021). Studies have shown that the consumption of PJ can improve the concentration of spermatids, spermatocytes, and spermatogonia, increase sperm motility and testosterone levels, and enhance sexual behaviors (Al-Mutary and Abu-Taweel, 2020; Türk et al., 2008). Literature has reported that PJ can prevent oxidative stress and boost fertility (Al-Mutary and Abu-Taweel, 2020; Alahmadi, 2020; Bououza et al., 2022). In addition, PJ contains anthocyanins delphinidin-3-glucosidase, delphinidin-3.5 glucosidase, cyanidin, pelargonidin, and ellagitannins. The antioxidant property of PJ is due to punicalagin, one of the main ellagitannins in its content (El-Beltagi et al., 2020). Adıyaman hicaz pomegranate, rich in vitamins and minerals, is a fruit grown in Turkiye.

Oxidative stress occurs because of increased reactive oxygen species (ROS) by decreasing antioxidant enzyme activities. Excessive production of ROS caused by lead acetate affects the blood-testicular barrier and leads to degeneration in testicular tissue, resulting in decreased sperm count and quality (Dolati et al., 2020; El-Khadragy et al., 2020; Ileriturk et al., 2021). Major components of the sperm cell membrane are highly susceptible to oxidative damage. Therefore, free radicals can directly damage cells at high concentrations of superoxide anion, hydrogen peroxide, and nitric oxide (Dorostghoal et al., 2020; Ozkaya et al., 2018). It has been observed that pomegranates increase testosterone levels and help spermatogenesis (Dkhil et al., 2013). In addition, it is known that pomegranate extract positively affects oxidative stress parameters in testicular tissue and prevents spermatogenic deterioration (Leiva et al., 2011).

Antioxidant molecules, alone or in combination, are used for preventive or therapeutic purposes. Studies investigating pomegranate juice's antioxidant, neuroprotective, antineoplastic, and anti-inflammatory properties have been used safely in traditional and modern medicine for centuries (Annaç et al., 2022). The objective of our study is to investigate the potential of pomegranate juice in mitigating the detrimental effects of lead acetate on testicular tissue. Our examination includes analysis of biochemical parameters such as malondialdehyde (MDA), glutathione (GSH), glutathione S-transferase (GST), carboxylesterase (Ces), element levels, and histopathological findings in rats.

MATERIALS AND METHODS

Pomegranate juice preparation

The pomegranates obtained from Adıyaman were washed, filtered, and cut in half. Then, the seeds and the whole white pulp were crushed using an electric mixer. The juice was stored at -20 °C in qies of 1 mL/kg for later use.

Chemical composition of pomegranate juice

Our researcher investigated the chemical content of a local product obtained from Adıyaman province in a study funded by the Silk Road Development Agency as part of the "My City Adıyaman" project numbered "TRC1/18/KBG/0.036" by the "Development of Urban Culture and Urban Awareness Financial Support Program". The phenolic acid content of PJ was determined to be 490.75 mg/kg, anthocyanin 137.1 mg/L, ellagic acid 175 mg/100 g, total flavonoids 63 mg/kg, and total antioxidants 1530 mg/kg by researchers (Annaç et al., 2022).

Preparation of lead acetate

500 ppm Lead acetate was dissolved in 1 liter of distilled water (Annaç et al., 2022).

Preparation of pomegranate juice

PJ is prepared with a juicer for gavage application (Annaç et al., 2022).

Animals

A total of 28 male Wistar albino rats were obtained from the Fırat University Animal Experiment Centre. All animals were housed at a temperature of 22 ± 20°C and a 12-hr light/darkness cycle. Rats were fed ad libitum with normal tap water and a standard pellet diet (purchased from Korkutelim Yem Gıda, Antalya, Turkey; % 3.15 crude fat, % 4.96 crude cellulose, crude ash % 4.91, % 0. 43 methionine, % 1.30 lysine, % 0.62 calcium, % 0.74 phosphor, 0.04 sodium, % 24.00 crude protein). The Fırat University Animal Experiments Centre Ethics Committee approved all animal procedures that followed National Institutes of Health (NIH) guidelines (2022/16).

The study groups and applications are given in Table 1.

The rats were sacrificed using ketamine hydrochloride and xylazine hydrochloride at the end of the 30-day experiment. The left testis was stored in 10% formaldehyde for histopathological and morphological analysis, while the right testis was stored at -20 °C for biochemical analysis.

Biochemical Procedures

The testes samples were first homogenized in a cooled homogenization buffer (0.1 M, pH 7.4 in potassium phosphate buffer; 0.15 M KCl, one mM EDTA, one mM DTT) at four times the total tissue weight (w/v) using a polytron homogenizer (Heidolph RZ 2021, Germany). The MDA levels in one portion of the homogenates were calculated. The leftover homogenates were put into Eppendorf tubes and centrifuged for 20 min at 16.000 g and 4 °C (Sigma Centrifuge Model 2–16K, Sigma). The supernatant was used to determine the reduced amounts of GSH, GST, and Ces.

Determination of testes MDA and reduced GSH levels

Using a microplate reader spectrophotometer equipment, MDA and decreased GSH levels were measured (Thermo TM Varioskan Flash, Thermo Scientific). The thiobarbituric acid reaction was employed to evaluate the testicular malondialdehyde levels (Buege and Aust, 1978). Wet tissue weight (nmol/mg) was used to express the results (Koksal et al., 2003). The substance's interaction with DTNB to produce a molecule that absorbs at 412 nm was used to gauge reduced GSH activity. As nmol/mg tissue, reduced GSH was expressed (Moron et al., 1979).

Table 1. The study groups and application. Four groups were formed, with seven animals in each group.

C	Rats were given distilled water for 30 days.
PJ	Rats were given PJ via 1 mL/kg gavage every two days for 30 days.
LA	Rats were given an average of 50 mL/kg LA from a stock solution per animal every day for 30 days.
LA+PJ	Rats were given 50 mL/kg LA from stock solution daily and 1 mL PJ every two days for 30 days.

Determination of testes trace element levels

Pb, Fe, Mn, Zn, and Cu were measured by Agilent 7700 x ICP-MS in rat testes tissues. Spex Certiprep Multi-element calibration standard was used to prepare an external calibration solution.

Measurement of testes GST activity

The substrate used to test GST activity was a solution containing 20 mM of 1-chloro-2.4- dinitrobenzene (CDNB), which was initially produced in 96% ethanol. In the reaction, reductive glutathione (0.002 M) served as the cofactor (Habig et al., 1974). Briefly, the microplate wells were filled with ten microliters of supernatant, 100 microliters of phosphate buffer (0.1 M, pH 6.5), 100 microliters of the GSH mixture, and ten microliters of CDNB. These were inserted into the microplate reader system, and the change in absorbance was monitored for two min at 25°C while the light was at 344 nm. As nmol/min/mg protein, specific GST activity was determined.

Determination of testicular total Ces activity

Spectrophotometric methods adapted to the microplate reader system (ThermoTM Varioskan Flash-Thermo Fisher Scientific, Vantaa, Finland) were used to measure the total Ces activity. The (p-nitrophenolacetate) PNPA used for the substrate was prepared in 26 mM ethanol (96%). Differences in absorbance were recorded at 405 nm for 2 min at 25 °C.

Determination of total testis protein

250 µl of Bradford reagent and 5 µl of diluted supernatant (1:4) were applied to each microplate well to determine the total protein concentration in the supernatant samples (Bradford, 1976). After 15 min of incubation, the absorbance was measured at 595 nm. The protein concentration was determined using measurements of bovine serum albumin (BSA) standard solutions (0-1.4 mg BSA/mL) to create a calibration curve. Calculated protein values were used to determine specific activity levels of the enzyme under study (Lowry et al., 1946).

Determination of testis Pb concentrations

Testis Pb levels were measured at Adıyaman University Central Research Laboratory. Lead concentration was determined in the testis using NexION 350 inductively coupled plasma mass spectrometry (ICP-MS, Perkin Elmer, MA, USA)

Determination of testosterone levels

Serum testosterone analyses were performed on the Beckman coulter Dxl 800 device at the Central Biochemistry Laboratory of İnönü University Turgut Özal Medical Center.

Histopathological Evaluation

The standard histological tissue follow-up process involved dehydrating and polishing the testicular tissues once fixation was complete. The tissues were turned into paraffin blocks after the follow-up procedure. For histological analysis, sections of 5-µm thickness were cut from paraffin blocks. The acquired sections were deparaffinized, dyed with Masson trichrome and H&E, and then mounted. Using a Carl Zeiss brand Axiocam ERc5 type digital camera microscope, the sections were examined histopathologically, and photos were taken for morphometric analysis.

Serial sections of 10-micrometer thickness were obtained by applying 1/20 sampling from testicular tissues for analysis. In addition, seminiferous tubule area, seminiferous epithelial thickness, and connective tissue sheath measurements were made on the photographs taken from the sections. For these measurements, “closed polygon calculation” and “correct calculation” tools were selected in the Image j software program.

Statistical analysis

SPSS 22.0 program was used for statistical calculations. Results were tabulated as mean ± SEM. Differences were considered significant when $P \leq 0.05$. For the statistical evaluation One way ANOVA was used. Also, the Turkey-HSD test was used to classify the significant groups.

Table 2. Testis biochemical parameters in C, LA, PJ, and LA +PJ treated groups.

Parameters	C	LA	PJ	LA +PJ
MDA (nmol/mg protein)	15,3±0,75	34,8±2,32c	17,1±0,70z	19,6±1,04z
GSH (nmol/mg protein)	49,8±3,25	25,3±2,15c	52,8±6,25z	44,8±4,29y
GST (nmol/min/mg protein)	81,4±4,32	138,2±2,83c	101,2±4,27az	115,9±2,80cy
Ces (nmol/min/mg protein)	1,60±0,13	0,54±0,02c	0,65±0,03c	1,84±0,04bz

Values are expressed as means ± SEM; n=7 for each treatment group.
Comparison with group C. a: p <0.05, b: p <0.01, c: p <0.001
Comparison with group LA. x: p <0.05, y: p <0.01, z: p <0.001

RESULTS

MDA, reduced GSH, GST, and Ces levels in the testes

Testicular tissue biochemical parameter levels are given in Table 2.

The MDA levels of group C and group PJ showed no statistically significant difference in our investigation. It was found that the MDA level was higher in the LA group than in the control group (p<0.001). When compared to the LA group, the MDA level in the LA+PJ group reduced (p<0.001). The GSH level of the LA group decreased compared to other groups (p<0.001; p<0.01**).** In addition, GSH levels increased in the PJ and LA+PJ groups compared to the LA group **(**p<0.001; p<0.01) (Table 2).

When compared to the C group, it was seen that the LA group's level of GST enzyme activity increased (p<0.001). It was shown that the PJ group's level of GST enzyme activity increased in comparison to the C group (p<0.05) and decreased compared to the LA group (p<0.001). Additionally, the LA + PJ group's level of GST enzyme activity increased in comparison to the C group (p<0.001) and decreased compared to the LA group (p<0.01). Comparing the LA + PJ group to the C and LA groups, it was found that the Ces enzyme activity level increased in the LA + PJ group (p<0.01; p<0.001) (Table 2).

Findings on the testis elements analysis

Testicular tissue element concentration levels are given in Table 3. In our investigation, it was found that the LA group's Pb level increased in comparison to the control group (p<0.001). The PJ group was at a lower level than the LA group (p<0.001). It was discovered that the LA + PJ group's Pb level was lower than that of the LA group and higher than that of the C group (p<0.001) (Table 3).

The LA showed lower levels of Mn compared to the C group (p<0.01; p<0.05). It was observed that the PJ and LA + PJ group's Mn level increased relative to the LA group (Table 3).

Findings on the serum testosterone levels

Serum testosterone levels are given in Table 4. In this study, serum testosterone levels were found to be lower in the LA group compared to

Table 3. Elements' concentrations in the rat testis tissues.

Parameters	C	LA	PJ	LA +PJ
LA (ppb)	27,33±3,28	138,01±3,39c	26,96±1,39z	60,42±6,52cz
Fe	24077,80±1432,44	26346,98±1255,81	22797,85±850,75	22548,51±853,18
Mn	329,43±4,82	275,99±13,23b	312,99±5,22x	315,20±9,81x
Zn	19218,71±5610,33	18993,39±304,89	23906±222,85	22790,89±634,07
Cu	1888,02±185,05	1705,28±150,02	1820,15±205,02	1945,17±285,02

Values are expressed as means ± SEM; n=7 for each treatment group.
Comparison with group C. a: p <0.05, b: p <0.01, c: p <0.001
Comparison with group LA. x: p <0.05, y: p <0.01, z: p <0.001

the control group (p<0.05). In contrast to the LA group, testosterone levels were found to be higher in the PJ and LA+PJ groups (p<0.01) (Table 4).

Table 4. Testicular biochemical parameters: testosterone levels.

Parameters	Testosterone Level
C	6.54±0.67
LA	4.16±0.25a
PJ	7.27±0.39y
LA+PJ	8.16±0.71z

Values are expressed as means ± SEM; n=7 for each treatment group.
Comparison with group C. a: p <0.05, b: p <0.01, c: p <0.001
Comparison with group LA. x: p <0.05, y: p <0.01, z: p <0.001

Histologic findings of testis tissue

In the histopathological evaluation of testicular tissue, it was determined that the seminiferous tubule, seminiferous epithelial cells, and interstitial connective tissue in the C and PJ groups were histologically normal. No pathology was found in the evaluation (Figs. 1, 1a-c and 2a-c). When compared to the C and PJ groups, the histopathological evaluation of the LA group showed significant deterioration. Degeneration of the seminiferous epithelium, irregular shapes of the seminiferous tubules, and edema in the interstitial connective tissue were observed (Fig. 1, 3a-c). In the examination of the LA+PJ group, it was determined that the histological structure was similar to that of the C and PJ groups. It was observed that the smoothness of the seminiferous tubule shapes was preserved, and the edema in the interstitial connective tissue decreased. Degeneration findings were observed in the seminiferous epithelium (Fig. 1, 4a-c).

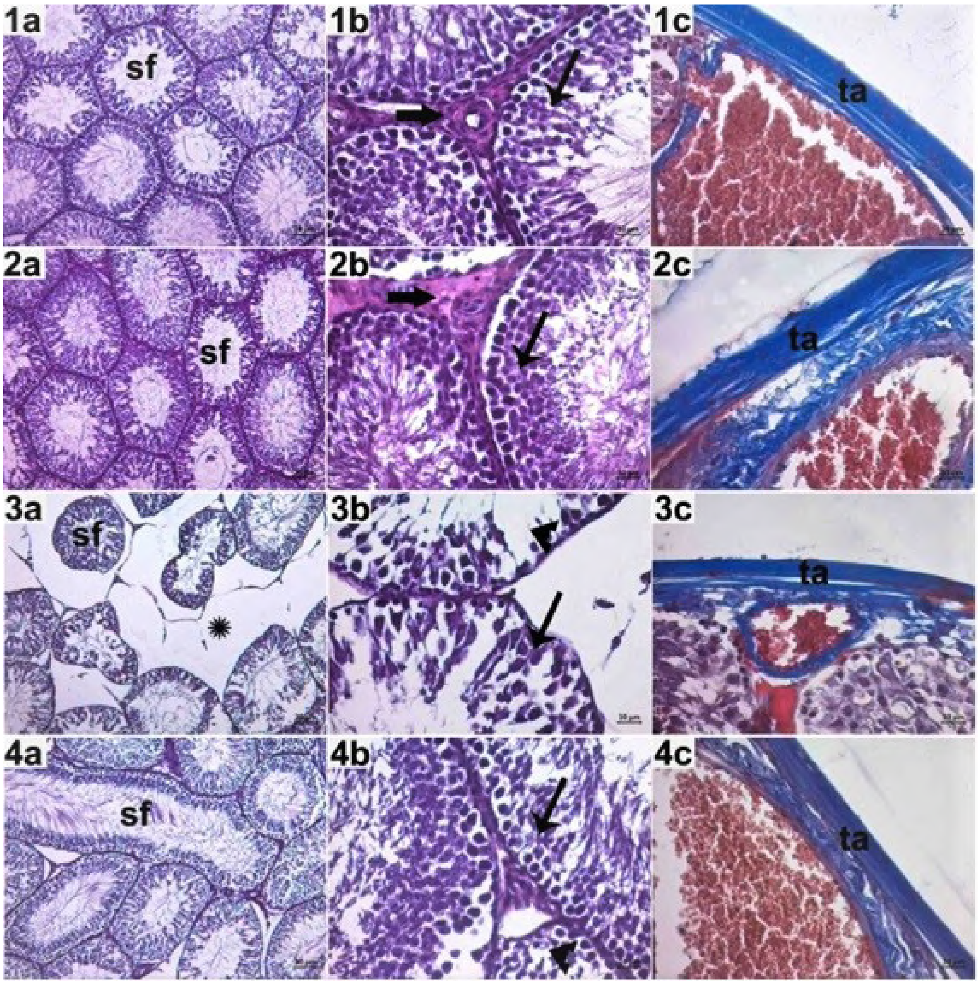

Fig. 1.- (**1a-c**): Images of testicular tissue of the C Group. (**2a-c**): Images of testicular tissue of the PJ Group. (**3a-c**): Images of testicular tissue of the LA group. (**4a-c**): Images of testicular tissue of the LA + PJ group. (1a, 2a, 3a and 4a; x10 objective magnification, 1b-c, 2b-c, 3b-c and 4b-c, x40 objective magnification. a and b: H&E staining, c: Masson trichrome staining). SF; seminiferous tubule, ta; connective tissue sheath, thick arrow; interstitial connective tissue area, thin arrow; seminiferous epithelium, arrowhead; seminiferous epithelial degeneration, star; edema in the interstitial connective tissue area.

Table 5. Histomorphometric analysis results of testicular tissue.

Groups	Tubule Area (mm^2)	Tubule Epithelial Thickness (µm)	Sheath thickness (µm)
C	385 ± 28,23	9235 ± 401,56	19761,83 ± 1451,42
LA	219,16 ± 16,81 *	6387,83 ± 405,03 *	12709,83 ± 925,97 *
PJ	373 ± 39,77	9600 ± 226,10	17227,66 ± 891,79
PJ+LA	338,16 ± 21,38	8136,33 ± 283,40	13982,83 ± 771,81

* Values are expressed as means ± SE; n=7 for each treatment group.
Statistical significance compared to the LA group: *: $p<0.01$

Histomorphometric findings

Histomorphometric findings are given in Table 5. The measurements revealed that the lead acetate group had a statistically significant decrease in seminiferous tubule area, seminiferous epithelial thickness, and connective tissue thickness when in comparison to the other groups ($p < 0.01$) (Table 5).

DISCUSSION

Pb is one substance that harms the male reproductive system in humans and animals. Pb causes testicular dysfunction and infertility. It also causes a decrease in body weight (Al-Megrin et al., 2019). Our study aimed to find a new way of treating Pb toxicity in rats by administering PJ.

Álvarez-Cervantes et al. (2021) investigated the effect of PJ in their study and found no negative harm to pomegranate juice. In their study, the tissues and serum of rats were found to have normal biochemical and hematological parameters. Al-Olayan et al. (2014) found normal histopathological findings in testicular tissue in the treatment group, in which they gave PJ. In our study, normal histological findings were observed in the PJ group (Fig. 1). Thus it was concluded that PJ has no toxic effect.

Kolawole et al. (2014) stated in their study that Pb-administered Wistar albino male rats had a deterioration in sperm count and motility, and, histopathologically, there were significant changes in testicular tubules and tubule walls. According to Sudjarwo et al. (2017) reported that Pb reduces sperm count and motility and causes altered histopathological findings (testicular damage, necrosis of seminiferous tubules, and spermatid) in testicular tissue. In their study, Ibrahim et al. (2021) found deterioration in testicular tissue, a decrease in sperm cell count, and a decline in spermatogenesis in general in rats to which Pb was administered. In comparison to the other groups, rats given Pb had a statistically significant decrease in seminiferous tubule area, seminiferous epithelial thickness, and connective tissue thickness.

Aksu et al. (2017) studied forty adults male Sprague Dawley rats. Pb application to the rat group resulted in histopathological changes, including seminiferous tubule atrophy, intertubular edema, tubule wall thinning, and decreased sperm motility. They stated that the PJ they used in the treatment group repaired the atrophy of the seminal tubules and the thinning of the tubule wall. They have also shown in their studies that it increases sperm motility. Our research showed signs of degeneration in the seminiferous epithelium, irregular shapes of the seminiferous tubules, and edema in the interstitial connective tissue in the LA group. After examining the LA+PJ groups, it was concluded that the testes' histological structure was similar to that of the C and PJ groups. The LA+PJ group demonstrated preserved smoothness of the seminiferous tubule shapes and a reduction in interstitial connective tissue edema. Degenerative findings were also observed in the seminiferous epithelium. Our study confirms the positive and restorative effects of PJ, with histopathological findings that are consistent with Aksu et al. (2017).

Owolabi et al. (2014) and Asadpour et al. (2013) reported that testicular toxicity of lead increases MDA levels and lipid peroxidation that cause tissue damage, and decreases the activity of antioxidant defense mechanisms to prevent excessive free radical formation (Asadpour et al., 2013;

Owolabı et al., 2014; Sudjarwo and Sudjarwo, 2017). In their study on testicular tissue, Aksu et al. (2017) found that PJ significantly decreased MDA levels in Pb exposure. In our investigation, similarly, the MDA level decreased in the LA+PJ group compared to the LA group. Also, in their study, it was observed that the GSH level was significantly reduced in all tissues when comparing the group receiving lead alone with the control group. However, the levels of GSH were found to significantly increase in the PJ treated groups compared to the LA and control groups. In our study, the GSH level of the LA group decreased compared to the other groups. In addition, it was significantly increased in rats given PJ compared to the LA group.

In our study, the LA group had higher levels of GST enzyme activity compared to the C group, whereas the PJ group had higher levels compared to the C group, but lower levels compared to the LA group. In addition, the LA+PJ group's GST enzyme activity was shown to be higher than in the C group, while it was lower in the LA group. The role of GST in GSH metabolism is crucial. Lead-induced inhibition of GST activity can lead to a decrease in GSH levels (Wang et al., 2013). When the activity of the Ces enzyme was measured, it was found to decrease in the LA group in comparison to the C group. However, it increased in the PJ and LA+PJ groups. In addition, Ces level increased in the LA+PJ group compared to the LA group. The role of Ces enzymes in metabolizing drugs is crucial, as it can greatly impact their effectiveness in the body's tissues (Xing et al., 2010). Ces is thought to be involved in testosterone biosynthesis and protect testicular cells from the effects of harmful and toxic agents (Özkaya et al., 2021). The results of our research on Ces demonstrate that the detoxification process of testicular tissue is affected by exposure to Pb, whereas the management of the toxic outcomes arising from this exposure is attributed to PJ.

Aksu et al. (2017) stated in their study that PJ reduced lead accumulation in testicular tissue. Furthermore, it was observed that the diminished concentration of Cu in the testes of the LA group was elevated in the groups where PJ was administered. Fe level increased in the LA group but fell to the control level in the PJ-treated groups. The amount of Zn in the PJ-applied groups was even higher than in the control group. The findings of our study exhibited similarities to those of Aksu et al.; however, the levels of Fe, Cu, and Zn in our research did not yield statistically significant results compared to other groups. The observed variance could potentially be attributed to the Adıyaman pomegranate, which contains a distinct composition compared to the pomegranate utilized in the study conducted by Aksu et al. (2017). The amount of Mn was also examined in our study, and a significant decrease was found in the LA group compared to the C group. Furthermore, when compared to the LA group, the PJ and LA+PJ groups showed a significant increase. Mn functions as an antioxidant, shielding sperm from harm caused by free radicals. Moreover, it plays a crucial role as a coenzyme in the production of sex hormones including progesterone, estrogen, and testosterone (Qureshi and Abbas, 2013). The levels of Mn might have decreased due to damage to the testicles caused by LA, while PJ contributed to an increase in this level.

AL-Megrin et al. (2020) stated in their study that Pb significantly reduces testosterone levels. Al Olayan et al. (2014) found an increase in testosterone levels in rats given PJ against toxicity in their study. In our study, the administration of Pb resulted in a decline in testosterone levels, whereas the consumption of PJ led to an increase in testosterone levels. The analysis shows that PJ has the potential to heal due to its positive impact on hormone levels.

Pb is a heavy metal that can harm tissues. Our histological data reveals that Adıyaman-PJ can help treat Pb-induced toxicity in testicular tissue. Moreover, PJ can effectively increase the reduced testosterone level caused by Pb exposure. Therefore, using PJ in alternative medicine to treat toxicity would be beneficial. Increasing testosterone levels can be a preferred option to treat infertility. Our research has examined the impact of PJ on the male reproductive system in rats. However, more studies are required to determine the potential effects and adverse impacts of PJ on the female reproductive system. It is important to note that our study was conducted on rats, and therefore, future research may focus on the effects of PJ on the human reproductive system.

ACKNOWLEDGEMENTS

The author would like to express thanks to the Adıyaman University's Department of Chemistry.

AUTHORS' CONTRIBUTIONS

All authors contributed to the preparation of the article. Coordinator, organization and arrangement of the research [Hıdır Pekmez], practical application, supply of serum and tissue samples at the end of the experiment, biochemical analysis of serum and tissue samples [Özgür Bulmuş, Hıdır Pekmez], tissue follow-up, sectioning, staining, taking pictures and histopathological evaluation [Ebru Annac (ELİBOL)]. Statistical assessment of the results in the article [Ali Aydın], writing, preparation, and finalization of the report [Gökçe Bağcı Uzun, Merve Aydın, Hıdır Pekmez].

REFERENCES

ABDELHAMID FM, MAHGOUB HA, ATEYA AI (2020) Ameliorative effect of curcumin against lead acetate–induced hemato-biochemical alterations, hepatotoxicity, and testicular oxidative damage in rats. *Environ Sci Pollut Res*, 27(10): 10950-10965.

AKSU DS, SAGLAM YS, YILDIRIM S, AKSU T (2017) Effect of pomegranate (Punica granatum L.) juice on kidney, liver, heart and testis histopathological changes, and the tissues lipid peroxidation and antioxidant status in lead acetate-treated rats. *Cell Mol Biol*, 63(10): 33-42.

AL-MEGRIN WA, ALKHURIJI AF, YOUSEF AOS, METWALLY DM, HABOTTA OA, KASSAB RB, ABDEL MONEIM AE, EL-KHADRAGY MF (2019) Antagonistic efficacy of luteolin against lead acetate exposure-associated with hepatotoxicity is mediated via antioxidant, anti-inflammatory, and anti-apoptotic activities. *Antioxidants*, 9(1): 10.

AL-MEGRIN WA, ALOMAR S, ALKHURIJI AF, METWALLY DM, MOHAMED SK, KASSAB RB, ABDEL MONEIM AE, EL-KHADRAGY MF (2020) Luteolin protects against testicular injury induced by lead acetate by activating the Nrf2/HO-1 pathway. *IUBMB Life*, 72(8): 1787-1798.

AL-MUTARY MG, ABU-TAWEEL GM (2020) Effects of pomegranate juice on the sexual behavior, fertility and protective activity against aluminum exposure in male mice. *J King Saud Univ-Sci*, 32(6): 2688-2695.

AL-OLAYAN EM, EL-KHADRAGY MF, METWALLY DM, ABDEL MONEIM AE (2014) Protective effects of pomegranate (Punica granatum) juice on testes against carbon tetrachloride intoxication in rats. *BMC Complement Altern Med*, 14(1): 1-9.

ALAHMADI BA (2020) Effect of herbal medicine on fertility potential in experimental animals-An update review. *Mater Socio-Med*, 32(2): 140.

ALSATAF S, BAŞYIĞIT B, KARAASLAN M (2021) Multivariate analyses of the antioxidant, antidiabetic, antimicrobial activity of pomegranate tissues with respect to pomegranate juice. *Waste Biomass Valori*, 12(11): 5909-5921.

ÁLVAREZ-CERVANTES P, IZQUIERDO-VEGA JA, MORÁN-LEÓN J, GUERRERO-SOLANO JA, GARCÍA-PÉREZ BE, CANCINO-DÍAZ JC, BELEFANT-MILLER H, BETANZOS-CABRERA G (2021) Subacute and subchronic toxicity of microencapsulated pomegranate juice in rats and mice. *Toxicol Res*, 10(2): 312-324.

ANNAÇ E, UÇKUN M, ÖZKAYA A, YOLOĞLU E, PEKMEZ H, BULMUŞ Ö, AYDIN A (2022) The protective effects of pomegranate juice on lead acetate-induced neurotoxicity in the male rat: A histomorphometric and biochemical study. *J Food Biochem*, 46(4): e13881.

ASADPOUR R, SHAHBAZFAR A, KIANIFARD D, AZARI M, ZABOLI N (2013) Comparison of the protective effects of garlic (Allium sativum L) extract, vitamin E and N acetyl cystein on testis structure and sperm quality in rats treated with lead acetate. *Revue Med Vet*, 164(1): 27-41.

BOUOUZA F, LEILA M, HALOUI M, AJABI N, ABDENOUR C (2022) Effects of pomegranate juice consumption on the fertility and protective activity against a fungicide exposure in male wistar rats. *Uttar Pradesh J Zool*, 20-27.

BRADFORD MM (1976) A rapid and sensitive method for the quantitation of microgram quantities of protein utilizing the principle of protein-dye binding. *Anal Biochem*, 72(1-2): 248-254.

BUEGE JA, AUST SD (1978) Microsomal lipid peroxidation. *Methods Enzymol*, 52: 302-310.

DAVULJIGARI CB, GOTTIPOLU RR (2020) Late-life cardiac injury in rats following early life exposure to lead: reversal effect of nutrient metal mixture. *Cardiovasc Toxicol*, 20(3): 249-260.

DKHIL MA, AL-QURAISHY S, MONEIM AEA (2013) Effect of pomegranate (Punica granatum L.) juice and methanolic peel extract on testis of male rats. *Pak J Zool*, 45(5).

DOLATI P, KHODABANDEH Z, ZAMIRI MJ, JAMHIRI I, MEHRABANI D (2020) The effect of lead acetate and quercetin on the tight and gap junctions in the mouse testis. *Biol Trace Elem Res*, 198(2): 535-543.

DOROSTGHOAL M, SEYYEDNEJAD SM, NEJAD MNT (2020) Cichorium intybus L. extract ameliorates testicular oxidative stress induced by lead acetate in male rats. *Clin Exp Reprod Med*, 47(3): 161.

DUMITRESCU E, CHIURCIU V, MUSELIN F, POPESCU R, BREZOVAN D, CRISTINA RT (2015) Effects of long-term exposure of female rats to low levels of lead: ovary and uterus histological architecture changes. *Turkish J Biol*, 39(2): 284-289.

EL-BELTAGI HS, DHAWI F, ASHOUSH IS, RAMADAN K (2020) Antioxidant, anti-cancer and ameliorative activities of Spirulina platensis and pomegranate juice against hepatic damage induced by CCl4. *Not Bot Horti Agrobot Cluj-Napoca*, 48(4): 1941.

EL-KHADRAGY M, AL-MEGRIN WA, ALSADHAN NA, METWALLY DM, EL-HENNAMY RE, SALEM FEH, KASSAB RB, ABDEL MONEIM AE (2020) Impact of coenzyme Q10 administration on lead acetate-induced testicular damage in rats. *Oxid Med Cell Longev*, 2020: 4981386.

HABIG WH, PABST MJ, JAKOBY WB (1974) Glutathione S-Transferases. *J Biol Chem*, 249(22): 7130-7139.

IBRAHIM IA, SHALABY AA, ABD ELAZIZ RT, BAHR HI (2021) Chlorella vulgaris or Spirulina platensis mitigate lead acetate-induced testicular oxidative stress and apoptosis with regard to androgen receptor expression in rats. *Environ Sci Pollut Res*, 28(29): 39126-39138.

ILERITURK M, BENZER F, AKSU EH, YILDIRIM S, KANDEMIR FM, DOGAN T, DORTBUDAK MB, GENC A (2021) Chrysin protects against testicular toxicity caused by lead acetate in rats with its antioxidant, anti-inflammatory, and antiapoptotic properties. *J Food Biochem*, 45(2): e13593.

JAHAN M, ISLAM M, GAUTAM M, BHUIYAN M (2021) Lead acetate induced toxicities and antitoxic effect of Vitamin E and selenium in mice. *Bangladesh J Vet Med (BJVM)*, 19(1): 75-85.

KHODABANDEH Z, DOLATI P, ZAMIRI MJ, MEHRABANI D, BORDBAR H, ALAEE S, JAMHIRI I, AZARPIRA N (2021) Protective effect of quercetin on testis structure and apoptosis against lead acetate toxicity: an stereological study. *Biol Trace Elem Res*, 199(9): 3371-3381.

KOKSAL I, USTA M, ORHAN I, ABBASOGLU S, KADIOGLU A (2003) Potential role of reactive oxygen species on testicular pathology associated with infertility. *Asian J Androl*, 5(2): 95-100.

KOLAWOLE T, DAPPER D, OJEKA S (2014) Ameliorative effects of the methanolic extract of the rind of citrullus lanatus on lead acetate induced toxicity on semen parameters and reproductive hormones of male albino wistar rats. *Eur J Med Plants*, 4(9): 1125.

KUCUKLER S, BENZER F, YILDIRIM S, GUR C, KANDEMIR FM, BENGU AS, AYNA A, CAGLAYAN C, DORTBUDAK MB (2021) Protective effects of chrysin against oxidative stress and inflammation induced by lead acetate in rat kidneys: a biochemical and histopathological approach. *Biol Trace Elem Res*, 199(4): 1501-1514.

LEIVA KP, RUBIO J, PERALTA F, GONZALES GF (2011) Effect of Punica granatum (pomegranate) on sperm production in male rats treated with lead acetate. *Toxicol Mech Methods*, 21(6): 495-502.

LI N, ZHAO Y, SHEN Y, CHENG Y, QIAO M, SONG L, HUANG X (2021) Protective effects of folic acid on oxidative damage of rat spleen induced by lead acetate. *Ecotoxicol Environ Saf*, 211: 111917.

LOWRY E, BEARD D, HEWIT L, BARNER J (1946) Tumor of the testicle: analysis of one hundred cases: a preliminary report. *J Urol*, 55(4): 373-384.

MAYUONI-KIRSHENBAUM L, BAR-YA'AKOV I, HATIB K, HOLLAND D, PORAT R (2013) Genetic diversity and sensory preference in pomegranate fruits. *Fruits*, 68(6): 517-524.

MORON MS, DEPIERRE JW, MANNERVIK B (1979) Levels of glutathione, glutathione reductase and glutathione S-transferase activities in rat lung and liver. *Biochim Biophys Acta*, 582(1): 67-78.

OWOLABI J, WILLIAMS F, FABIYI O (2014) Evaluation of moringa's effects against lead-induced disruption of the hippocampus in animal models. *World J Life Sci Med Res*, 3(2): 39.

OYEYEMI WA, AKINOLA AO, DARAMOLA O-O, AIKPITANYI I, DUROTOLUWA OT, ALELE P-GO, OGIERIAKHI IO, OKORO TD (2022) Vitamin E and quercetin attenuated the reproductive toxicity mediated by lead acetate in male Wistar. *Bull Natl Res Cent*, 46(1): 22.

OZKAYA A, SAHIN Z, DAG U, OZKARACA M (2016) Effects of naringenin on oxidative stress and histopathological changes in the liver of lead acetate administered rats. *J Biochem Mol Toxicol*, 30(5): 243-248.

OZKAYA A, SAHIN Z, KUZU M, SAGLAM YS, OZKARACA M, UCKUN M, YOLOGLU E, COMAKLI V, DEMIRDAG R, YOLOGLU S (2018) Role of geraniol against lead acetate-mediated hepatic damage and their interaction with liver carboxylesterase activity in rats. *Arch Physiol Biochem*, 124(1): 80-87.

ÖZKAYA A, ŞAHIN Z, ŞAHIN Y, BULMUŞ Ö, UÇKUN M, YOLOĞLU E (2021) Evaluating effects of black carrot extract on testicular carboxylesterase activity and oxidative stress parameters in rats exposed to bisphenol A. *Adıyaman University J Sci*, 11(1): 73-86.

PEPE G, RAPA SF, SALVIATI E, BERTAMINO A, AURIEMMA G, CASCIOFERRO S, AUTORE G, QUARONI A, CAMPIGLIA P, MARZOCCO S (2020) Bioactive polyphenols from pomegranate juice reduce 5-Fluorouracil-induced intestinal mucositis in intestinal epithelial cells. *Antioxidants*, 9(8): 699.

QURESHI IZ, ABBAS Q (2013) Modulation of testicular and whole blood trace element concentrations in conjunction with testosterone release following kisspeptin administration in male rabbits (Oryctolagus cuniculus). *Biol Trace Elem Res*, 154: 210-216.

YOUSEF AO, FAHAD A, ABDEL MONEIM AE, METWALLY DM, EL-KHADRAGY MF, KASSAB RB (2019) The neuroprotective role of coenzyme Q10 against lead acetate-induced neurotoxicity is mediated by antioxidant, anti-inflammatory and anti-apoptotic activities. *Int J Environ Res Public Health*, 16(16): 2895.

SAMARGHANDIAN S, SHIRAZI FM, SAEEDI F, ROSHANRAVAN B, POURBAGHER-SHAHRI AM, KHORASANI EY, FARKHONDEH T, AASETH JO, ABDOLLAHI M, MEHRPOUR O (2021) A systematic review of clinical and laboratory findings of lead poisoning: lessons from case reports. *Toxicol Appl Pharmacol*, 429: 115681.

SUDJARWO SA, SUDJARWO GW (2017) Protective effect of curcumin on lead acetate-induced testicular toxicity in Wistar rats. *Res Pharm Sci*, 12(5): 381.

TÜRK G, SÖNMEZ M, AYDIN M, YÜCE A, GÜR S, YÜKSEL M, AKSU EH, AKSOY H (2008) Effects of pomegranate juice consumption on sperm quality, spermatogenic cell density, antioxidant activity and testosterone level in male rats. *Clin Nutr*, 27(2): 289-296.

WANG Y, FANG J, HUANG S, CHEN L, FAN G, WANG C (2013) The chronic effects of low lead level on the expressions of Nrf2 and Mrp1 of the testes in the rats. *Environ Toxicol Pharmacol*, 35(1): 109-116.

XING H, WANG J, LI J, FAN Z, WANG M, XU S (2010) Effects of atrazine and chlorpyrifos on acetylcholinesterase and carboxylesterase in brain and muscle of common carp. *Environl Toxicol Pharmacol*, 30(1): 26-30.

ORIGINAL ARTICLE Eur J Anat, 28 (5): 569-578 (2024)

Anatomical analysis of proximal tibia: selecting ideal sites for pediatric intraosseous infusion

Daniël J. van Tonder[1,2], Layla Al Safadi[1], Paula Samaha[1], Farhana E. Suleman[3], Martin L. van Niekerk[4], Albert van Schoor[2]

[1] *Department of Biological Sciences, College of Medicine and Health Sciences, Khalifa University, Abu Dhabi, United Arab Emirates*
[2] *Department of Anatomy, Basic Medical Sciences Building, Prinshof Campus, Faculty of Health Sciences, University of Pretoria, South Africa*
[3] *Department of Radiology, Kalafong Provincial Academic Hospital, Pretoria, South Africa*
[4] *Department of Paediatric Surgery, Faculty of Health Sciences, University of Pretoria, South Africa*

SUMMARY

Intraosseous access is a safe and efficient method to administer medications to patients that require advanced life support when intravenous access is not easily available. This study aims to narrow down the ideal insertion site for intraosseous access within the proximal tibia in a pediatric population. The study utilized computed tomography scans that were retrospectively collected from scans of five infant patients between four-weeks and two-years old, seven young children between two-years and six-years old, and ten children between six-years and twelve-years of age. Analysis of the computed tomography scans started at 10mm and extended to 50mm distally to the tibial tuberosity at 10mm increments.

The smallest cortical thickness to medullary space ratio and most desirable cortical thickness to anteromedial border ratio across all three groups – infants, young children, and child – was identified as 10mm inferior to the tibial tuberosity. Meanwhile, the largest medullary space to anteromedial border ratio was at 10mm inferior to the tibial tuberosity for the infants and young child groups, and at 30mm for the child group. This study showed that, overall, the ideal needle insertion site to gain vascular access for an intraosseous infusion procedure in the proximal tibial in infants, young child, and children is 10mm distal to the tibial tuberosity.

Key words: Cortex – Medullary – Proximal tibia – Tibia – Vascular access – Computed tomography – DICOM

INTRODUCTION

In patients that require advanced life support, administration of intravenous medications is not always quick and easily achieved. Especially in neonates and infant patients, the intraosseous (IO) route offers a comparable and advantageous alternative. IO infusions have been used since the twentieth century and have been included in pediatric

Corresponding author:
Daniël Johannes van Tonder. Department of Biological Sciences, College of Medicine and Health Sciences, Khalifa University, Abu Dhabi, United Arab Emirates. Phone: +971 02 312 4721. E-mail: daniel.tonder@ku.ac.ae - ORCID: 0000-0001-8246-915X

Submitted: February 20, 2024. **Accepted:** April 14, 2024

https://doi.org/10.52083/FIFB5847

advanced support guidelines since 1988 (Clemency et al., 2017). IO access is considered a safe and efficient method of administering all medications that can be administered intravenously with a comparable onset of action (Kleinman et al., 2010). Multiple studies have identified various IO sites of insertion, including proximal tibia, proximal humerus, clavicle, sternum, and radius. Among the ideal insertion sites for the IO route, the proximal tibia can be easily palpated with surface landmarks and is a distance away from vital areas where resuscitation efforts might be required, for example, the chest (Ngo et al., 2009).

The proximal tibia was reported to have a higher first-attempt success rate compared with other sites such as the humeral head (Clemency et al., 2017). In 2003, Boon et al. studied the ideal site on the proximal tibia for IO needle insertion in neonates. In this study, they used 18-gauge spiral needles on a total of 14 neonate cadavers (28 tibias), noting the ease of needle insertion and relation of the needle to the epiphyseal growth plate in the four different sites of insertion tested. They found that the ideal site of IO needle insertion was at least 10mm distal to the tibial tuberosity on the anteromedial surface; they showed that this site best fitted both parameters studied. On the other hand, they found that sites 10mm proximal to the distal tuberosity and 20mm distal to the tibial tuberosity were resistant to needle insertion due to increased cortical bone thickness and resulted in a perforated epiphyseal plate respectively (Boon et al., 2003). Another study by Chokshi et al. (2010) had similar findings, as they reported that the ideal place for needle insertion is between 10 and 30mm distal to the tibial tuberosity, with the needle angled inferiorly 40 to 60 degrees (Chokshi et al., 2010). Previously, Ellemunter et al. (1999) reported successful IO resuscitation in preterm and full-term infants admitted to the neonatal intensive care units, with no major reported complications and zero failed insertion attempts; their chosen needle insertion site was between 5mm to 10mm distal to the tibial tuberosity on the medial surface.

The tibia is a long, weight-bearing bone that has important landmarks for muscle attachments. For example, the tibial tuberosity can be easily palpated approximately 50mm distal to the patella in an adult population, and it is a protrusion on the anterior tibial surface that serves for the attachment site of the patellar ligament (White and Folkens, 2005). The tibia develops through a process called endochondral ossification, where ossification starts from the cartilaginous model of the tubular bone and continues till birth. The growth plates (physis) of the tibia are situated at the proximal and distal ends between the epiphysis and diaphysis, known as the shaft of the tibia. Longitudinal bone growth ensues until late adolescence, marked by the ossification of the growth plate and fusion of epiphysis and metaphysis, which is the portion of the bone that flairs outwards (Monsell et al., 2018).

Although IO infusion is a relatively safe and easy route for resuscitation, there are some important contraindications to keep in mind. These include bone diseases such as osteogenesis imperfecta, osteoporosis, osteomyelitis, fractured lower limb, and cutaneous infection in the area. In addition, difficulty identifying landmarks and accessing the area due to inflammation, any past surgical history on the tibia or knee, and any mass or malignancy near the insertion site would be considered contraindications for IO resuscitation. Lastly, if the needle is inserted incorrectly, potential complications include subcutaneous infusion, osteomyelitis, extravasation of fluid, infection at injection site, and compartment syndrome (Ryder et al., 1991; Ngo et al., 2009). This study focuses on narrowing down the ideal insertion site for the IO route to better guide medical providers and emergency responders.

MATERIALS AND METHODS

Patients and Methods

The sample consisted of CT scans of 5 infant patients between four weeks and two years old, 7 young child patients between two years and six years, and 10 child patients between six years and twelve years of age. These were retrospectively obtained from the Department of Radiology at the Steve Biko Academic Hospital in South Africa, with permission from both the Head of the Department of Radiology and the CEO of the hospital (Ethics clearance: 447/2018). The mean sample

Table 1. Age (in days) of the cadavers used to measure the dimensions of the proximal tibia. (n= number of individuals).

	n	Range	Minimum	Maximum	Mean	Std. Deviation
Infants	5	670	34	704	377.20 (1 year)	250.06 (0.7 years)
Young Child	7	744	1402	2146	1796.71 (4.9 years)	252.69 (0.7 years)
Child	10	1876	2478	4354	3267.70 (9 years)	628.67 (1.7 years)

age for each age category is presented in Table 1. The study excluded patients that were diagnosed by the consulting radiologist to either have an abnormal degree of kyphosis and/or scoliosis, obvious visceromegaly or a space-occupying lesion. Additionally, sex and ancestry were not considered as an exclusion factor.

RadiAnt, a Digital Imaging and Communications in Medicine (DICOM) viewer, was used to analyze the CT scans starting at the plane of the tibial tuberosity and extending 50mm inferior to the tibial tuberosity at 10mm increments. The following measurements were used (see Fig. 1).

The width of the anteromedial border of the tibia was determined by measuring the distance between the anterior and the medial border of the tibia. By measuring from the outer cortical layer of the anteromedial surface to the inner cortical layer, the cortical thickness of the tibial bone was determined. The medullary space of the tibia was measured from the inner cortical layer of the anteromedial surface to the opposite inner cortical layer, perpendicular to the anteromedial surface (Fig. 2).

Statistical Analysis

The data were summarized using descriptive statistics, including mean, standard deviation and 95% confidence intervals. Measurements from the respective left and right sides were compared using a paired t-test or Wilcoxon Signed Rank test, depending on the distribution of the data.

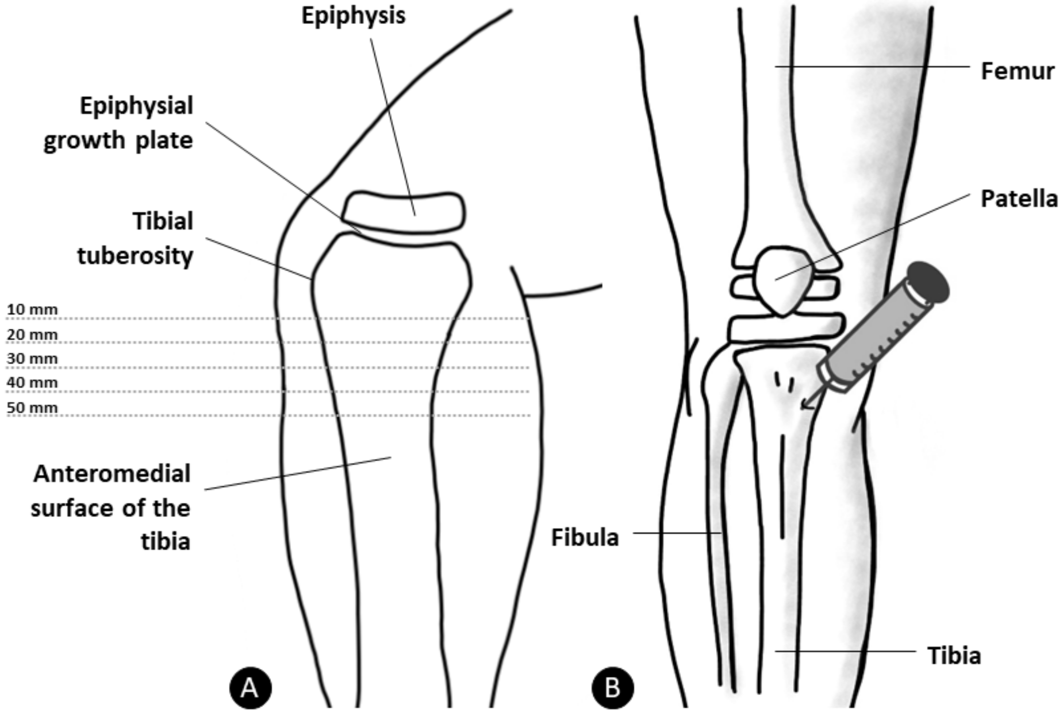

Fig. 1.- A. Schematic representation of IO needle insertion at levels 10, 20, 30, 40, and 50mm respectively inferior to the tibial tuberosity on the anteromedial surface of the leg. **B**. Schematic frontal view of the approximate site of IO needle insertion on the proximal tibia.

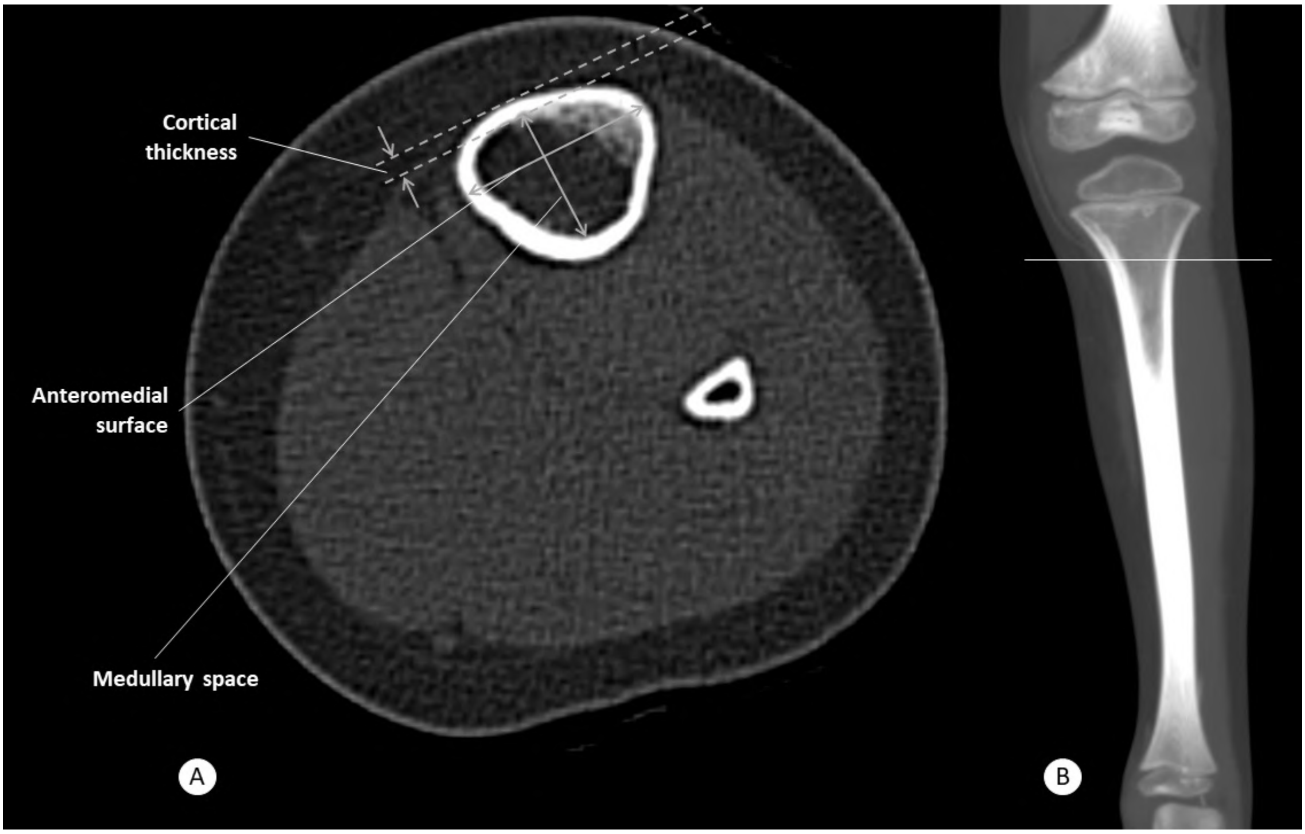

Fig. 2.- A. Transverse CT scan distal to the tibial tuberosity in a 3-year-old child. The measurements show the anteromedial surface, cortical thickness, and medullary space. **B**. Indicate line at which horizontal section was determined.

RESULTS

The sample size for the infants was insufficient for a Paired t-test and a Wilcoxon Signed Rank test to reveal any significant difference between the measurement pairs involved. As such, each measurement pair was compared in order to determine whether there was any clinically significant difference between the two. If no clinical significance was present, the applicable left and right sides were then combined. However, for both the young child and child, a Paired t-test and the Wilcoxon Signed Rank test was conducted and revealed no significant difference between the measurement pairs involved. The applicable left and right sides were then combined. Descriptive statistical analysis for the combined measurements together with a 95% confidence interval is shown for each of the respective measurements.

Infants (4 weeks – 2 years)

Anteromedial surface of the Tibia

At 10mm inferior to the tibial tuberosity, the largest anteromedial surface was observed with a mean distance of 13.8 ± 4.4mm (mean ± standard deviation), and the smallest average anteromedial surface was determined at 30mm inferior to the tibial tuberosity. With a confidence interval of 95%, the anteromedial surface of the tibia at 10mm ranged from 12.8 to 19.3mm (Table 2).

Cortical thickness

At 50mm inferior to the tibial tuberosity, the thickest cortical thickness was observed, and the smallest average cortical thickness of 3.1 ± 0.3mm was measured at 10mm inferior to the tibial tuberosity (Table 2).

Medullary space

The largest medullary space was seen at 10mm inferior to the tibial tuberosity with a mean diameter of 5.1 ± 2.3mm. With a confidence interval of 95%, the medullary space of the tibia at 10mm ranged from 4.4 to 7.9mm (Table 2).

Young Child (2-years to 6-years)

Anteromedial surface of the Tibia

The largest anteromedial surface was seen 10mm inferior to the tibial tuberosity at a mean distance of 23.4 ± 4.2mm, with a confidence inter-

Table 2. Descriptive statistical analysis and 95% confidence interval in mm for the combined left and right sides of the tibia in infants. (n= number of individuals).

mm	n	Range	Min	Max	Mean		Std. Deviation	95% Confidence Interval of Mean	
					Statistic	Std. Error		Lower	Upper
Anteromedial surface									
10	7	11.9	7.7	19.5	13.8	1.7	4.4	12.8	19.3
20	7	9.4	8.8	18.2	13.5	1.2	3.0	11.2	17.8
30	7	6.1	10.6	16.7	13.0	1.0	2.6	10.4	17.1
40	6	7.4	9.9	17.3	13.4	1.1	2.8	9.5	17.3
50	6	6.8	10.5	17.3	13.6	1.0	6.0	10.2	16.9
Medullary space									
10	8	7.3	2.2	9.4	5.1	0.8	2.3	4.4	7.9
20	7	6.0	2.1	8.1	4.1	0.7	1.9	2.6	6.4
30	7	4.7	2.6	7.3	3.6	0.6	1.7	1.7	5.5
40	6	4.3	2.3	6.6	3.3	0.7	1.7	1.6	5.1
50	6	3.4	2.8	6.2	4.2	0.6	1.5	2.7	5.8
Cortical thickness									
10	8	2.2	2.0	4.2	3.1	0.3	0.7	2.8	3.9
20	7	2.3	2.3	4.5	3.3	0.3	0.8	2.7	4.2
30	7	3.0	1.9	4.9	3.5	0.4	1.0	3.1	4.6
40	6	2.3	2.9	5.1	3.8	0.3	0.8	3.0	4.7
50	6	1.6	3.0	4.5	3.6	0.3	0.6	3.0	4.3

val of 95%, the anteromedial surface of the tibia at 10mm ranged from 20.9 to 25.9mm. At 50mm below the tibial tuberosity, the anteromedial surface ranged between 17.1 to 20.4mm (Table 3).

Cortical thickness

The smallest average cortical thickness of 3.0 ± 1.3mm was measured at 10mm inferior to the tibial tuberosity, ranging from 2.2 to 3.8mm with a confidence interval of 95% at 10mm (Table 3).

Medullary space

The largest medullary space was seen at 10mm inferior to the tibial tuberosity with a mean diameter of 14 ± 3.2mm, while the smallest average medullary space was measured at 50mm inferior to the tibial tuberosity with an average diameter of 10.2 ± 2.9mm. With a confidence interval of 95%, the medullary space of the tibia at 10mm ranged from 12.1 to 16.0mm (Table 3).

Child (6 years to 12-years)

Anteromedial surface of the Tibia

The largest anteromedial surface was seen 10mm inferior to the tibial tuberosity at a mean distance of 27.7 ± 4.4mm. With a confidence interval of 95%, the anteromedial surface of the tibia at 10mm ranged from 25.6 to 29.7mm, while at 50mm inferior to the tibial tuberosity it ranged from 21.3 to 25.3mm (Table 4).

Cortical thickness

The thinnest cortical thickness was observed at 10mm and 50mm inferior to the tibial tuberosity at a mean thickness of 3.2 ± 0.6mm, and the thickest average cortical thickness of 3.3 ± 0.8mm was measured at 20, 30, and 40mm inferior to the tibial tuberosity. With a confidence interval of 95%, the cortical thickness of the tibia at 30mm ranged from 2.9 to 3.6mm (Table 4).

Medullary space

The largest medullary space was seen at 10mm inferior to the tibial tuberosity with a mean diameter of 15.9 ± 3.0mm, while the smallest average medullary space was measured at 50mm inferior to the tibial tuberosity with an average diameter of 12.9 ± 2.9mm. With a confidence interval of 95%, the medullary space of the tibia at 10mm ranged from 14.5 to 17.3mm, and at 50mm be-

Table 3. Descriptive statistical analysis and 95% confidence interval in mm for the combined left and right of the tibia in young children. (n= number of individuals).

mm	n	Range	Min	Max	Mean		Std. Deviation	95% Confidence Interval of Mean	
					Statistic	Std. Error		Lower	Upper
Anteromedial surface									
10	13	13.0	16.9	29.9	23.4	1.2	4.2	20.9	25.9
20	13	10.8	16.1	26.9	21.7	1.0	3.6	19.56	23.9
30	13	11.1	15.1	26.2	20.6	1.0	3.6	18.4	22.7
40	13	8.9	14.8	23.7	19.4	0.8	3.0	17.6	21.2
50	13	8.3	14.9	23.2	18.7	0.8	2.7	17.1	20.4
Cortical thickness									
10	13	5.1	1.5	6.6	3.0	0.4	1.3	2.2	3.8
20	13	4.0	1.6	5.5	2.9	0.3	1.0	2.3	3.6
30	13	3.6	1.4	5.0	3.0	0.3	0.9	2.4	3.5
40	13	2.8	1.7	4.6	2.9	0.2	0.8	2.4	3.4
50	13	2.8	1.9	4.7	2.9	0.2	0.8	2.4	3.5
Medullary space									
10	13	10.5	9.4	19.9	14.0	0.9	3.2	12.1	16.0
20	13	9.5	9.1	18.6	13.0	0.8	3.1	11.2	14.9
30	13	8.1	8.2	16.3	11.9	0.8	2.8	10.2	13.6
40	13	8.6	7.4	16.0	11.0	0.8	2.7	9.4	12.7
50	13	8.4	6.5	14.9	10.2	0.8	2.9	8.4	11.9

Table 4. Descriptive statistical analysis and 95% confidence interval in mm for the combined left and right of the tibia in children. (n= number of individuals).

mm	n	Range	Min	Max	Mean		Std. Deviation	95% Confidence Interval of Mean	
					Statistic	Std. Error		Lower	Upper
Anteromedial surface									
10	20	17.2	20.6	37.8	27.7	1.0	4.4	25.6	29.7
20	20	16.0	20.3	36.3	26.4	1.0	4.4	24.4	28.4
30	20	15.1	19.9	35.0	25.2	1.0	4.4	23.1	27.2
40	20	15.5	17.9	33.4	23.8	1.0	4.3	21.8	25.8
50	20	14.8	18.3	33.1	23.3	1.0	4.3	21.3	25.3
Cortical thickness									
10	20	2.3	2.3	4.7	3.2	0.1	0.6	2.9	3.5
20	20	3.5	2.4	5.9	3.3	0.2	0.8	2.9	3.6
30	20	2.9	2.5	5.4	3.3	0.2	0.8	2.9	3.6
40	20	3.6	2.4	6.1	3.3	0.2	0.8	2.9	3.7
50	20	2.3	2.5	4.8	3.2	0.1	0.6	2.9	3.5
Medullary space									
10	20	12.4	9.3	21.7	15.9	0.7	3.0	14.5	17.3
20	20	11.7	8.7	20.4	15.1	0.7	3.0	13.7	16.5
30	20	14.2	5.4	19.6	14.5	0.7	3.3	12.9	16.0
40	20	15.5	3.0	18.5	13.5	0.7	3.3	11.9	15.0
50	20	12.8	4.5	17.3	12.9	0.7	2.9	11.6	14.3

low the tibial tuberosity it was between 11.6 and 14.3mm (Table 4).

DISCUSSION

This study builds on the previous work of Boon et al. (2003) and van Tonder et al. (2022) to determine the ideal tibial IO insertion sites. Although the studies conducted by Boon et al. (2003) and van Tonder et al. (2022) focused on newborn infants, this study expanded this to three categories; infants (28 days to 2 years), young children (2 years to 6 years), and children (6 years to 12 years). Boon et al. (2003) suggested that the best insertion site on their sample size of 14 neonatal cadavers was at least 10mm distal to the tibial tuberosity to avoid injury to the epiphyseal growth plate (Boon et al., 2003). The study by van Tonder et. al. (2022) on 15 neonatal cadavers showed that vascular access was ideal at 10mm inferior to the tibial tuberosity (van Tonder et al., 2022). On further application, this study aimed to prove this efficacy on older children to apply this to their guidelines as well. To do so, the ratios between the cortical thickness and the size of the medullary space were used to find the most suitable location and ease of insertion for each age category. This study's results align with previous neonatal research, indicating that 10mm distal to the tibial tuberosity is still the optimum insertion point, even in children up to 12 years old (n=22). These measurements should be emphasized as the epiphyseal growth plates in all three age groups have not yet closed, and the ideal needle insertion site is crucial to avoid damage to the epiphyseal growth plates (Crowder and Austin, 2005).

It is important to recognize the necessity in gaining quick vascular access in children under urgent care, especially those that are in dehydrated or shocked states (Boon et al., 2003; Chokshi et al., 2010; Clemency et al., 2017). However, in those conditions, hypovolemia, vasoconstriction, and peripheral vessel collapse are possible, increasing venipuncture difficulty (De Sá et al., 2012). This requires a mix of the provider's skills and the patient's stability, with timely parenteral access required before it is associated with an increase in morbidity (Neuhaus, 2014). Thereafter, the IO infusion technique should be considered where it reaps its benefits in those difficult-venous-access pediatric cases (Neuhaus, 2014), including when umbilical venous catheterization (UVC) is not possible due to the umbilical cord drying out (Scrivens et al., 2019). Any infusible intravenous substance can be administered intraosseously, which indicates the value of IO administration in life-threatening cases, especially neonates, where drug delivery is critical for survival (Dornhofer and Kellar, 2022). In those cases, IO access can be achieved in as few as 20 seconds compared to the challenging intravenous access, which is when it should be prioritized (Dornhofer and Kellar, 2022). Its plausibility emerged due to the high vascularization in bones, especially the red bone marrow, which allowed for quick fluid infusions into the bloodstream bypassing the absorption process (De Sá et al., 2012). In addition, blood collection is possible from these sites (De Sá et al., 2012). However, upon tibial metaphyseal examination, it was found that there was trabecular bone instead of a developed marrow cavity in neonatal patients, making aspiration difficult. Having said that, the decreased bone marrow cavity seemed to have a positive association with needle stability (Eifinger et al., 2021). There was less dislodgement of the IO needle during angled insertion (Eifinger et al., 2021). In this study, cross-sectional dimensions of the tibia were obtained starting with 10mm inferior to the tibial tuberosity and progressing at 10mm intervals to determine the optimal insertion site.

The aim of the needle insertion is to maximize vascular access while minimizing the risk of harming the epiphyseal plate. Hence, it is more favorable to have a larger anteromedial surface (due to larger surface area) and higher medullary space likewise (since this space is what the needle should be inserted into). Whereas, for the cortical thickness it is more favorable to have as little as possible to encounter the least resistance with needle insertion. The anteromedial surface remains the largest at 10mm across the three groups (infant, young child, and child), measuring 13.8mm, 23.4mm, and 27.7mm, respectively. Similarly, the medullary space follows the same trend, with the biggest measurement for all three groups being at 10mm, measuring 5.1mm, 14.0mm, and 15.9mm,

Table 5. Mean statistic of the measurements at 10mm interval inferior to the tibial tuberosity for an infants, young child, and child.

Infant (4-week to 2-years)			
	Anteromedial surface (mm)	**Cortical thickness (mm)**	**Medullary space (mm)**
10mm	13.8	3.1	5.1
20mm	13.5	3.3	4.1
30mm	13.0	3.5	3.6
40mm	13.4	3.8	3.3
50mm	13.6	3.6	4.2
Young child (2-years to 6-years)			
	Anteromedial surface (mm)	**Cortical thickness (mm)**	**Medullary space (mm)**
10mm	23.4	3.0	14.0
20mm	21.7	2.9	13.0
30mm	20.6	3.0	11.9
40mm	19.4	2.9	11.0
50mm	18.7	2.9	10.23
Child (6-years to 12-years)			
	Anteromedial surface (mm)	**Cortical thickness (mm)**	**Medullary space (mm)**
10mm	27.7	3.2	15.9
20mm	26.4	3.3	15.1
30mm	25.2	3.3	14.5
40mm	23.8	3.3	13.5
50mm	23.3	3.2	12.9

respectively (Table 5). However, the cortical thickness hardly varies within each group and across groups. Therefore, taking the ratios of these three measurements is a more useful tool to have an indication of the ideal proportions of these measurements to direct the needle insertion site.

The smallest (most desirable) cortical thickness to medullary space ratio across all three groups – infants, young children, and child – was at 10mm. The largest (least desirable) cortical thickness to medullary space ratios across the same groups was at 40mm, and 50mm for young child and children, respectively (Table 6). This study's results are comparable to those of Boon et al. (2003) and van Tonder et al. (2022), with the conclusion that the ideal insertion site for IO needle insertion is 10mm distally inferior to the tibial tuberosity border. In addition, they suggest angling the needle inferiorly to avoid damage to the epiphyseal plates (Boon et al., 2003). Along the same lines, the smallest (most desirable) cortical thickness to anteromedial border ratio across the three groups – infants, young child, and child – was again at 10mm. Lastly, the largest (most desirable) medullary space to anteromedial border ratio for the three groups was at 10mm for the infants and young child groups, and at 30mm for the child group. The smallest (least desirable) medullary space to anteromedial border ratio for the infants' group was at 40mm, whereas, for the young child and child groups it was at 50mm for both (Table 6).

For clinicians, anatomical landmarks such as the tibial tuberosity can be of great help in directing needle insertion via the IO route. Harcke et al. (2020) reported the ideal needle insertion site was one finger below the tibial tuberosity. In this study, the difference between the various age groups is highlighted as several authors (Ryder et al., 1991; Ellemunter et al., 1999; Boon et al., 2003; Chokshi et al., 2010; Neuhaus, 2014; Scrivens et al., 2019; Dornhofer and Kellar, 2022) have found these tibial landmarks advantageous. Eifinger et al. (2021)

Table 6. Ratios of the mean distances between measurements for an infants, young child, and child.

Infant			
	Cortical thickness / Medullary space*	**Cortical thickness / Anteromedial border***	**Medullary space / Anteromedial border****
10mm	0.61	0.22	0.37
20mm	0.80	0.24	0.30
30mm	0.97	0.27	0.28
40mm	1.15	0.28	0.25
50mm	0.86	0.26	0.31
Young child			
	Cortical thickness / Medullary space*	**Cortical thickness / Anteromedial border***	**Medullary space / Anteromedial border****
10mm	0.21	0.13	0.60
20mm	0.22	0.13	0.60
30mm	0.25	0.15	0.58
40mm	0.26	0.15	0.57
50mm	0.28	0.16	0.55
Child			
	Cortical thickness / Medullary space*	**Cortical thickness / Anteromedial border***	**Medullary space / Anteromedial border****
10mm	0.20	0.12	0.57
20mm	0.22	0.13	0.57
30mm	0.23	0.13	0.58
40mm	0.24	0.14	0.57
50mm	0.25	0.14	0.55

* Smaller values are better
** Bigger values are better

compared measurements of humerus, tibia, and femur bones in neonates, infants, and children in a cadaveric and CT-based study; of particular relevance to this study, they found that in contrast to the distal tibia, the proximal tibia had the largest diameter and cross-sectional area. Additionally, the tibial bone is more oval shaped in its proximal end, making the proximal tibia ideal for IO access by providing more surface area for the needle insertion (Eifinger et al., 2021).

CONCLUSION

Considering the analysis conducted in this study, it is evident that determining the ideal tibial IO insertion sites for infants, young children, and children holds significant clinical implications. By building upon prior research and extending the investigation across multiple age categories, this study not only reaffirms but also expands upon the findings of previous studies conducted on neonatal cadavers. This study showed that the ideal needle insertion site to gain vascular access in IO infusions in infants, young children, and children is at 10mm distal to the tibial tuberosity, as compared with all other more distal insertion sites analyzed such as at 20, 30, 40, and 50mm. This was shown by obtaining the lowest cortical thickness to medullary space ratio, the lowest cortical thickness to anteromedial surface ratio, and one of the largest medullary spaces to anteromedial surface ratio, all at the 10mm insertion site across the three age groups. The consistent identification of the 10mm distal to the tibial tuberosity as the optimal insertion point underscores the robustness and generalizability of this conclusion across various pediatric age groups, emphasizing its practical relevance and applicability in clinical settings.

Limitations

Obtaining CT scans of healthy pediatric patients is not easy, as for this demographic group data such as weight and height of patients is not always regularly available. Hence, the results within this study may be limited by the small sample size. To locate the optimum insertion site, this study utilized ratio comparisons between measurements, whereas previous studies only used mean diameters, which may affect comparability.

ACKNOWLEDGING DONOR CADAVERS

The authors sincerely thank those who donated their bodies to science so that anatomical research and teaching could be performed. Results from such research can potentially increase scientific knowledge and improve patient care. Therefore, these donors and their families deserve our highest respect. Additionally, the authors would like to thank Jade Sterling for her invaluable assistance with language editing.

AUTHORS' CONTRIBUTIONS

Mr. DJ van Tonder was primary responsible for protocol development, data collection, data analysis, manuscript writing, and critical review of the final manuscript.

Ms. L Al Safadi and Ms. P Samaha both participated in manuscript writing, and the critical review of the final manuscript.

Prof FE Suleman was responsible for data collection as well as protocol development, manuscript editing, and the critical review of the final manuscript.

Prof ML van Niekerk initiated research idea and was involved in protocol development, manuscript editing, together with the critical review of the final manuscript.

Prof A van Schoor supervised the design and execution of the study by partaking in protocol development, data collection, data analysis, manuscript writing, and the critical review of the final manuscript.

Ethics approval and consent to participate

The studies involving human participants were reviewed and approved (Ethics clearance number: 447/2018) by the Health Sciences Research Ethics Committee at the University of Pretoria, South Africa. All methods and observations were carried out in accordance with the relevant requirements, guidelines, and regulations stipulated in the South African National Health Act (61 of 2003).

REFERENCES

BOON JM, GORRY DLA, MEIRING JH (2003) Finding an ideal site for intraosseous infusion of the tibia: An anatomical study. *Clin Anat,* 16: 15-18.

CHOKSHI NK, NGUYEN N, CINAT M (2010) Access in the neonatal and pediatric patient. In: Samuel EW (ed.). *Vascular Access: Principles and Practice, Fifth Ed*. Philadelphia: Lippincott Williams & Wilkins, pp 137-149.

CLEMENCY B, TANAKA K, MAY P, INNES J, ZAGROBA S, BLASZAK J, HOSTLER D, COONEY D, MCGEE K, LINDSTROM H (2017) Intravenous vs. intraosseous access and return of spontaneous circulation during out of hospital cardiac arrest. *Am J Emerg Med,* 35: 222-226.

CROWDER C, AUSTIN D (2005) Age ranges of epiphyseal fusion in the distal tibia and fibula of contemporary males and females. *J Forensic Sci,* 50: 1001-1007.

DORNHOFER P, KELLAR JZ (2022) Intraosseous Vascular Access. StatPearls [Internet]. URL: https://www.ncbi.nlm.nih.gov/books/NBK554373/.

EIFINGER F, SCAAL M, WEHRLE L, MAUSHAKE S, FUCHS Z, KOERBER F (2021) Finding alternative sites for intraosseous infusions in newborns. *Resuscitation,* 163: 57-63.

ELLEMUNTER H, SIMMA B, TRAWÖGER R, MAURER H (1999) Intraosseous lines in preterm and full-term neonates. *Arch Dis Childhood-Fetal and Neonatal Edition,* 80: F74-F75.

HARCKE HT, CURTIN RN, HARTY MP, GOULD SW, VERSHVOVSKY J, COLLINS GL, MURPHY S (2020) Tibial intraosseous insertion in pediatric emergency care: a review based upon postmortem computed tomography. *Prehospital Emergency Care,* 24: 665-671.

KLEINMAN ME, CHAMEIDES L, SCHEXNAYDER SM, SAMSON RA, HAZINSKI MF, ATKINS DL, BERG MD, CAEN AR DE, FINK EL, FREID EB, HICKEY RW, MARINO BS, NADKARNI VM, PROCTOR LT, QURESHI FA, SARTORELLI K, TOPJIAN A, VAN DER JAGT EW, ZARITSKY AL (2010) Part 14: Pediatric Advanced Life Support. *Circulation,* 122(18 Suppl 3): S876-S908.

MONSELL F, GARGAN M, EASTWOOD D, TURNER J, KATCHKY R (2018) Genetic disorders, skeletal dyplasias and malformations. In: Blom A, Warwick D, Whitehouse MR, (eds.). *Apley & Solomon's System of Orthopaedics and Trauma, Tenth ed.* Boca Raton: Taylor & Francis Group, pp 157-178.

NEUHAUS D (2014) Intraosseous infusion in elective and emergency pediatric anesthesia: When should we use it? *Curr Opin Anaesthesiol,* 27: 282-287.

NGO ASY, OH JJ, CHEN Y, YONG D, ONG MEH (2009) Intraosseous vascular access in adults using the EZ-IO in an emergency department. *Int J Emerg Med,* 2: 155-160.

RYDER IG, MUNRO HM, DOULL IJM (1991) Intraosseous infusion for resuscitation. *Arch Dis Child,* 66: 1442-1443.

SÁ RAR DE, MELO CL, DANTAS RB, DELFIM LVV (2012) Vascular access through the intraosseous route in pediatric emergencies. *Rev Bras Ter Intensiva,* 24: 407-414.

SCRIVENS A, REYNOLDS PR, EMERY FE, ROBERTS CT, POLGLASE GR, HOOPER SB, ROEHR CC (2019). Use of intraosseous needles in neonates: a systematic review. *Neonatology,* 116: 305-314.

VAN TONDER DJ, VAN NIEKERK ML, VAN SCHOOR A (2022) Proximal tibial dimensions in a formalin-fixed neonatal cadaver sample: an intraosseous infusion approach. *Surg Radiol Anat,* 44: 239-243.

WHITE TD, FOLKENS PA (2005) Leg: femur, patella, tibia, & fibula. In: White TD, Folkens PA (eds.). *The Human Bone Manual*, San Diego: Academic Press, pp 255-286.

ORIGINAL ARTICLE Eur J Anat, 28 (5): 579-590 (2024)

Systemic localization of vascular inflammation biomarkers in rats with depression

---

Magda A. Eldomiaty[1,2], **Nawal Almohammadi**[3], **Zeinab A. Hassan**[3,4], **Neven A. Ebrahim**[3,5]

[1] *Department of Basic Medical Sciences, Faculty of Medicine, Al Rayan Colleges, Saudi Arabia*
[2] *Department of Anatomy, Faculty of Medicine, Tanta University, Egypt*
[3] *Department of Basic Medical Sciences, Faculty of Medicine, Taibah University, Madinah, Saudi Arabia*
[4] *Department of Histology, Faculty of Medicine, Zagazig University*
[5] *Department of Anatomy and Embryology, Faculty of Medicine, Mansoura University, Mansoura, Egypt*

SUMMARY

This study aims at investigating the influence of depression on vascular inflammation in the vital organs of the body. Thirty male Sprague-Dawley rats were used as control and experimental groups. Forced swimming protocol was used for 21 days to initiate depression in the experimental rats. Depression was evaluated through automatically measuring the rats' locomotor activity by the 6-minutes forced swimming test (FST) and by analyzing their serum corticosterone levels. Sera were collected from all rats before sacrifice and then tissue specimens of heart, lung, kidney, and liver were collected after sacrifice. The mean corticosterone level and the mean immobility duration were significantly increased in depression group. Through using the enzyme linked immunosorbent assay (ELISA), the serum levels of inflammatory biomarkers, tumor necrosis factor-alpha (TNF-α), vascular endothelial growth factor (VEGF), and inducible nitric oxide synthase (iNOS) were measured, and their tissue expression were examined. The area percentage of immune expression was measured using the Image J program.

The mean serum levels of TNF-α and iNOS elevated significantly in the depression group compared to the control, whereas serum level of VEGF decreased significantly in depressed rats compared to control ones. Intense immuno-expression of inflammatory cytokines was detected in the endothelium of blood vessels of all examined tissues in depression group compared to control ones. Except for TNF-α expression in the lung tissues, the area percentage of immune expression of all the examined inflammatory cytokines were significantly increased in all the examined tissues. The study demonstrated that vasculitis can be a harmful outcome of stress and depression.

Key words: Depression – Vasculitis – Inflammatory cytokines - Vital organs

---

Corresponding author:
Neven A. Ebrahim. Department of Anatomy and Embryology, Faculty of Medicine, Mansoura University, Mansoura, Egypt, 35516. E-mail: nevenebrahim@mans.edu.eg – Orcid: 0000-0002-7358-6618

Submitted: January 30, 2024. **Accepted:** May 1, 2024

https://doi.org/10.52083/POWW8803

INTRODUCTION

Depression is a common disorder affecting a wide range of the population, it is one of the commonest psychiatric diseases all over the world (Pedersen et al., 2014). According to the WHO, depression is the second largest healthcare problem in the disabled population (Moon et al., 2012). There is a great association between chronic stress, its subsequent depression, and the development of vascular diseases (Taylor et al., 2013).

The relationship between depression and inflammation is believed to be bidirectional. Vascular depression is a common term, postulating that vascular inflammation and endothelial dysfunction might induce depression symptoms and precipitate depressive syndrome (Taylor et al., 2013). Depression related modification like stress response, and neurotransmitter imbalances can enhance inflammation and increase the risk of vascular damage by increasing the levels of proinflammatory cytokines and reducing anti-inflammatory cytokine levels (Kristen, 2022).

Depression activates proinflammatory cytokines release, including interleukin-6 (IL-6) and tumor necrosis factor-alpha (TNF-α), which are strongly related to endothelial dysfunction and vasculitis (Black and Garbutt, 2002; Doney et al., 2022; Saadat et al., 2022). TNF-α is a crucial vascular inflammatory biomarker that engages inflammatory immune cells and advances tissue destruction. It plays critical role in enhancing chronic uncontrolled proinflammatory mediators' production (Parlindungan et al., 2023). TNF-α has multiple effects that control various intracellular functions and play an essential role in the regulation of emotions assumed to be involved in depression (Jang et al., 2021).

Vascular endothelial growth factor (VEGF) is a potent angiogenic agent. It is considered the master regulator for cytokines of angiogenesis and vasculogenesis, as it promotes endothelial cell migration and survival, as well as the formation and maintenance of capillary fenestrations (Maharaj et al., 2006; Xie et al., 2017). VEGF-A is secreted by endothelial cells, macrophages, and activated T cells (Ferrara, 2004). It is located in the central nervous system (CNS), and it is capable of crossing the blood-brain barrier, playing a vital role in the pathomechanism of depression disorder (Halmai et al., 2013; Rigal et al., 2020).

Nitric oxide (NO) is an essential signaling molecule, which mediates a variety of essential physiological processes. It is produced by inducible nitric oxide synthase (iNOS) and has been implicated in various hypoxic diseases, vascular injury, and inflammation (Cassini-Vieira et al., 2015). Its expression was detected in both serum and cortical tissues of depressed mice, and was aggravated in post-stroke depression patients (Peng et al., 2012; Wang et al., 2021).

The widespread vascular impacts of depression on the body offer a fascinating avenue to investigate cellular and molecular processes in different organs throughout the disease progression. This study was designed to investigate the influence of depression on the body's vasculature by analyzing the expression of biomarkers associated with vascular inflammation (namely TNF-α, VEGF, and iNOS) in key tissues such as the lung, kidney, liver, and heart after induction of depression in a rat model. The underlying hypothesis is that depression triggers a broad-spectrum inflammatory and damaging response in the vascular systems across various vital body organs.

MATERIALS AND METHODS

Animal model preparation

Thirty male Sprague-Dawley rats, each 150-250 g weight, were used in this controlled experiment. Animal experiments were conducted at the medical college research lab, Al-Rayan colleges and Taibah University, Saudi Arabia. All animal handling and procedures were carried out following the EC Directive 86/609/EEC for animal manipulations (https://www.researchgate.net/publication/10962580_Directive_86609EEC_on_the_Protection_of_Animals_Used_for_Experimental_and_Other_Scientific_Purposes) and the guidelines of the National Committee of Bio Ethics in Saudi Arabia (https://ncbe.kacst.edu.sa/media/xphlbp1e/كتاب-الأخلاقيات-إنجليزي.pdf). Ethical approval was taken from IRB of Al-Rayan Colleges (HA-03-M-122-038).

Thirty-five rats were purchased from Taibah University experimental animal center. They were fed with a standard pellet diet and water ad libitum and noted for any abnormal behavior either in their movement or food intake. Thirty of the most apparently normal behavioral rats were included in the study. The selected rats were individually housed in pathogen-free conditions at 20-22°C and 45-55% humidity in a twelve hours light/dark cycle (Garrett et al., 2012).

Experimental groups:

Rats were divided randomly into two groups (15 rats each):

1. Control group: the rats were maintained on a standard chow diet for 3 weeks, including the weekends. Following this, their locomotor activity was evaluated with a 6-minute forced swimming test (FST) and then sacrificed immediately.
2. Depression group: The rats underwent the FS protocol daily for three weeks, including weekends (21 days). Following this, their locomotor activities were evaluated with a 6-minute FST and then sacrificed immediately.

In forced swimming protocol, the rats were forced to swim individually inside 60 x 22 cm glass cylinders with 45 cm water depth for 15 min daily for 21 days, temperature was maintained at a 25-28°C. The rats were let to dry in a 32°C heated enclosure before returning to their cages (Porsolt et al., 1978; Eldomiaty et al., 2017).

Assessment of the depression in the rats

The depression state of the rats was evaluated through two methods (Petit-Demouliere et al., 2005; Eldomiaty et al., 2023):

1. Detection of corticosterone level in sera collected from rats just before killing: the sera were collected from the retro-orbital vein, centrifuged at 4°C, and stored at -80°C till handled for determination of the level of corticosterone using ELISA kits (ALPCO Diag-nostics, Orangeburg, NY, USA following the manufacturer’s recommendations.
2. Automatic Measurement of the locomotor activity of the rats: the locomotor activities of the rats were traced through computer software (Ethovision XT version: 8.0) during FST to detect the immobility duration in seconds.

Venous blood sample collection and determination of serum levels of inflammatory biomarkers

One hour before sacrifice, blood samples were collected from tail veins of the rats of each group. Centrifugation and serum storage took place at -20°C regarding Nyakoe et al. (2009). Serum concentrations of TNF-α, VEGF and iNOS were calculated using enzyme linked immunosorbent assay (ELISA) kits (R&D Systems, cat no; RTA00 and RRV00, Nuoyuan, Shanghai, China and MY-BIOSOURCE, cat no; MBS263618 respectively) in both control and depression-induced groups. The optical absorbance was read at 450 nm (TECAN, Switzerland). The concentrations were calculated from standard curves and analyzed with One-way ANOVA; different samples were compared.

Dissection, collection, and immunostaining of the tissues for analysis

At the assigned time, the rats were sacrificed, fresh samples from the cardiac wall, lung, kidney, and liver were collected, fixed, and embedded in paraffin blocks. Sections (5 µm) were collected, stained utilizing primary polyclonal antibodies adverse to the selected inflammatory cytokines (anti-VEGF Rabbit polyclonal antibody; Abcam; cat no: ab53465, anti TNF-α Rabbit polyclonal antibody; BIO-RAD; cat no: AAR33 and anti-iNOS Rabbit polyclonal antibody; Abcam; cat no: ab3523) 1:100 dilution. Tissue samples were fixed with 4% paraformaldehyde in PBS at pH 7.4 for 10 min at RT after scarification. They were permeabilized for 10 min with 0.15 % Triton X-100 in 0.1% bovine serum albumin (BSA) in phosphate buffer saline (PBS), blocked with 5% goat serum for 30 min and incubated with the antibodies overnight at 4°C. The tissue samples were then incubated with the secondary antibodies, washed with PBS, and counterstained with hematoxylin and viewed under a light microscope. Stained sections were examined using an Olympus BX 36 Bright field Automated microscope. The images were digitized in a 2448 × 1920-pixel matrix using a DP27 color digital video camera to detect the development of vascular injury through exploring inflammatory biomarkers expression.

Measuring the area percentage of immune stained sections

The area percentage of brown-colored VEGF, TNF-α and iNOS immunohistochemically stained sections were measured by the Image J program (National Institute of Health, Bethesda, Maryland, USA), to separate the brown stained color pixels (DAB) from the background (H&E-stained pixels) in the selected images. Non-overlapped sectors of five stained slides of all the groups and images at ×200 magnification with a clear contrast and consistent DAB and H&E stain and saved as JPEG format were used. To define color threshold range for the brown stained areas, the saturation and the brightness for the selected images were adjusted. Color deconvolution was applied to separate colors and DAB was analyzed; then threshold was used to measure the area of immunohistochemical positivity using the method mentioned in Yuan and Munson (Yuan and Munson, 2017).

Statistical analysis

The statistical analysis was conducted employing the IBM SPSS (version 21) statistical package. All data are conveyed as the means ± standard errors of the means (SEM). For Assessment of the depression (corticosterone level and the locomotor activity), comparisons between groups were conducted using the Independent Samples test with 95% confidence interval of the difference. For comparing the area percentage of immune stained sections, one-way analysis of variance (ANOVA) followed by Bonferroni pairwise was used. For all tests, the level of significance and comparisons were determined < 0.05.

RESULTS

Evaluation of the depressive state

The mean corticosterone serum level was significantly elevated in the depression group (2.89±0. 082pg/ml) compared to the control (2.53±0.027 pg/ml) (p < 0.001) (Fig. 1A).

The mean immobility duration was significantly augmented in the depression group (273.67±6.30 s) compared to the control (71.67±2.99 s) (p <0.001) (Fig. 1B).

Serum levels of TNF-α, VEGF and iNOS (Fig. 2)

The mean of TNF-α serum levels increased significantly in the depression group (327.47 ±3.00 ng/L) compared to control group (278.20±4.39 ng/L) (p < 0.001). Also, the mean serum levels of iNOS increased significantly in the depression group (14.99±0.59 ng/ml) compared to control group (5.47±0.13 ng/ml) (p < 0.001), whereas the mean serum level of VEGF decreased significantly in serum of depressed rats (136.20 ±3.20 pg/ml) compared with control ones (171.33 ±2.87) pg/ml) (p < 0.001).

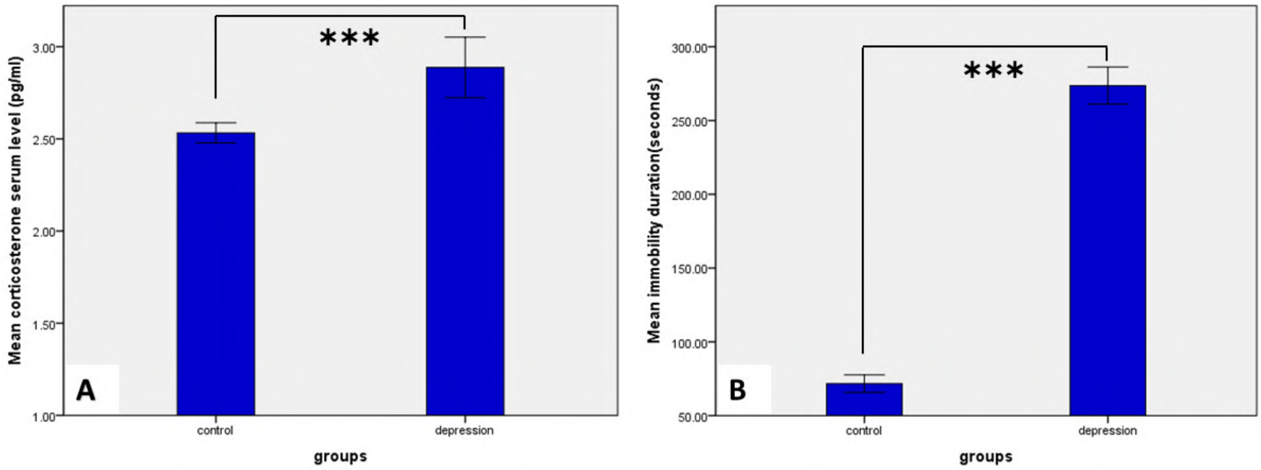

Fig. 1.- Graphs illustrating the mean corticosterone levels in control and depression groups (15 rats each) (**A**) and showing the immobility duration for control and depression groups (15 rats each) during the 6-min forced swimming test (**B**). Data are represented as mean ± SEM. *** means significance at P<0.001.

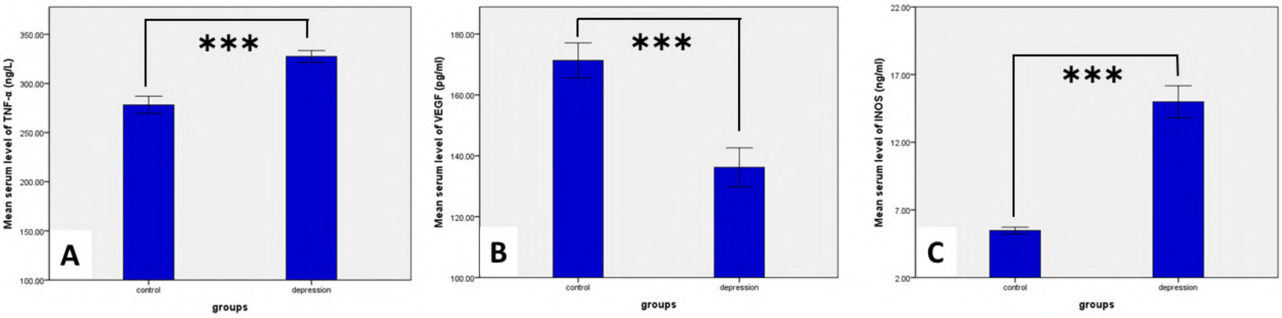

Fig. 2.- Graphs showing the mean serum levels of TNF-α (**A**), VEGF (**B**) and iNOS (**C**) in control and depression groups (15 rats each). Data are represented as mean + SEM. *** means significance at P<0.001.

Immunohistochemistry results

TNF-α, VEGF and iNOS expression in the heart tissue (Fig. 3):

The sarcoplasm of control sections showed weak TNF-α immunoreactivity in the cardiomyocytes and moderate immunostaining of the blood vessels' endothelium. In the depression group, intense immunostaining was detected in the blood vessels' endothelium and some cardiomyocytes, especially those close to the blood vessels.

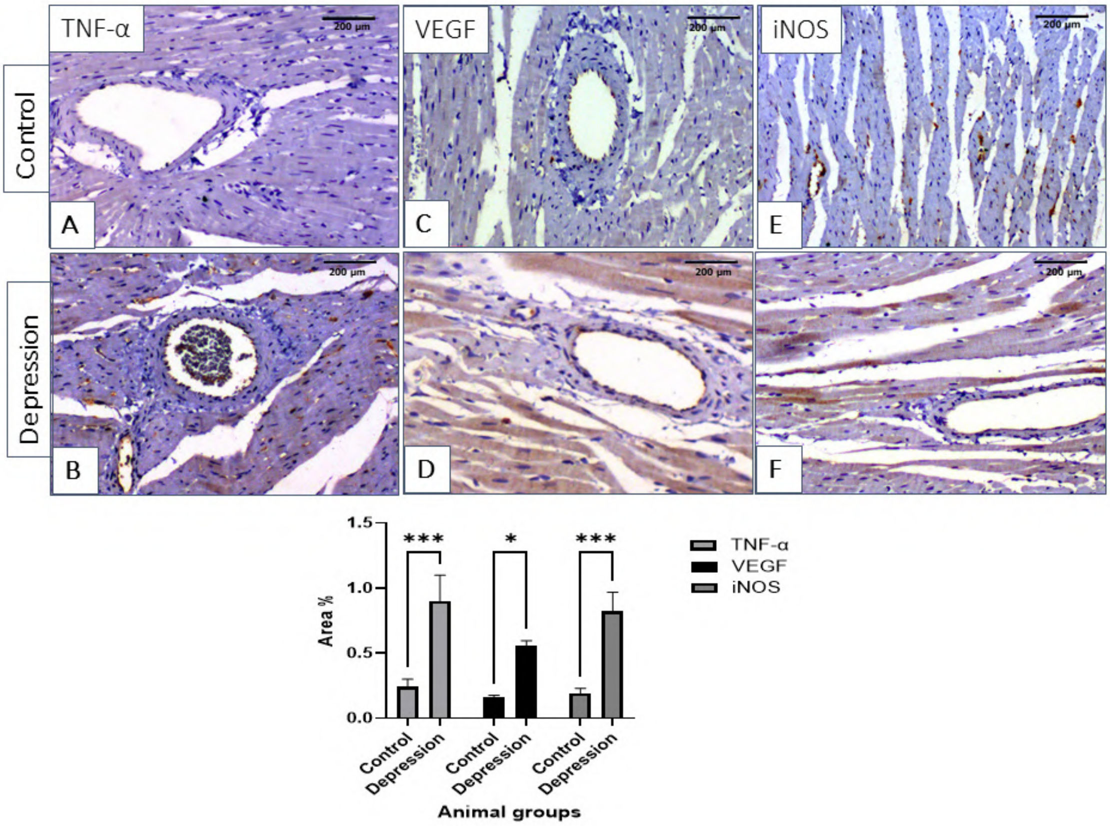

Fig. 3.- Sections of rat's heart after TNF-α, VEGF & iNOS immunohistochemical technique: (**A, B**) control and depression groups of TNF-α stained sections, in which the expression of TNF-α in the endothelium of blood vessels and some cardiomyocytes increased in depression group compared to the control group. (**C, D**) control and depression groups of VEGF-stained sections, in which the expression of VEGF in the endothelium of blood vessels and cardiomyocytes increased compared to the control group. (**E, F**) control and depression groups of iNOS stained sections, in which the expression of iNOS increased in the endothelium of blood vessels in depression group compared to control group. (**G**) Histogram illustrating the quantitative analysis of the intensity of TNF-α, VEGF & iNOS stain in different experimental groups. The depression group demonstrated a significant increase in TNF-α VEGF, & iNOS area % as compared to the control group. Data are represented as mean ± SEM. * means significance at p< 0.05 while *** means significance at p< 0.001. Scale bars = 200 µm.

In control sections, VEGF was uniformly and weakly expressed in sarcoplasm of cardiomyocytes, with moderate immunostaining of endothelium of blood vessels. In the depression group, intense immunostaining was found in the endothelium of blood vessels and cardiomyocytes.

Immune-stained section for iNOS expression showed weak immunostaining in the sarcoplasm of cardiomyocytes of control group, which became intense in cells of the depression group. The blood vessels' endothelium expressed moderate immunostaining in the control group, but intense expression appeared in the depression group.

Measuring the intensity of immuno-expression through the area percentage of immuno-expression revealed that the depression group demonstrated significant increases in the means of area percentage of TNF-α (0.9 ± 0.22) as compared to the control (0.24 ± 0.07), VEGF (0.55 ± 0.11) in comparison with the control group (0.2 ± 0.05), and iNOS (0.82 ± 0.19) compared to the control (0.19 ± 0.08), ($p < 0.001$, $p < 0.05$, $p < 0.001$ respectively).

TNF-α, VEGF and iNOS expression in the lung tissue (Fig. 4):

TNF-α immunostaining expression was weak in lining alveolar and bronchioles of control group which moderately increased in depression group.

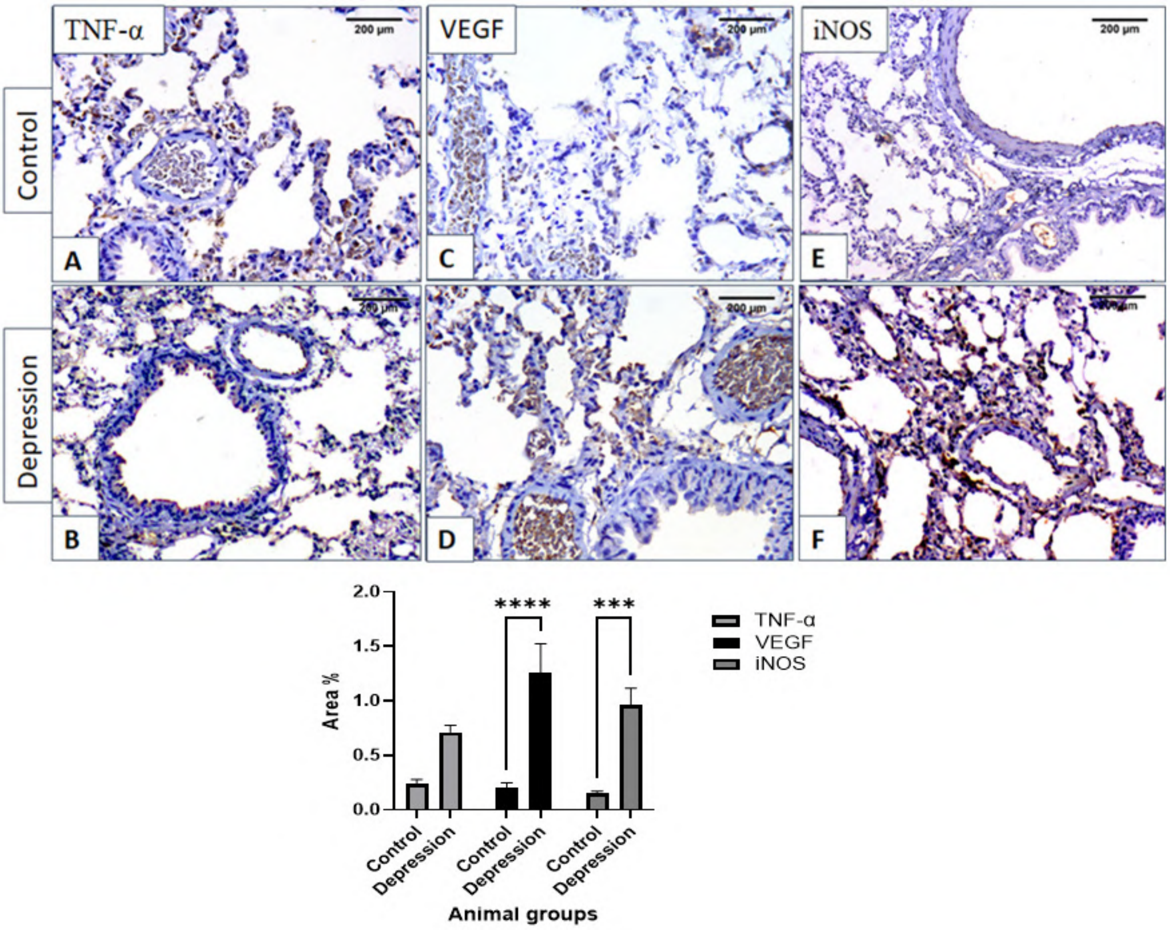

Fig. 4.- Sections of rat's lung after TNF-α, VEGF & iNOS immunohistochemical technique: (**A, B**) control and depression groups of TNF-α stained sections, in which there is a little increase of TNFα expression in alveolar epithelium, and bronchioles in depression group compared to the control group. (**C, D**) Control and depression group of VEGF-stained sections showing the increase VEGF expression in the terminal gas exchange alveoli and the epithelium of small vessels and bronchioles of the alveolus in the depression group compared to the control group. (**E, F**) Control and depression group of iNOS stained sections showing the increased expression of iNOS in the endothelial cells of pulmonary vessels, vascular smooth muscle cells and in the epithelium of bronchiolar epithelial in depression group compared to control group. (**G**) Histogram illustrating the quantitative analysis of the intensity of TNF-α, VEGF & iNOS stains in different experimental groups. The depression group demonstrated a significant increase in VEGF & iNOS area percentage as compared to the control group. However, the TNF-α area percentage showed non-significant differences. Data are represented as mean + SEM. *** means significance at $p< 0.001$ while **** means significance at $p< 0.0001$. Scale bars = 200 µm.

VEGF expression in control sections was weak and appeared in the terminal gas exchange alveoli, in the endothelium of some blood vessels, and the epithelium of bronchioles. The reaction became intense in the depression group.

Weak iNOS immunostaining was detected in all types of pulmonary vessels (arteries, veins, and capillaries) endothelial cells, smooth muscle cells of lung vessels and in the bronchiolar epithelial cells of the control group. In the depression group, the intensity of iNOS-positive expression was high as compared with the control.

When measuring the area percentage of immuno-expression, the depression group demonstrated significant increases in the means of area % for VEGF (1.26 ± 0.32) as compared to the control group (0.2 ± 0.06), of iNOS (0.96 ± 0.24) compared to the control group (0.15 ± 0.07) ($p < 0.0001$, $p < 0.001$ respectively). However, the mean area percentage for TNF-α expression showed a non-significant difference between groups.

TNF-α, VEGF and iNOS expression in the kidney tissue (Fig. 5):

Weak glomerular and tubular TNF-α immune-expression was detected in control sections. Meanwhile, in the depression group, intense TNF-α immunostaining was observed in both renal glomeruli and tubular epithelial cells.

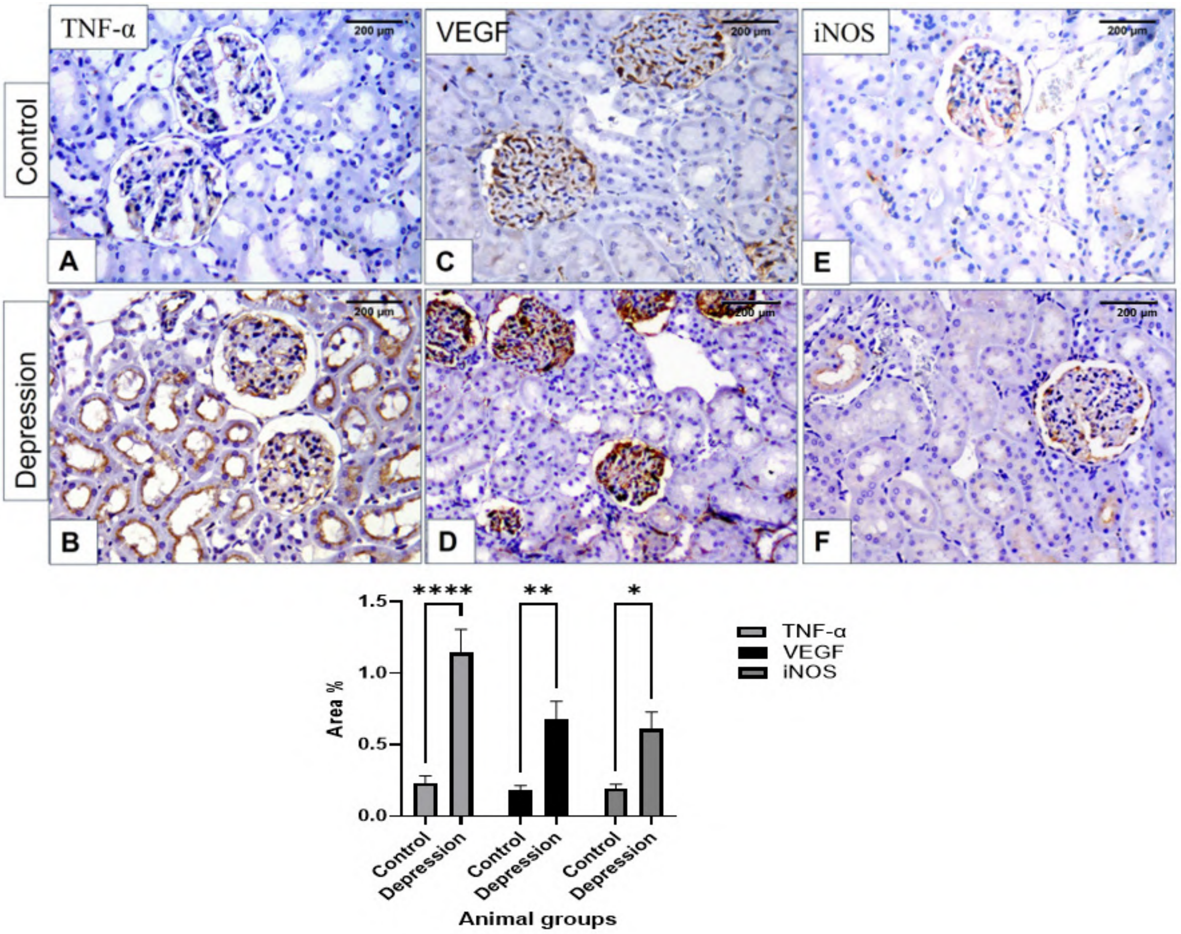

Fig. 5.- Sections of rat's Kidney after TNF-α, VEGF & iNOS immunohistochemical technique. (**A, B**) control and depression groups of TNF-α stained sections, showing the increased expression of TNF-α in renal glomeruli and tubular epithelial cells in depression group compared to the control group. (**C, D**) Control and depression group of VEGF-stained sections showing the increased VEGF expression in the epithelial glomerular cells, and blood vessels of the depression groups compared to the control group. (**E, F**) control and depression group of iNOS stained sections showing the increased iNOS expression in renal glomerular endothelial cells and capsule and in tubular cells of the depression group compared to control group. (**G**) Histogram illustrating the quantitative analysis of the intensity of TNF-α, VEGF & iNOS stain in different experimental groups. The depression group demonstrated a significant increase in TNFα, VEGF & iNOS area percentage as compared to the control group. Data are represented as mean ± SEM. * means significance at $p< 0.05$, ** means significance at $p< 0.01$ while **** means significance at $p< 0.0001$. Scale bars = 200 µm.

VEGF immune expression was weak in the glomeruli of the control sections, but it was obviously increased in the epithelial glomerular cells, blood vessels of the depression groups.

Weak iNOS expression in the glomerular endothelial cells and in the visceral and parietal glomerular capsule was found in the control group. In the depression group, the expression appeared in the renal tubule cells and increased in the glomerular endothelial cells and capsule.

Measuring the intensity of immuno-expression through the area percentage of immuno-expression, the depression group demonstrated a significant increase in the means of area percentage for TNF-α (1.2 ± 0.52) as compared to control (0.2 ± 0.16), VEGF (0.65 ± 0.39) as compared to control group (0.15 ± 0.1), and iNOS (0.55 ± 0.38) as compared to the control group (0.2 ± 0.1)($p < 0.0001$, $p < 0.01$, $p < 0.05$ respectively).

TNF-α, VEGF and iNOS expression in the liver tissue (Fig. 6):

TNF-α immune expression of the control group showed weak intracytoplasmic TNF-α positive hepatocytes, Kupfer cells, and endothelium of blood sinusoids. The depression group showed strong intracytoplasmic TNF-α expression hepatocyte, especially those surrounding the central vein, with strong expression in the endothelium of blood sinusoids and Kupfer cells.

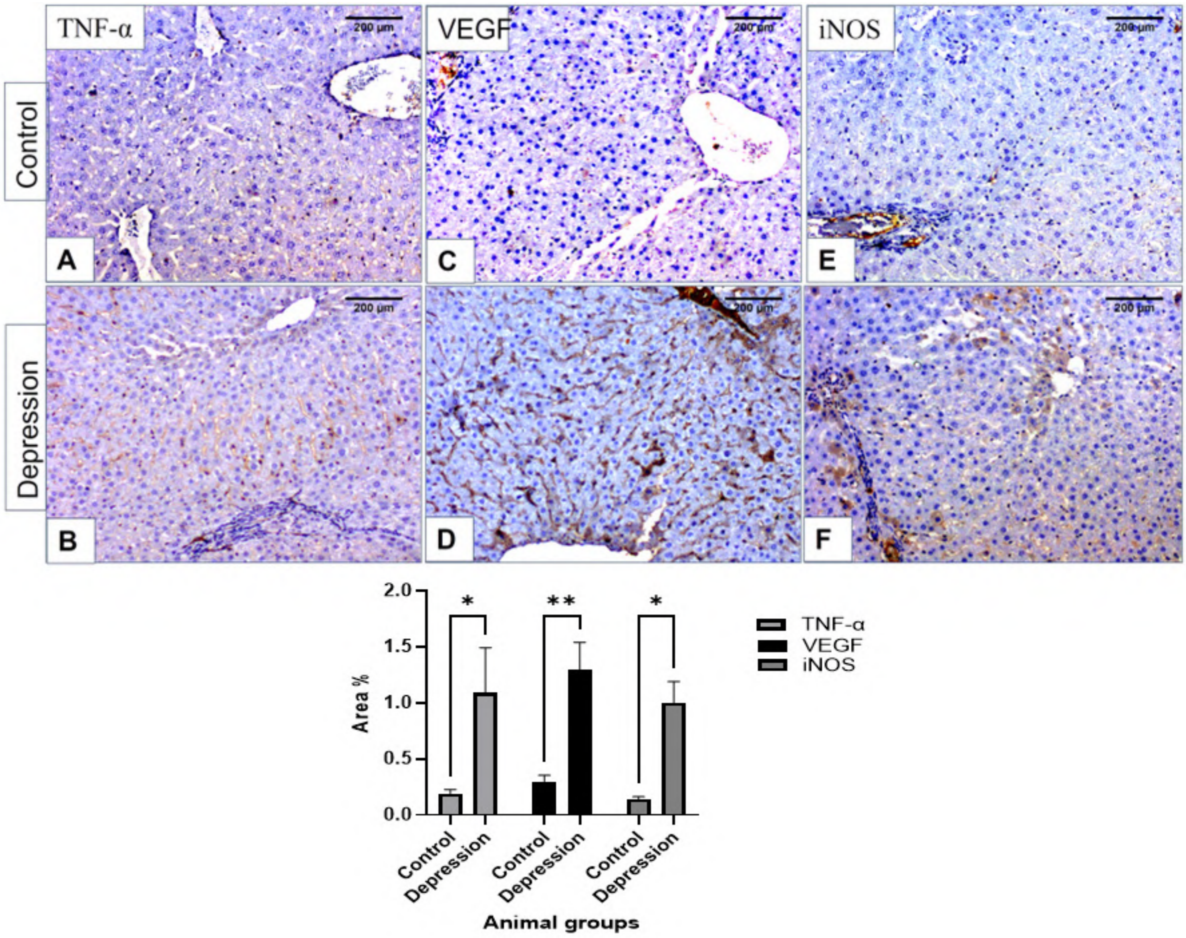

Fig. 6.- Sections of rat's liver after TNF-α, VEGF & iNOS immunohistochemical technique. (**A, B**) control and depression groups of TNFα stained sections, showing the increased intracytoplasmic expression of TNF-α in the hepatocyte, especially those surrounding the central veins and the strong expression in the blood sinusoids and Kupfer cells of the depression group compared to the control group. (**C, D**) Control and depression group of VEGF-stained sections showing the increased VEGF expression in the hepatocytes and cells of blood sinusoids in the depression group compared to the control group. (**E, F**) control and depression group of iNOS stained sections showing the increased iNOS expression in the endothelium of blood vessels and hepatocytes especially in zones surrounding the central vein and portal tract in the depression group compared to control group. (**G**) Histogram illustrating the quantitative analysis of the intensity of TNF-α, VEGF & iNOS expression in different experimental groups. The depression group demonstrated a significant increase in TNFα, VEGF & iNOS area % as compared to the control group. Data are represented as mean ± SEM. Data are represented as mean ± SEM. * means significance at $p< 0.05$ while ** means significance at $p< 0.01$. Scale bars = 200 µm.

Control sections showed moderate VEGF expression in blood sinusoids and uniformly weak expression in hepatocytes. However, in the depression group, VEGF immuno-expression was obviously increased in the endothelium of blood sinusoids and hepatocytes.

In control sections, weak iNOS immune expression was uniformly distributed in hepatocytes with moderate expression in the blood vessels' endothelium and in the epithelium of adjacent bile duct. In the depression group, intense expression was observed in the endothelium of blood vessels, and moderate intracytoplasmic hepatocytes expression appeared especially in zones surrounding the central veins and portal tract.

When measuring the intensity of immuno-expression through the area% of immuno-expression, the depression group demonstrated significant increases in the means of area % for TNFα (0.8 ± 1.27) as compared to the control group (0.2 ± 0.12), of VEGF (1.15 ± 0.77) as compared to the control group (0.25 ± 0.17), and iNOS (0.8 ± 0.6) as compared to the control group (0.1 ± 0.07) ($p < 0.05$, $p < 0.01$, $p < 0.05$ respectively).

DISCUSSION

The study hypothesized the generalized vascular inflammatory effect of depression on various body systems and tried to explore this through investigating the expression of vascular inflammatory biomarkers (TNF-α, VEGF and iNOS) (Zhang et al., 2009; Shaik-Dasthagirisaheb et al., 2013) in vital parenchymal tissues (heart, lung, kidney, and liver) after induction of depression in rats, and through studying the changed serum levels of these biomarkers in the rats with depression.

In this study, the TNF-α serum level increased significantly in the depressed rats, and its expression was significantly increased in the blood vessels' endothelium and cardiomyocytes of the heart, in renal glomeruli and tubular epithelial cells of the kidney, as well as in the blood sinusoids, Kupfer cells and hepatocyte surrounding the central vein of the liver tissue. However, the TNF-α expression did not significantly increase in the lung epithelial tissues.

The significant elevation of serum TNF-α levels in depressed rats, accompanied by heightened expression in the endothelium of blood vessels in multiple vital organs, underlines the systemic nature of inflammation associated with depression. The elevated TNF-α expression leads to the reactive oxygen species (ROS) generation, which induces endothelial dysfunction and vasculitis in various pathological conditions (Zhang et al., 2009). This systemic inflammatory response has raised the recognition that inflammation may represent a common mechanism of the disease (Miller et al., 2010). However, in this study, TNF-α was predominantly expressed in the vascular endothelium after induction of depression, and so vascular inflammation might be a detrimental consequence of depression.

In the heart tissue, the elevated TNF-α expression levels in the endothelium of blood vessels and cardiomyocytes can denote endothelial dysfunction and other cardiac ailments (Libby et al., 2002). Depression itself has long been correlated to an increased risk of cardiovascular disease, and the observed increase in TNF-α might provide a mechanistic link, indicating a direct pathophysiological pathway of depression (Mosovich et al., 2008). The increased TNF-α expression in the renal glomeruli and tubular epithelial cells of the kidney could denote vascular impairment of the kidney as was reported by Bautista et al., who suggested that TNF-α could mediate renal damage in various pathological states (Bautista et al., 2005). In the liver tissue, the TNF-α elevated expression in the blood sinusoids can denote vascular affection and hepatic inflammation (Tilg and Moschen, 2010).

On the other hand, the non-significant TNF-α expression in the lung vascular tissue reported in this study can be attributed to the molecular mechanisms included in the control of tissue damage in the lung, as was described by Xu et al., which can directly inhibit TNF-α-induced effects and attenuate the severity of lung injury (Meng et al., 2020; Xu et al., 2023).

In the present study, there were unexpected significant decrease of the serum VEGF level in the depressed rats, though its significant increased expression in the blood vessels' endothelium of all the examined tissues. The increased tissue expression is in accordance with the reported pivotal role of VEGF as a regulator of angiogenesis, vascular permeability and tissue repair in various pathological states, including neurodegenerative diseases (Shibuya, 2011). At the same time, VEGF is proved to be a mediator of inflammation and pathological angiogenesis (Shaik-Dasthagirisaheb et al., 2013), so we can depict its increased expression in the endothelium due to its role in inflammatory processes.

On the other hand, the decreased serum level of VEGF detected in this study is in accordance with some recent studies that strongly suggested that neuronal degeneration can be due to lower circulation level of VEGF in neuronal cells and that pro-angiogenic therapy could be beneficial in treating ischemic heart and brain diseases (Oosthuyse et al., 2001; Storkebaum E et al., 2005). From other point of view, the decreased VEGF serum level does not necessarily mirror its tissue expression, as tissues can locally upregulate VEGF expression in response to local factors like hypoxia, without a corresponding increase in the systemic levels. Further, and in consistent with our results, certain stress conditions might lead to sequestration or increased uptake of VEGF in the tissues, leading to decrease of its serum levels (Shibuya, 2011).

The elevated VEGF in the heart tissue might indicate attempts at angiogenesis to tolerate the increased metabolic demand or reduced oxygen supply due to the increased proinflammatory cytokines and inflammatory processes in cardiovascular system in depression (Grippo and Johnson, 2009). Also, in the lung tissues, the reported increased VEGF expression in the endothelial cells reflects the role of this cytokine in the maintenance and repair of the alveolar structures affected by the raised inflammatory cytokines. This might suggest a reparative or defensive response against potential alveolar damage in the context of depression (Compernolle et al., 2002). In the kidney, the elevated VEGF expression in the glomerular epithelium can indicate a stress response for the potential damage produced by the increased proinflammatory cytokines in depression. Its expression can denote a protective restoration of endothelial cells and glomerular capillary circumference through the tubular repair mechanisms (Stevens et al., 2017). Elevated VEGF expression in blood sinusoids of the liver can indicate increased vascular permeability or angiogenesis, which might be a response to metabolic changes or altered detoxification demands in depression (Apte et al., 2019). Importantly, the increased VEGF expression can represent a protective mechanism for the liver sinusoidal endothelial cells, as it plays a special role in other growth factors' tissue release from hepatic endothelial cells, to protect the hepatocytes from the damage caused by the hepatotoxin (LeCouter et al., 2003).

The significant increased serum level and tissues expression of iNOS in endothelial tissues of depressed rats, offers a convincing insight for the potential connection between depression and vasculitis. The excessive production of NO, particularly from iNOS, has been associated with pro-inflammatory and oxidative processes (Förstermann and Sessa, 2012). Its association with development of depression and its severity is recently documented by Wang et al. (2021), and hense, the increased serum levels and tissue expression of iNOS can denote overproduction of NO that might exacerbate endothelial dysfunction, predisposing to inflammatory vasculitis that can impact various organ systems (Pacher et al., 2007; Wang et al., 2021).

The elevated iNOS in cardiomyocytes could indicate cardiac stress, potentially linking depression to cardiovascular diseases as was reported by Paulus and Tschope. Besides, its upregulation in pulmonary vessels and bronchiolar epithelial cells might relate depression to pulmonary complications, such as pulmonary hypertension or bronchitis seen in some patients with vasculitis (Han et al., 2004; Paulus and Tschöpe, 2013). The enhanced iNOS expression in renal tissues might predispose to renal inflammation or nephritis which is a common manifestation in certain types of vasculitis, while its increased expression in the liver's blood vessels and bile ducts might signify hepatic inflammation or cholangitis (Yaylak et al., 2008; Sedaghat et al., 2019). The systemic increase of iNOS expression in depressed rats might suggest that depression could predispose or exacerbate vascular inflammation or vasculitis. (Pober et al., 2009).

The association of depression with systemic inflammation, particularly vascular inflammation can be considered a double-edged blade, because though depression can elevate pro-inflammatory markers like TNF-α and iNOS, these inflammatory cascades could further accentuate depressive symptoms, establishing a vicious cycle (Pober et al., 2009; Miller et al., 2010).

The study aimed to display the reverse of the conventional understanding of the association between depression and vascular inflammation. As the study demonstrated that vasculitis can be a harmful outcome resulting from stress and depression, and that vascular inflammation can be a serious reaction associated with the onset of depression.

More research is necessary to investigate the direct causative link between depression and vascular inflammation. Studies should focus on the functional implications of these vascular changes and whether they represent adaptive or maladaptive responses in the context of depression. The observed upregulation of the pro-inflammatory cytokines in endothelial lining of the vital organs can serve as a basis for future development of endothelial protective therapies that could help treatment of depression associated with chronic proinflammatory diseases.

ACKNOWLEDGEMENTS

The authors acknowledge the technicians in the medical college research lab, Al-Rayan colleges and Taibah University, Saudi Arabia.

REFERENCES

APTE RS, CHEN DS, FERRARA N (2019) VEGF in signaling and disease: beyond discovery and development. *Cell*, 176: 1248-1264.

BAUTISTA LE, VERA LM, ARENAS IA, GAMARRA G (2005) Independent association between inflammatory markers (C-reactive protein, interleukin-6, and TNF-α) and essential hypertension. *J Hum Hypertens*, 19: 149-154.

BEHESHTI F, HASHEMZEHI M, HOSSEINI M, MAREFATI N, MEMARPOUR S (2020) Inducible nitric oxide synthase plays a role in depression- and anxiety-like behaviors chronically induced by lipopolysaccharide in rats: Evidence from inflammation and oxidative stress. *Behav Brain Res*, 392: 112720.

BLACK PH, GARBUTT LD (2002) Stress, inflammation and cardiovascular disease. *J Psychosom Res*, 52(1): 1-23.

CASSINI-VIEIRA P, ARAÚJO FA, DA COSTA DIAS FL, RUSSO RC, ANDRADE SP, TEIXEIRA MM, BARCELOS LS (2015) iNOS activity modulates inflammation, angiogenesis, and tissue fibrosis in polyether-polyurethane synthetic implants. *Mediators Inflamm*, 2015: 138461.

COMPERNOLLE V, BRUSSELMANS K, ACKER T, HOET P, TJWA M, BECK H, PLAISANCE S, DOR Y, KESHET E, LUPU F, NEMERY B, DEWERCHIN M, VAN VELDHOVEN P, PLATE K, MOONS L, COLLEN D, CARMELIET P (2002) Loss of HIF-2α and inhibition of VEGF impair fetal lung maturation, whereas treatment with VEGF prevents fatal respiratory distress in premature mice. *Nat Med*, 8: 702-710.

DONEY E, CADORET A, DION-ALBERT L, LEBEL M, MENARD C (2022) Inflammation-driven brain and gut barrier dysfunction in stress and mood disorders. *Eur J Neurosci*, 55: 2851-2894.

ELDOMIATY MA, A.HASSAN Z, HALAWA AM, ELNAJAR AM, ALMOHAMADI N (2023) Structural changes and neurotrophic factors upregulation in submandibular gland in a rat model of depression: proposed correlation with stress indicators during and after the relief of depression. *Anat Sci Int*, 98: 185-195.

ELDOMIATY MA, ALMASRY SM, DESOUKY MK, ALGAIDI SA (2017) Voluntary running improves depressive behaviours and the structure of the hippocampus in rats: A possible impact of myokines. *Brain Res*, 1657: 29-42.

FERRARA N (2004) Vascular endothelial growth factor: Basic science and clinical progress. *Endocr Rev*, 25: 581-611.

FÖRSTERMANN U, SESSA WC (2012) Nitric oxide synthases: Regulation and function. *Eur Heart J*, 33: 829-837.

GARRETT L, LIE DC, HRABÉ DE ANGELIS M, WURST W, HÖLTER SM (2012) Voluntary wheel running in mice increases the rate of neurogenesis without affecting anxiety-related behaviour in single tests. *BMC Neurosci*, 13: 61.

GRIPPO AJ, JOHNSON AK (2009) Stress, depression and cardiovascular dysregulation: A review of neurobiological mechanisms and the integration of research from preclinical disease models. *Stress*, 12: 1-21.

HALMAI Z, DOME P, DOBOS J, GONDA X, SZEKELY A, SASVARI-SZEKELY M, FALUDI G, LAZARY J (2013) Peripheral vascular endothelial growth factor level is associated with antidepressant treatment response: Results of a preliminary study. *J Affect Disord*, 144: 269-273.

HAN X, FINK MP, YANG R, DELUDE RL (2004) Increased iNOS activity is essential for intestinal epithelial tight junction dysfunction in endotoxemic mice. *Shock*, 21: 261-270.

JANG DI, LEE AH, SHIN HY, SONG HR, PARK JH, KANG TB, LEE SR, YANG SH (2021) The role of tumor necrosis factor alpha (Tnf-α) in autoimmune disease and current TNF-α inhibitors in therapeutics. *Int J Mol Sci*, 22: 1-16.

KRISTEN F (2022) The relationship between inflammation and depression [www Document]. *September 4, 2020*.

LECOUTER J, MORITZ DR, LI B, PHILLIPS GL, LIANG XH, GERBER HP, HILLAN KJ, FERRARA N (2003) Angiogenesis-independent endothelial protection of liver: role of VEGFR-1. *Science*, 299: 890-893.

LIBBY P, RIDKER PM, MASERI A (2002) Inflammation and atherosclerosis. *Circulation*, 105: 1135-1143.

MAENG SH, HONG H (2019) Inflammation as the potential basis in depression. *Int Neurourol J*, 23: S63-S71.

MAHARAJ ASR, SAINT-GENIEZ M, MALDONADO AE, D'AMORE PA (2006) Vascular endothelial growth factor localization in the adult. *Am J Pathol*, 168: 639-648.

MENG C, WANG S, WANG X, LV J, ZENG W, CHANG R, LI Q, WANG X (2020) Amphiregulin inhibits TNF-α-induced alveolar epithelial cell death through EGFR signaling pathway. *Biomed Pharmacother*, 125: 109995.

MILLER AH, MALETIC V, RAISON CL (2010) Inflammation and its discontents: The role of cytokines in the pathophysiology of major depression. *Psiquiatria Biologica*, 17: 71-80.

MOON HY, KIM SH, YANG YR, SONG P, YU HS, PARK HG, HWANG O, LEE-KWON W, SEO JK, HWANG D, CHOI JH, BUCALA R, RYU SH, KIM YS, SUH P-G (2012) Macrophage migration inhibitory factor mediates the antidepressant actions of voluntary exercise. *Proc Natl Acad Sci USA*, 109: 13094-13099.

MOSOVICH SA, BOONE RT, REICHENBERG A, BANSILAL S, SHAFFER J, DAHLMAN K, HARVEY PD, FARKOUH ME (2008) New insights into the link between cardiovascular disease and depression. *Int J Clin Pract*, 62(3): 423-432.

NYAKOE NK, TAYLOR RP, MAKUMI JN, WAITUMBI JN (2009) Complement consumption in children with Plasmodium falciparum malaria. *Malar J*, 8: 3-10.

OOSTHUYSE B, MOONS L, STORKEBAUM E, BECK H, NUYENS D, BRUSSELMANS K, VAN DORPE J, HELLINGS P, GORSELINK M, HEYMANS S, THEILMEIER G, DEWERCHIN M, LAUDENBACH V, VERMYLEN P, RAAT H, ACKER T, VLEMINCKX V, VAN DEN BOSCH L, CASHMAN N, FUJISAWA H, DROST MR, SCIOT R, BRUYNINCKX F, HICKLIN DJ, INCE C, GRESSENS P, LUPU F, PLATE KH, ROBBERECHT W, HERBERT JM, COLLEN D, CARMELIET P (2001) Deletion of the hypoxia-response element in the vascular endothelial growth factor promoter causes motor neuron degeneration. Nat Genet, 28(2): 131-138.PACHER P, BECKMAN JS, LIAUDET L (2007) Nitric oxide and peroxynitrite in health and disease. *Physiol Rev*, 87: 315-424.

PARLINDUNGAN F, HIDAYAT R, ARIANE A, SHATRI H (2023) Association between proinflammatory cytokines and anxiety and depression symptoms in rheumatoid arthritis patients: a cross-sectional study. *Clin Pract Epidemiol Mental Health*, 19: 9-11.

PAULUS WJ, TSCHÖPE C (2013) A novel paradigm for heart failure with preserved ejection fraction: Comorbidities drive myocardial dysfunction and remodeling through coronary microvascular endothelial inflammation. *J Am Coll Cardiol*, 62: 263-271.

PEDERSEN CB, MORS O, BERTELSEN A, LINDUMWALTOFT B, AGERBO E, MCGRATH JJ, MORTENSEN PB, EATON W (2014) A comprehensive nationwide study of the incidence rate and lifetime risk for treated mental disorders. *JAMA Psychiatry*, 71: 573-581.

PENG YL, LIU YN, LIU L, WANG X, JIANG CL, WANG YX (2012) Inducible nitric oxide synthase is involved in the modulation of depressive behaviors induced by unpredictable chronic mild stress. *J Neuroinflammation*, 9: 75.

PETIT-DEMOULIERE B, CHENU F, BOURIN M (2005) Forced swimming test in mice: A review of antidepressant activity. *Psychopharmacology (Berl)*, 177: 245-255.

POBER JS, MIN W, BRADLEY JR (2009) Mechanisms of endothelial dysfunction, injury, and death. *Ann Rev Pathol Mech Dis*, 4: 71-95.

PORSOLT RD, ANTON G, BLAVET N, JALFRE M (1978) Behavioural despair in rats: A new model sensitive to antidepressant treatments. *Eur J Pharmacol*, 47: 379-391.

RIGAL A, COLLE R, ASMAR KE, TRABADO S, LOEB E, MARTIN S, CHOUCHA W, GRESSIER F, COSTEMALE-LACOSTE JF, DE LARMINAT D, DEFLESSELLE E, FÈVE B, CHANSON P, BECQUEMONT L, VERSTUYFT C, CORRUBLE E (2020) Lower plasma vascular endothelial growth factor A in major depressive disorder not normalized after antidepressant treatment: A case control study. *Austr N Z J Psychiatry*, 54: 402-408.

SAADAT N, ZHANG L, HYER S, PADMANABHAN V, WOO J, ENGELAND CG, MISRA DP, GIURGESCU C (2022) Psychosocial and behavioral factors affecting inflammation among pregnant African American women. *Brain Behav Immun Health*, 22: 100452.

SEDAGHAT Z, KADKHODAEE M, SEIFI B, SALEHI E (2019) Inducible and endothelial nitric oxide synthase distribution and expression with hind limb per-conditioning of the rat kidney. *Arch Med Sci*, 15: 1081.

SHAIK-DASTHAGIRISAHEB YB, VARVARA G, MURMURA G, SAGGINI A, POTALIVO G, CARAFFA A, ANTINOLFI P, TETÈ S, TRIPODI D, CONTI F, CIANCHETTI E, TONIATO E, ROSATI M, CONTI P, SPERANZA L, PANTALONE A, SAGGINI R, THEOHARIDES TC, PANDOLFI F (2013) Vascular endothelial growth factor (VEGF), mast cells and inflammation. *Int J Immunopathol Pharmacol*, 26: 327-335.

SHIBUYA M (2011) Vascular endothelial growth factor (VEGF) and its receptor (VEGFR) signaling in angiogenesis: a crucial target for anti- and pro-angiogenic therapies. *Genes Cancer*, 2: 1097-1105.

STEVENS M, NEAL CR, SALMON AHJ, BATES DO, HARPER SJ, OLTEAN S (2017) VEGF-A165b protects against proteinuria in a mouse model with progressive depletion of all endogenous VEGF-A splice isoforms from the kidney. *J Physiol*, 595: 6281-6298.

STORKEBAUM E, LAMBRECHTS D, DEWERCHIN M, MORENO-MURCIANO MP, APPELMANS S, OH H, VAN DAMME P, RUTTEN B, MAN WY, DE MOL M, WYNS S, MANKA D, VERMEULEN K, VAN DEN BOSCH L, MERTENS N, SCHMITZ C, ROBBERECHT W, CONWAY EM, COLLEN D, MOONS L, CARMELIET P (2005) Treatment of motoneuron degeneration by intracerebroventricular delivery of VEGF in a rat model of ALS. *Nat Neurosci.*, 8(1): 85-92.

TAYLOR WD, AIZENSTEIN HJ, ALEXOPOULOS GS (2013) The vascular depression hypothesis: mechanisms linking vascular disease with depression. *Mol Psychiatry*, 18(9): 963-974.

TILG H, MOSCHEN AR (2010) Evolution of inflammation in nonalcoholic fatty liver disease: The multiple parallel hits hypothesis. *Hepatology*, 52: 1836-1846.

WANG X, FANG C, LIU X, WEI W, ZHANG M, CHEN S, SHI F (2021) High serum levels of inos and mip-1α are associated with post-stroke depression. *Neuropsychiatr Dis Treat*, 17: 2481-2487.

XIE T, STATHOPOULOU MG, DE ANDRÉS F, SIEST G, MURRAY H, MARTIN M, COBALEDA J, DELGADO A, LAMONT J, PEÑAS-LIEDÓ E, LLERENA A, VISVIKIS-SIEST S (2017) VEGF-related polymorphisms identified by GWAS and risk for major depression. *Transl Psychiatry*, 7(3): e1055.

XU J, XIAO N, ZHOU D, XIE L (2023) Disease tolerance: a protective mechanism of lung infections. *Front Cell Infect Microbiol*, 13: 1-11.

YAYLAK F, CANBAZ H, CAGLIKULEKCI M, DIRLIK M, TAMER L, OGETMAN Z, POLAT Y, KANIK A, AYDIN S (2008) Liver tissue inducible nitric oxide synthase (iNOS) expression and lipid peroxidation in experimental hepatic ischemia reperfusion injury stimulated with lipopolysaccharide: the role of aminoguanidine. *J Surg Res*, 148: 214-223.

YUAN JX, MUNSON JM (2017) Quantitative immunohistochemistry of the cellular microenvironment in patient glioblastoma resections. *J Vis Exp*, 125: 56025.

Zhang H, Park Y, Wu J, Chen XP, Lee S, Yang J, Dellsperger KC, Zhang C (2009) Role of TNF-α in vascular dysfunction. *Clin Sci*, 116: 219-230.

ORIGINAL ARTICLE Eur J Anat, 28 (5): 591-600 (2024)

Cadmium implication in massive hepatocellular necrosis and hepatic amyloidosis and the protective role of ivermectin and *Allium cepa* in adult Wistar rats (*Rattus Novergicus*)

Dare J. Babatunde[1], Babawale O. Damilola[1], Alabi P. Adegoke[2], A. Adebiyi[1], Obembe O. Olawale[3], Ebele Cinderela[4], John O. Fatoki[5]

[1]*Department of Anatomy, Osun State University, Osogbo, Nigeria*
[2]*Department of Microbiology, Osun State University, Osogbo, Nigeria*
[3]*Department of Physiology Osun State University, Osogbo, Nigeria*
[4]*Department of Medical Laboratory Science, Osun University, Osogbo, Nigeria*
[5]*Department of Biochemistry, Osun State University Osogbo, Nigeria*

SUMMARY

The liver remains the target organ for the accumulation of cadmium toxicity, mediated by the upregulation of reactive oxygen species. *Allium cepa* constitutes a potential source of natural antioxidants, while Ivermectin has been identified to treat a range of diseases, having antimicrobial, antiviral, and anti-cancer properties. Therefore, this study investigated the protective effects of Ivermectin and *Allium cepa* on cadmium-induced liver damage in adult Wistar rats. Twenty-eight (28) adult female Wistar rats were randomly divided into six (6) groups. Group A, control received distilled water; Group B, treated with 1.2 mg/kg b.w of Ivermectin; Group C, treated with 1.2 mg/kg b.w of Ivermectin and 2 mg/kg b.w Cadmium respectively; Group D, treated with 2 mg/kg b.w cadmium; Group E, treated with 2 mg/kg b.w Cadmium and 1.5 ml *Allium cepa* respectively; and Group F, treated with 1.5 ml *Allium cepa*. Single dose administration of cadmium was done intraperitoneally, while administration of Ivermectin and *Allium cepa* were given orogastrically for four (4) weeks. Animals were sacrificed twenty-four (24) hours after the last administration, and the right lobe of liver was excised following the abdominal incision, and then fixed in Bouin's fluid for histological observation, while the left lobe of the liver was homogenated in 5% sucrose solution for biochemical assay using LDH, MDA, SOD and Catalase enzyme activity.

Cadmium administration caused elevation of MDA enzyme activity, promoting cell membrane lipid peroxidation following cellular non-traumat-

---

Corresponding author:
Dare, Babatunde Joseph. Osun State University, College of Health Sciences, Anatomy Department. Phone: +2348077805474. E-mail: babatunde.dare@uniosun.edu.ng

Submitted: February 7, 2024. **Accepted:** May 1, 2024

https://doi.org/10.52083/ZZNX4761

ic injury, similarly significantly increased LDH and Catalase activity, while it reduced the SOD enzyme activity. Histopathological changes associated with cadmium showed vacuolar and granular degenerations in hepatocytes, heterochromatic nucleuses and sinusoidal, hepatic deposits of amyloidal plaques. However, Ivermectin and *Allium cepa* treatment maintained the biochemical parameter integrity and the histological features relative to the control animals. Administration of *Allium cepa* and Ivermectin preserved liver histoarchitecture and maintained biochemical integrity of antioxidants and carbohydrate metabolic enzyme. More importantly, the antioxidant properties of the *Allium cepa* and the therapeutic action of Ivermectin had proved efficient against cadmium-induced liver damage in adult Wistar rats.

Keywords: *Allum Cepa* – Cadmium – Ivermectin – Liver – Oxidative stress – Wistar rats

INTRODUCTION

Ivermectin (22, 23-dihydroavermectin B), a semi-synthetic macrocyclic lactone, is a macrolide antibiotic produced from streptomyces avermitilis. Ivermectin is an acaricide that belongs to the avermectin family (Al-Jassimet al., 2015). Ivermectin is a class of chemicals that have a novel mode of action against all gastrointestinal and lung nematodes, arthropods, and certain ectoparasites of various animal species (Roberson et al., 1988; Abdeltawab et al., 2020). Ivermectin has marked neural effects on some liver function parameters at therapeutic or toxic dose of Ivermectin in animals (Button et al., 1988; Behera et al., 2011). Ivermectin radically lowered the incidence of river blindness and lymphatic filariasis. Ivermectin has rapid oral absorption, high liposolubility, and is widely distributed in the body, metabolized in the liver and excreted almost exclusively in feces (Rizzo, 2020). Ivermectin has been reported to exert a compartmentalized immunomodulatory effect, and to prevent clinical deterioration as well as olfactory deficit in infected animals. Zhang et al. (2008) and Park et al. (2020) explained the anti-inflammatory action of Ivermectin through the inhibition of cytokine production by macrophages, blockade of activation of NF-kB, the stress-activated MAP kinases JNK and p38, and inhibition of TLR4 signaling.

Onion (*Allium cepa* L.) has been valued as a food and a medicinal plant since ancient times (Agnieszka, 2017). *Allium cepa* is a pool of free amino acids, and has the highest level of flavonoids such as quercetin, present in dry skin (Albishiet al., 2013). *Allium cepa* contains sallylsulfides and flavonoids including quercetin which exert antioxidant activities and reduce hepatocytes apoptosis. Also, *Allium cepa* contains steroid saponins, sapogenins, and b-chlorogeni. The other constituents of *Allium cepa* are organosulfur compounds, including diallyl disulphide (DADS), ajoene, and sallylmercaptocysteine (SAMC), a very potent cell cycle arrest effect in cancer cells (Upadhyay, 2017). *Allium cepa* contains high levels of phenolic compounds, mainly flavonoids, which have antioxidant properties, besides other pharmacological effects such as antibiotic, antidiabetic, anti-atherogenic, and anticancer activities (Benkeblia, 2005; Hedges and Lister, 2007).

Flavones, flavanones, flavonols, isoflavones, flavanonols, chalcones, and anthocyanins, which are subclasses of flavonoids and flavonols, are the most abundant flavonoids in *Allium cepa*. Several studies reported the antioxidant activities of *Allium cepa* and its constituents as potential sources of natural antioxidants (Roldan et al., 2008; Oliveira et al., 2015; De Ancos et al., 2015).

Liu et al. (2001) reported that cadmium can be found in the atmosphere, water, and food at trace amount, and can cause serious health problems, including a probable death. Sources of cadmium exposure include: fossil fuels, iron and steel production, cement nonferrous metals production, waste incineration, smoking, and fertilizers (Roseet al., 2005). Cadmium in small amount absorbed in the kidney cause proteinuria; it is also absorbed and distributed in other organs and tissues such as the liver, spleen, pancreas, heart and testis. Cadmium exerts its toxic effects via oxidative damage to cellular organelles by inducing the generation of ROS. Reactions of these ROS with cellular biomolecules have been shown to lead to lipid peroxidation, membrane protein damage, altered antioxidant system, DNA damage, altered gene expression, and apoptosis (Slimestad et al., 2007). The liver is the most important target organ when considering cadmium-induced toxicity, because cadmium (Cd) primarily accumulates in the liver. Lipid peroxidation is considered to be the primary mechanism for Cd-induced toxicity, as it is involved in the generation of free radicals (Griffithes et al., 2002).

The histopathological changes of the liver treated with Cd are associated with the formation of highly reactive radicals and subsequent lipid peroxidation (Naseriet al., 2008). The accumulated hydroperoxidase caused hepatoxicity, which is associated with the peroxidation of membrane phospholipids by lipid hydroperoxidase, the basis of hepatocellular damage (Renugadevi, 2010). Therefore, this study aimed at investigating the protective role of Ivermectin and *Allium cepa* on Cd-induced liver damage in adult Wistar rats.

MATERIALS AND METHODS

Experimental animals and care

Twenty-eight (28) adult Wistar rats weighing between 143.79 and 188.29 g were used in this study. All animals were obtained and maintained under constant room temperature and humidity (50%), with natural light and dark cycle in the animal facility. The procedures used in this study were approved by the Health Research Institute Ethics Committee (HREC), Osun State University, Nigeria. All animals were given free access to feeding, and water was provided *ad libitum*. The animals were acclimatized two weeks before the start of the experiments.

Ethical approval

All experimental procedures were performed in accordance with the regulations stipulated by the Health Research Ethics Committee, College of Health Sciences, Osun State University, Osogbo Nigeria, in line with the guidelines of the National Institute of Health guide for the care and use of laboratory animals. The study was conducted in the animal holding unit of the Osun State University, Nigeria.

Experimental design

Twenty-eight adult female Wistar rats were randomly divided into six groups. Group A, control group, received distilled water; Group B, treated with 1.2 mg/kg b.w of Ivermectin; Group C, induced with a single dose of 2 mg/kg b.w of Cadmium and treated with 1.2 mg/kg bw of Ivermectin; Group D, treated with single dose of 2 mg/kg b.w Cadmium; Group E, induced with single dose of 2 mg/kg b.w Cadmium and treated with 1.5 ml of *Allium cepa*; and Group F, treated with 1.5 ml *Allium cepa* only. A single dose of Cadmium was given intraperitoneally, while administration of Ivermectin and *Allium cepa* were done orogastrically on a daily basis for the period of four weeks. Animals were monitored daily for water and food intake.

Animal sacrifice and sample collection

Twenty-four hours after the administration of the last respective doses, animals were euthanized by cervical dislocation; the liver was excised following abdominal incision, and the left lobe of the liver homogenized in 5% sucrose solution at 15,000 rpm and stored in the refrigerator at -80°C. The right lobe of the liver was fixed in Bouin's fluid for histological assessment.

Histological analysis

The liver was carefully excised, cut in slabs of 0.5 cm thick, fixed in Bouin's fluid, and processed routinely for paraffin embedding. Five µm sections were obtained with a rotatory microtome and processed for Heamatoxylin and Eosin (H/E), Masson Trichrome, Toluidine blue and Feulgen stains. Sections were observed with a light microscope and photomicrographs were taken for further analysis (Dare et al., 2021).

Enzyme biochemistry

The homogenized liver tissues were utilized for Malondialdehyde (MDA), Superoxide dismutase (SOD), Lactate dehydrogenase (LDH), and Catalase (CAT) assays. The oxidative stress and bioenergetics markers were assessed by an enzyme-linked immunosorbent assay kit (IBL-America, Minneapolis, Minnesota, USA). Excised liver tissues were put in Lao style mortar containing 1 ml of 0.25 Mn (5%) sucrose solutions and were homogenized thoroughly. Tissue homogenate was collected in a 5 ml plain serum bottle for enzyme assay; superoxide dismutase, Malondialdehyde, Catalase, and Lactate Dehydrogenase. Malondialdehyde levels in tissues were measured according to the protocol outlined by Stock and Dormandy (1971) and activity of LDH in the homogenate. The homogenates were centrifuged at 10,000g for 10 minutes at 4°C. The clear supernatant obtained was used for the measurement of LDH activity. Superoxide dismutase activities in homogenates were determined using the method of Misra and Fridovich, as described by Nna et al. (2017).

Statistical analysis

Data collected were analyzed using a one-way analysis of variance (ANOVA), followed by Tukey's (HSD) multiple comparison test with the aid of graph-pad prism version 6 (GraphPad Software, Inc., La Jolla, CA, USA). Data were presented as means ± SEM (standard error of the mean). $p<0.05$ was considered statistically significant.

RESULTS

Table 1 revealed significantly increased MDA enzyme activity in the cadmium-treated animals, while treatment with Ivermectin showed significant decrease in the MDA activity relative to the control and the animals induced with cadmium toxicity. However, animals induced with cadmium toxicity and liver damage treated with Ivermectin, group D, and also those treated with *Allium cepa*, group E, showed reduced lipid peroxidation in the cell membrane, as indicated by the reduced activities of the MDA. More importantly, treatment with *Allium cepa* only, as shown in group F, revealed significant reduction in the level of lipid peroxidation. Carbohydrate enzyme activity measured by LDH enzyme activity revealed elevated levels among the animals induced with cadmium toxicity, group D; this enzyme concentration was lowered in the animals treated with Ivermectin only, group B, and those that were given *Allium cepa* only, group F, as shown Table 1. Significant reduction in the concentration of LDH enzyme was observed in the cadmium-induced liver damage that were treated with Ivermectin and *Allium cepa*, groups C and E respectively in relation to the control animals.

Oxidative enzyme markers using SOD and Catalase activities showed increased SOD activities and reduced catalase activities in the liver tissue of the animals induced with cadmium damage. However, reduced SOD activities and increased catalase activities were observed in animals treated with Ivermectin only, group B. A similar trend was observed in the animals treated with *Allium cepa* only, group F. More importantly, co-treatment of cadmium and Ivermectin, group C, as well as co-treatment of cadmium with *Allium cepa* followed a similar trend of observations as seen in Table 1, i.e., SOD activities lowered while the catalase activities increased relative to the control animals.

Table 1. Showing activities of Malondialdehyde (MDA), Superoxide dismutase (SOD), Lactate dehydrogenase (LDH), and Catalase enzymes in the liver.

GROUP	MDA	LDH	SOD	Catalase
	(µg/m)	(u/l)	(u/mg)	(µmol/l)
GROUP A	5.63±4.58	3.63±2.18	1.61±1.36	5.38±3.81
GROUP B	2.58±1.60*	1.28±0.98*	1.61±1.43	8.96±5.16*
GROUP C	7.10±6.76	2.08±1.84	1.043±1.39	5.16±8.95
GROUP D	9.53±5.38*	9.44±8.09*	2.53±1.38	1.95±0.95
GROUP E	7.76±7.218	3.24±2.80	2.38±0.86	3.79±2.55
GROUP F	5.17±4.88*	2.48±1.44	0.92±0.83	6.97±5.24

P<0.05 level of significance, *shows significant result

Figure 1 reveals that administration of Ivermectin and *Allium cepa* maintained the histological architecture of the liver in line with the histological observations in the control liver (Fig. 1B). The hepatic plates were well arranged, along the sinusoid. However, administration of cadmium caused alterations in the hepatic arrangement, massive hepatocellular necrosis, necrosis of peri-acinar hepatocytes, dilated blood sinusoids, hemorrhage in sinusoids, and hepatic amyloidosis (Fig. 1D). The Ivermectin group showed normal architecture with hepatic parenchymal cells radiating from the central vein, and normal sinusoidal space, absence of hepatic amyloidal deposit and the peri-acinar hepatocytes exhibited normal histological appearances as shown in Fig. 1C. Ivermectin-treated rat liver showed hepatic architecture with central vein and surrounding hepatocytes, sinusoids, and no traces of foci of hepatic cell necrosis. Cadmium-treated animals showed the central vein, altered hepatocyte morphology with loss of hepatic parenchyma and connective tissue infiltration (Fig.1D). Group E showed liver tissue with irregular hepatocytes, sinusoid space dilatation, and congested central vein (Fig. 1E). *Allium cepa* treatment in group F maintained histological integrity of the hepatocytes arrangement, hepatic sinusoid and the regeneration of the hepatocytes plates.

Figure 2A reveals, in the control group A, normal cellular architecture, moderate expression collagen deposit in the liver tissue. However, administration of cadmium in Group D showed vacuolated hepatocytes with the central vein congested and dilated with the deposit of collagen connective tissue fibers (Fig. 2D). It was observed in the cadmium-induced and liver damage treated with Ivermectin, group C, as well as those treated with *Allium cepa*, group E, mild hydropic degeneration and dilatation of the hepatic plate arrangement, collagen fibers deposit around sinusoids, while the integrity of hepatocytes was maintained (Figs. 2C and 2E). Ivermectin and *Allium cepa*treatment showed apparently scanty collagen fibers deposit along the hepatic plate arrangement.

Figure 3 reveals that animals treated with Ivermectin only, group B, as well as those treated with *Allium cepa* only, group F, showed slightly stained granules mast cells/mucins (Figs. 3B and 3F),

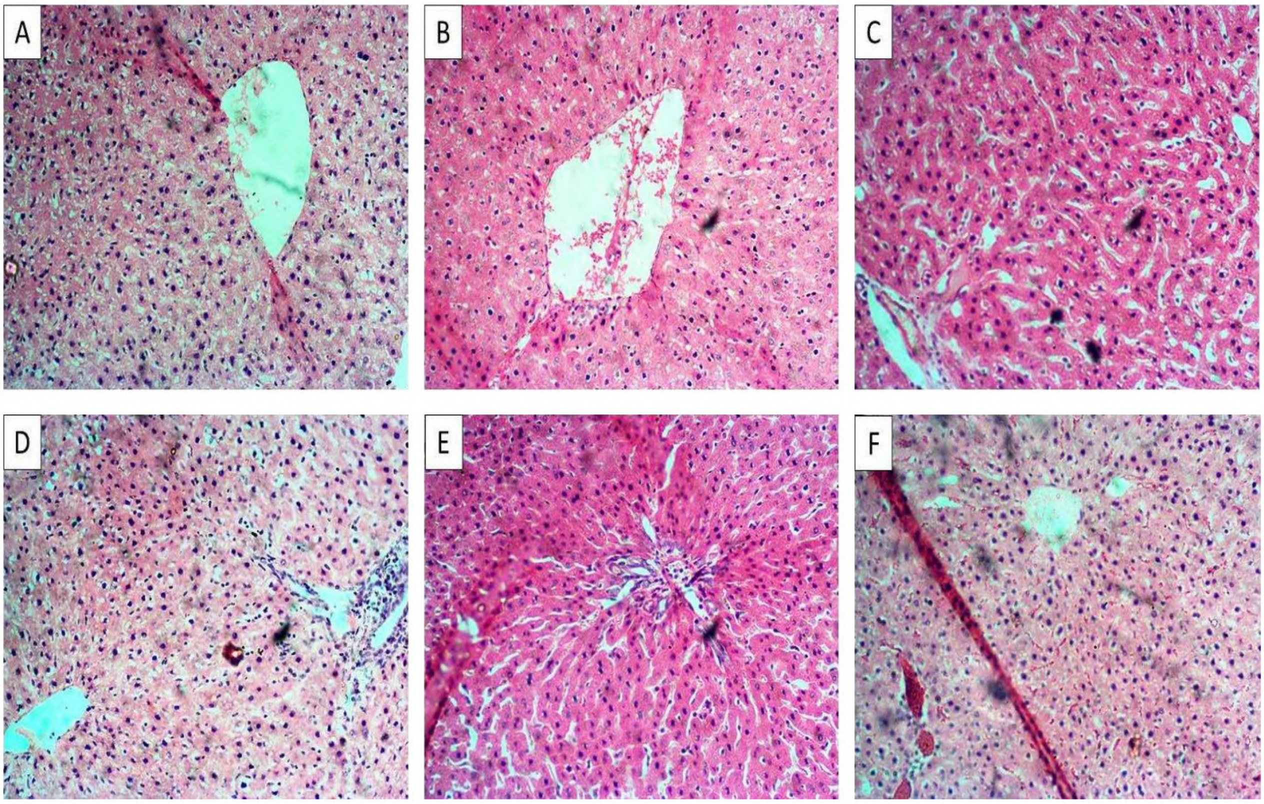

Fig. 1.- Sections of the liver in adult Wistar rats. H/E stain (x100). **A** = Control; **B** = Ivermectin only; **C** = Ivermectin + Cadmium; **D** = Cadmium only; **E** = Allium cepa + Cadmium; **F** = Allium cepa treatment. **CV** = Central Vein. **S** = Sinusoids.

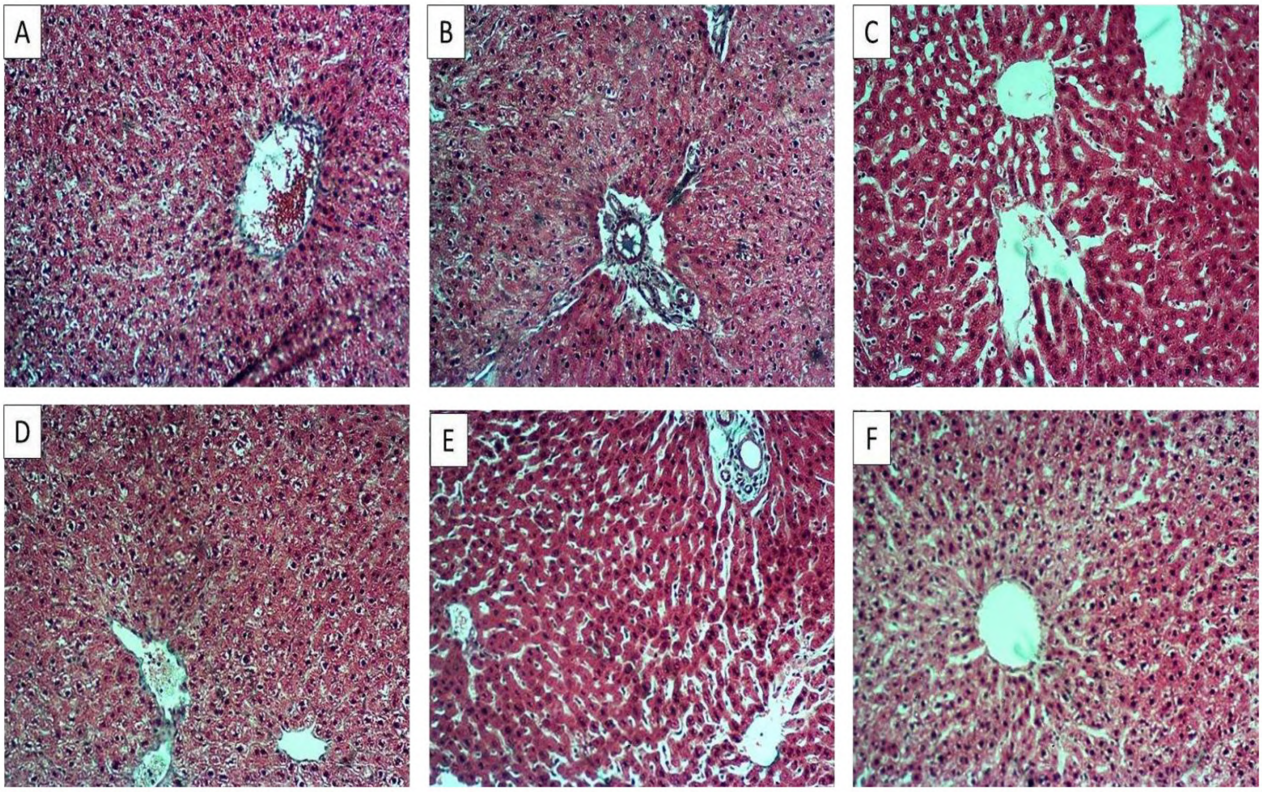

Fig. 2.- Sections of the liver in adult Wistar rats. Masson Trichrome stain (x100). **A** = Control; **B** = Ivermectin only; **C** = Ivermectin + Cadmium; **D** = Cadmium only; **E** = Allium cepa + Cadmium; **F** = Allium cepa treatment. **CV**= Central Vein. **S** = Sinusoids.

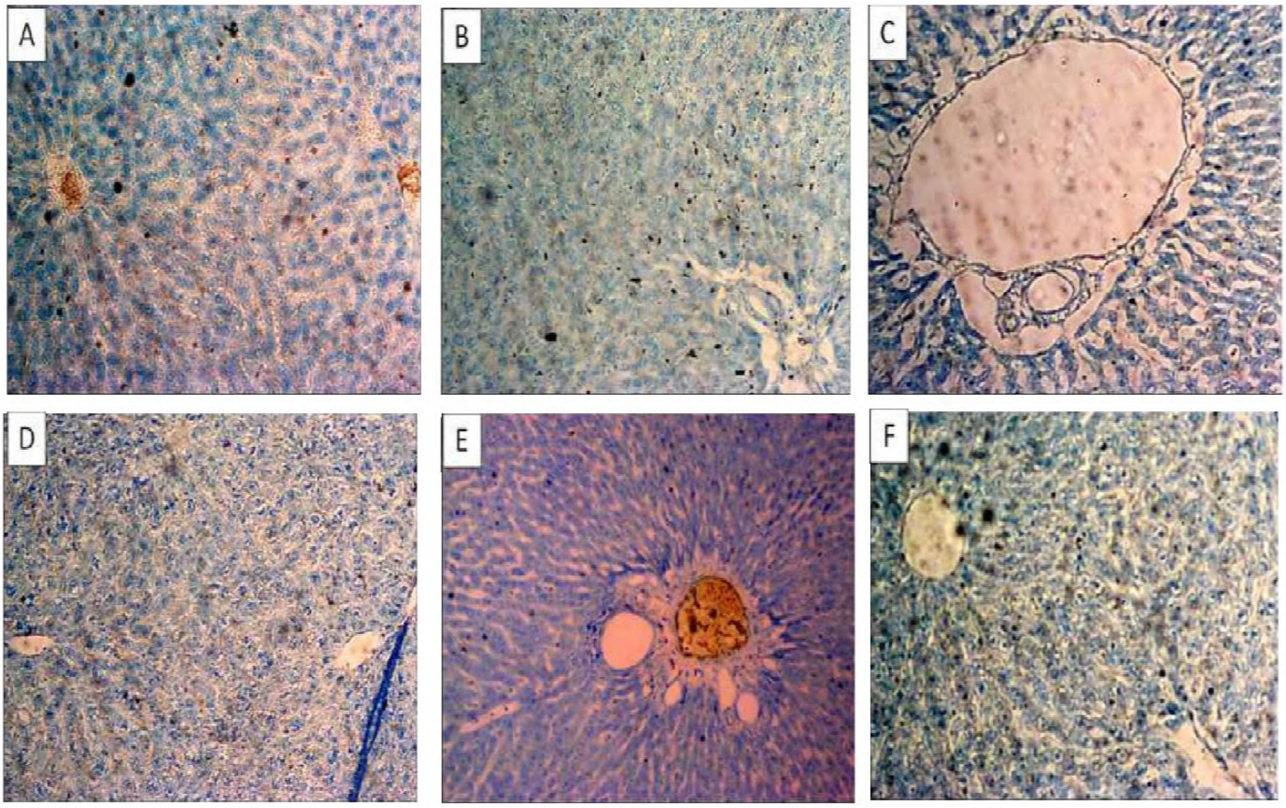

Fig. 3.- Sections of the liver in adult Wistar rats. Toluidine blue (x100). **A** = Control; **B** = Ivermectin only; **C** = Ivermectin + Cadmium; **D** = Cadmium only; **E** = Allium cepa + Cadmium; F = Allium cepa treatment. **CV** = Central Vein. **S** = Sinusoids.

compared to the animals that were induced with the cadmium toxicity liver damage, group D. Mast cells infiltration was observed as well as the mucin deposit (Fig. 3D) among the animals treated with cadmium toxicity. In group D, more deposit of mast cells and mucin associated with enlarged vacuole was observed, massive fatty changes, cellular necrosis, vacuolization and ballooning degeneration. Similar trend of observation in group E, mast cells infiltration in liver tissue in animals treated with Allum Cepa and Cadmium (Fig. 3E).

Figure 4 shows normal hepatoctye architecture, moderate expression of DNA materials following cadmium-induced liver damage treated with Ivermectin, group C, as well as *Allium cepa*, group E, respectively (Figs. 4C and 4E). The control animals showed similar histological features with the animals treated with Invermectin and *Allium cepa*respectively, i.e., normal expression of DNA in the nuclei of hepatocytes and normal histological structure of hepatic lobules and central veins (Figs. 4A and 4B). Cadmium.treated rats indicate fibrosis in hepatocytes when compared to the control group, deeply expressed DNA nuclei materials along the hepatic plates and the sinusoids, indicating non-traumatic injury to the liver hepatocytes (Fig. 4D).

DISCUSSION

Cadmium toxicity had been reported by Dare et al. (2021) on the testes of adult Wistar rats, while Arroyo et al. (2012), reported cadmium damage on the soft tissues. In this study, the activities of antioxidant enzymes (SOD and Catalase) were examined following induced liver damage by cadmium administration. The activity of SOD was reduced, but was, however, associated with the elevated level of catalase among the animals treated with cadmium only. Weydert and Cullen (2010) had noticed that SOD convert superoxide radicals into hydrogen peroxide and molecular oxygen, while catalase and peroxidase convert hydrogen peroxide into water. SOD has been found to be decreased in cell injuries and the cell undergoing trauma. These findings established the bottom line action of cadmium administration effect on the SOD and catalase activities promoting non-traumatic cell injuries to the liver tissue. However, administra-

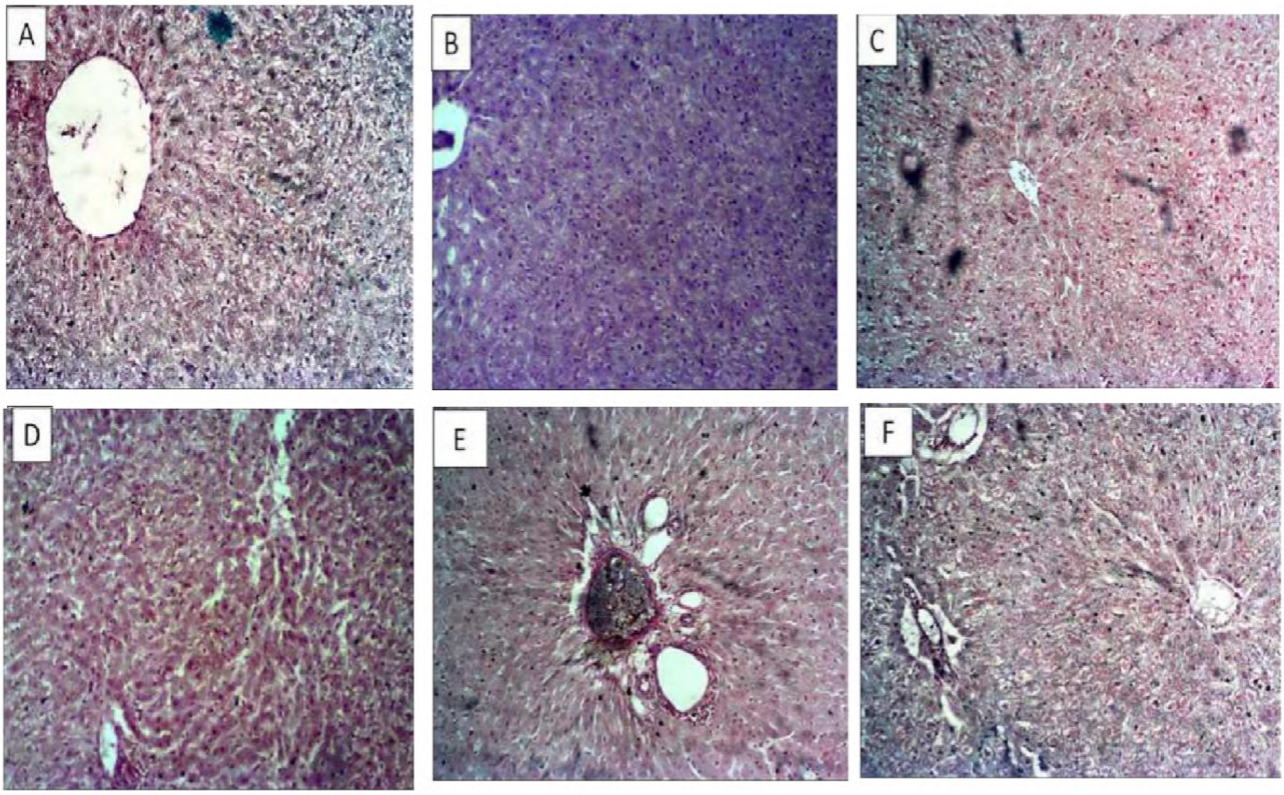

Fig. 4.- Sections of the liver in adult Wistar rats. Feulgen stain (x100). **A** = Control; **B** = Ivermectin only; **C** = Ivermectin + Cadmium; **D** = Cadmium only; **E** = Allium cepa + Cadmium; **F** = Allium cepa treatment. **CV** = Central Vein. **S** = Sinusoids.

tion of *Allium cepa* and Ivermectin proved more efficient in maintaining cell integrity.

Enzyme of carbohydrate metabolism, LDH, elevated in the cadmium-induced liver damage, while significantly reduced in Ivermectin- and *Allium-cepa*-treated group. Lactate dehydrogenase is present in almost all body tissues; however, increase in LDH activities in liver disease has been shown. Farhana and Lappin (2023) showed that LDH could be used as a useful biomarker for assessing metastatic melanoma and malignancy. Jurisic et al. (2015) equally explained that tumor cell growth utilized LDH-mediated energy production to fulfill the demand for fast cellular growth. Therefore, elevated LDH remained an established marker of metastases, especially in the liver, as equally revealed in the works of Mishra et al. (2019), Liu et al. (2018), and Gallo et al. (2015). Lipid peroxidation level was estimated by the activities of MDA in the liver tissue, as shown in Table 1; cadmium-induced liver damage caused an increase in lipid peroxidation, as shown by the increase in the activities of MDA. However, administration of *Allium cepa* and Ivermectin significantly reduced the activities of MDA.

Ayala et al. (2014) emphasized that the survival and maintenance of the cells largely depend on the antioxidant defense systems that upregulate antioxidant proteins in an adaptive stress response. Therefore, any substances that would promote cell defense antioxidant system would maintain the cells' integrity; this is obvious in the results obtained from this study. Liver tissue integrity was maintained by the administration of *Allium cepa* and Ivermectin against the liver damage induced by the administration of cadmium. High levels of free radicals or reactive oxygen species (ROS) can inflict direct damage to lipids leading to lipid peroxidation in the tissue, particularly in the liver tissue as equally explained by Cohen et al. (2013) and Hedges et al. (2006). It was noted in this study, in line with the relevant studies, that cadmium-induced hepatotoxicity was mediated by oxidative stress and cellular inflammation. However, *Allium cepa* and Ivermectin showed that hepatic tissue displayed a low level of MDA and high activities of SOD and catalase. This indicated that the positive influence of *Allium cepa* on liver function biomarkers was mediated by a low MDA/antioxidant enzyme ratio. The beneficial effects of *Allium cepa* on arsenic-acid-induced- and cadmium-induced hepatic damage in rats and humans have been reported by Valko et al. (2006), While Griffiths et al. (2002) confirmed the non-toxic effect of *Allium cepa*,Liu et al. (2001) studied biochemical effects of cadmium using different animal models. Cadmium toxicity had been reported in increased serum ALT and AST observed in rats exposed to cadmium.

The administration of cadmium in this study caused alteration in the hepatic histoarchitecture, derangement in the hepatocytes plates, and increased vacuolation. However, Ivermectin is widely used for protection against a wide spectrum of parasitic diseases. Several studies have shown that Ivermectin has a strong insecticidal effect that could be explored as a potential tool against malaria transmission (Chacour et al., 2015; Ashang, 2009). In this study, co- administration of Ivermectin and cadmium presented minimal histological alteration in the enzymes of antioxidants, and maintained the histological integrity of the liver relative to control animals. *Allium cepa* mitigates aluminum-chloride-induced hepatotoxicity in male Wistar rats as demonstrated by Slimestad et al. (2007). This was coherent with the observation recorded in this study. Many studies inhibit liver damage in cadmium, and improved the activities of the enzymes of antioxidants in line with Slimestad et al. (2007).

Results from this study showed improved histological appearances of the liver in animals treated with *Allium cepa* and Ivermectin respectively. Koyu et al. (2006) noticed histopathologic changes, such as vacuolar and granular degenerations in hepatocytes, heterochromatic nucleuses, and sinusoidal and portal widening in cadmium-treated animals; in this study, among the animals treated with cadmium only, liver damage was similarly expressed: hydropic degeneration and dilatation of the hepatic plate arrangement, collagen fibers deposit around sinusoids as seen in Figs. 1 and 2. However, the hepatocytes integrity was maintained. Ivermectin and *Allium cepa* treatment showed scanty collagen fibers deposit along the hepatic plate arrangement.

This study revealed mast cell infiltration and mucin deposit in cadmium damage to the liver tissue; more deposits of mast cells and mucin associated with enlarged vacuole were observed, massive fatty changes, cellular necrosis, vacuolization and ballooning degeneration, as seen in Fig 3. A similar trend of observation in the work of Gattea et al. (2021), chronic exposure to cadmium in mice caused liver and kidney damage. Yu et al. (2021) showed DNA damage in the liver tissue treated with cadmium. This agreed with the similar trend of observations in this study: cadmium treated rats indicate fibrosis in hepatocytes when compared to the control group, deeply expressed DNA nuclei materials along the hepatic plates and the sinusoids, indicating non-traumatic injury to the liver hepatocytes.

However, normal hepatocyte architecture, and moderate expression of DNA materials were expressed in animals treated with Ivermectin, as well as with *Allium cepa* (Fig. 4). The control animals showed similar histological features with the animals treated with Ivermectin and *Allium cepa* respectively: normal expression of DNA in nuclei of hepatocytes and normal histological structure of hepatic lobules and central veins. Poli et al. (2022) had earlier justified the use of antioxidants in ameliorating cadmium toxicity: this could align to the antioxidant content present in *Allium cepa* and Ivermectin in maintaining the histological integrity of the liver tissue against cadmium-induced liver damage in adult Wistar rats.

In conclusion, the result of the study showed that *Allium cepa* mitigated cadmium-induced hepatotoxicity through regulation of hepatic oxidant/antioxidant system. The results of the present study clearly indicate that heavy metal cadmium causes oxidative stress in adult Wistar rats and concluded that Ivermectin poses antioxidant properties, attributed to its protective action on lipid peroxidation and to the enhancing effects of cellular antioxidant defenses, which might be further implicated in its protective role against the damage due to cadmium toxicity in rats. The use of Ivermectin and *Allium cepa* to counter oxidative damage serves as a therapeutic approach to restore normal body function. The current results also contribute towards improving our knowledge on the possible development of oxidative stress induced by cadmium treatment in rats indicating a possible role of antioxidant system.

REFERENCES

ABDELTAWAB MSA, RIFAIE SA, SHOEIB EY, EL-LATIF HAA, BADAWI M, SALAMA WH, EL-AAL AAA (2020) Insights into the impact of Ivermectin on some protein aspects linked to Culex pipiens digestion and immunity. *Parasitol Res*, 119(1): 55-62.

AGNIESZKA S, ROBERT P, DEL VL, SILVANO S, GIANLUCA C (2017) Interactions among genotype, environment and agronomic practices on production and quality of storage onion (Allium cepa L.)–A review. *J Hortic Sci Biotech*, 44: 21-42.

KOYU A, GOKCIMEN A, OZGUNER F, BAYRAM DS, KOCAK A (2006) Evaluation of the effects of cadmium on rat liver. *Mol Cell Biochem*, 284(1-2): 81-85.

FARHANA A, LAPPIN SL (2023) Biochemistry, Lactate dehydrogenase. In: StatPearls [Internet]. Treasure Island (FL): StatPearls Publishing.

ALBISHI T, JOHN JA, AL-KHALIFA AS, SHAHIDI F (2013) Antioxidant, anti-inflammatory and DNA scission inhibitory activities of phenolic compounds in selected onion and potato varieties. *J Funct Foods*, 5(2): 590-600.

AL-JASSIM AB, JAWAD HA, AL-ASOUDI E, JEEDKHADIM S (2015) Biochemical and histological alterations in the liver due to repeated administration of Ivermectin alone or with combination of vitamin c in local female rabbits. *J Int Acad Res Multidisciplinary*, 3: 349-364.

ARROYO VS, FLORES KM, ORTIZ LB, GOMEZ-QUIROZ LE, GUTIERREZ-RUIZ MC (2012) Liver and cadmium toxicity. *J Drug MetabToxicol*, S5: 1-7.

ASHANG BU (2009) Effect of therapeutic and toxic doses of Ivermectin (Mectizan) on total serum proteins and hepatic enzymes of Wistar albino rats”. *Int J Biol Chem*, 3: 142-147.

BENKEBLIA N (2005) Free-radical scavenging capacity and antioxidant properties of some selected onions (Allium cepa L.) and garlic (Allium sativum L.) extracts. *Braz Arch Biol Technol*, 48(5): 753-759.

BUTTON C, BARTON R, HONEY P (1988) Avermectin toxicity in calves and an elevation in picrotoxin as an antidote. *Aust Vet J*, 65: 157-158.

YU C, YANG C, SONG X, LI J, PENG H, QIU M, YANG L, DU H, JIANG X, LIU Y (2021) Long non-coding RNA expression profile in broiler liver with cadmium-induced oxidative damage. *Biol Trace Elem Res*, 199(8): 3053-3061.

CHOUDARY AK, DEVI RS (2014) Serum biochemical responses under oxidative stress of aspartame in Wistar albino rats. *Asian Pac J Trop Dis*, 4: S403-410.

COHEN G, RIAHI Y, SUNDA V, DEPLANO S, CHATGILIALOGLU C, FERRERI C, KAISER N, SASSON S (2013) Signaling properties of 4-hydroxyalkenals formed by lipid peroxidation in diabetes. *Free Radical Biol Med*, 65: 978-987.

DARE BJ, OLANIYAN OT, OYENIYI OI, OKOTIE GE, LAWAL IA, EWEOYA O (2021) Aqueous extract of *Adansonia digitata* prevents cadmium chloride-induced testicular damage in Wistar rats. *J Basic Clin Physiol Pharmacol*, 33(3): 347-353.

DE ANCOS B, COLINA-COCA C, GONZALEZ-PENA D, SANCHEZ-MORENO C (2015) Bioactive compounds from vegetable and fruit by-products. In: Gupta VK, Tuohy MG (Eds). *Biotechnology of Bioactive Compounds. Sources and Applications*. Section I. Wiley Blackwell, pp 3-36.

GALLO M, SAPIO L, SPINA A, NAVIGLIO D, CALOGERO A, NAVIGLIO S (2015) Lactic dehydrogenase and cancer: an overview. *Front Biosci (Landmark Ed)*, 20(8): 1234-1249.

GATTEA AL-RIKABI Z, ABBAS AH, KADHUM OUDAH H, SAJER NASSIR H, ALI SA (2021) Histopathological study of liver and kidney tissues in C57 mice via chronic exposure to cadmium and zinc. *Arch Razi Inst*, 76(5): 1501-1508.

GRIFFITHS G, TRUEMAN L, CROWTHER T, THOMAS B, SMITH B (2002) Onions- a global benefit to health. *Phytother Res*, 16(7): 603-615.

HEDGES L, LISTER C (2007) The nutritional attributes of Allium species. Crop and food research confidential report. 1814. New Zealand Institute for Crop & Food Research Limited.

JURISIC V, RADENKOVIC S, KONJEVIC G (2015) The actual role of LDH as tumor marker, biochemical and clinical aspects. *Adv Exp Med Biol,* 867: 115-124.

LIU J, CHEN G, LIU Z, LIU S, CAI Z, YOU P, KE Y, LAI L, HUANG Y, GAO H, ZHAO L, PELICANO H, HUANG P, MCKEEHAN WL, WU CL, WANG C, ZHONG W, WANG F (2018) Aberrant FGFR tyrosine kinase signaling enhances the Warburg effect by reprogramming LDH isoform expression and activity in prostate cancer. *Cancer Res,* 78(16): 4459-4470.

LIU J, SHEN HM, ONG CN (2001) Role of intracellular thio depletion, mitochondrial dysfunction and reactive oxygen species in Salvia mitltiorrhiza-induced apoptosis in human hepatoma HepG2 cells. *Life Sci,* 69(16): 1833-1850.

MISHRA D, BANERJEE D (2019) Lactate dehydrogenases as metabolic links between tumor and stroma in the tumor microenvironment. *Cancer (Basel),* 11(6): 750.

NASERI MKG, YAHYAVI H, ARABIAN M (2008) Antispasmodic activity of onion (Allium cepa L.) peel extract on rat ileum. *Iran J Pharm Res,* 7: 155-159.

OLIVEIRA TT, CAMPOS KM, CERQUEIRA-LIMA AT, CANA BRASIL CARNEIRO T, DA SILVA VELOZO E, RIBEIRO MELO IC, FIGUEIREDO EA, DE JESUS OLIVEIRA E, DE VASCONCELOS DF, PONTES-DE-CARVALHO LC, ALCÂNTARA-NEVES NM, FIGUEIREDO CA (2015) Potential therapeutic effect of Allium cepa L. and quercetin in a murine model of Blomia tropicalis induced asthma. *Daru,* 23(1): 18.

PARK A, IWASAKI A (2020) Type I and type III interferons—induction, signaling, evasion, and application to combat COVID-19. *Cell Host Microbe,* 27: 870-879.

POLI V, MADDURU R, APARNA Y, KANDUKURI V, MOTIREDDY SR (2022) Amelioration of cadmium-induced oxidative damage in Wistar rats by vitamin C, zinc and N-acetylcysteine. *Med Sci (Basel),* 10(1): 7.

RENUGADEVI J, PRABU SM (2010) Cadmium-induced hepatotoxicity in rats and the protective effect of naringenin. *Exp Toxicol Pathol,* 62(2): 128-134.

RIZZO E (2020) Ivermectin, antiviral properties and COVID-19: a possible new mechanism of action. *Naunyn Schmiedebergs Arch Pharm,* 393: 1153-1156.

ROBERSON FL (1988) Antinematodal drugs. In: Booth NH, Mc Donald LE (eds). *Veterinary Pharmacology and Therapeutics,* 3rd Ed. Iowa State University Press, Ames, Iowa, pp 340-345.

ROLDÁN E, SÁNCHEZ-MORENO C, DE ANCOS B, CANO MP (2008) Characterisation of onion (Allium cepa L.) by-products as food ingredients with antioxidant and antibrowning properties. Food Chem, 108: 907-916.

ROSE P, WHITEMAN M, MOORE PK, ZHU YZ (2005) Bioactive S-alk(en)yl cysteine sulfoxide metabolites in the genus Allium: the chemistry of potential therapeutic agents. *Natural Product Rep,* 22(3): 351-368.

SLIMESTAD R, FOSSEN T, VÅGEN IM (2007) Onions: a source of unique dietary flavonoids. *J Agric Food Chem,* 55(25): 10067-10080.

STOCKS J, DORMANDY TL (1971) The autoxidation of human red cell lipids induced by hydrogen peroxide. *Brit J Haematol,* 20: 95-111.

BEHERA SK, DIMRI U, SINGH SK, MOHANTA RK (2011) The curative and antioxidative efficiency of Ivermectin and Ivermectin + vitamin E-selenium treatment on canine Sarcoptes scabiei infestation. *Vet Res Commun,* 35(4): 237-244.

UPADHYAY RK (2017) Nutritional and therapeutic potential of Allium vegetables. *J Nutr Ther,* 6(1): 18-37.

VALKO M, MORRIS H, CRONIN MTD (2005) Metals, toxicity and oxidative stress. *Current Med Chem,* 12(10): 1161-1208.

NNA VU, USMAN UZ, OFUTET EO, OWU DU (2017) Quercetin exerts preventive, ameliorative and prophylactic effects on cadmium chloride - induced oxidative stress in the uterus and ovaries of female Wistar rat. *Food Chem Toxicol,* 102: 143-155.

WEYDERT CJ, CULLEN JJ (2010) Measurement of superoxide dismutase, catalase and glutathione peroxidase in cultured cells and tissue. *Nat Protoc,* 5(1): 51-66.

WICZKOWSKI W, ROMASZKO J, BUCINSKI A, SZAWARA-NOWAK D, HONKE J, ZIELINSKI H, PISKULA MK (2008) Quercetin from shallots (Allium cepa L. var. aggregatum) is more bioavailable than its glucosides. *J Nutr,* 138(5): 885-888.

ZHANG X, SONG Y, CI X, AN N, JU Y, LI H, WANG X, HAN C, CUI J, DENG X (2008) Ivermectin inhibits LPS-induced production of inflammatory cytokines and improves LPS-induced survival in mice. *Inflamm Res,* 57: 524-529.

Morphometric analysis of the frontal horns of the lateral ventricles using normal computed tomographic images

Beryl S. Ominde[1], **Emmanuel C. Ogbolu**[1], **Joyce E. Ikubor**[2], **Orovwoghene F. Omoro**[1], **Patrick S. Igbigbi**[1]

[1] Department of Human Anatomy and Cell Biology, Delta State University, Abraka, Nigeria

[2] Department of Radiology, Delta State University Teaching Hospital, Oghara, Nigeria

SUMMARY

The ventricular system is altered by the normal aging process and various pathological conditions such as Alzheimer's, schizophrenia, hydrocephalus, and tumors. This study aimed at establishing the normal baseline data regarding the dimensions of the frontal horns of the lateral ventricles in adults Nigerians. This retrospective observational study evaluated CT brain images stored in a Radiology unit in Delta State, Nigeria. Ethical clearance was sought from the Hospital's ethics board. Images of 202 patients, aged 18 years and above, were included. Measurements of frontal horn length and width were conducted using a standardized digital caliper approach. The data were analyzed based on gender and age groups, employing statistical methods such as t-tests and Pearson correlation. A p-value of < 0.05 in the inferential statistics was deemed statistically significant. The length of the bilateral frontal horns and distance between their tips were significantly higher in males than in females ($p<0.05$). The left frontal horn length was consistently larger than the right. Both lengths and widths exhibited significant variations across age groups and had a positive correlation with age ($p<0.05$). The study provides standard reference values for clinicians in the study center to consider during neuroimaging and diagnostic assessments. The gender-, age- and side-related findings enhance the understanding of the normal anatomical diversity, which has crucial clinical implications.

Key words: Frontal horn – Length – Width – Diameter – Surgery

INTRODUCTION

The emergence of the cerebral ventricular system can be traced back to the central lumen of the neural tube, marking the embryonic origin of a complex network of interconnected spaces (Agegnehu et al., 2021). This system comprises the lateral ventricle, a spacious region located in each cerebral hemisphere; the third ventricle, a narrow slit-like space situated between the diencephalon; and the fourth ventricle, positioned between the pons and medulla anteriorly and the cerebellum posteriorly (Annongu et al., 2017; Arun et al., 2017; Agegnehu et al., 2021). Filled with cerebrospinal fluid (CSF), the ventricular system is an essential component

---

Corresponding author:
Dr. Beryl S. Ominde. Department of Human Anatomy and Cell biology, Delta State University, P.M.B. 1, Abraka, Nigeria. Phone: +2347085458946. E-mail: berylominde@gmail.com

Submitted: January 11, 2024. **Accepted:** May 1, 2024

https://doi.org/10.52083/BVBF3444

of the brain, contributing to its mechanical protection, buoyancy, and metabolic support (Arun et al., 2017). The lateral ventricles, having a roughly C-shaped configuration, enfold the dorsal portions of the basal ganglia. Comprising the inferior (temporal), frontal, and occipital horns, along with a central body, each lateral ventricle plays a distinct role in the distribution and circulation of CSF (Bijaylakshmi et al., 2014; Arun et al., 2017).

As individuals age, there is a regression of thalamic nuclei, which is associated with the early demonstration of third ventricular enlargement (Blinkouskaya et al., 2021). Age-related changes are also evident in the frontal cortex, brain stem, cerebellum and diencephalon, with the left lateral ventricle exhibiting a larger size than the right (Honnegowda et al., 2017). Ventricular enlargement is a reliable indicator of age-related brain atrophy, which commences by the seventh decade and accelerates with advancing age (Moawia et al., 2015; Arun et al., 2017).

Multiple studies highlight the clinical significance of the changes in the ventricular system. Degenerative conditions such as Alzheimer's, Huntington's and Parkinson's diseases, are characterized by an increase in cerebrospinal fluid (CSF) spaces (Patnaik et al., 2016; Annongu et al., 2017; Olawande et al., 2020; Blinkouskaya et al., 2021). Additionally, psychiatric disorders like bipolar disorders, schizophrenia, and depression, as well as conditions with cognitive decline such as chronic alcoholism, dementia, malignant, and traumatic lesions, have been associated with alterations of the ventricular size (Polat et al., 2019; Agegnehu et al., 2021). The diagnosis, classification, and follow-up of hydrocephalus after ventricular shunting therapy is dependent on morphometric evaluation of the ventricular system (Annongu et al., 2017; Arun et al., 2017). For accurate localization and excision of space occupying lesions such as gliomas, the morphometry of the ventricular system is also important (Agegnehu et al., 2021). It is challenging for clinicians to establish whether the ventricular size is within the normal limits, or enlarged due to aging process or pathological changes. Moreover, subjective analysis can cause misdiagnosis (Annongu et al., 2017; Quarshie et al., 2021).

Advancements in imaging technologies, particularly computerized tomography and magnetic resonance imaging (MRI), have significantly improved our understanding of the normal structural development and organization of the brain (Honnegowda et al., 2017; Sharmin et al., 2020). Computed tomography, being both safe and non-invasive, serves as a valuable tool for evaluating ventricular morphometry, and spatial characteristics of the ventricular system (Farheen and Sukre, 2017; Polat et al., 2019). It remains the most widely used, accessible, cost-effective, and rapid method for imaging the brain.

Establishing normal reference values for specific populations is imperative, providing neuroradiologists, neurosurgeons, and neurologists with essential guidance in the accurate assessment and effective management of conditions associated with alterations in ventricular size, hence improving patient outcomes (Honnegowda et al., 2017). This study aimed at determining the dimensions of the frontal horn of the lateral ventricles using CT images of a selected Nigerian population in Delta State.

MATERIALS AND METHODS

Brain CT images stored in the digital archives (Picture Archiving Communications Systems [PACS]) of a Radiology unit in Delta State, Nigeria, were assessed in this study. These images belonged to patients referred for imaging between May 1, 2015, and May 30, 2020, due to suspected intracranial space-occupying lesions, head injury, pulmonary embolism, or stroke. Institutional approval (DELSUTH/HREC/2023/058/0712) was obtained for the retrospective review of these images. A total of 202 adult patients (109 males and 93 females), aged 18 years and above, were purposively selected for this study. The imaging data were acquired using a 64-slice Toshiba Aquilon CT scanner (Japan, 2009) with the following parameters: 120kV and 300mA.

Exclusion criteria comprised CT images of patients below 18 years, images of poor quality with artifacts or evidence of patient rotation, and images displaying intracranial pathologies such as bleeds, tumors, infarcts, cerebral hydrocephalus, or raised intracranial pressure.

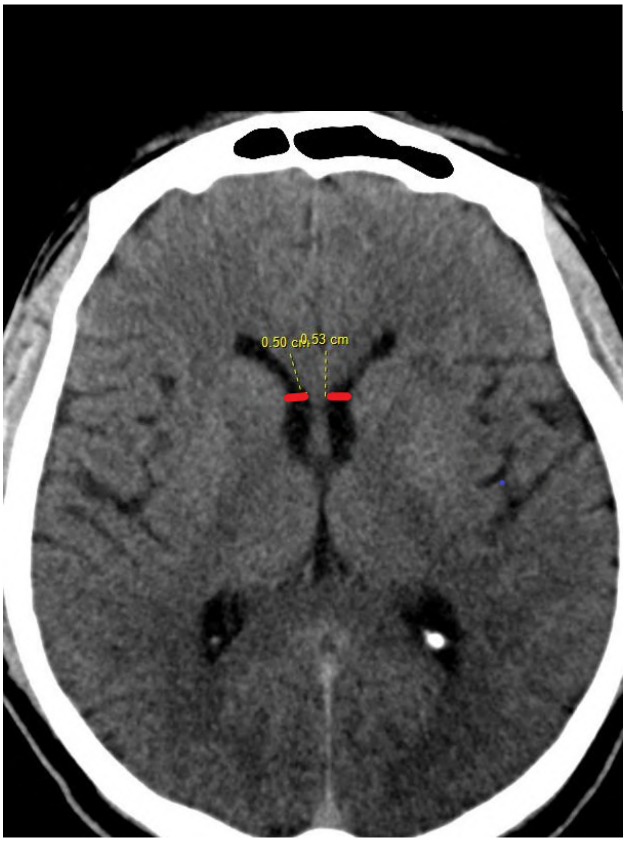

Fig. 1.- Axial CT sections of the brain showing measurement of the maximum frontal horn width.

Identification of the frontal horns of the lateral ventricles was performed on axial sections. The length and width of the frontal horn were quantified in centimeters using a digital caliper. Width was determined as the maximum transverse distance from the medial to lateral walls of each frontal horn (Fig. 1), while length was defined as the maximum distance from the interventricular foramen to the tip of the frontal horn on both sides (Fig. 2). The distance between the bilateral frontal horn tips (FHTD) was measured as the maximum distance between the right and left frontal horn tips (Singh et al., 2020) (Fig. 3).

Data analysis was conducted using the International Business Machine (IBM) Statistical Package for Social Sciences (SPSS), version 25. The data were categorized according to gender and 10-years age groups. Independent and paired sample t-tests were employed for gender and side comparisons of mean variables, respectively. Bivariate Pearson's correlation was utilized to assess the correlation of frontal horn parameters with age. One-way Analysis of Variance (ANOVA) was employed to evaluate differences in means

Fig. 2.- Axial CT sections of the brain showing the measurement of the frontal horn length.

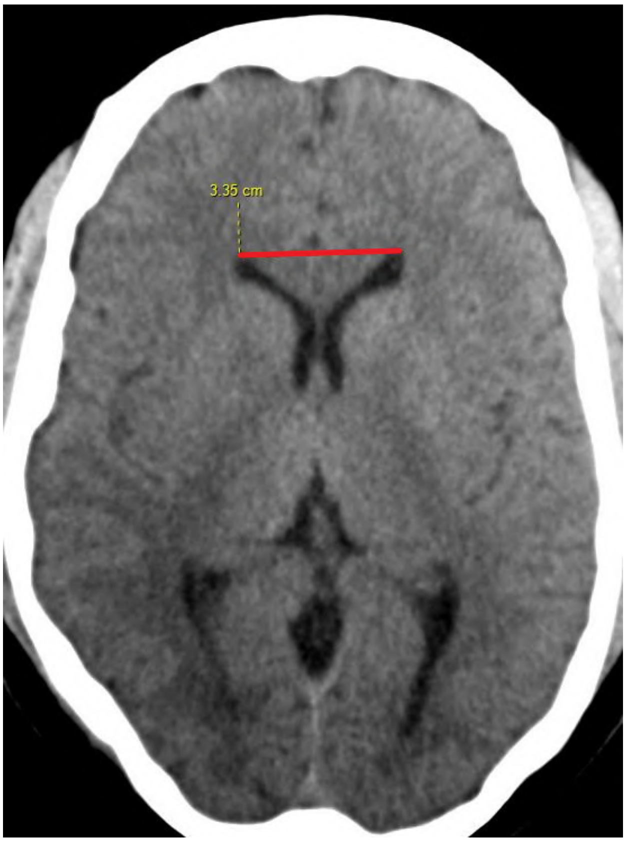

Fig. 3.- Axial brain CT scans showing the maximum distance between the tip of frontal horns.

within various age groups. All tests of significance were two-tailed, and a significance level of P ≤ 0.05 was deemed statistically significant. Data were summarized using means and standard deviations, and the results were presented in tables.

RESULTS

This investigation examined the dimensions of the frontal horn of the lateral ventricles by analyzing CT brain images of 202 adult patients, with a larger proportion of males (109, 54.0%) than of females (93, 46%). The age range of the participants was 18 to 65 years, with a mean age of 44.42 ± 13.27 years. The mean length and width of the right and left frontal horns, as well as the mean FHTD, are presented in Table 1. Additionally, the maximum and minimum values for each dimension are also included in Table 1.

Table 1. Descriptive statistics of the studied parameters.

Parameter	Minimum	Maximum	Mean ± S.D.
Age (Years)	18.00	65.00	44.42±13.27
LL (cm)	1.73	3.86	2.71±0.41
RL (cm)	1.79	3.67	2.63±0.40
LW (cm)	0.14	2.59	0.64±0.28
RW (cm)	0.19	1.78	0.61±0.25
FHTD (cm)	1.95	3.73	2.93±0.31

LL = left length, RL = right length, LW = left width, RW = right width, FHTD = frontal horn tip diameter

All the dimensions demonstrated larger measurements in males compared to females. The gender differences in the length of bilateral frontal horns and the FHTD exhibited statistical significance (p<0.05), whereas the width of both right and left frontal horns did not show any significant association with gender (p>0.05) (Table 2). Further investigation revealed a significant asymmetry in the length of frontal horns between the left and right sides (p=0.001). Conversely, no significant side differences were observed in the width of the frontal horns (p=0.068) (Table 3).

Analysis across different age groups revealed significant variations in the frontal horn length and width bilaterally (p <0.05). However, no significant age differences were detected in the FHTD (p= 0.451) (Table 4). The investigation into the correlation between frontal horn dimensions and age revealed a significant weak positive correlation bilaterally in terms of length (r=0.245, 0.157; p<0.05) and width (r=0.249,0.388; p<0.05) of the frontal horn. Conversely, the FHTD displayed a weak positive correlation (r=0.059) with age that did not reach statistical significance (p=0.401) (Table 5). A comparative summary of frontal horn dimensions across various study populations is presented in Table 6.

Table 2. Gender differences in the frontal horn parameters.

Parameter	Mean ± S.D (cm)		P value
	Male	Female	
LL	2.82 ± 0.42	2.58 ± 0.35	0.001*
RL	2.71 ± 0.41	2.54 ± 0.36	0.002*
LW	0.67 ± 0.32	0.59 ± 0.23	0.052
RW	0.62 ± 0.27	0.60 ± 0.22	0.432
FHTD	3.01 ± 0.33	2.84 ± 0.28	0.001*

LL- left frontal horn length, RL- right frontal horn length, LW- left frontal horn width, RW-right frontal horn width, FHTD- distance between the frontal horn tips, *p considered significant at <0.05

Table 3. Side differences of the frontal horn length and width.

Parameter	Side	Mean ± S.D (cm)	P value
Length	Left Right	2.71 ± 0.41 2.63 ± 0.40	0.001*
Width	Left Right	0.64 ± 0.28 0.61 ± 0.25	0.068

DISCUSSION

The mean length of the right and left frontal horn in this study was lower than the measurements reported in several earlier studies in different populations (Usman et al., 2012; Arun et al., 2017; Agegnehu et al., 2021; Quarshie et al., 2021; Farheen and Sukre, 2017) (Table 6). The width of the frontal horn was higher than the findings by Agegnehu et al. (2021). These authors also reported larger FHTD compared to our findings. Discrepancies among studies in frontal horn dimensions could stem from methodological variations (using CT versus MRI), differences in sample sizes, diverse measurement techniques, and the age composition of the participants (Arun et al., 2017). Furthermore, variations could be due to the influence of racial and geographical factors (Quarshie et al., 2021). Understanding the population variations in frontal horn dimensions ensures accurate

Table 4. Age differences in the frontal horn parameters.

Parameter (cm)			Age (Years)				P value
	<20	21-30	31-40	41-50	51-60	61-70	
Mean ±SD							
LL	2.60 ± 0.21	2.61 ± 0.45	2.52 ± 0.36	2.82 ± 0.35	2.84 ± 0.37	2.75 ± 0.44	0.001*
RL	2.53 ± 0.29	2.60 ± 0.42	2.46 ± 0.35	2.70 ± 0.37	2.75 ± 0.35	2.66 ± 0.48	0.012*
LW	0.48 ± 0.13	0.59 ± 0.43	0.56 ± 0.20	0.63 ± 0.25	0.69 ± 0.22	0.76 ± 0.29	0.024*
RW	0.39 ± 0.11	0.51 ± 0.24	0.52 ± 0.22	0.59 ± 0.21	0.71 ± 0.21	0.77 ± 0.29	0.001*
FHTD	2.85 ± 0.41	2.90 ± 0.32	2.89 ± 0.33	2.95 ± 0.36	3.01 ± 0.29	2.89 ± 0.30	0.451

LL- left frontal horn length, RL- right frontal horn length, LW- left frontal horn width, RW-right frontal horn width, FHTD- distance between the frontal horn tips, *p considered significant at <0.05

Table 5. Age correlation with the frontal horn parameters.

Parameter	r	P value
LL	0.245	0.001*
RL	0.157	0.026*
LW	0.249	0.001*
RW	0.388	0.001*
FHTD	0.059	0.401

LL- left frontal horn length, RL- right frontal horn length, LW- left frontal horn width, RW-right frontal horn width, FHTD- distance between the frontal horn tips, *p considered significant at <0.05

Table 6. Frontal horn measurements in diffèrent populations.

Author	Country	N	Unit	Side	Mean ± SD		Average
					Male	Female	
Agegnehu et al. (2021)	Ethiopia	169	mm	RL LL	27.79±3.62 28.66±3.67	26.96±3.97 27.95±4.01	
Honnegowda et al. (2017)	Manipal, India	250	mm	RL LL	30.54±3.4 30.14±4.7	28.4±4.2 27.4±3.2	28.7±2.90 29.2±3.72
Moawia et al. (2015)	Saudi Arabia	152	mm	RL LL	28.5±3.8 28.5±3.8	26.16±4.2 26.2±4.2	
Sharmin et al. (2020)	Bangladesh, India	60	mm	RL LL	28.82±2.56 29.31±2.53	26.54±2.9 26.79±2.44	
Farheen and Sukre, (2017)	Aurangabad, India	500	mm	RL LL	28.5±1.06 30.3±1.46	25.9±1.46 29.7±1.22	
Yadav et al. (2015)	Meerut, India	200	mm	RL LL	29.8±2.6 31.1±2.5	28.9±2.3 29.9±2.3	29.3 30.5
Current study	Nigeria	202	cm	RL LL	2.71±0.41 2.82±0.42	2.54±0.36 2.58±0.35	2.71±0.41 2.63±0.40

RL- right frontal horn length, LL- left frontal horn length

diagnostic assessments and treatment planning (Agegnehu et al., 2021). Recognizing population-specific norms allows clinicians to interpret imaging results with greater precision, reducing the risk of misinterpretation and unnecessary interventions (Annongu et al., 2017; Arun et al., 2017). This knowledge is particularly relevant for neurosurgical planning, as variations in frontal horn dimensions can influence the approach and strategies employed in surgical procedures such as endoscopic surgeries or ventriculoperitoneal shunt insertions while minimizing complications (Arun et al., 2017; Quarshie et al., 2021).

Significant gender differences were observed in the length of the frontal horn and the FHTD, which were larger in males than in females. Agegnehu et al. (2021) reported significantly larger width and FHTD in males compared to their female counterparts. Yadav et al. (2015) and Sharmin et al. (2020) also reported larger frontal horn lengths in males, and this was contrary to the observations by Farheen and Sukre (2017). In Ukraine, the width of the frontal horn lacked significant association with gender (Polat et al., 2019). Gender differences in the size of the lateral ventricles can be attributed to larger skull capacity and brain volumes in males that influence the ventricular size (Bijaylakshmi et al., 2014; Yadav et al., 2015; Annongu et al., 2017). This is because the sex hormones impact the brain structure and fluid dynamics, which is crucial in maintaining brain homeostasis. There could also be sex-specific genetic influences that may contribute to the observed sexual dimorphism in the ventricular size (Yadav et al., 2015). This dimorphism in ventricular size may have implications for diagnosis and management of neurological disorders such as dementia or neurodegenerative diseases, which may exhibit sex-related variations in their impact on brain structures including the ventricles (Usman et al., 2012). Additionally, neurosurgical procedures need to account for sex-related variations in ventricular size (Arun et al., 2017; Quarshie et al., 2021).

The left frontal horn length was significantly larger than the right, aligning with results reported by some earlier studies (Bijaylakshmi et al., 2014; Quarshie et al., 2021). Conversely, Farheen and Sukre (2017) and Annongu et al. (2017) did not observe any significant side differences in the frontal horn length. No significant side difference was observed in frontal horn width in our study, in contrast to the findings of Agegnehu et al. (2021) and Zhuravlova and Montgomery, (2023) who reported significantly wider frontal horn on the left and right side respectively. Asymmetry in normal lateral ventricle size is influenced by various factors such as functional lateralization of cognitive functions, handedness, neurodevelopmental processes, genetic and environmental factors (Bijaylakshmi et al., 2014; Arun et al., 2017; Quarshie et al., 2021). While some degree of asymmetry is considered normal, extreme or consistent, asymmetry may prompt further investigation to rule out underlying neurological conditions or abnormalities (Arun et al., 2017). This knowledge informs diagnostic assessments and helps avoid unnecessary interventions related to normal anatomical variability in the human brain.

The length and width of the bilateral frontal horns exhibited significant differences across various age groups while the FHTD did not. Among the Ethiopians evaluated by Agegnehu et al. (2021), the frontal horn length, width and FHTD showed significant differences between the age-groups. On the contrary, Fareen and Sukre (2017) did not observe any significant differences age-wise. This discrepancy might be attributed to variations in sample size and gender distribution within each age group (Arun et al., 2017; Quarshie et al., 2021).

This study identified a significant weak positive correlation between the length and width of the frontal horns and age bilaterally. The FHTD had no significant correlation with age. Agegnehu et al. (2021) observed a strong positive correlation between each of the three dimensions (length, width and FHTD) with age. The population examined by Sharmin et al. (2020) showed an increasing frontal horn length up to the age of 40 years, while later a reduction was observed. Zhuravlova and Montgomery (2023) also reported increasing frontal horn width with age. The increase in ventricular sizes with age is attributed to natural changes in brain structure and volume during the aging process (Yadav et al., 2015). Brain atrophy or shrinkage is associated with compensatory enlargement of CSF spaces (Bijaylakshmi et al., 2014; Annongu et al., 2017). Understanding these age-related variations aids in distinguishing normal age-related changes from potentially pathological conditions, guides treatment planning in neurosurgery, and informs the interpretation of neuroimaging results in different age cohorts, contributing to more accurate diagnoses and choice of interventions (Quarshie et al., 2021; Zhuravlova and Montgomery, 2023).

In this current study, the use of a CT and a standardized methodology for measurements enhance the reliability and reproducibility of the findings. The inclusion of gender- and age-specific analyses provide valuable reference for clinicians and researchers in neurology and neurosurgery. However, the retrospective nature of the research limited the sample size which may impact the generalizability of the findings. Additionally, the study does not associate the dimensions measured with clinical symptoms or conditions. The future research endeavors can assess the clinical implications of frontal horn variations in relation to neurological symptoms or disorders. The age-related changes in frontal horn dimensions could be tracked over-time to aid in the early detection of pathological conditions.

CONCLUSION

The study provides the standard reference values of the dimensions of the frontal horns on CT based on age and gender groups. This has important implications for accurate diagnostic interpretation in clinical settings, and is therefore useful to neurosurgeons, psychiatrists and neurologists, and neuroradiologists in Delta State.

ACKNOWLEDGEMENTS

We thank the staff in the Radiology Department for their technical help in accessing the database. We also extend our gratitude to Emmanuel Akpoyibo, who assisted with data collection and analysis.

REFERENCES

AGEGNEHU A, TENAW B, GEBREWOLD Y, JEMBERIE M (2021) Morphometric study of frontal horn of the lateral ventricles of the brain and its correlation with age, gender and side among adults in the University of Gondar Comprehensive Specialized Hospital, Gondar, Northwest Ethiopia, 2019. *Aust J Anat,* 8(1): 1096.

ANNONGU IT, MOHAMMAD H, ACHINGE G, MAGAJI OG, IYUA K, IKUBOR JE (2017) Morphometric study of the adult human brain ventricular sizes on computed tomography scans in Nigerian. *Eur J Biomed Pharm Sci,* 4(6): 95-98.

ARUN KS, KUMARI SM, ANAND MV, SARASWATHY R, RAJESHWARI M (2017) Evaluation of Evan's index in South Indian population using computed tomography. *Int J Anat Radiol Surg,* 6(3): 28-31.

BIJAYLAKSHMI P, NIRANJAN SR, RABINDRA NP (2014) Age related changes in ventricular system of brain in normal individuals assessed by computed tomography. *Siriraj Med J,* 66: 225-230.

BLINKOUSKAYA Y, WEICKENMEIER J (2021) Brain shape changes associated with cerebral atrophy in healthy aging and Alzheimer's disease. *Front Mech Eng,* 7: e705653.

FARHEEN SF, SUKRE SB (2017) Morphometric study of frontal horn of lateral ventricle by computerised tomography. *Int J Anat Res,* 5(3.1): 4063-4066.

HONNEGOWDA TM, NAUTIYAL A, DEEPANJAN M (2017) A morphometric study of ventricular system of human brain by computerised tomography in an Indian population and its clinical significance. *Aust J Anat,* 4(4): id1075.

MOAWIA G, ABDALRAHIM A, AMIR A, AL-RADDADI M (2015) Morphometric analysis of the brain ventricles in normal subjects using computerized tomography. *Open J Radiol,* 5: 13-19.

OLAWANDE T, AJAYI MP, AMOO EO, OLAWOLE-ISAAC A (2020) Treatment pathways of Alzheimer in Nigeria. *Heliyon,* 6(12): e05724.

PATNAIK P, SINGH V, SINGH D, SINGH S (2016) Age and gender related variations in lateral ventricle brain ratios. *Int J Health Sci Res,* 6(5): 7884.

POLAT S, OKSUZLER FY, OKSUZLER M, KABAKCI AG, YUCEL AH (2019) Morphometric MRI study of the brain ventricles in healthy Turkish subjects. *Int J Morphol,* 37(2): 1-5.

QUARSHIE JT, MENSAH EN, QUAYE O, AIKINS A (2021) The current state of parkinsonism in West Africa: A systematic review. *Hindawi,* 2021: 1-4.

SHARMIN S, AKHTARI A, ATIQUR R, SYED AI (2020) Morphometric study of lateral ventricles of brain by MRI in healthy adults in Northern zone of Bangladesh. *Ibrahim Card Med J,* 10(1&2): 45-50.

SINGH S, BHOJ RS, URUSHA P, PUJAN S, MANOJ B, NAWARAJ P (2020) Estimation of ventricles size of human brain by Magnetic Resonance Imaging in Nepalese population: a retrospective study. *J Gandaki Med Coll Nepal,* 13(1): 45-50.

USMAN JD, YUNUSA GH, SAIDU SA, BELLO SM, ABDULHAMEED A, BELLO SS, TRADROS AA (2012) Morphometric study of the lateral ventricles using computerized tomography. *Afr J Online,* 14(1): 1-5.

YADAV A, SHARMA A, NIGAM GL, YADAV A, CHAUHAN K, PANDEY VD (2015) Morphometric study of frontal horn of the lateral ventricles of the brain by computed tomography in Western population. *J Anat Sci,* 23(2): 22-27.

ZHURAVLOVA I, MONTGOMERY A (2023) The anatomic variability of the lateral ventricles of the human brain depending on age and sex. *Cureus,* 15(9): e45915.

ORIGINAL ARTICLE

Eur J Anat, 28 (5): 609-619 (2024)

Microcellular approach to submandibular gland senescence. Myoepithelial markers between aging and tumors

Shereen AbdelFattah, Hossam Yehia, Tarek AbdelGalil

Anatomy and Embryology, Kasralainy, Faculty of Medicine, Cairo University, Cairo, Egypt

SUMMARY

Advance in age outcomes changes that disrupts the function of the salivary glands which are weakened vigorously. Advanced worsening in the histological structure of submandibular gland alters production of saliva. This study was hypothesized to point out the micro-cellular variations with aging in submandibular salivary glands, moreover to detect the role of myoepithelial markers and the propensity of malignant transformation with aging. Fifty male rats were used: group I (young adult), group II (senile). Light microscopic techniques (H&E, Masson trichrome, immunohistochemistry for vimentin, cytokeratin and PCNA) and electron microscopy were used. MDA, GSH and SOD, and a molecular study for p53 was evaluated.

The submandibular gland of old rats shows variable sized, shrunken acini, and necrosis. Swollen intercalated ducts with eccentric lumina, and irregular striated ducts are reported. E.M. revealed degenerated myoepithelial cells, cytoplasmic rarefaction, marked reduction of the nuclear chromatin, large macrophages with large lysosomes and many endocytic vesicles. The mean area percent of collagen fibers, vimentin, and cytokeratin in senile rats exposed significant increase and a significant decrease of mean number of PCNA cells when compared to young rats. The mean values of MDA, P53 revealed a significant surge, while that of GSH and SOD exhibited a significant decline when compared to adult rats. Vimentin and cytokeratin have a direct correlation with aging in the submandibular gland. They are concomitant with hyperplastic changes in the gland so they might be a strong indicator of presence of a tumor.

Key words: Submandibular gland – Aging – Vimentin – Cytokeratin – Tumor markers

INTRODUCTION

Aging causes physiological changes that disrupt the function of all tissues (Lopez-Otin et al., 2023), as well as significant damage to the salivary glands. Numerous investigations have demonstrated gradual deterioration in the architecture of salivary glands, as well as changes in saliva capacity with age. Age-related salivary changes are mostly induced by acinar cells; as a result, decreased saliva levels have unsettling consequences, includ-

Corresponding author:
Shereen Abdelfattah. Dept. of Anatomy and Embryology, Kasralainy, Faculty of Medicine, Cairo University, Cairo 11562, Egypt. Phone: 01099060936; Fax: 0235875958. E-mail: dr_shery.fattah@yahoo.com

Submitted: November 29, 2023. **Accepted:** May 2, 2024

https://doi.org/10.52083/NDHQ3891

ing vulnerability to alveolar caries, infections, and deglutition issues, all of which impair life quality (Toan and Ahn, 2021; Smith et al., 2013). Multiple variables contribute to salivary gland aging. Unfortunately, there is no absolute cure to repair the irreversible damage to the salivary glands. Therefore, examining the corresponding underlying etiology and molecular biology affecting salivary gland efficiency throughout aging is beneficial (Li et al., 2013).

Reactive oxygen species (ROS) liberation was exhibited to cause oxidative insult to oral proteins, lipids, and DNA, leading in cellular damage (Zalewska, 2016).

There are multiple epithelial tumors in salivary glands, which can be benign or malignant, according to the sorting of the World Health Organization. These tumors reveal diversity in histology and features. While diagnosis can be done with hematoxylin-eosin, immunohistochemistry constutes an important tool to categorize the cellular differentiation and allocate precise organizations in several cases (Zhu et al., 2015). Myoepithelial carcinoma is a tumor in the salivary glands, in which cancer cells display exclusively myoepithelial differentiation. Immune-expression for keratins and a myoepithelial marker is compulsory to identify myoepithelial tumors. Myoepithelial tumors commonly prompt vimentin and cytokeratins (Barnes, 2005; Saveral et al., 2005). Vimentin is an indicator of epithelial–mesenchymal transition EMT (Adams et al., 2015). Raised vimentin levels have been distinguished in several cancers, such as prostate cancer (Satelli, 2011) and esophageal carcinoma (Irani et al., 2014).

Apoptosis is a dynamic process, in which cell reduction, chromatin condensation and DNA fragmentation are indorsed. Cancers often derestrict apoptosis in, being this technique an appropriate goal as anticancer agent (Cotter, 2009). p53 normally is a tumor suppressor gene. Mutation of p53 is amongst the most frequently perceived gene abnormalities in neoplasia (Tarakji et al., 2012). The damage of function of p53 might result in the progress of various types of cancer.

Furthermore, the presence of genes involved in cell proliferation and oncogenesis appears to be correlated with the prognosis of oral cancers. Proliferating cell nuclear antigen (PCNA) determines the course of cellular proliferation, and thus the susceptibility to malignant conversion (Alves, 2002). Tumor development is dependent on its angiogenic activity. Blood vessels are newly produced and necessary for the development of the tumor (Tadbir et al., 2012).

This study was carried out in order to study the microcellular alterations with aging in submandibular salivary glands, as well as the role of myoepithelial markers and the tendency of malignant transformation with aging; moreover, the role of p53 and PCNA in the senescence process were illustrated.

MATERIALS AND METHODS

Animals

Fifty adult Wistar male rats, their weights range being from 150 to270 g, were used. The male rats were used in order to avoid any possible hormonal effects on the experiment.

The rats were obtained from the House of Animals, Faculty of Medicine, Cairo University. The study followed the guidelines of the Committee of Ethics of the Faculty of Medicine of Cairo University and the University of New Giza. All procedures observed the controlling principles for experimental rats. The work was carried out in accordance with the ethical guidelines of the Institutes of National Health's directory for the care of Laboratory Animals (NIH Publications No. 8023, revised 1978). The rats underwent a two-week period of adaptation in the laboratory before carrying out the experiment. They were kept in cages, five rats per cage, under standard laboratory and environmental conditions and were given standard rodent food and water *ad libitum.*

Experimental Design: 50 rats were used in this study, divided into 2 groups: Group I (25 rats): young adult rats (age ranged from 4-6 months); Group II (25 rats): senile rats (age ranged from 22-24 months). The rats of each group were sacrificed with an overdose of intraperitoneal phenobarbital sodium (40 mg/kg).

Ultrastructural preparations

For electron microscope, parts of the submandibular gland from each rat were fixed in 2% paraformaldehyde and 2% glutaraldehyde solution in 0.1 mol/L phosphate buffered saline (PBS) pH 7.2, and reserved in the refrigerator overnight, rinsed in 0.1 mol/L PBS and postfixed in phosphate-buffered 1% osmium tetroxide. To acquire cross-sections, the gland samples were oriented longitudinally in a flat mold and then embedded in resin. Semithin cross-sections were stained with 1% toluidine blue, and then examined by light microscope for proper orientation and image analysis of axons number. Ultrathin sections (50-60 nm) were stained with uranyl acetate and lead citrate. These sections were examined and photographed using a Jeom-1400 transmission electron microscope (JEOL Ltd./Japan a Joel), Electron Microscopy Department, Faculty of Agriculture, Cairo University, Egypt.

Light microscopic study

The submandibular gland of each rat was expunged and organized for paraffin blocks, 5 µm thick, which were obtained using a microtome then mounted on glass slides (Bancroft and Gamble, 2008). The slides were used for both histological and immunohistochemical study.

- Hematoxylin and eosin stain
- Masson's trichrome stain
- Immunohistochemistry

Paraffin sections were dewaxed, rehydrated and incubated with 3% hydrogen peroxide solution for half an hour at room temperature (RT) and endogenous peroxidase activity was blocked by treatment with 0.9% hydrogen peroxide in absolute methanol for 10 min. Then, the sections were washed with distilled water; a microwave was utilized for tissue antigen retrieval with sodium citrate buffer solution (pH = 6). Afterwards, slices were splashed with distilled water, and put into phosphate-buffered saline (PBS) for 5 min. After PBS was rubbed off, 5% normal goat serum was added onto the section at RT for 30 min. Deparaffinized sections of the submandibular gland were incubated for 30 min at RT with vimentin mouse monoclonal antibody (V9) (#:MA5-11883 dilution 1:100), anti-pan cytokeratin (anti-CK AE1/AE3) (#:MA5-13156 dilution 1:100) and anti-PCNA, which is a mouse monoclonal antibody ([PC10] antibody ab29, 1:200). Antibodies were obtained from Thermo Fisher Scientific Industries (Waltham, MA, USA). Slides were bathed well in PBS (3 times, 2 minutes each), incubated for 20 minutes with 2 drops of biotinylated secondary antibody for each section, and then rinsed well with PBS. Substrate chromogen (DAB) mixture 2 drops were applied for 5 minutes then rinsed well with distilled water. Slides were counterstained with hematoxylin, dehydrated and mounted. Negative controls were accomplished with a method similar to the one declared, except that the primary antibody was exchanged by non-immune serum.

Histomorphometric study

Quantitative data were attained using Leica Qwin 500 Image Analyzer software system (National Institute of Mental Health, Bethesda, Maryland, USA). The slides were examined within the standard measuring frame of a known area equal to 11694 µm^2. The removal of quantitative information from images was the final stage of analysis. The following parameters were examined at X40 objective lens in 10 non-overlapping fields for each gland in all animal groups:

i. Area percentage of collagen fibers in Masson's trichrome-stained sections.

ii. Area percentage of vimentin, cytokeratin and the cell count of PCNA.

Biochemical assays

Tissue levels of oxidative/ antioxidative markers

- **Oxidative stress markers (MDA):**

The submandibular MDA was measured according to the manufacturer's instructions. The resources for this method were delivered as kits by (Biodiagnostics, Cairo, Egypt).20 mg of tissue was homogenized in 1 mL PBS, pH 7.0 with a micro pestle in a micro tube. 20% TCA was added to tissue homogenate to precipitate the protein and centrifuged. Supernatants were collected and thiobarbituric acid (TBA) solution was added to the supernatants. After boiling for 10 minutes in water bath, the absorbance was measured. The concentration of MDA was calculated using the standard curve.

- **Anti-oxidative stress markers:**

The SOD (Biodiagnostics, Cairo, Egypt) activity in tissue homogenate was premeditated by the clampdown of nitroblue tetrazolium drop via the generated O2 by the oxidase system (xanthine/ xanthine). Single SOD action unit was demarcated as the amount of enzyme instigating 50% embarrassment in 1 ml reaction solution per milligram tissue protein. The procedures were prepared affording the manufacturer's information. GSH (Biodiagnostics, Cairo, Egypt) calculations are built on the discount of 5, 5 dithiobis (2-nitrobenzoic acid) (DTNB) with condensed glutathione to yield a yellow composite. The condensed chromogen is straightly proportionate to GSH application (absorbance is measured at 405 nm).

Real time Quantitative PCR P53, VEGF

The qualified abundance of mRNA species was evaluated using theSYBR Green method on an ABI prism 7500 sequence detector system (Applied Biosystems, Foster City, CA). PCR primers were designed with Gene Runner Software (Hasting Software, Inc., Hasting, NY) from RNA sequences from Gen Bank.All primer sets had a calculated annealing temperature of 60°C. Quantitative RT-PCR was performed in a 25 µl reaction volume consisting of 2X SYBR Green PCR. Gene primers sequences were as follows:

P53:

Forward primer: (5-ATGTTTTGCCAACTGGCCAAG-3)

Reverse primer: (5-TGAGCAGCGCTCATGGTG-3)

Beta-Actin:

Forward primer: (5-ATC TGG CAC CAC ACC TTC-3)

Reverse primer: (5-AGC CAG GTC CAG ACG CA-3)

Master Mix (Applied Biosystems), 900 nM of separate primer and 2-3 µl of cDNA. Augmentation conditions were 2 min at 50°C, 10 minat 95°C and 40 cycles of denaturation for 15s and annealing/extension at 60°C for 10 min. Data from real-time assays were measured using the v1•7 Sequence Detection Software from PE Biosystems (Foster City, CA).Relative countenance of studied gene mRNA was designed using the comparative Ct method. All values were normalized to the beta actin gene and reported as fold change**.**

Statistical analysis

Statistical analysis was performed using statistical package for social sciences (SPSS) version 21.0 (IBM Corporation, Somers, NY, USA) statistical software. The results were expressed as means ± standard deviation (SD). Statistical evaluation was done using independent T test. Significance was considered when p value is ≤ 0.05 throughout the study.

RESULTS

Histological study on age-related changes in submandibular glands

H & E-stained sections

The submandibular gland of young rats is taken at the junction of the serous and mucous parts of the gland. There are large numbers of serous acini and mucous acini which are apparently healthy, intercalated ducts, and striated ducts. The field shows a large number of apparently healthy mucous acini. The acinar cells are pyramidal in shape, with vacuolated cytoplasm and peripheral flattened nuclei. Some acini are capped with serous demilunes, myoepithelial cells and intercalated ducts, striated ducts with vesicular nuclei and clear basal striations are observed (Fig. 1a, b). The submandibular gland of old rats shows large number of serous acini that are variable in size and shape. Many acini are shrunken and some of their cells have lost their nuclei; the other cells show variable position of their nuclei. The intercalated ducts show swelling of the lining epithelium with eccentric lumina. Few striated ducts are healthy in appearance, while most of them are irregular in lining with disruption of their lining epithelium. The vessels in the vicinity of the main ducts are dilated and congested. The main ducts show hyperplasia of the lining epithelium. The striated duct shows cytoplasmic vacuolation with nuclear pyknosis. The arterioles show concentric hyperplasia of their media. The venules are dilated and congested, with swelling of the lining endothelial cells. There are areas of interstitial haemorrhage (Fig. 1c, d, e).

Ultrastructure (electron microscope)

Cross sections of the submandibular gland of a young rat show several mucus cells. Cells are healthy, with basal nuclei, rough endoplasmic reticulum and large number of mucus droplets. Blood vessels are noticed (Fig. 2a, b). Sections of the submandibular gland of senile rats, display some mucus cells. There are degenerated myoepithelial cells, with areas of cytoplasmic rarefaction. Most of the acinar cells are degenerated with marked reduction of the nuclear chromatin and

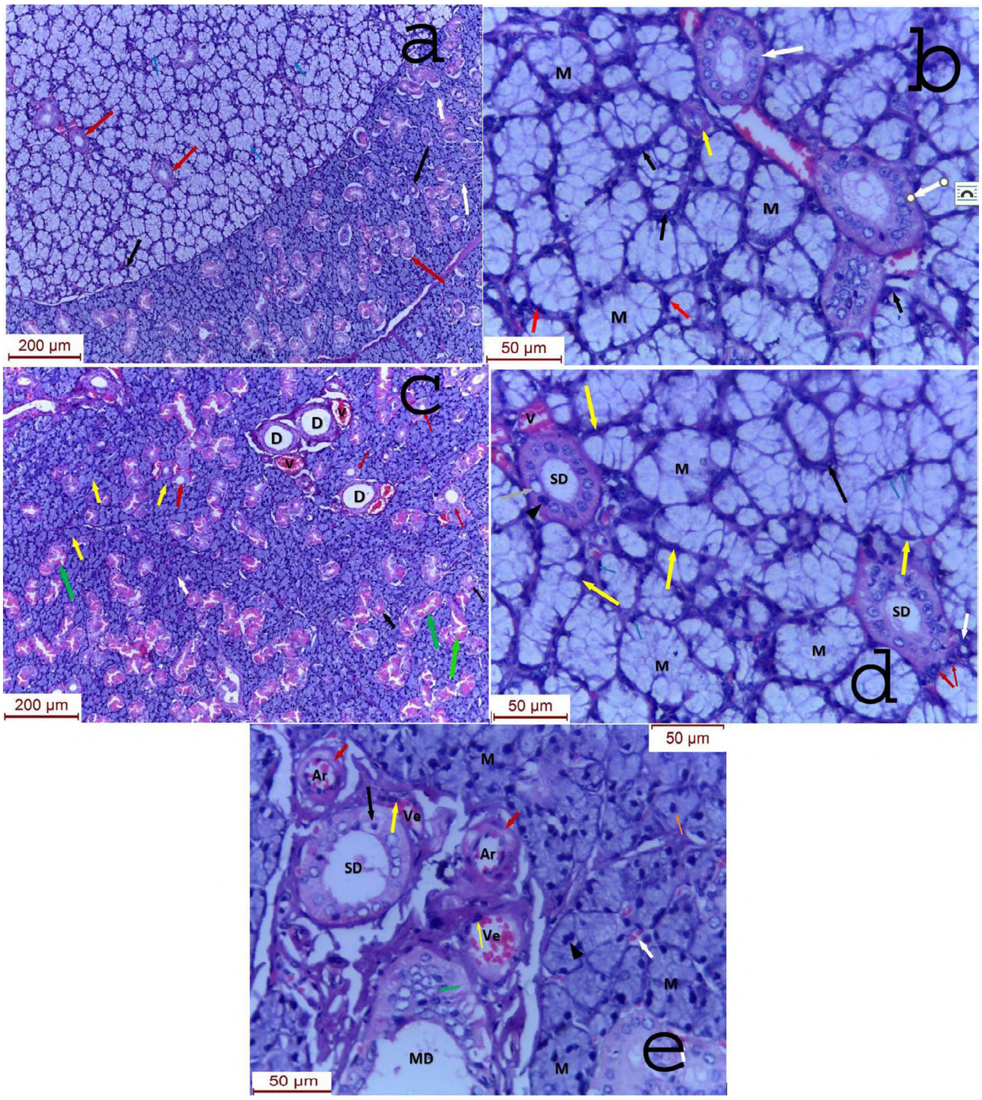

Fig. 1.- Cross sections of submandibular gland of a young rat. **a, b:** junction of the serous and mucous parts, serous acini (white arrows) and mucous acini (blue arrows) which are healthy. The black arrows indicate intercalated ducts, red arrows indicate striated ducts. There are healthy mucous acini, the acinar cells are pyramidal in shape, with vacuolated cytoplasm and peripheral flattened nuclei. Some acini are capped with serous demilunes (black arrows). The red arrows indicate myoepithelial cells. The yellow arrow indicates an intercalated duct, while the green arrows indicate striated ducts with vesicular nuclei and clear basal striations. Section of submandibular gland of an old rat. **c, d, e:** large number of variable sized serous acini (yellow arrows); shrunken acini and necrotic cells, and the other cells show variable position of their nuclei (white arrow). The intercalated ducts show swelling of the lining epithelium with eccentric lumina (black arrows). Few striated ducts are healthy (red arrows), while most of them are irregular with disruption of epithelium (green arrows). The vessels (V) in the vicinity of the main ducts (D) are dilated and congested. Most of the nuclei of the acinar cells are pyknotic (blue arrow). Most of the myoepithelial cells show pyknotic nuclei (yellow arrows). The intercalated ducts (white arrow) are reduced in size and its lining cells show pyknotic nuclei. The striated ducts (SD) are more or less healthy in appearance, with some of their lining cells are pyknotic (arrow head), and other cells show fatty degeneration (grey arrow). The serous demilunes (black arrow) are reduced in size, with disruption of their cells (red arrows). The vessels (V) in the vicinity of the striated ducts are dilated and congested. The main duct (MD) shows hyperplasia of the lining epithelium (green arrow). The striated duct (SD) shows cytoplasmic vacuolation with nuclear pyknosis (black arrow). The arterioles (Ar) show concentric hyperplasia of their media (red arrows). The venules (Ve) are dilated and congested, with swelling of the lining endothelial cells (yellow arrows). There are areas of interstitial haemorrhage (white arrows). (H&E). Scale bars: a, c = 200 µm; b, d, e = 50 µm.

marked cytoplasmic rarefaction. The rough endoplasmic reticulum is swollen and fragmented. There are macrophages with large lysosomes and many endocytic vesicles. The acinar basement membrane is thickened. Cells show marked cytoplasmic rarefaction with dispersion and fragmentation of the rER (Fig. 2c, d. e).

Masson trichrome stain

Masson's trichrome-stained sections of young rats showed slight amount of collagen fibers (Fig. 3a). Sections in old rats elucidated massive amount of collagen fibers around the ducts (Fig. 3b).

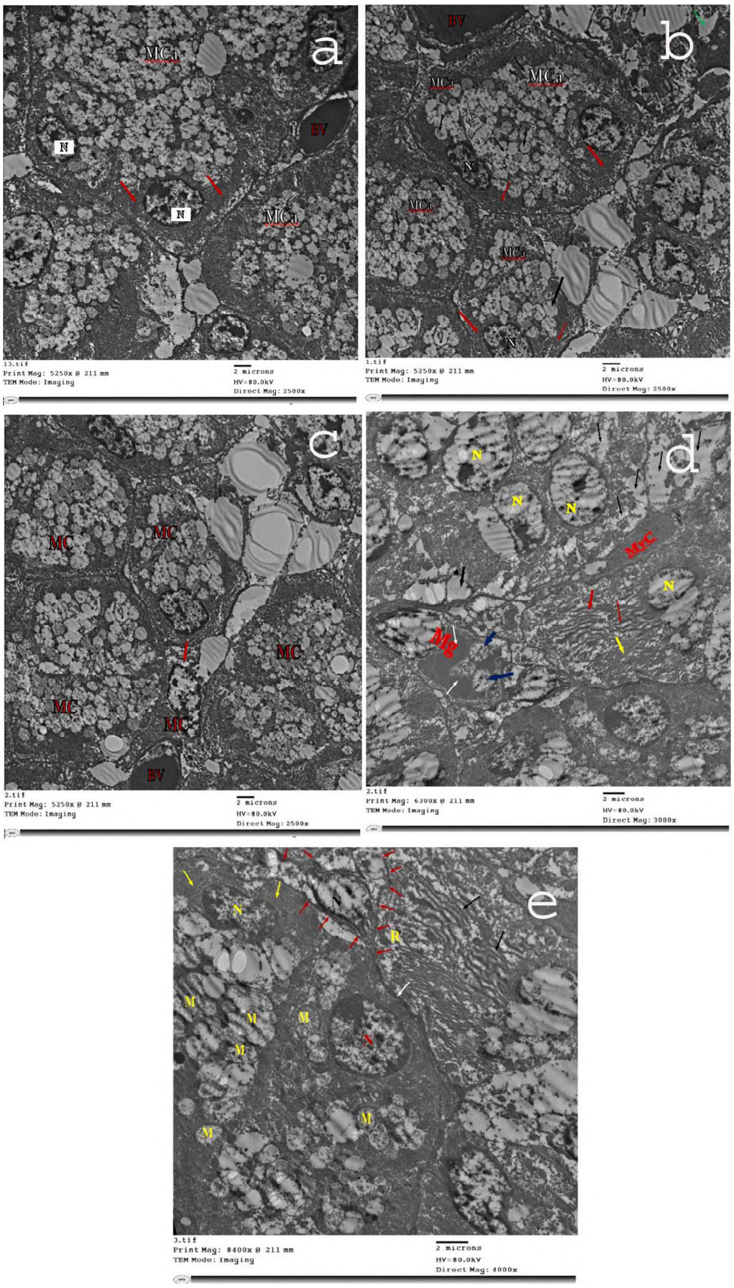

Fig. 2.- Electron micrographs of sections of the submandibular gland of a young rat (group I). **a, b:** several mucus cells. Healthy cells (MCa), basal nuclei (N), rough endoplasmic reticulum (red arrows) large number of mucus droplets (black arrows). BV refers to a blood vessel. Senile rats (group II) **c, d, e:** degenerated myoepithelial cell (MC), areas of cytoplasmic rarefaction (red arrow), blood vessel (BV), marked reduction of the nuclear chromatin (yellow N) and marked cytoplasmic rarefaction (black arrows), rough endoplasmic reticulum is intact in limited regions (yellow arrow), and is swollen and fragmented in other regions (red arrows), degenerated myoepithelial cell (MyC), macrophage (Mg) with large lysosomes (white arrows) and many endocytic vesicles (blue arrows). **e:** Section of the submandibular gland of an old rat, displaying the mucous portion of the gland. Some of the acinar cells are apparently normal, with basal flat nuclei (yellow N), parallel arrays of rough endoplasmic reticulum (yellow arrow) and large number of mucous droplets (M). Other cells show rounded nuclei (red N), with fewer areas of rER and mucous droplets. The acinar basement membrane is thickened (white arrow). Some cells show marked cytoplasmic rarefaction (R) with dispersion and fragmentation of the rER (black arrows). The red arrows delineate a necrotic myoepithelial cell with marked cytoplasmic rarefaction with a destroyed nucleus (black N). Scale bars: a-e = 2 µm.

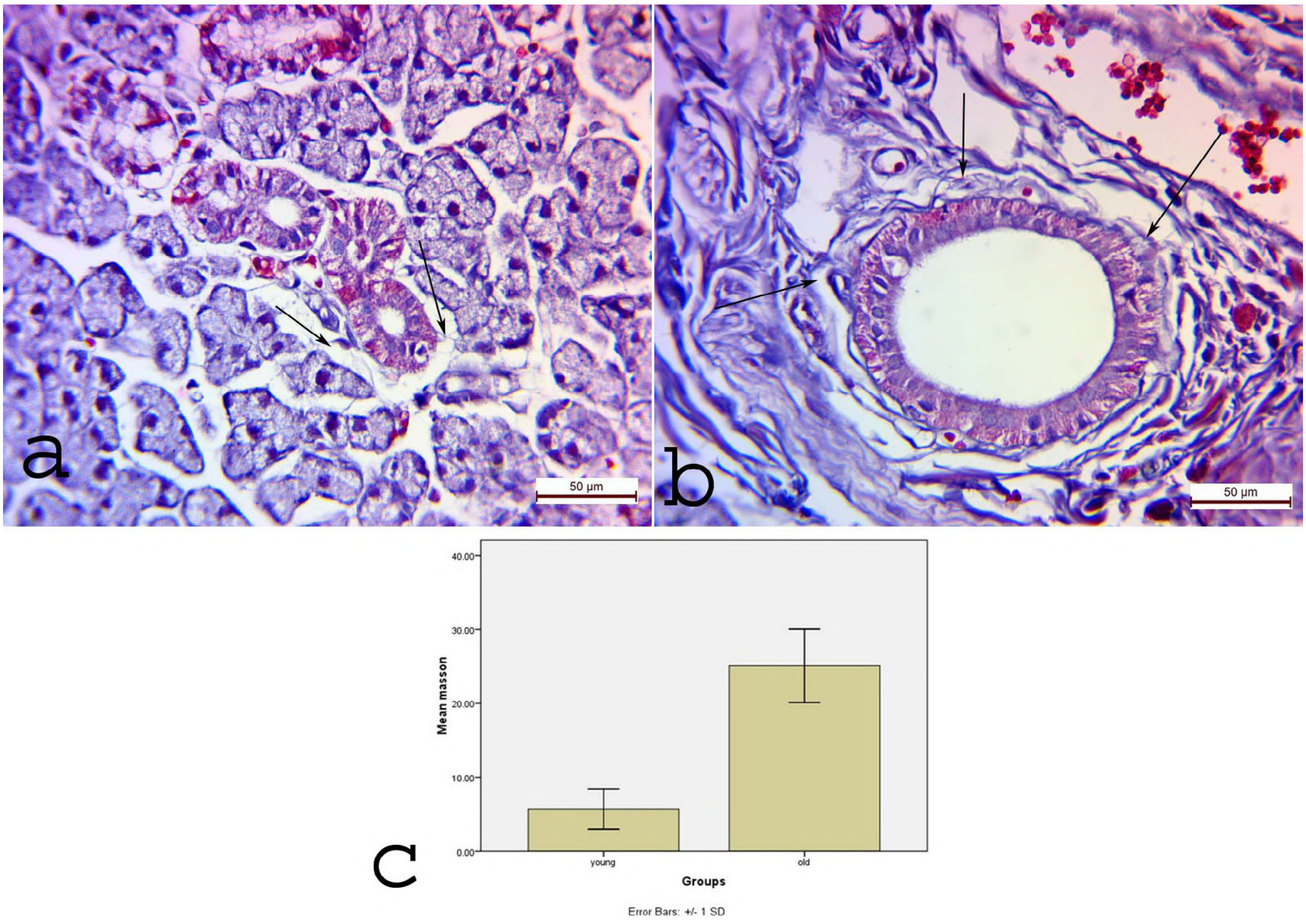

Fig. 3.- Sections of submandibular gland from group I. **a:** negligible amount of collagen fibers (arrows) around the duct (SD). Group II, **b:** immense amount of collagen fibers (arrows). Masson trichrome. Scale bars a-b = 50 µm.

Immunohistochemistry

Immune-expression; vimentin, cytokeratin young rats displayed weak positive immune-reaction and strong PCNA reaction in young rats (Fig. 4a, c, e). Sections of group old rats revealed strong positive immune-reaction around the acini of vimentin and cytokeratin and weak reaction of PCNA (Fig. 4b, d, f).

Histomorphometry

The mean area percent of collagen fibers, vimentin, and cytokeratin in senile rats revealed significant increment when compared to results of group I. Yet it showed a significant decrement of the mean number of PCNA cells (Tables 1 and 2).

Biochemical

MDA, SOD and GSH

The mean values of MDA in group II expressed a significant upsurge, while the mean values of SOD and GSH showed a significant reduction when compared to the values of group II (Table 3).

Real time PCR

P53

The mean values of P53 group II displayed significant raise when compared to the values of group II (Table 2).

Table 1. The mean area percent of collagen among the different groups.

	Group	**Mean ± SD**	**Versus group**	**P value**
Mean are % of collagen	young	5.68 ±2.71		
	Old	25.08 ±4.96	young	0 .004 *

* = Statistically significant

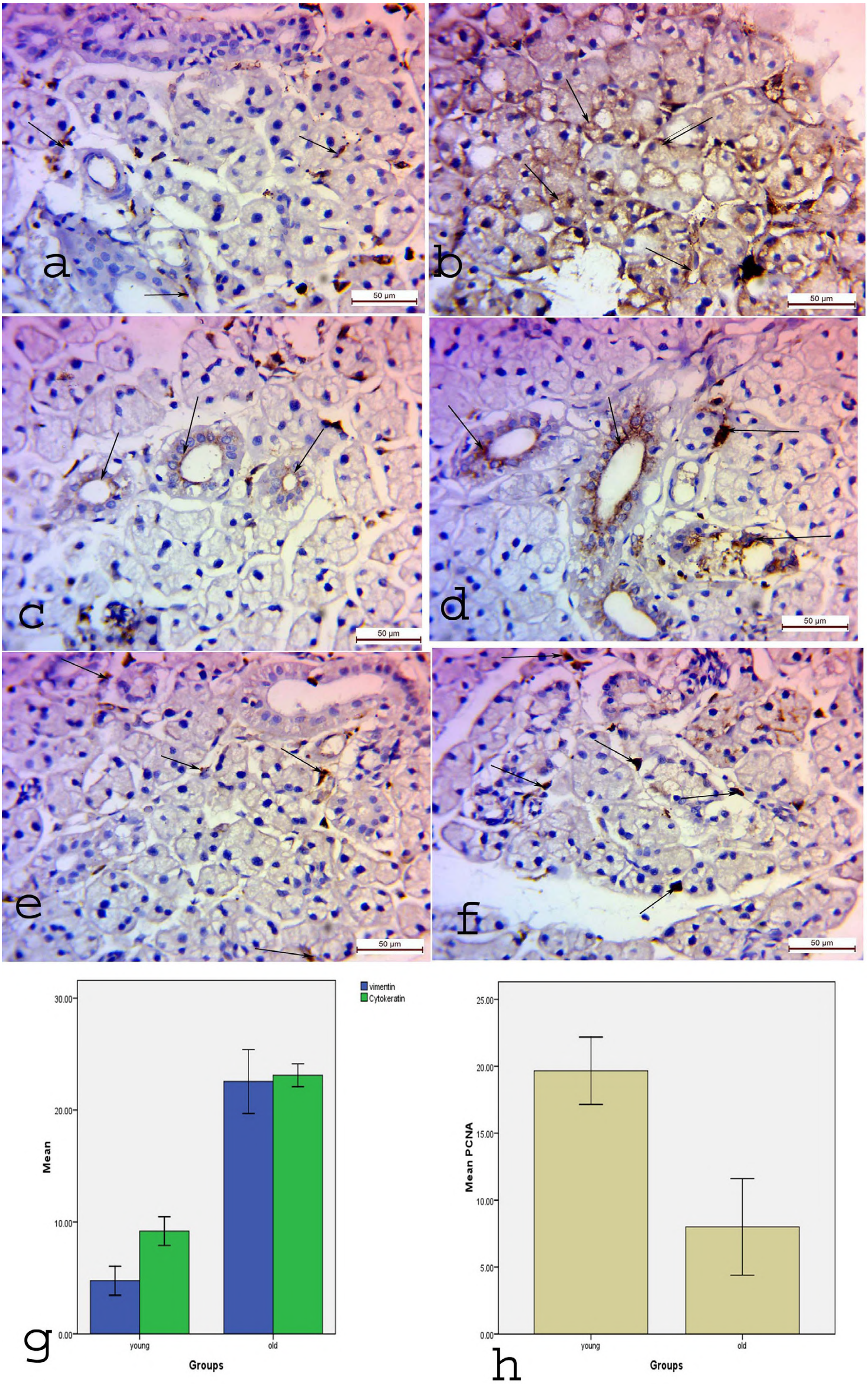

Fig. 4.- Sections of submandibular gland from group I. **a, c, e:** weak immunoexpression of vimentin, cytokertin and PCNA (arrows). Group II, **b, d, f:** strong immunoexpression of the previous parameters. Vimentin (a, b), Cytokertin (c, d) and PCNA (e, f). Scale bars = 50 µm.

Table 2. Comparison of cytokeratin, vimentin, P53 and PCNA among the different groups.

	Group	Mean ± SD	Versus group	P value
cytokeratin	Young	9.16±1.26		
	Old	23.11±1.018	young	0.000*
Vimentin	Young	4.75±1.29		
	Old	22.54± 2.85	young	0.001*
P53	Young	10.29±0.62		
	Old	31.84±7.59	young	0.008*
PCNA	Young	20 ±2.52		
	Old	8 ± 3.61	Young	0.01*
VEGF	Young	2.3 ± 1.1		
	Old	5.75±1.29	young	0.001*

* = Statistically significant

Table 3. Comparison of the oxidative markers among the different groups.

	Group	Mean ± SD	Versus group	P value
MDA	Young	5.45±3.28		
	Old	44.85±4.87	young	0.000*
GSH	Young	60.067±3.63		
	Old	27.56±6.017	young	0.001*
SOD	Young	5.07±1.71		
	Old	1.47±0.32	young	0.02*

* = Statistically significant

DISCUSSION

Many factors disrupt salivary glands as they age, causing compromise in their shape and function (Li et al., 2023). Senile rats’ submandibular glands exhibited pathological changes, including variable-sized shrunken acini, necrotic cells, and a large intercalated disc with eccentric lumina. The veins in the area are dilated and clogged. The major ducts exhibit hyperplasia, cytoplasmic vacuolation, nuclear pyknosis, and increased collagen fiber content. The arterioles have concentric hyperplasia in their media. The venules are dilated and crowded, with enlargement of the endothelial cells that line them. There are places with interstitial hemorrhage. These findings agreed with Li et al. (2023), who attributed the structural change to a huge increase in connective tissue. This is verified with our results which illustrated a high significance when comparing the old group to the young ones

On the microcellular level we found degenerated myoepithelial cells, with areas of cytoplasmic rarefaction. Degenerated acinar cells with marked reduction of the nuclear chromatin and marked cytoplasmic rarefaction. The rough endoplasmic reticulum is swollen and fragmented. There are macrophages with large lysosomes and many endocytic vesicles. The acinar basement membrane is thickened. Cells show marked cytoplasmic rarefaction with dispersion and fragmentation of the rER. Li et al. (2023) propose an adverse correlation between autophagy and aging (Tai et al., 2017). The existence of traced constituents in lysosomes may be due to their decreased aptitude to wipe off intracellular contents (autophagy). The authors correlated the slow diminution of mitochondrial and autophagic actions with aging, which plays a critical part in the deterioration of glandular function (Green et al., 2011).

The mean values of MDA in group II exposed significant raise, while the mean values of SOD and GSH bare a significant reduction when compared to the values of group II. Oxidative stress has newly been a cause to interrupt cellular morphology, and this injurious procedure is a chief moderator in aging that ensues from disturbance of cell structure (Indo et al., 2015). ROS leads to stress and biological factors accumulate inside the body with the advance of age. Additionally, the interior anti-oxidative capability diminishes with age,and therefore the redox monitoring no longer works with full capacity (Dröge, 2003). This outcomes are oxidative strain and oxidative impairment.

Myoepithelial differentiation occurs in intermediate to senior age groups. One of its most prevalent sites is the submandibular gland (Vilar-González et al., 2015). Although myoepithelial tumors of the salivary gland are benign, they can progress to atypical malignancy if not treated properly (Weitzel et al., 2017).

Our results revealed that old rats displayed a strong positive immune-reaction of vimentin and cytokeratin around the acini, with a statistically significant surge compared to that of young rats. Similar results were reported by Zaki, et al.(2018). The authors reported that these transitional filaments were strongly exaggerated by oxidative stress. Zaki et al., (2018) instituted a positive correlation among amplified appearance of the myoskeletal filaments and MDA in the thyroid of senile groups. On the other hand, there is an adverse correlation between the countenance of intermediate filaments and antioxidative GSH and SOD, and these results were on the same line with our results, which documents the impact of the role of oxidative insult on the amplified expression of cytokeratin and vimentin.

Cytokeratin and vimentin intermediate filaments have like functions: they convey stress fight, part in signaling pathways, and backbone the cytoskeleton. Yet, their overexpression outcomes life-threatening variances in epithelial- and mesenchymal-like cells (Kuburich et al., 2024). Considering the properties of intermediate filaments in the cells that co-express of vimentin and cytokeratin as they might be a sign of cancer is critical for developing novel therapeutic options.

Group II displayed significant raise in p53 and decline in PCNA when compared to the values of group I. Senescence handicaps cellular proliferation, and it is well-thought-out as a process to defeat tumor-genesis (Campisi, 2001). However, senescence might trigger cells’ robust apoptosis (Sasaki et al., 2001) and may permit mutations. Consequently, it has been claimed that senescence might protect creatures from cancers, but might induce cancers in elder life (Fossel, 2000; Sasaki t al., 2001).

Cao et al. (2003) assumed that senescence is most likely triggered by the stimulation of a p53-linked cell cycle that avoids cell proliferation. p53 activation is a key reason for the detected senescence. However, the genetic variability triggered can alter p53 and ultimately lead to tumorigenesis. The authors assumed that aging serves as a double-edged weapon that conquers tumorigenesis primary, but has lethal possessions far along.

We concluded that vimentin and cytokeratin have a direct correlation with aging in submandibular salivary gland. At the same time, they are concomitant with hyperplastic changes in the gland, so they might be a strong indicator of presence of tumor. Further studies are needed to investigate the correlation between the increment of expression of these filaments, senescence and tumorigenesis

REFERENCES

ADAMS A, WARNER K, PEARSON AT, ZHANG Z, KIM HS, MOCHIZUKI D, BASURA G, HELMAN J, MANTESSO A, CASTILHO RM, WICHA MS, NÖR JE (2015) ALDH/CD44 identifies uniquely tumorigenic cancer stem cells in salivary gland mucoepidermoid carcinomas. *Oncotarget*, 6(29): 26633.

ALVES FA, PEREZ DE, ALMEIDO OP, LOPES MA, KOWALSKI LP (2002) Pleomorphic adenoma of the submandibular gland: clinicopathological and immunohistochemical features of 60 cases of Brazil. *Arch Otolaryngol Head Neck Surg*, 128: 1400-1403.

BARNES L (ed.) (2005) *Pathology and genetics of head and neck tumour.* Vol. 9. IARC.

CAMPISI J (2001) Cellular senescence as a tumor-suppressor mechanism. *Trends Cell Biol*, 11(11): S27-S31.

CAO L, LI W, KIM S, BRODIE SG, DENG CX (2003) Senescence, aging, and malignant transformation mediated by p53 in mice lacking the Brca1 full-length isoform. *Genes Develop*, 17(2): 201-213.

COTTER TG (2009) Apoptosis and cancer: the genesis of a research field. *Nat Rev Cancer*, 9: 501-507.

DRÖGE W (2003) Oxidative stress and aging. *Adv Exp Med Biol*, 543: 191-200.

FOSSEL M (2000) Cell senescence in human aging: A review of the theory. *In Vivo*, 14: 29-34.

GREEN DR, GALLUZZI L, KROEMER G (2011) Mitochondria and the autophagy–inflammation–cell death axis in organismal aging. *Science*, 333(6046): 1109-1112.

INDO HP, YEN HC, NAKANISHI I, MATSUMOTO KI, TAMURA M, NAGANO Y, MATSUI H, GUSEV O, CORNETTE R, OKUDA T, MINAMIYAMA Y, ICHIKAWA H, SUENAGA S, OKI M, SATO T, OZAWA T, CLAIR DK, MAJIMA HJ (2015) A mitochondrial superoxide theory for oxidative stress diseases and aging. *J Clin Biochem Nutrit*, 56(1): 1-7.

IRANI S, SALAJEGHEH A, SMITH RA, LAM AK (2014) A review of the profile of endothelin axis in cancer and its management. *Crit Rev Oncol Hematol*, 89: 314-321.

KNAŚ M, MACIEJCZYK M, DANISZEWSKA I, KLIMIUK A, MATCZUK J, KOŁODZIEJ U, WASZKIEL D, ŁADNY JR, ŻENDZIAN-PIOTROWSKA M, ZALEWSKA A (2016) Oxidative damage to the salivary glands of rats with streptozotocin-induced diabetes-temporal study: oxidative stress and diabetic salivary glands. *J Diabetes Res*, 2016: 4583742.

KUBURICH NA, DEN HOLLANDER P, PIETZ JT, MANI SA (2022) Vimentin and cytokeratin: Good alone, bad together. In: *Seminars in cancer biology.* Vol. 86, pp 816-826. Academic Press.

LI N, YE Y, WU Y, LI L, HU J, LUO D, LI Y, YANG J, GAO Y, HAI W, XIE Y, JIANG L (2023) Alterations in histology of the aging salivary gland and correlation with the glandular inflammatory microenvironment. *iScience*, 26(5): 106571.

LOPEZ-OTIN C, BLASCO MA, PARTRIDGE L, SERRANO M, KROEMER G (2023) The hallmarks of aging: An expanding universe. *Cell*, 186(2): 243-278.

SASAKI M, KUMAZAKI T, TAKANO H, NISHIYAMA M, MITSUI Y (2001) Senescent cells are resistant to death despite low Bcl-2 level. *Mech Ageing Dev*, 122: 1695-1706.

SATELLI A, LI S (2011) Vimentin in cancer and its potential as a molecular target for cancer therapy. *Cell Mol Life Sci*, 68: 3033-3046.

SAVERA AT, SLOMAN A, HUVOS AG, KLIMSTRA DS (2000) Myoepithelial carcinoma of the salivary glands: a clinicopathologic study of 25 patients. *Am J Surg Pathol*, 24(6): 761-774.

SMITH CH, BOLAND B, DAUREEAWOO Y, DONALDSON E, SMALL K, TUOMAINEN J (2013) Effect of aging on stimulated salivary flow in adults. *J Am Geriatr Soc*, 61(5): 805-808.

TADBIR AA, PARDIS S, ASHKAVANDI ZJ, NAJVANI AD, ASHRAF MJ, TAHERI A, ZADEH MA, SARDARI Y (2012) Expression of Ki67 and CD105 as proliferation and angiogenesis markers in salivary gland tumors. *Asian Pac J Cancer Prev*, 13(10): 5155-5159.

TAI H, WANG Z, GONG H, HAN X, ZHOU J, WANG X, WEI X, DING Y, HUANG N, QIN J, ZHANG J, WANG S, GAO F, CHRZANOWSKA-LIGHTOWLERS ZM, XIANG R, XIAO H (2017) Autophagy impairment with lysosomal and mitochondrial dysfunction is an important characteristic of oxidative stress-induced senescence. *Autophagy*, 13(1): 99-113.

TARAKJI B, BAROUDI K, HANOUNCH S, NASSANI MZ, ALOTAIBI AM, KHARMA MY, AZZEGHAIBY SN (2012) Expression of P21 independent on or independent of P53 in carcinoma ex pleomorphic adenoma (undifferentiated and adenocarcinoma types). *Pol J Pathol*, 63(4): 286-291.

TOAN NK, AHN SG (2021) Aging-related metabolic dysfunction in the salivary gland: a review of the literature. *Int J Mol Sci*, 22(11): 5835.

VILAR-GONZÁLEZ S, BRADLEY K, RICO-PÉREZ J, VOGIATZIS P, GOLKA D, NIGAM A, SIVARAMALINGAM M, KAZMI S (2015) Salivary gland myoepithelial carcinoma. *Clin Transl Oncol*, 17(11): 847-855.

WEITZEL M, COHN JE, SPECTOR H (2017) Myoepithelioma of the parotid gland: a case report with review of the literature and classic histopathology. *Case Rep Otolaryngol*, 2017: 6036179.

ZAKI SM, MOHAMED EA, FATTAH SA, ABDULLAH H, KASZUBOWSKA L (2018) Age-associated functional morphology of thyroid and its impact on the expression of vimentin, cytokeratins and VEGF. The role of nigella in refinement. *Folia Histochem Cytobiol*, 56(3): 159-171.

ZHU S, SCHUERCH C, HUNT J (2015) Review and updates of immunohistochemistry in selected salivary gland and head and neck tumors. *Arch Pathol Lab Med*, 139(1): 55-66.

CASE REPORT Eur J Anat, 28 (5): 621-624 (2024)

Unveiling an uncommon anatomical variation: a case report on mandibular coronoid foramen

Karthikeya Patil, Sanjay C.J., Eswari Solayappan, Varusha Sharon Christopher

Department of Oral Medicine and Radiology, JSS Dental College and Hospital, JSS Academy of Higher Education and Research, Mysuru – 570015, Karnataka, India

SUMMARY

This case report highlights the rare discovery of a coronoid foramen in the mandible of a 55-year-old woman, a finding that deviates from conventional anatomical norms. The coronoid foramen, an unusual anatomical variation in adults, is often overlooked, emphasizing the need for meticulous exploration and diagnostic imaging in clinical practice. This discovery not only contributes to the growing body of knowledge on anatomical variations but also emphasizes the significance of thorough radiographic assessments for accurate diagnosis and treatment planning in dental and maxillofacial practice.

Key words: Coronoid foramen – Mandible – Anatomical variation

INTRODUCTION

The skeletal system serves as the framework of the human body, providing structural support, protection for vital organs, and guiding a range of movements. The fundamental unit of anatomy is the basis for medical diagnosis, care, and treatment. Human anatomy was once considered highly notable, and frequently represented cases of severe anomalies or variations (Bergman, 1988). There have been a handful of documented anatomical investigations of the human mandible that have demonstrated morphological diversity.

Although the existence of these variations as supplementary foramina may presumably support medical personnel in determining appropriate anesthesia and nearly flawless surgical abilities, few individuals still confront challenges for intuitive dental operations (Sferlazza et al., 2022). Using conventional radiographs, this anatomical variation is rarely seen in clinical practice. However, in panoramic radiography, the superimposition of anatomical components that cause distortion and magnification can be misinterpreted by the diagnostician. Conversely, in order to examine these anatomical variations, CBCT is an effective imaging modality that may provide excellent spatial resolution. This was noticeable in our case since the coronoid foramina had been overlooked by the panoramic radiography.

Corresponding author:
Dr. Sanjay C J. Department of Oral Medicine and Radiology, JSS Dental College and Hospital, JSS Academy of Higher Education and Research, Mysuru – 570015, Karnataka, India. Phone: +91 97425 65566. E-mail: drsanjaycj_dch@jssuni.edu.in - Orcid: 0000-0003-2830-1481

Submitted: January 10, 2024. **Accepted:** March 1, 2024

https://doi.org/10.52083/ZUST3744

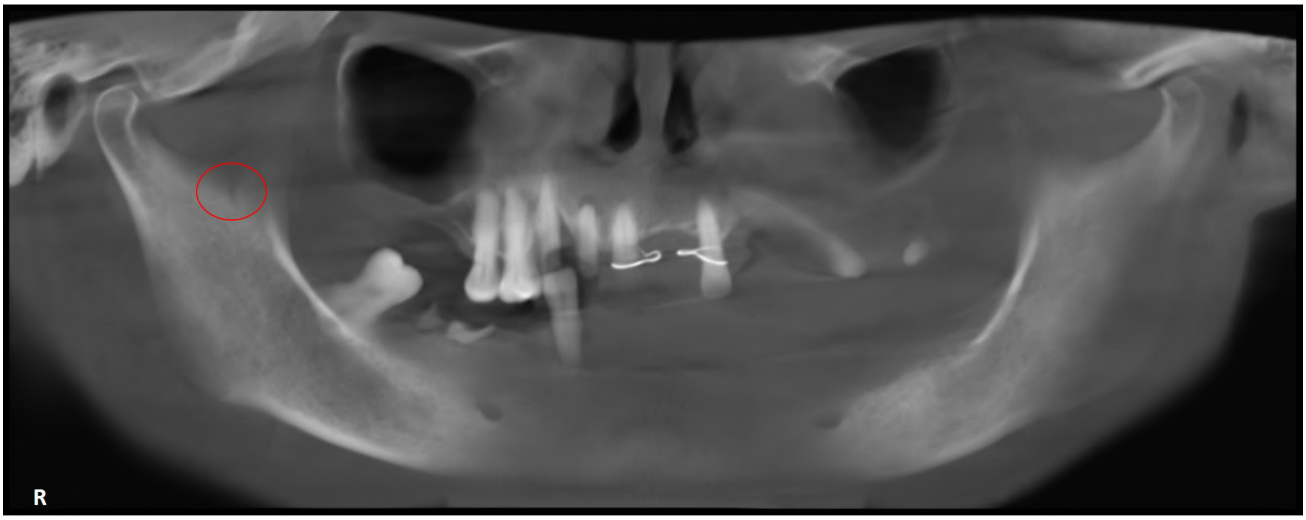

Fig. 1.- Presence of coronoid foramen in the orthopantomogram.

Understanding such anatomical variations helps in learning various surgical methods, such as treatment planning and resolving diagnostic issues (Hast and Garrison, 2000). Therefore, it is crucial to have a solid grasp of clinical anatomy and any potential individual variances in anatomy in order to execute safe and invasive procedures. One such rare variation in the structural morphology of the coronoid process of the mandible is the presence of the coronoid foramen.

Cone-beam computed tomography (CBCT) detected an unforeseen presence of a clearly delineated coronoid foramen in the patient's right mandibular region in this particular instance. The rarity of this anatomical attribute in adult individuals, specifically in the mandible, emphasizes the criticality of thorough anatomical examination and diagnostic imaging in the field of medicine.

CASE REPORT

A 55-year-old female patient presented with a chief complaint of loose teeth in the upper and lower arch and desired to get them replaced. The patient was hypertensive and had Type-2 diabetes mellitus, for which she was getting treatment through medical management. Intraoral examination revealed generalized gingival recession with deep periodontal pockets due to poor oral hygiene. The patient was diagnosed with chronic generalized periodontitis, with a partially edentulous upper and lower arch. A preliminary panoramic radiograph was advised for full mouth extraction, which exhibits widespread horizontal and vertical bone loss, with a poor prognosis and a questionable oval-shaped radiolucency on the right sigmoid notch, measuring about 1 x 2 mm (Fig. 1).

As the oval-shaped radiolucency was intriguing, CBCT (cone beam computed tomography) was further advised. The 3D-rendered image of the mandible shows a defect in the right sigmoid notch (Fig. 2). Sagittal view shows well-defined radiolucency measuring about 2 x 2 mm, which is 2 cm away from the coronoid process. Orienting in coronal view shows communication with the lingual cortical plate. It was finally found to be a coronoid foramen. The patient was recalled after six months for follow-up; there was no apparent alteration in the panoramic image or CBCT investigation (Fig. 3).

DISCUSSION

Coronoid foramen, also known as 'Foramen of Nyer' (FN), was first discovered by clinical series using CBCT (Firdoose Chintamani Subhan et al., 2023). The coronoid foramen is a small opening that can sometimes be present in the coronoid process of the mandible as a unilateral or bilateral representation. However, it is essential to note that the coronoid foramen is not always present, as its occurrence can vary among individuals and is considered a normal anatomical variation (Keats, 1993).

During fetal development, the mandible forms through a series of intricate processes involving

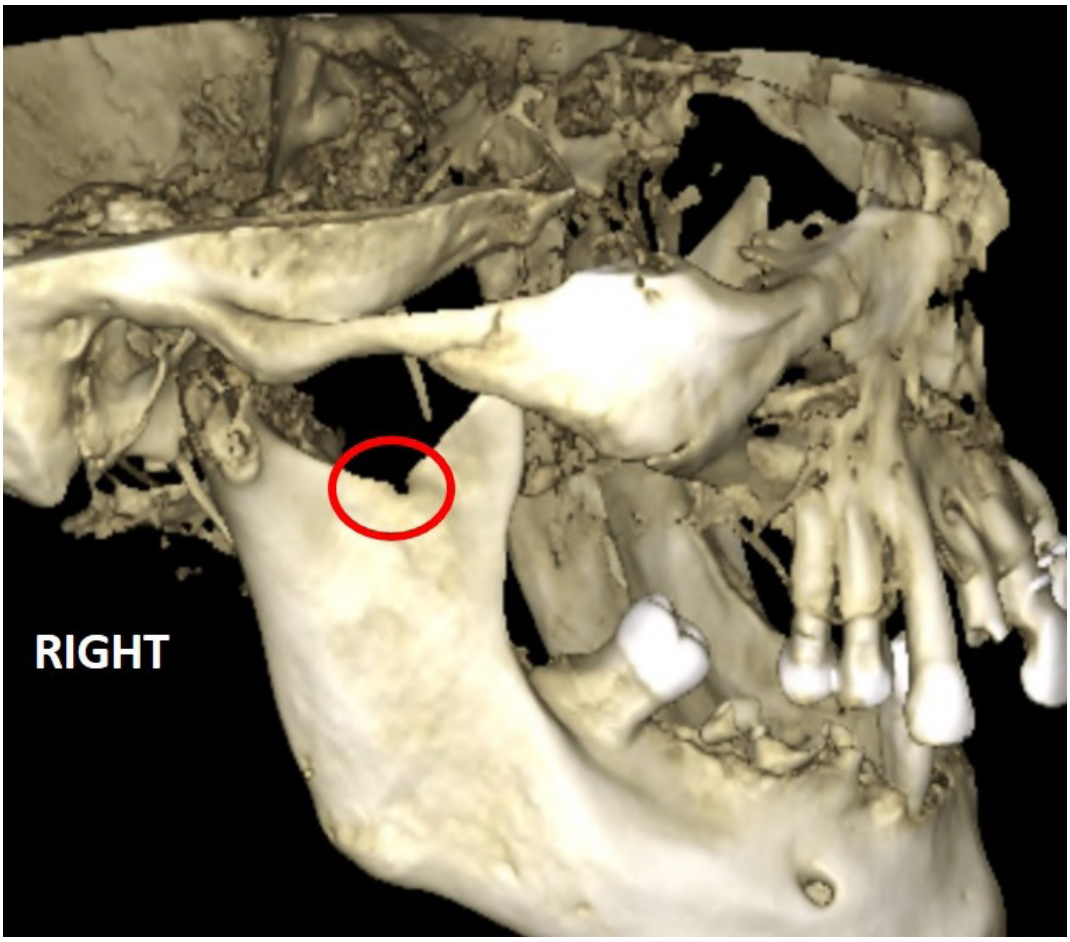

Fig. 2.- Coronoid foramen in the right sigmoid notch in the 3D rendered image.

the migration and fusion of neural crest cells, which give rise to various craniofacial structures. The specific factors that lead to the formation or absence of the coronoid foramen are not entirely understood, and they are likely influenced by genetic and environmental factors (Hauser and De Stefano, 1989). In some cases, the coronoid foramen may be present due to incomplete fusion or perforations in the bone during development. The majority of the foramina and canals gradually disappear between birth and the first year of life. It is important to emphasize that the presence of the coronoid foramen is generally considered a normal anatomical variation, and is not necessarily associated with any pathology or functional impairment (Arey, 1924; Hast and Garrison, 2000; Hauser and De Stefano, 1989; Keats, 1993).

The mandibular coronoid foramen's evolutionary hypothesis states that, apart from the elephant's, no coronoid foramina have ever been

Fig. 3.- Coronoid foramen in CBCT sections; **A**: Sagittal; **B**: Coronal; **C**: Axial.

seen in humans or any other Proboscidean. A specimen of “Elephas Maximus” was interpreted by Ferretti and Debruyne in 2010 to have a coronoid foramen that “merged with the alveolus of the distal most erupting molar” to produce a coronoid canal (Ferretti and Debruyne, 2010). Tassy and Shoshani (1988) originally recognized this coronoid canal as a synapomorphy of paenungulates. This feature has been documented in the fossil Macroscelididae and is regularly found in the majority of adult paenungulates (Tassy and Shoshani, 1988).

Sometimes anatomical landmarks may be difficult for the surgeon to locate due to these variations. When reviewing head and neck imaging, it is the radiologist’s responsibility to closely examine the topographic anatomy to look for variations and record them, especially if surgery is being considered. Higher imaging modalities, including magnetic resonance imaging, are required in order to comprehend and analyze the contents of the coronoid foramen (Sferlazza et al., 2022).

Such variability in the mandible could render it difficult to provide appropriate anesthesia for routine dental treatments. Because neurovascular bundles can occupy such foramina, in such instances treatment plans for jaw surgeries may also need to be modified. Furthermore, the involvement of the contents of such foramina may result in unanticipated consequences such as hemorrhage and postsurgical paresthesia. Recognizing such variances has special significance for dental implants and other surgical procedures like orthognathic or corrective mandibular surgeries, which entail diagnostic methods and therapeutic measures (Iwanaga et al., 2020; Yammine, 2014).

In conclusion, the identification and understanding of anatomical variations such as the mandibular coronoid foramen are crucial for dental and maxillofacial professionals in clinical practice. This case report sheds light on the presence of a rare accessory foramen in the mandibular coronoid process, emphasizing the significance of meticulous anatomical knowledge in surgical and diagnostic procedures. The recognition of such variations holds implications for oral surgery, anesthesia administration, and even forensic investigations. As we continue to uncover the intricacies of craniofacial anatomy, this report underscores the importance of comprehensive pre-operative assessments and interdisciplinary collaboration, ensuring optimal patient care and contributing to the evolving landscape of oral and maxillofacial sciences.

REFERENCES

AREY LB (1924) *Developmental anatomy: A text-book and laboratory manual of embryology*. WB Saunders.

BERGMAN RA (1988) Compendium of human anatomic variation: text, atlas, and world literature. https://cir.nii.ac.jp/crid/1130000798277464448

FERRETTI MP, DEBRUYNE R (2010) Anatomy and phylogenetic value of the mandibular and coronoid canals and their associated foramina in proboscideans (Mammalia). *Zool J Linnean Soc*, 161(2): 391-413.

FIRDOOSE CHINTAMANI SUBHAN N, AWADALLA ALSALEH MM, BEGUM SYED G, KHAIR SU (2023) Clinical anatomy of coronoid foramina of mandible and review of its implications in maxillofacial surgery. *Surg Radiol Anat*, 45(4): 445-452.

HAST MH, GARRISON DH (2000) Vesalius on the variability of the human skull: Book I chapter V of De humani corporis fabrica. *Clin Anat*, 13(5): 311-320.

HAUSER G, DE STEFANO GF (1989) *Epigenetic variants of the human skull*. Schweizerbart Stuttgart, pp 230-243.

IWANAGA J, KIKUTA S, IBARAGI S, WATANABE K, KUSUKAWA J, TUBBS RS (2020) Clinical anatomy of the accessory mandibular foramen: application to mandibular ramus osteotomy. *Surg Radiol Anat*, 42(1): 41-47.

KEATS TE (1993) Normal anatomic variation: a never ending saga. *Clin Imaging*, 17(2): 169.

SFERLAZZA L, ZACCHEO F, CAMPOGRANDE ME, PETRONI G, CICCONETTI A (2022) Common anatomical variations of neurovascular canals and foramina relevant to oral surgeons: a review. *Anatomia*, 1(1): 91-106.

TASSY P, SHOSHANI J (1988) The Tethytheria: Elephants and their relatives. In: Benton MJ (ed.). *The Phylogeny and Classification of the Tetrapods: Vol. 2. Mammals*. The Systematics Association, Special Volume No. 35B. Oxford University Press, Oxford (UK), pp 283-315.

YAMMINE K (2014) Evidence-based anatomy. *Clin Anat*, 27(6): 847-852.

CASE REPORT Eur J Anat, 28 (5): 625-629 (2024)

Bilateral cogwheel grooves observed on lateral condyles of femur and patellar articular surfaces: a cadaveric case report

Schafer Paladichuk, Ronald F. Walser, Alex Gonzaga, Jonathan Lindsey, Charles Martin

Anatomy Department, Pacific Northwest University of Health Sciences, College of Osteopathic Medicine, Yakima, Washington, USA

SUMMARY

The knee joint comprises the articulation of the femur and tibia, the femorotibial joint, and articulation between the femur and patella, the patellofemoral joint. In non-pathological anatomy, the articular surfaces of the femur, tibia, and patella are smooth, allowing for fluid motion of all joints associated with the knee. The bilateral knees of a cadaver were dissected and analyzed due to the presence of bilateral longitudinal, parallel cogwheel grooves on the lateral femoral condyles and dorsal surface of the patella. The evenly organized grooves are an odd occurrence, especially since very few cases have been reported. Termed Cogwheel grooves, they are grossly visible longitudinal grooves on femoral condyles and the articular surface of patellae that interlock together. Health practitioners should be aware of the potential presence of cogwheel grooves in the knees. In knees with cogwheel grooves, the knee motion may initially appear appropriate with flexion or extension of the knee; however, restriction could be expected when lateral movement of the patella is facilitated. Depending on the depth of the cogwheel grooves, patients may be diagnosed with a hypomobile patellae, as the only way to likely manipulate the patellae laterally or medially would be to distract the patella to disengage the grooves prior to lateral or medial movement.

Key words: Cogwheel grooves – Patellofemoral joint – Osteoarthritis – Cadaver – Knees

INTRODUCTION

The patellofemoral and femorotibial joints assist in establishing the functional foundation for the lower extremity through the formation of unique pulleys and levers (Bandovic et al., 2021; Brennan et al., 2002; Bump and Lewis, 2023; Flandry and Hommel, 2011). In normal anatomy, the hyaline cartilage-lined articular surfaces of the femur and patella should be smooth (Brennan et al., 2002), allowing for fluid motion of the femorotibial and patellofemoral joints. These joints must articulate smoothly and seamlessly, as the lower extremity is typically exposed to constant compressive forces and complex movements (Bump and Lewis, 2023).

The presence of bilateral longitudinal, parallel, and evenly organized ridges on lateral femoral condyles and articular surface of patellae is an abnormal occurrence, only noted in literature once (Rogers and Dieppe, 1993). In the report, these

Corresponding author:
Ronald F Walser. 200 University Parkway, Yakima, Washington, 98901, USA. Phone: (509) 249-7895. E-mail: rwalser@pnwu.edu

Submitted: March 4, 2024. **Accepted:** April 1, 2024

https://doi.org/10.52083/AKIC7738

Fig. 1.- Gross image of left knee looking from distal to proximal demonstrating the observed cogwheel grooves of the lateral femoral condyle.

Fig. 2.- Gross image of left knee looking from proximal to distal displaying the relationship between the cogwheel grooves on the lateral femoral condyle and articular surface of patella.

ridges were reported with varying depths and peak-to-peak distances, but when the articulating surfaces of the femur and patellae were approximated, they matched up, giving a cogwheel appearance (Rogers and Dieppe, 1993). The purpose of this case report is to describe the abnormal occurrence of bilateral longitudinal ridges, or cogwheel grooves (as described in Rogers and Dieppe article), found in the knees of a cadaver.

MATERIALS AND METHODS

The bilateral knees of a 98-year-old female cadaver used in a university anatomy course were analyzed. The past medical history of the doner was unobtainable and the rights of the donor were protected. To secure an appropriate view of the patellofemoral joints and obtain measurements of the internal aspects of bilateral knees, the quadriceps tendons were severed, and the patellae were reflected inferiorly. Both femoral heads were then dislocated to measure femoral length in millimeters from the head of the femur to the distal end of the medial condyle. Tibias were also measured bilaterally from the tibial plateau to the plafond of the tibia. These measurements were completed to determine if there was a difference in femur length between sides. Photos of the bilateral femoral condyles and the articular surfaces of patellae were taken (Figs. 1-3), and radiographs of the left patellofemoral joint were completed (Figs. 4-6) to show the cogwheel grooves.

RESULTS

Cogwheel grooves were observed bilaterally on the lateral femoral condyles and the articular surface of the patellae (Figs. 1-6). No ridges or grooves were seen within the hip or talocrural joints. A slight bilateral genu valgum was apparent upon inspection of the cadaver in the supine position. The right femur length was 423 mm, and the left femur length was 419 mm; however, left hip replacement was present. The right tibial length was 345 mm, and the left tibial length was 343 mm. The cogwheel grooves were well isolated to the lateral femoral condyle and the near entirety of the articular surface of the patellae bilaterally (Figs. 1-2). The grooves also were more prominent within the left knee than the right knee.

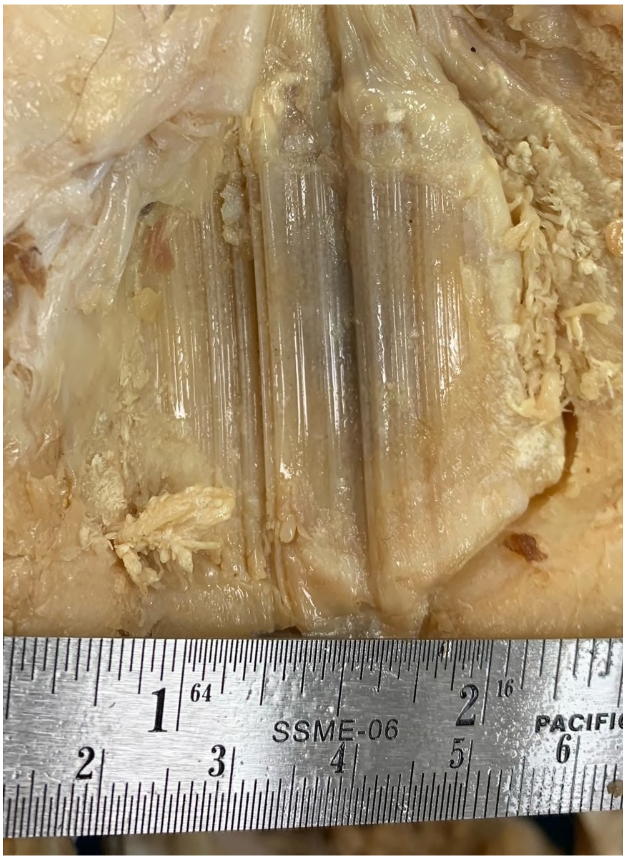

Fig. 3.- Gross image of the articular surface of the left patella demonstrating the observed cogwheel grooves.

Fig. 4.- Anterior/Posterior radiographic image of the left lower extremity.

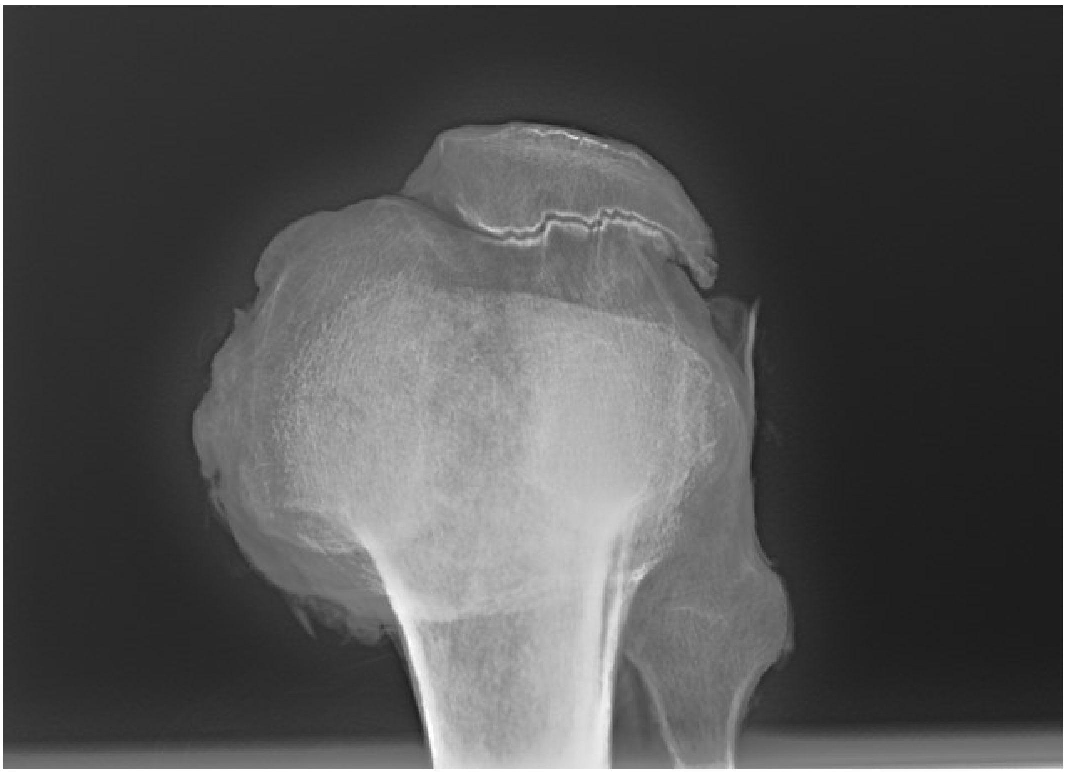

Fig. 5.- Radiographic image of the left knee displaying the cogwheel grooves observed on the lateral femoral condyle and articular surface of patella.

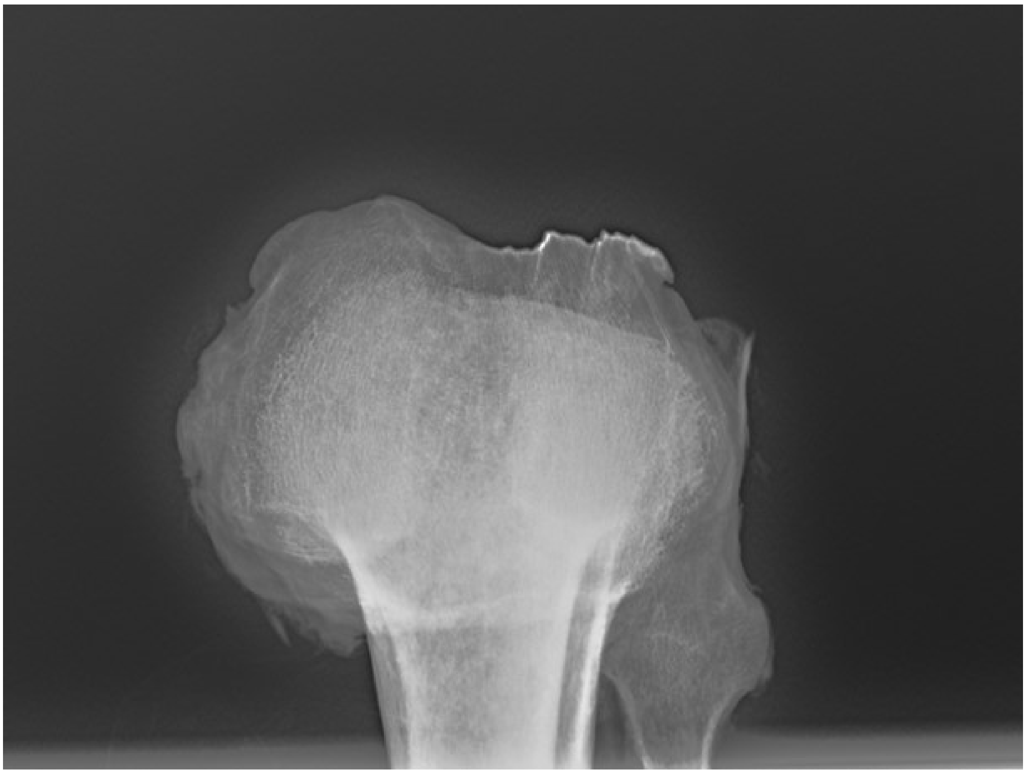

Fig. 6.- Radiographic image of the left knee with the patella removed demonstrating the cogwheel grooves observed on the lateral femoral condyle.

DISCUSSION

The absence of reports and literature to support the occurrence of bilateral longitudinal grooves on lateral femoral condyles and articular surfaces of patellae may be the result of underreporting or the rare occurrence of cogwheel grooves (Rogers and Dieppe, 1993). Potential etiologies that should be considered include, but are not limited to, osteoarthritis and patellofemoral syndrome (Brennan et al., 2002; Bump and Lewis, 2023).

The grooves observed in the cadaver on the lateral femoral condyles and patellae could be due to a primarily isolated genu valgum or secondary to weakened musculature (Bump and Lewis, 2023). It is plausible that an increased Q-angle and resultant increased contact of the patellae on the lateral femoral condyles over time could potentially result in advanced osteoarthritis (Eckenrode et al., 2018; Flury et al., 2020). Additionally, the biomechanical effects of the left hip replacement may have contributed to the more pronounced ridges observed on the left lateral femoral condyle and patella. However, these cannot positively be linked. In this case, it cannot be ascertained whether the cogwheel grooves are the result of pathological sequelae or secondary to aging or both. Future studies should focus on correlating medical history and demographic information to cases of cogwheel grooves found in knees. This case report may offer clinicians documentation of this presentation of cogwheel grooves.

ACKNOWLEDGEMENTS

The authors sincerely thank those who donated their bodies to science so that anatomical research and teaching could be performed. Results from such research can potentially increase scientific knowledge and improve patient care. Therefore, these donors and their families deserve our highest respect.

REFERENCES

BANDOVIC I, HOLME MR, FUTTERMAN B (2021) Anatomy, bone markings. In: StatPearls. Treasure Island (FL): StatPearls Publishing; November 2, 2023.

BRENNAN DD, BRUZZI JF, THAKORE H, O'KEANE JC, EUSTACE S (2002) Osteosarcoma arising in a femur with melorheostosis and osteopathia striata. *Skeletal Radiol*, 31(8): 471-474.

BUMP JM, LEWIS L (2023) Patellofemoral syndrome. In: StatPearls. Treasure Island (FL): StatPearls Publishing. Available from: https://www.ncbi.nlm.nih.gov/books/NBK557657/.

ECKENRODE B, KIETRYS D, PARROTT S (2018) Effectiveness of manual therapy for pain and self-reported function in individuals with patellofemoral pain: Systematic review and meta-analysis. *JOSPT*, 48(5): 358-371.

FLANDRY F, HOMMEL G (2011) Normal anatomy and biomechanics of the knee. *Sports Med Arthrosc*, 19(2): 82-92.

FLURY A, HOCH A, ANDRONIC O, FRITZ B, IMHOFF FB, FUCENTESE SF (2020) Increased femoral antetorsion correlates with higher degrees of lateral retropatellar cartilage degeneration, further accentuated in genu valgum. *Knee Surg Sports Traumatol Arthrosc*, 29(6): 1760-1768.

ROGERS JM, DIEPPE PA (1993) Ridges and grooves on the bony surfaces of osteoarthritic joints. *Osteoarthritis Cartilage*, 1(3): 167-170.

TEACHING IN ANATOMY Eur J Anat, 28 (5): 631-634 (2024)

A comparative analysis to assess anatomical illustrations via three AI-Driven Text-to-Image generators

Ayesha Sikandar, Hafiza Moatter Bahar

Department of Biological Sciences, Faculty of Science and Technology, Virtual University of Pakistan

SUMMARY

In recent years the popularity of artificial intelligence (AI) has increased rapidly. While the machine itself can be built for deep learning in order to enhance its own efficiency through sophisticated networks, artificial intelligence (AI) uses machine-learning models to store, calculate, analyze, and even enhance extensive volumes of data that have to be retrieved whenever needed. Text-to-image AI models like Midjourney, Microsoft Bing Image Creator Powered by DALL- E, and Craiyon can generate artistic and impressive images. In this study, anatomical representations of the human ribs, brain, and lungs were produced by evaluating the above three AI-powered text-to-image producers. The generators were evaluated based on how well they represented the basic structure of ribs including correct number of ribs, false and floating ribs, sulcus and gyrus, as well as the structure of the cerebellum and thalamus. Not a single generator generated anatomically correct anatomical structures. It is required to add accurate images to the training databases to increase the accuracy. The study highlights the continued need of human medical illustrators, particularly in guaranteeing the availability of precise and understandable pictures. Improving their accuracy necessitates augmenting the training databases with anatomically correct images to help students.

Keywords: Anatomy – Anatomical structures – AI model – Text to image – Brain – Ribs and Lungs

INTRODUCTION

The aim of this study is to determine the usability of images in education that are produced using artificial intelligence. Educators of anatomy are frequently in the forefront of implementing cutting-edge and novel technology, such artificial intelligence (AI), into their curricula. Hard lessons gained from the application of AI tools in other fields, even though it may present new chances for anatomical teaching (Lazarus et al., 2022). Creation of images through text has made an abrupt change towards becoming a prevailing phenomenon. With the system of text-to-image creation, anyone can create artworks and digital images. This arises the question whether text-to-image synthesis is creative (Oppenlaender, 2022). Current techniques for generating text to images offer a fascinating way to convert between the im-

---

Corresponding author:
Ayesha Sikandar. Department of Biological Sciences, Faculty of Science and Technology, Virtual University of Pakistan. E-mail: ayesha.sikandar@vu.edu.pk

Submitted: January 15, 2024. **Accepted:** April 1, 2024

https://doi.org/10.52083/DLQJ8889

age and text domains. The generated image fidelity and text relevancy have gradually improved thanks to these techniques, but their applicability and quality are still constrained by a number of critical gaps that need to be filled. (Gafni et al., 2022) The process of creating visuals from written descriptions is known as text-to-image synthesis. Creating images on its own is a difficult task. Text and picture production together increase complexity because the data have to be merged from two distinct modalities. A similar strategy is used in the majority of current efforts on text-to-image synthesis when it comes to neural architectures (Souza et al., 2020). For medical image analysis to be used for both diagnostic and interventional purposes, robust and quick identification of anatomical structures is required. Currently available anatomy detection methods are mostly based on machine-learning approaches that use massively annotated image databases to understand how the collected anatomy should look. The use of less-than-ideal feature engineering approaches and, most significantly, computationally inadequate search algorithms for anatomy detection are the shortcomings of these technologies. (Ghesu et al., 2019).

Medical imaging has made substantial use of AI algorithms for pathology diagnosis, segmentation, and identification of anatomical structures. Research has demonstrated the efficacy of AI-based techniques in the interpretation of radiological images, such as CT scans, X-rays and MRIs for accurate anatomical localization and anomaly detection (Litjens et al., 2017).

Early uses of AI in the medical field mostly concentrates on automating medical tasks; more recently, prognostication and risk prediction have gained attention. Numerous studies look into how AI might help physicians with routine chores, helping with workflow optimization, quantification, and reporting.

Nevertheless, many clinical AI applications are still mostly utilized in research settings and are not yet widely adopted in clinical practice (Greenstein, 2018).

The rapid expansion of information and communication technology has led to substantial advancements in recent years, particularly in the software space. Artificial intelligence is without a doubt one of these advancements. Many artificial intelligence programs can be utilized for educational objectives, even though they can also be used for personal goals like amusement and usefulness. It is evident from a review of the area text that defining artificial intelligence is a challenging task. According to Wang (1995), the concept must be updated on a regular basis, because artificial intelligence is always evolving. According to Encyclopedia Britannica (2022), artificial intelligence is the capacity of a computer or computer-controlled robot to carry out tasks that are normally performed by intelligent entities. Furthermore, it has been suggested that the dimensions of artificial intelligence talents and capacities should take precedence over a precise definition (Schuett, 2019). Due to all of these factors, artificial intelligence is a phenomenon that spans multiple academic disciplines, including biology, linguistics, computer science, neuroscience, anthropology, and philosophy (Luckin et al., 2016). Barillot (1994) focuses on creating a knowledge base with a symbolic model of the anatomical structures of the brain and hypermedia tools for presenting and retrieving information related to the objects in order to enable efficient communication between the user and the system.

MATERIAL AND METHODS

The following prompts were entered during the study: “accurate anatomical illustration of the human ribs”, “accurate anatomical illustration of the human lungs”, and “detailed anatomical illustration of the human brain” into Microsoft Bing Image Creator Powered by DALL- E (https://www.bing.com/create). The Midjourney bot was also fed wiyh the same text prompts using https://discord.gg/midjourney discord service and Craiyon V3 (https://www.craiyon.com/). All the three platforms were accessed on October 30, 2023. These three platforms were chosen because of their popularity, algorithm quality, ease of use and support. The ethical considerations were also kept in mind. For the execution of results (ribs, brain, and lungs), these were chosen because the differences and deficiencies that arise in the anatomical structures by the use of these image generators could easily be predicted and identified by the educators and students.

RESULTS

According to the results, the image generators can generate aesthetically pleasing anatomical images that could be included in blog posts, presentations, and other materials but did not meet the exact standards of anatomical accuracy. Exploring the anatomical structure of ribs and their connections to the spine and sternum the three generators were discovered to have consistent flaws. Important anatomical structures were missing from the images. The floating ribs (11th and 12th) are missing in all three images generated by the three different AI models (Fig. 1– (1 to 3)); on the other hand, the false ribs (8th,9th and 10th) that indirectly articulate with ribs are not illustrated properly in all three images either. The position of the prominent surface folds and grooves known as gyri and sulci, which are essential to comprehending the functional organization of the brain, were poorly depicted. Additionally, the structure of the cerebellum and the thalamus is poorly depicted, along with the medulla oblongata. Examining the intricate anatomical structure of the lungs, elucidating their bilateral placement within the thoracic cavity, the relationship between lobes, encompassing bronchi, bronchioles, and alveoli, are unclear. The number of cartilages in trachea is wrongly predicted and absent in all the images.

DISCUSSION AND CONCLUSION

Although the AI image generators look very attractive, overall, the analysis of the three AI- powered text-to-image generators showed that their

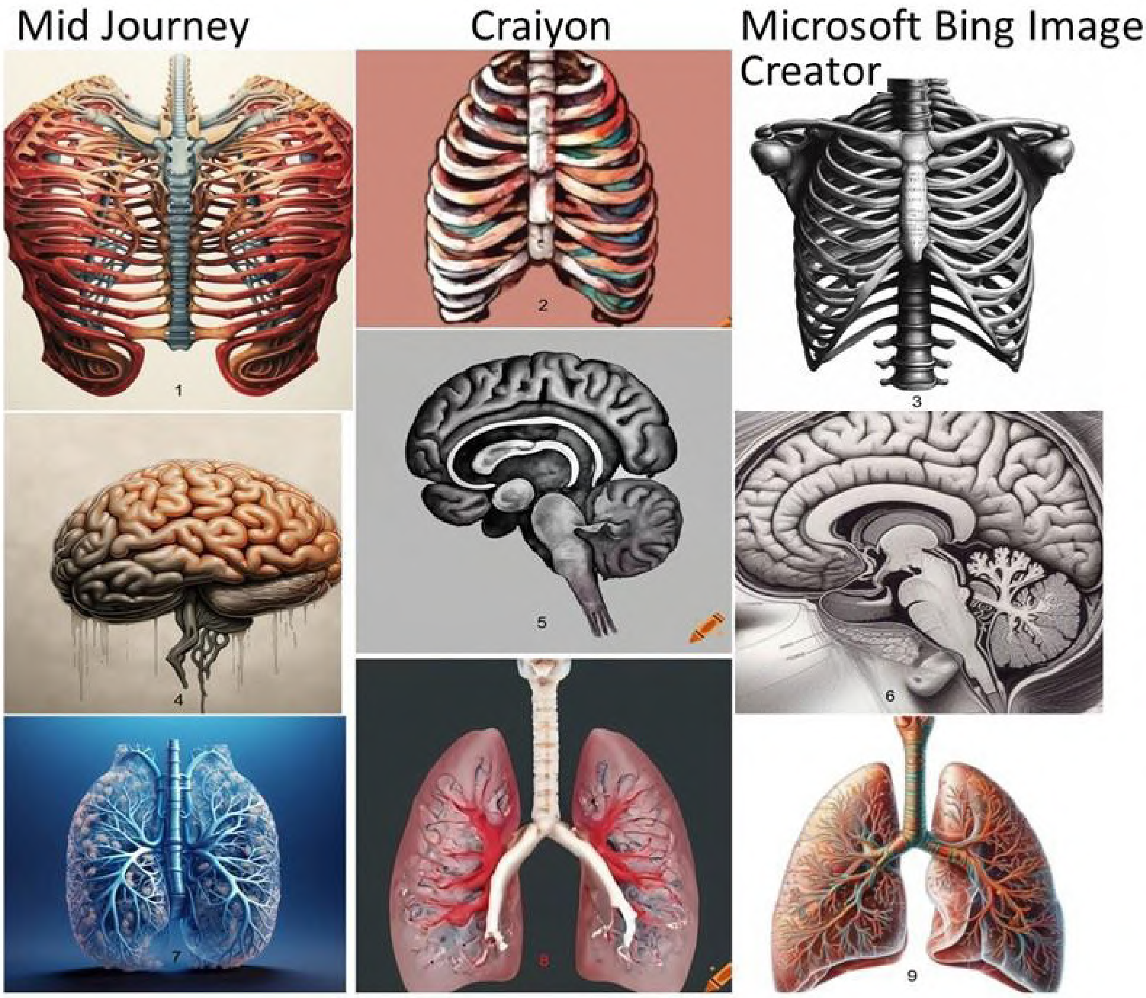

Fig. 1.- Anatomical illustrations of ribs, brain and lungs generated by AI text to image generators: Midjourney (1,4,7), Microsoft Bing Image Creator (3,6,9) and Craiyon (2,5,8).

capacity to produce precise and in-depth anatomical representations was severely limited. A similar study was conducted by Noel (2023); according to him, none of the three generators could provide illustrations that were precise and detailed enough. The author investigated that how well different AI-powered text-to-image generators could produce precise and in-depth anatomical representations of the human heart, brain, and skull. The authors attempt to evaluate these generators' potential for automating the production of medical illustrations by looking at their output, and found out greater limitations in their execution. These flaws demonstrate how AI technology is now unable to replicate the degree of accuracy and precision needed in medical anatomical representations. While AI-powered text-to-image generators have potential for a variety of uses, including medical illustration, it is important to remember that more developments and improvements are needed to guarantee that the illustrations produced meet the standards of anatomical accuracy and detail needed for clinical practice, research, and education in medicine. Medical illustrators are trained to collaborate with others to create purposeful visualizations and to communicate information visually to a specific audience. They are an essential part of the community for anatomical education; their knowledge and contributions are still crucial to the effective delivery of anatomy instruction, and they should not be disregarded or replaced (Cornwall et al., 2023). AI's potential will be regulated with the support of an ethical framework that maintains human control. AI is more than just a cutting-edge technology that needs to be regulated. It is a strong force that is changing settings, interpersonal relationships, and daily routines. It is imperative that this power be used for good purposes in order to ensure the welfare of humanity. In this process, ethics is crucial because it guarantees that AI regulations maximize its promise while minimizing its risks (Taddeo and Floridi, 2018). There are still many unexamined ethical and societal implications of using AI (Goisauf and Abadía, 2022). It is important to recognize that even the most advanced AI image generators have their constraints. Artificial intelligence (AI) image generators frequently produce esoteric graphics rather than accurate representations, which could not always meet the demands of medical illustration (Noel, 2023). The growing prevalence and use of AI in education places a responsibility on educators to learn about the capabilities and limitations of the technology, even if it needs to require new technical skills (Cornwall et al., 2023). However, it is a complex concept that requires a careful balancing of the following factors: the purpose and character of the use and the nature of the copyrighted work.

REFERENCES

BARILLOT C, GIBAUD B, MONTABORD E, GARLATTI S, GAUTHIER N, KANELLOS I (1994) Information system to manage anatomical knowledge and image data about the brain. *In Visualization in Biomedical Computing,* 2359: 424-434.

CORNWALL J, KREBS C, HILDEBRANDT S, GREGORY J, PENNEFATHER P (2023) Considerations on the use of artificial intelligence in generating anatomical images: Comment on "Evaluating AI-powered text-to-image generators for anatomical illustration: A comparative study." *Anat Sci Educ,* 2023, doi: 10.1002/ase.2347.

GAFNI O, POLYAK A, ASHUAL O, SHEYNIN S, PARIKH D, TAIGMAN Y (2022) Make-A-Scene: Scene-Based Text-to-Image Generation with Human Priors. *In European Conference on Computer Vision,* 89-106.

GHESU F, GEORGESCU B, ZHENG Y, GRBIC S, MAIER A, HORNEGGER J, COMANICIU D (2019) Multi-scale deep reinforcement learning for real-time 3D-landmark detection in CT scans. *IEEE Trans Pattern Anal Mach Intell,* 41(1): 176-189.

GOISAUF M, ABADÍA M (2022) Ethics of AI in radiology: a review of ethical and societal implications. *Frontiers in Big Data,* 5: 850383.

GREENSTEIN S, GULICK S (2018) Zebra medical vision. *Harvard Business School,* Case 619-014.

LAZARUS MD, TRUONG M, DOUGLAS P, SELWYN N (2022) Artificial intelligence and clinical anatomical education: Promises and perils. *Anat Sci Educ,* 17: 249-262.

LITJENS G, KOOI T, BEJNORDI BE, SETIO AAA, CIOMPI F, GHAFOORIAN M, VAN DER LAAK JA, VAN GINNEKEN B, SÁNCHEZ CI (2017) A survey on deep learning in medical image analysis. *Med Image Anal,* 42: 60-88.

LUCKIN R, HOLMES W, GRIFFITHS M, FORCIER LB (2016) Intelligence unleashed: An argument for AI in education. *UCL Knowledge Lab: London, UK.*

NOEL GP (2023) Evaluating AI-powered text-to-image generators for anatomical illustration: A comparative study. *Anat Sci Educ,* doi: 10.1002/ase.2336.

OPPENLAENDER J (2022) The creativity of Text-to-Image generation. *Proc 25th Int Acad Mindtrek Conference,* pp 192-202.

SCHUETT J (2019) A legal definition of AI. *arXiv preprint arXiv:1909.01095.*

SOUZA D, WEHRMANN J, RUIZ D (2020) Efficient neural architecture for Text-to-Image synthesis. *2020 International Joint Conference on Neural Networks (IJCNN),* pp 1-8.

TADDEO M, FLORIDI L (2018) How AI can be a force for good. *Science,* 361: 751-752.

WANG P (1995) On the working definition of intelligence. *Technical Report 94, Center for Research on Concepts and Cognition, Indiana University,* pp 1-32.

LETTER TO THE EDITOR Eur J Anat, 28 (5): 635-637 (2024)

First Human Dissector of colonial India

Uma SV[1], Chaithra Rao BR[2]

[1]Professor, Department of Anatomy, Sri Madhusudan Sai Institute of Medical Sciences and Research, Sathya Sai Grama, Muddenahalli, Chikkaballapur District, Karnataka-562101, India
[2]Associate Professor, Department of Anatomy, Nandi Medical college & Research institute, Chikkaballapura district, Karnataka

Anatomy teaching is never complete without dissection and medical education is incomplete without anatomy, which is the foundational basic medical science for all the branches of medicine. Moreover, practising medicine without understanding the human body is impossible [1]. It is a well-known fact that India has made many medical contributions to the rest of the world [1]. Almost 175-year-old dissection papers were unearthed from Calcutta Medical College and Hospital in the Anatomy Department in the year 2011[2], which are related to Asia's first human dissection carried out secretly in the city by a Bengal, Vaidya Pandit Madhusudan Gupta (1800-1856) [1,2]. He was trained in Western medicine and is credited with having performed India's first human dissection at Calcutta Medical College (CMC) in 1836, almost 3,000 years after Susruta. In fact, this is also Asia's first human dissection [3]. This act of dissection was a revolutionary move towards modern medicine. Unfortunately, Dr Gupta's name is mostly missing in the annals of historical medical records.

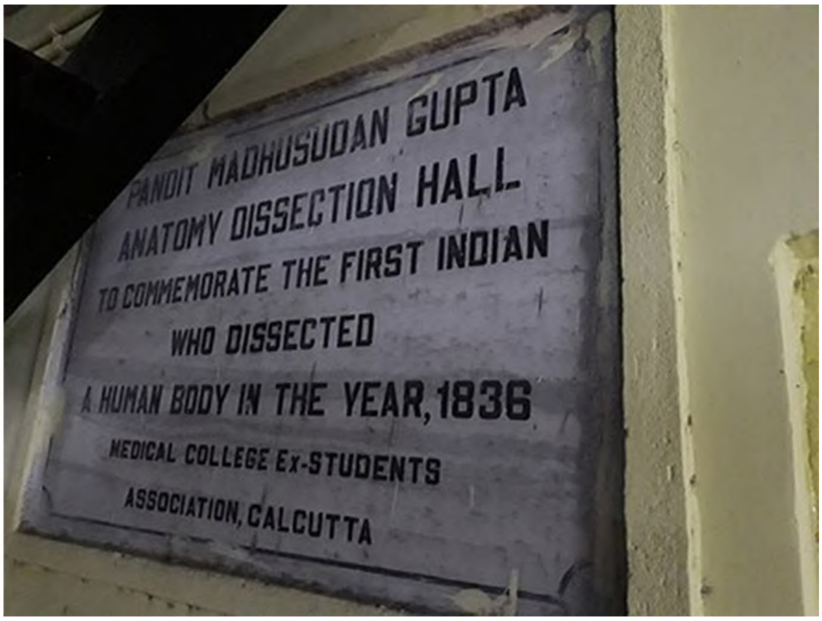

Pandit Madhusudan Gupta (picture courtesy: Wikipedia)

Corresponding author:
Dr. Uma SV. Phone: 998601861. E-mail: drsvuma@gmail.com

Submitted: March 19, 2024. **Accepted:** May 2, 2024
https://doi.org/10.52083/COFW7942

Dr Gupta was born into a Vaidya (traditional ayurvedic practitioners) family in Hooghly[1]. Being a Sanskrit scholar, he was teaching in Sanskrit college and was also an Ayurvedic practitioner. He voluntarily attended several anatomy and medicine lectures given by British doctors [1].

In 1833, the British army were not satisfied with the services of Kolkata's medical staff, who were trained in native medicine [2]. A committee was formed by the then Governor General Lord William Bentinck in October 1833, which consisted of 6 members: viz., Dr John Grant, J.C.C. Sutherland, C.E. Trevelyan, Thomas Spence, Dr. M.J. Bramley and Ram Comul Sen, the only Indian member. This committee was to replace native medical institutions with scientific medical school, with English as the language of instruction, and the curriculum was fashioned at par with the European medical institutions [4]. As a consequence, the Ayurvedic and Unani courses taught at the Sanskrit College and Native medical institution were abolished [1,2]. The British replaced these native medical schools with a fully equipped Calcutta Medical College (CMC), to educate and train the natives in "the art of healing" in western medicine. On January 28, 1835, the then Governor-General William Bentinck passed a government order (G.O. No. 28, dt.28.1.1835) declaring the establishment of the first medical college in India, Medical College Bengal, which became affiliated with the University of London [4].

The College began with three European Professors, Dr M.J. Bramley, Dr H.H. Goodeve, and Dr W.B. O'Shaughnessy, as well as three native physicians, Pandit Madhusudan Gupta, Nabakrishna Goopta, and Ram Issur Awasthi. These last three persons became demonstrators in Medical College [4]. In 1835, Gupta was transferred to the CMC, as a native teacher. Even as the course began, teaching anatomy dissection remained a problem because of religious taboo [3,5].

Pandit Madhusudan Gupta, on 10 January 1836[4,5], carried out the dissection work on a dead body with the assistance of four students who were Rajkrishna Dey, Umacharan Seth, Dwarkanath Gupta, and Nabin Chandra Mitra [3, 5]. He held the knife with strong and steady hand, made a deep and long incision in the breast, and relieved the stress of the spectators and his guides [1,5]. It was also revealed that Dwarkanath Tagore, successful entrepreneur and grandfather of Rabindranath Tagore, also helped smuggle the corpse in for dissection [1,5]. Outside the hospital, a crowd had gathered to protest this unholy act, so the administration secured the gates and guarded them [1,6]. Madhusudan Gupta was counselled, influenced, and guided to carry out dissection by British doctors Goodeve and Bremley, who were then Head of the Department of Anatomy and the Principal of Calcutta medical college respectively [5,7]. Scottish Philanthropist David Hare and educationist John Elliot Drinkwater Bethune also played an important part in convincing Gupta to break the social taboo and become the pioneer of the Western Medical system of medicine in India [5].

Following the first dissection, Gupta completed formal medical qualifications and received a medical degree, G.M.C.B. (Graduate of the Medical College of Bengal) on 26 November 1840 [7]. However, it is completely true that before Madhusudan Gupta, in ancient India, Susruta had conducted examination, surgeries and C-sections on dead bodies, which has been mentioned in *Susruta Samhita* (III CE). Later the handling of cadavers was discouraged, and the advantage of gaining knowledge through cadavers lost its scientific purpose for religious reasons [5].

Dr. Gupta also conducted extensive studies on puberty, medical uses of leeches and high neonatal and maternal mortality in Indian women, fought vaccine hesitancy concerning smallpox, and advocated for proper sanitation to reduce diseases [1]. He also wrote books like *London Pharmacopoeia* in Bengali, *Shoreer-vidya*, and also translated *Shusruta Samhita*, and Hooper's *Anatomist Vademecum*, etc. [4,6].

Madhusudan Gupta died of diabetic gangrene and septicemia on November 15, 1856 [3,4,5]. His contributions to the progress of the medical education in India should be remembered forever, as becoming an expert in Western medical science from being an Ayurveda practitioner is not an easy task [4]. Great honor should therefore be due to Pandit Madhusudan Gupta [6]. Appeals have been sent by various associations to the concerning authority to declare 10 January as "National

Medical Education Day", to commemorate the day on which a dissection of a dead human body was practiced in modern India, in honor and respect for this great anatomist's contribution to medical education [4].

"Pandit Madhusudan Gupta Memorial Lifetime Achievement Award" in Anatomy was awarded to Professor A.K. Dutta for his laudable work.

REFERENCES

1. Behind Asia's 1st Human Dissection: The Doctor Who Brought Modern Medicine to India, Divya Sethu.2022
2. 175 years old dissection paper unearthed, Jan 13, 2011. Available from: https://timesofindia.indiatimes.com/city/kolkata/175-year-old-dissection-papers-unearthed/articleshow/7272410.cms
3. Pundit Madhusudan Gupta: The first human dissector of India. *J Anat Soc India*, (2012) 61(1): 60. doi:10.1016/s0003-2778(12)80018-9
4. SANKAR KR NATH (2017) First Human Dead Body Dissection in the History of Medical Education in India & Pundit Madhusudan Goopta (1806-1856). Available from: https://aroiwb.org/pdf/ejournal/e-journal-jan-mar-2017/SankarNath.pdf [Internet]. [cited 2023 Jun 6].
5. PANDEY S (2017) Madhusudan Gupta: The man who carried out India's first dissection [Internet]. NISCAIR-CSIR, India; 2017 [cited 2023 Jun 6]. Available from: https://nopr.niscpr.res.in/handle/123456789/43018
6. Asia's first human dissection was by a Bengali doctor in colonial Calcutta, Tales, Talks, Walks, 16 March, 2022. https://www.getbengal.com/author/ttw
7. CHATTERJEE S, RAY R, CHAKRABORTY DK (2013) Medical College Bengal – A pioneer over the eras. *Indian J Surg*, 75(5): 385-390.

EJA

European Journal of Anatomy